Theory & observations of the PWN-SNR complex

Jonatan Martín Rodríguez
Institut d'Estudis Espacials de Catalunya (IEEC-CSIC)
Universitat Autònoma de Barcelona

This dissertation was supervised by:
Prof. Diego F. Torres
Dr. Nanda Rea
Tutor: Dr. Lluís Font Guiteras

Barcelona (Spain) July 2014

Pels que pensen,
pels que lluiten,
pels que pateixen,
pels que somien

Declaration and list of publications

I hereby declare that except where specific reference is made to the work of others, the contents of this dissertation are original and have not been submitted in whole or in part for consideration for any other degree or qualification in this, or any other University. This dissertation is the result of my own work and includes nothing which is the outcome of work done in collaboration, except where specifically indicated in the text. This dissertation is based in works already published detailed below:

- Martín, J., Torres, D. F. & Rea, N. 2012, MNRAS, 427,415
- Torres, D. F., Cillis, A. N. & Martín Rodríguez, J. 2013, ApJL, 763, L4
- Torres, D. F., Martín, J., de Oña Wilhelmi, E. & Cillis, A. N. 2013, MNRAS, 436, 3112
- Torres, D. F., Cillis, A. N., Martín, J. & de Oña Wilhelmi, E. 2014, JHEAp, 1, 31
- Martín, J., Torres, D. F., Cillis A., & de Oña Wilhelmi, E. 2014, arXiv:1406.1344, accepted for publication in MNRAS
- Martín, J., Rea, N., Torres, D. F. & Papitto, A. 2014, submitted in MNRAS

Jonatan Martín Rodríguez
July 2014

Acknowledgements

Com resumir una cosa infinita en un espai finit? Aquest és el gran repte amb el que em trobo escrivint aquestes línies. Darrere d'aquest treball, no només hi ha hagut la feina, l'esforç i la tècnica, que són molt importants, però no hagués estat possible de cap manera si no m'hagués trobat amb totes les persones amb les que he pogut conviure durant aquest temps, que m'han donat tot el suport necessari i m'han ensenyat allò que no es troba als llibres. A tots vosaltres, des del primer pàragraf, us vull donar les gràcies.

En primer lugar, me gustaría dar las gracias a mis dos directores de tesis, Diego y Nanda, por la confianza que han depositado en mi desde el primer día. Vuestro esfuerzo, vuestro interés, vuestra paciencia (que conmigo a veces es necesaria) y vuestro buen trato han hecho de trabajar y pasar el día a día con vosotros una grata experiencia que espero que en el futuro siga dando sus frutos. També vull agraïr al Lluís Font que hagi acceptat ser el tutor d'aquesta tesi i pel seu interés.

También quiero agradecer a mis padres (Domingo y Carmen), a mi hermano Alejandro y a toda mi familia el apoyo que me han dado durante todo este tiempo. Sin su ayuda incondicional, todo esto hubiera sido imposible.

Especial agradecimiento a mis ángeles que hacen que todo sea más fácil y llevadero. Nataly, podría escribir páginas y páginas y no acabaría. Muchas gracias por tu compañia y por tu afecto. Por las bromas y por las risas, por las conversaciones más serias, por los paseos por los pasillos, por molestarte a cruzar al otro lado del cyber cada día a saludar, y como no, por los azucarillos :-). ¡No cambies nunca, porque eres única! Daniela, vielen Dank für dein Lächeln und deine Hilfe. Tu experiencia y simpatía me han ayudado mucho. Que hubiera hecho yo sin una alemana que supiera bailar salsa? En Barcelona siempre tendrás un amigo (o como mínimo, un amigo barcelonés). Elsa, a pesar de haber compartido cyber y grupo solo un año, has sido un referente y un gran apoyo en los inicios de esta aventura. Aún se echan de menos tus planes maléficos para salir los días laborables o momentos paranormales en el cyber en que pelotitas antiestrés volaban por el cyber. Alicia, gracias por tu alegría y por tu buen humor. Esos momentos de escapada al IFAE para tomar el café o tu motivación para hacer planes en el tiempo libre no tienen precio. Ahora es el turno de los no-tan-ángeles

;-). Jacobo, el maño que ha dejado un hueco en el cyber que no se puede llenar. Por eso, aún hay carteles dando una recompensa por encontrarte. Muchas gracias por tu espontaneidad, tu buen humor y tus locuras ya sean en persona o en la lejanía, por skype o por whatsapp. Adiv, eres un grande. Gracias por tu sencillez y por todos los momentos vividos ya sea en un bar llamado Kentucky o cuando hemos hecho alguna escapada. Felipe, moltes grácies per tot amic, mai oblidaré la teva simpatia i els bons moments que hem passat junts. Hem de trobar el moment de tornar al "Magic", sense que la Daniela s'enteri ;-).

No penseu que m'oblidava de vosaltres: Kike, Antonia, Albert, Carles, Laura, Carmen, Padu i Marina. M'alegro molt d'haver-vos conegut. M'ho he passat molt bé anant amb vosaltres al "laser-tag" (quina motivació!), els sopars, els partits de futbol... Espero poder seguir vient-vos i que els vostres somnis es compleixen. Josep, t'agraeixo moltíssim la teva ajuda en el fosc món de la informàtica i que, tot i les teves amenaçes, no m'hagis portat a veure al Pepe. Alina i Aina, moltíssimes gràcies per la vostra ajuda desinteressada. El vostre suport no té preu. También a la gente del IFAE a pesar que no he podido compartir mucho tiempo con ellos: Rubén, Dani Garrido (esas barbacoas!), Alba, Daniel (argentino) y Quim. Amb el vostre permís, deixo un petit raconet per la Núria i l'Arnau. Moltes gràcies pels vostres ànims durant la meva tesi, els sopars improvitzats i per fer dels matins al cotxe una cosa divertida i distreta. Núria, amb qui faràs ara carreres de cadires al cyber? ;-). Estic convençut que tot t'anirà bé. Et deixo l'encàrrec d'administrar les "meves" taules del cyber, del pa bimbo i la "nocilla". Arnau, vigila que la Núria faci bé la seva feina i no li robis el pa bimbo. No canviïs mai, crack!

I would like to thank insistently all the people that has been in our group during these years: Andrea, Giovanna, Choni, Ana and Eric. Special thanks to Analía (gracias por tu interés y tu afecto), Emma (gracias por tu trato y sentido del humor) and Alessandro (Daje, Lazio!) to work directly with me in some projects. Jian, thank you for your support. I'm very happy to know someone like you. Daniele, tot i que fa poc que estàs a Barcelona, també has sigut una gran ajuda quan el vent ha bufat en contra i m'alegro d'haver conegut algú amb la teva senzillesa i sinceritat. Moltes grácies, amic.

No voldria acabar sense dirigir-me als amics de sempre de l'escola que han estat al peu del canó: Albert (el GR-11 nos espera!), Joan ("au va!"), Marcel ("amigooo"), Angi, Dela, Pau ("tungs-tè!"), Cris, Carlos i Coke. Igualment pels del cau: Andrés (viva Las Vegas!), Lluna, Marta, Germán, Irene, Olga i Ignasi, i a tots els membres a l'Agrupament Escolta Champagnat pel seu suport i la seva comprensió.

Finalment, vull donar les gràcies a tots els contribuients que amb la seva aportació, encara que sigui en moments de dificultat, fan possible les beques que donen l'oportunitat a molts estudiants que, com jo, simplement lluitem pels nostres somnis i una vida digna.

Abstract

In this work, we study theoretical and observational issues about pulsars (PSRs), pulsar wind nebulae (PWNe) and supernova remnants (SNRs). In particular, the spectral modeling of young PWNe and the X-ray analysis of SNRs with magnetars comparing their characteristics with those remnants surrounding canonical pulsars.

The spectra of PWNe range from radio to γ-rays. They are the largest class of identified Galactic in γ-rays increasing the number from 1 to $\sim$30 during the last years. We have developed a detailed spectral code which reproduces the electromagnetic spectrum of PWNe in free expansion ($t_{age} \lesssim$10 kyr). We shed light and try to understand issues on time evolution of the spectra, the synchrotron self-Compton dominance in the Crab Nebula, the particle dominance in PWNe detected at TeV energies and how physical parameters constrain the detectability of PWNe at TeV. We make a systematic study of all Galactic, TeV-detected, young PWNe which allows to find correlations and trends between parameters. We also discuss about the spectrum of those PWNe not detected at TeV and if models with low magnetized nebulae can explain the lack of detection or, on the contrary, high-magnetization models are more favorable.

Regarding the X-ray analysis of SNRs, we use X-ray spectroscopy in SNRs with magnetars to discuss about the formation mechanism of such extremely magnetized PSRs. The alpha-dynamo mechanism proposed in the 1990's produces an energy release that should have influence in the energy of the SN explosion. We extend the work done previously done by Vink & Kuiper (2006) about the energetics of the SN explosion looking for this energy release and we look for the element ionization and the X-ray luminosity and we compare our results with other SNRs with an associated central source.

Contents

Contents xiii

List of Figures xvii

List of Tables xxi

1 Introduction 1

- 1.1 A brief historical view 1
- 1.2 Pulsars 4
  - 1.2.1 The magnetic dipole model 4
  - 1.2.2 Electric potential and -parameter 7
  - 1.2.3 What do we observe? 8
  - 1.2.4 Magnetars 9
- 1.3 Pulsar Wind Nebulae 11
  - 1.3.1 Morphology 11
  - 1.3.2 Spectrum characteristics 14
  - 1.3.3 Current models 17
- 1.4 PWN-SNR complex evolution 18
  - 1.4.1 Free expansion phase 19
  - 1.4.2 Sedov phase 20
  - 1.4.3 Later stages for SNRs 22
- 1.5 Supernova Remnants in X-rays 24
  - 1.5.1 Thermal emission 26
  - 1.5.2 Non-thermal emission 27
  - 1.5.3 Line emission 28
- 1.6 This thesis 30

2 Time-dependent spectra of PWNe **33**

- 2.1 Description of the code 33
  - 2.1.1 The difussion-loss equation 33
  - 2.1.2 Magnetic field evolution 37
  - 2.1.3 Energy losses and escape 38
  - 2.1.4 Photon luminosity 41
  - 2.1.5 PWN expansion 44
  - 2.1.6 Code design 45
  - 2.1.7 Other tools 49
- 2.2 The Crab Nebula 51
- 2.3 Improvements and caveats 56

3 Effects in time-dependent modelling of PWNe **59**

- 3.1 Impact of approximations 59
- 3.2 Effects of B, age and E on Crab-like PWNe 67
  - 3.2.1 IC contributions for different age and E 69
  - 3.2.2 The effect of on X-ray and TeV luminosity 77
  - 3.2.3 Luminosity ratios for different wavelengths 81
  - 3.2.4 Discussion and conclusions 83

4 Systematic modeling of young PWNe **87**

- 4.1 Characteristics of the sample 87
- 4.2 Individual modelling of young PWNe 91
- 4.3 Other cases 118
- 4.4 Discussion 123
- 4.5 Concluding remarks 139

5 Is there room for ultra-magnetized PWNe? **141**

- 5.1 Non-detected PWNe at TeV energies with high E PSRs 142
- 5.2 Non-Galactic PWNe at TeV energies 155
- 5.3 High- models for non-detected at TeV PWNe 158
- 5.4 Conclusions 159

6 Comparing SNRs around magnetars and canonical PSRs **163**

- 6.1 Data analysis and reduction 163
- 6.2 Spectral analysis and results 167

6.3 Spectral line and photometric comparison with other SNRs 173
6.4 Conclusions 179

7 Concluding remarks 181
7.1 On this thesis 181
7.2 Ongoing work 183

References 185

Appendix A Energy losses equations 209

Appendix B Luminosity equations 215

List of Figures

1.1 Henry III observing a new rised star 2
1.2 The nine historical SNRs 3
1.3 Radio pulses of CP 1919 4
1.4 PP-diagram 9
1.5 Crab Nebula in X-rays 12
1.6 Crab Nebula knots in infrared 14
1.7 An example of PWN spectrum 16
1.8 Free expansion stage scheme 20
1.9 Composite image of SNR G327.1-1.1 22
1.10 1.4 GHz radio image of SNR W44 23
1.11 Tycho's SNR X-ray spectrum 28
1.12 Fe-K shell line as a function of the ionization state 29

2.1 The F function 42
2.2 The U function 43
2.3 Ratio of the PWN radii from analytical and numerical models 45
2.4 Flowchart for a complete run of TIDE-PWN. 47
2.5 Crab Nebula evolution 53
2.6 Crab Nebula cooling times 54
2.7 Crab Nebula fitted spectrum 54
2.8 Luminosity ratios for the Crab nebula 56

3.1 Crab Nebula electron evolution in comparison with other models 63
3.2 Crab Nebula spectrum evolution in comparison with other models 64
3.3 Relative distance of the Crab Nebula electron distribution with other models 65
3.4 Relative distance of the Crab Nebula spectrum with other models 66
3.5 PP-diagram of ATNF PSRs and 4 fake PSRs 68

3.6 Luminosities between 1 and 10 TeV of the IC contributions of the spectrum as a function of age 72
3.7 Luminosities between 1 and 10 TeV of the contributions of the spectrum as a function of E 73
3.8 SEDs for E=0.1, 1, and 10% of the Crab as a function of the age 75
3.9 SEDs for an age of 940, 3000, and 9000 years (from top to bottom) as a function of E 76
3.10 X-ray and TeV luminosities as a function of 79
3.11 SEDs for an age of 940, 3000, and 9000 years as a function of 80
3.12 Luminosity ratios at 940, 3000, and 9000 years as a function of 82
3.13 SEDs for Crab's injection parameters and different FIR photon density . . . 83
3.14 SEDs for different injection parameters and different FIR photon density . . 84
3.15 SEDs for different magnetic fraction and different FIR photon density . . . 85

4.1 PWNe models that differ only in age 90
4.2 SED of G54.1+0.3 as fitted by our model 95
4.3 SED of G0.9+0.1 as fitted by our model 98
4.4 SED model of G21.5-0.9 100
4.5 SED model of MSH15–52 104
4.6 SED of MSH 15–52 fitted with different assumptions 105
4.7 SED model of G292.2-0.5 108
4.8 Spectrum of the three different models for G292.2–0.5 109
4.9 SED of Kes 75 as fitted by our model 111
4.10 SED model of HESS J1356-645 114
4.11 Comparison of the electron distributions for the two models considered for HESS J1356–645 115
4.12 SED model of CTA 1 116
4.13 Example of the comparison between the ISRF obtained from the GALPROP code and the assumptions made to fit the PWNe models 128
4.14 Magnetization of PWNe as a function of the radio, X-ray, and -ray efficiency 129
4.15 G54.1+0.3 (left) and G21.5-0.9 (right) modeled with an imposed equipartition of the energetics as compared with the adopted models 131
4.16 Comparison of PWNe results 133
4.17 Radio, X-ray, and -ray luminosities of young, TeV-detected PWNe as a function of E and $_c$ of their pulsars 135

4.18 PWNe properties as a function of pulsar properties 137

5.1 Spectral fits for G310.6-1.6 PWN 145
5.2 Spectral fits for G76.9+1.0 PWN 146
5.3 Multi-frequency models of the PWN 3C 58 under different assumptions for the background photon fields 151
5.4 New models for 3C 58 using the TeV flux detection by MAGIC 153
5.5 Spectral fits for G292.0+1.8 PWN 155
5.6 PWNe in the LMC 156

6.1 Color images of Kes 73, CTB 109, N 49 & Kes 75 165
6.2 Map of the backgrounds used in the spectrum analysis 167
6.3 Spectra obtained for the Kes 73, CTB 109, N 49 & Kes 75 169
6.4 X-ray luminosity of SNR versus PSR properties 178
6.5 Percentage of PSRs and magnetars having a detected SNR 179

B.1 Electron spiraling a magnetic field line in the synchrotron luminosity calculation 216

List of Tables

2.1 Crab Nebula fit parameters 51

2.2 Crab Nebula parameters for different versions of TIDE-PWN 57

3.1 Comparison of the values obtained in the different fits of the Crab Nebula today 61

3.2 Properties of the fake PSRs considered at 940 years 67

3.3 Physical magnitudes for the fake PWNe sets 70

3.4 Ratio of the bolometric radiated power of the spectra divided by E at the given age 78

4.1 Pulsars in the ATNF catalog with less than $_c$=10 kyr. 89

4.2 Examples of radiative time-dependent models used to fit observations of young PWNe 91

4.3 Physical magnitudes obtained for the young PWNe in our study 92

4.4 Properties of the fitted models 124

4.5 Goldreich & Julian (1969) estimation and multiplicity computed from our models. 126

4.6 Comparison between modeled (w,T) and GALPROP (w^G,T^G) energy densities and temperatures 127

4.7 Correlation fits shown in the figures 130

4.8 Parameters used in search of correlations, as a function of P and P 136

5.1 Model parameters for 3C 58, N157B, N158A, G76.9+1.0, G310–1.6 & G292.0+1.8. 143

5.2 Parameters proposed for 3C58 with the TeV flux given by MAGIC 152

6.1 Observations used in this work 166

6.2 Summary of the fitted models for Kes 73, CTB 109, N 49 & Kes 75 170

6.3 Table 6.2 continued. 172
6.4 Line detections for some important SNRs in comparison with our analysis . 175
6.5 Fits for Kes 73, CTB 109, N 49 & Kes 75 using `vnei` and `vpshock` models 176
6.6 SNRs considered in our X-ray luminosity analysis 177
6.7 Spearman coefficient comparing the X-ray luminosity with the PSR parameters. 178

Chapter 1

Introduction

1.1 A brief historical view

Supernova (SN) explosions of stars have been observed for centuries. For the first civilizations, these phenomena were known simply as very bright stars that appeared spontaneously in the sky, and thought to be related to extraordinary events. The Romans called these "stars" as *novae*, which in Latin means "new stars". There are many historical records of SN observations, but the Chinese were the ones who took the most detailed record of these events. The reminiscent gas and dust structures of these explosions, the *supernova remnants* (SNRs), were observed for the first time during the 18th century. The first claimed SNR was the Crab Nebula, reported by the english astronomer John Bevis in 1731. In 1757, Charles Messier confused the Crab Nebula with the Halley's comet in 1757. When he realized his error, he included it in the Messier's catalog as a non-comet like object two years later.

In the beginning of the 20th century, other objects started to be identified as SNRs. Thanks to records collected by several ancient civilizations, the years of the SN explosions are reported for nine of the brightest SNRs (see Clark & Stephenson 1982): RCW 86 (possibly observed by the Chinese in 185 D.C.), G11.2-0.3 (possibly observed by the Chinese in 386 D.C.), G347.3-0.5 (possibly observed by the Chinese in 393 D.C.), SN 1006 (observed by the Chinese, Japanese, Arabic and Europeans in 1006 D.C.), Crab Nebula (observed by the Chinese, Japanese, Arabic and probably native Americans in 1054 D.C.), 3C 58 (possibly observed by the Chinese and Japanese in 1181 D.C.), Tycho's SNR (observed by the Europeans, Chinese and Koreans in 1572 D.C.), Kepler's SNR (observed by the Europeans, Chinese and Koreans in 1604 D.C.) and Cassiopeia A (possibly observed by the Europeans in 1680 D.C.). An image of these remnants is shown in figure 1.2. Depending on the SNR morphology, they are now defined as: shell-like and composite SNRs. Historically, compos-

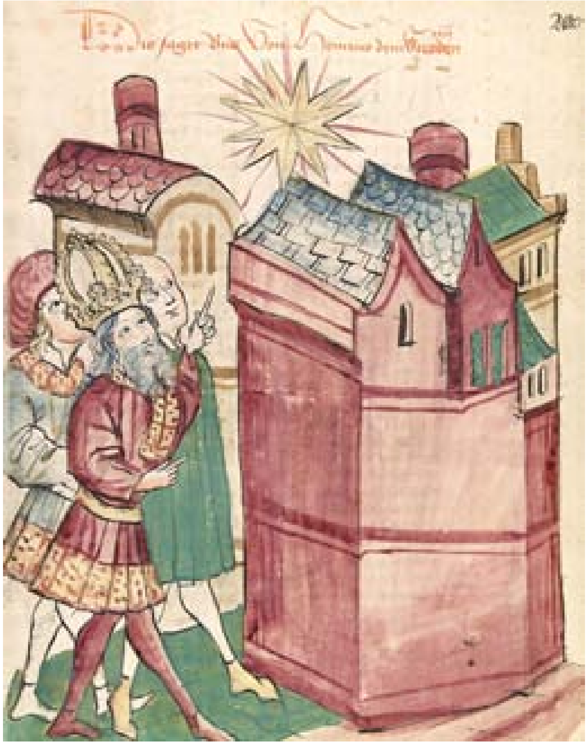

Fig. 1.1 Picture of the Holy Roman Emperor Henry III with two more people observing a new rised star over the city of Tivoli (Italy).

ite SNRs are characterized by a central non-thermal emission. These non-thermal nebulae are now recognized as *pulsar wind nebulae* (PWNe) or *plerions*, name derived from the ancient greek "pleres", which means "full" (name coined by Weiler & Panagia 1978).

In the 1930's, even before the discovery of the neutron (Chadwick, 1932), Landau (1932) suggested the existence of stars which would look like giant atomic nuclei. Later, Chandrasekhar (1935) suggested models of stars with degenerate cores, and Oppenheimer & Volkoff (1939) proposed the first equation of state for a neutron degenerate gas. Baade & Zwicky (1934) already suggested that these *neutron stars* (NS) could be formed in a supernova explosion. NS were also considered as candidates for unidentified sources in X-rays during the sixties (e.g., Morton 1964). In 1967, Jocelyn Bell dicovered the first rapidly rotating neutron star (or *pulsar*, which is an abbreviation for pulsating radio star) in the Mullard Radio Astronomy Observatory while she was analyzing radio data from quasars. The discovery was published one year later (Hewish et al., 1968). A few years later, Giacconi et al. (1971) discovered a 4.8 s pulsation from Cen X-3 in X-rays with the *UHURU* telescope, being the first X-ray pulsar discovered. Using radio observations from the Arecibo antenna, Taylor et al. (1974) discovered PSR B1913+16, the first binary pulsar (a binary system with

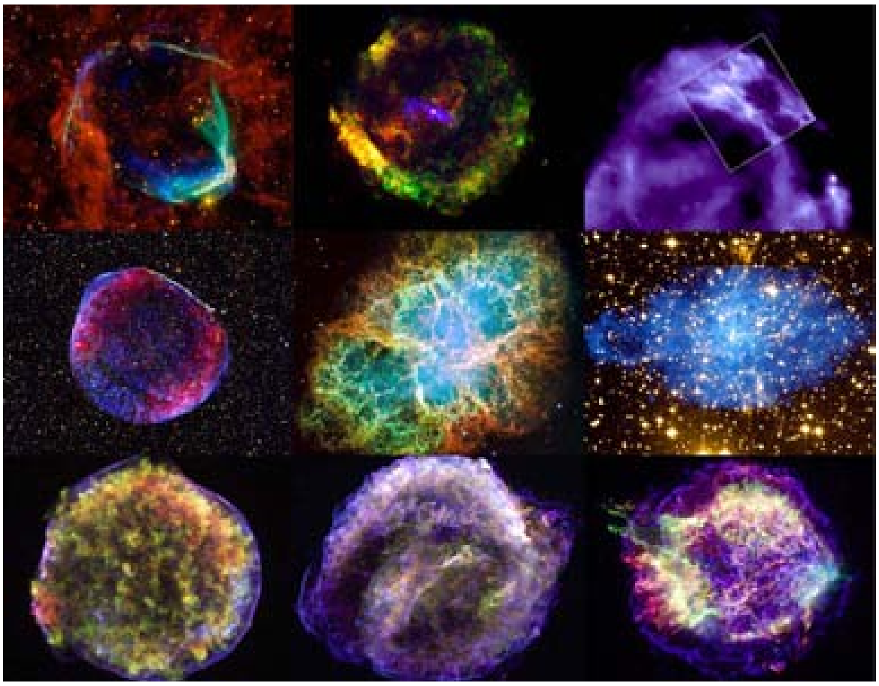

Fig. 1.2 The nine historical SNRs. From left to right, first row: RCW 86, G11.2-0.3, G347.3-0.5. Second row: SN 1006, Crab Nebula, 3C 58. Third row: Tycho's SNR, Kepler's SNR, Cassiopeia A.

two NSs, but only one is pulsating). Backer et al. (1982) discovered the first millisecond pulsar ($P \sim 1\ 5$ ms), one of the fastest rotators known. Burgay et al. (2003) discovered the first double neutron star system where both components are detectable as pulsars (PSR J0737-3039). Finally, the most massive neutrons stars were discovered only recently by Demorest et al. (2010) (PSR J1614-2230) and Antoniadis et al. (2013) (PSR J0348+0432), with $(1.97 \pm 0.04) M_{\odot}$ and $(2.01 \pm 0.04) M_{\odot}$, respectively.

In 1979, a new class of neutron stars was discovered through the detection of repeated bursts in hard X-rays and soft γ-ray energies in the source currently known as SGR 1900+14 (Mazets, Golenetskij & Guryan, 1979; Mazets et al., 1979a) in the SNR N 49, in the Large Magellanic Cloud (LMC). This kind of objects were called Soft Gamma Repeaters (SGRs). Two years later, Fahlman & Gregory (1981) reported an X-ray pulsar (1E 2259+586) in SNR CTB 109, with an X-ray luminosity larger than could be explained via its rotational power alone. It was thought that maybe a companion star was accreting material onto the neutron star surface, but no direct or indirect sign of a binary system was observed. This object and the others following this behavior were called "Anomalous X-ray Pulsars" (AXPs). Only in the 1990's, Duncan & Thompson (1992); Duncan et al. (1995); Thompson & Duncan (1996) proposed that the origin of the emission of SGRs (and later also of AXPs) was their

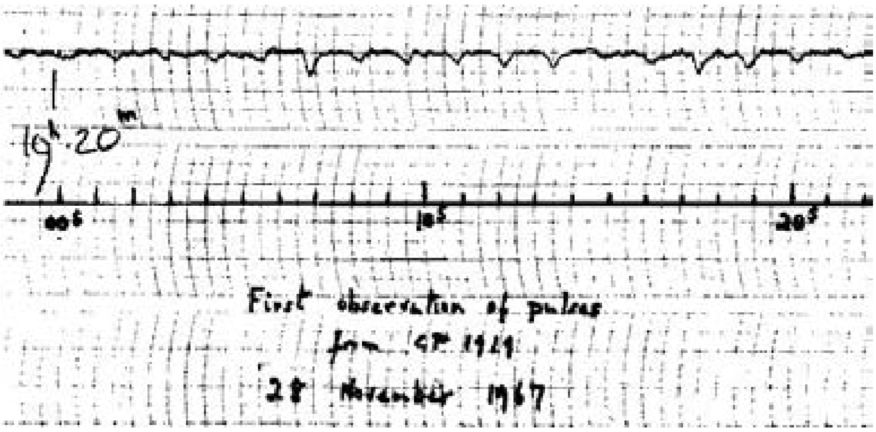

Fig. 1.3 Radio pulses observed for CP 1919 (PSR J1921+2153), the first pulsar known (Hewish et al., 1968).

magnetic energy, they were hence labelled as “magnetars” (see section 1.2 for details). This picture has been amplified with the discovery of low magnetic field magnetars (Rea et al., 2010, 2012, 2014).

1.2 Pulsars

Pulsars (PSRs) are compact objects left over from the reminiscent core of a star which has exploded as a supernova (SN). Their density is around $\sim 10^{14}$ g cm^{-3} and have a mass of $\sim 1-2M_{\odot}$. These quantities imply a radius of $\sim$ 10 km. PSRs are the fastest rotators known in the Universe with periods of $\sim 10^{-3}-10$ s and have associated dipole magnetic fields of $10^{8}-10^{15}$ G, also the highest known. This make pulsars excellent astrophysical laboratories to study matter, hydrodynamics, electrodynamics, particle acceleration and radiation processes under extreme conditions.

1.2.1 The magnetic dipole model

Two of the most important parameters of PSRs obtained by observations, generally in radio, X-rays and -rays in some cases, are the rotational period P, and the period derivative P. Using these parameters, we can deduce some important formulae from the magnetic dipole model. This model assumes that the pulsar rotates in vacuum with frequency Ω ($\Omega = 2\ /P$), with a magnetic moment $\vec{m}$, and an angle between the magnetic moment and the rotation axis. The magnetic moment for a pure rotating magnetic dipole is defined (e.g., Shapiro &

Teukolsky 2004)

$$\vec{m} = \frac{B_p R_{PSR}^3}{2}, \tag{1.1}$$

where B_p is the dipolar magnetic field and R_{PSR} is the radius of the PSR. The vector $\vec{m}$ is expressed as

$$\vec{m} = \frac{1}{2} B_p R_{PSR}^3 (\mathbf{e} \ \cos \quad + \mathbf{e} \ \sin \quad \cos\Omega t + \mathbf{e} \ \sin \quad \sin\Omega t), \tag{1.2}$$

where $\mathbf{e}$ is the parallel component with respect the rotation axis and $\mathbf{e}$ and $\mathbf{e}$ are perpendicular and mutually orthogonal vectors. As the configuration of the vector changes in time, the energy radiated is given by the Larmor formula

$$E = -\frac{2}{3c^3} \ \ddot{\vec{m}} \ ^2. \tag{1.3}$$

being c the speed of light. Substituting $\vec{m}$ in equation above, we obtain

$$E = -\frac{B_p^2 R^6 \Omega^4 \sin^2}{6c^3}. \tag{1.4}$$

The total rotational energy of the PSR is given by

$$E = \frac{1}{2} I \Omega^2 = \frac{2 \ \ ^2 I}{P^2}, \tag{1.5}$$

where I is the moment of inertia of the PSR. This value is typically assumed as $\sim 10^{45}$ g cm^2. The time derivative of equation (1.5) is

$$E = I\Omega\Omega = -\frac{4 \ \ ^2 I P}{P^3} \tag{1.6}$$

$E < 0$ as we have seen in equation (1.4), so $\Omega < 0$. Now, we define the *characteristic age* of the PSR $_c$ as

$$_c = -\frac{P}{2P} = -\frac{1}{2}\left(\frac{\Omega}{\Omega}\right)_{now} \tag{1.7}$$

where the subindex *now* means at the present time. Combining equation (1.4) with the latter, we find

$$_c = \frac{3Ic^3}{B_p^2 R_{PSR}^6 \Omega_t^2 \sin^2}, \tag{1.8}$$

and now we can integrate equations (1.4), (1.5) and (1.6) to solve the rotation frequency evolution of the magnetic dipole

$$\Omega(t) = \Omega_0 \left[1 + \left(\frac{\Omega_0}{\Omega_{now}}\right)^2 \frac{t}{{}_{c}}\right]^{-1/2}. \tag{1.9}$$

In terms of the period,

$$P(t) = P_0 \left[1 + \left(\frac{P_{now}}{P_0}\right)^2 \frac{t}{{}_{c}}\right]^{1/2}. \tag{1.10}$$

We can compute the age of the pulsar from equation (1.10) just setting $P(t) = P_{now}$. Thus,

$$t_{age} = \ {}_{c} \left[1 - \left(\frac{P_0}{P_{now}}\right)^2\right]. \tag{1.11}$$

Note that if $P_0 \ll P_{now}$, then t_{age} $\ {}_{c}$. Using the solution for the rotation frequency, we can rewrite the spin-down luminosity in terms of the initial period, period and period derivative

$$E = \frac{2\ {}^{2}I}{{}_{c}P_0^2}\left(\frac{P_{now}}{P_0}\right)^2 \left[1 + \frac{t}{\left(\frac{P_0}{P_{now}}\right)^2 {}_{c}}\right]^{-2}, \tag{1.12}$$

or to simplify,

$$E = E_0 \left(1 + \frac{t}{{}_{0}}\right)^{-2}, \tag{1.13}$$

where $\ {}_{0}$ is the initial spin-down age and E_0 is the initial spin-down luminosity.

Note that for a purely rotating magnetic dipole, the angular frequency evolution is ruled by an equation of the kind $\Omega \propto \Omega^3$. For some pulsars, the rotation evolves with a different power index n, also called the *braking index* and defined as

$$n = \frac{P\ddot{P}}{P}. \tag{1.14}$$

Under this condition, the period evolution is

$$P(t) = P_0 \left[1 + \frac{n-1}{2}\left(\frac{P_{now}}{P_0}\right)^{n-1} \frac{t}{{}_{c}}\right]^{\frac{1}{n-1}}, \tag{1.15}$$

the age of the pulsar,

$$t_{age} = \frac{2\ _{c}}{n-1}\left[1-\left(\frac{P_0}{P_{now}}\right)^{n-1}\right]. \tag{1.16}$$

and the spin-down evolution,

$$E = E_0\left(1+\frac{t}{\ _0}\right)^{-\frac{n+1}{n-1}}, \tag{1.17}$$

with

$$E_0 = \frac{2\ ^2 I}{{}_c P_0^2}\left(\frac{P_{now}}{P_0}\right)^{n-1} \qquad {}_0 = \frac{2}{n-1}\left(\frac{P_0}{P_{now}}\right)^{n-1}\ _c. \tag{1.18}$$

A relation for $_0$ and t_{age} can be derived using equation (1.16), such that

$${}_0 = \frac{2\ _c}{n-1} - t_{age}. \tag{1.19}$$

Another important physical property is the polar magnetic field B_p. Its expression can be easily obtained from equations (1.4) and (1.6) giving

$$B_p = \sqrt{\frac{3Ic^3}{2\ ^2R_{PSR}^6}PP} \quad 6.4\times 10^{19}\sqrt{PP}\ \mathrm{G}. \tag{1.20}$$

It is possible to find in the literature that0 the magnetic field is a factor 2 lower ($B_e \sim 3.2\times 10^{19}\ \overline{PP}$). This difference depends on where we define the magnetic moment. Here, we are defining the magnetic moment in the pole, but if we do it in the equator, then we find this difference of a factor 2 ($B_p = 2B_e$).

1.2.2 Electric potential and -parameter

According to the current picture, a charge-filled magnetosphere surrounds the PSR and the particle acceleration occurs in charged gaps in outer regions that extend to the light cylinder (defined as $R_{LC} = c/P$). The firstm magnetosphere model was proposed by Goldreich & Julian (1969) and they calculated the maximum electric potential generated by an aligned rotating magnetic field (i.e, magnetic and spin axes co-aligned). The expression is

$$\Delta V = \frac{B_p\Omega^2R_{PSR}^3}{2c}. \tag{1.21}$$

The associated particle current is $N = (\Omega^2 B_p R_{PSR}^3)/cZe$, where Ze is the ion charge.

The magnetization parameter (σ) is the ratio between the Poynting flux and the particle energy flux. This parameter is defined by Kennel & Coroniti (1984a):

$$\sigma = \frac{B_p^2}{4\pi \quad \gamma mc^2}, \tag{1.22}$$

where is the number density of particles, and γmc^2 is the energy of each particle. This ratio is expected to be dominated by the Poynting flux term as the wind flows from the light cylinder ($\sigma > 10^4$, see Arons 2002), but for the structure of the Crab Nebula, we need $\sigma \ll 1$ just behind the termination shock in order to meet flow and pressure boundary conditions at the outer edge of the PWN (Rees & Gunn, 1974; Kennel & Coroniti, 1984a). The particle-dominated wind is also required by the high ratio of the synchrotron luminosity to the total spin-down power (Kennel & Coroniti, 1984b), and implies $\gamma \sim 10^6$, a value considerably higher than that expected in the freely expanding wind (Arons, 2002). This change in the conditions of the pulsar wind between the termination shock and the light cylinder is still unclear (see Melatos 1998; Arons 2002), and is known as the "σ *problem*".

1.2.3 What do we observe?

Pulses of neutron stars are commonly detected at radio frequencies. This pulses are very stable which allow to measure the period of the sources with very high precision ($\Delta P \sim 10^{-10} s$). Despite the number of PSRs detected in radio, the physical mechanism that generates the coherent radio emission is not well understood. Thanks to this precision, long observations of these objects allow to measure also the period derivative ($\dot{P}$) and, in some cases, the second derivative of the period ($\ddot{P}$) and with it, the braking index.

When we plot the location of the PSRs in the period and period derivative phase space, we generate the socalled *PP-diagram* (see figure 1.4). In this plot we can distinguish different populations. In the lower-left part of the diagram, we find the recycled PSRs. Despite the large characteristic age of these PSRs, they have very low periods ($P \lesssim 0.01$ s). Recycled PSRs are in binary systems where they have been spin-up due to the presence of an accretion disk which transfers angular momentum to the PSR. The center of the diagram is domined by middle-aged pulsars. Regarding the band where we detect the pulses, we find radio, X-ray and γ-ray PSRs. Finally, *magnetars* are located in the upper-right part. Neutron stars with a thermal and with no signals of pulsations (or just hints), are referred as *Central Compact Objects* (CCO).

In some PSRs, we detect sudden spin-ups called glitches. It is thought that glitches are

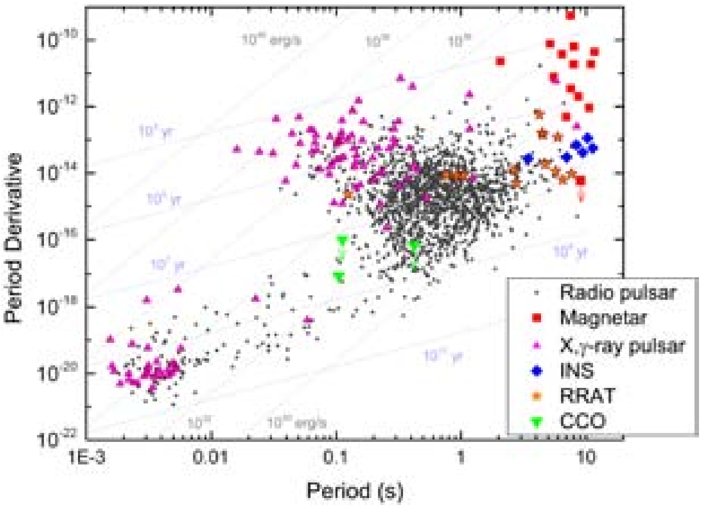

Fig. 1.4 *PP*-diagram for the known rotation-powered pulsars, isolated neutron stars (INS), central compact objects (CCO), rotating radio transients (RRAT) and magnetars (Harding, 2013). The lines of constant characteristic age and spin-down luminosity are superposed.

produced by superfluid neutron vortices in the crust (Anderson & Itoh, 1975).

Regarding other wavelengths as the ultraviolet, optical and infrared, NS are very faint at these energies, but some counterparts has been identified (e.g., Mignani 2012. Optical observations are useful to determine the presence of debris disks in isolated neutron stars and their good resolution allows to measure proper motions and parallaxes to determine distances.

1.2.4 Magnetars

As we have explained in section 1.1, magnetars is a class of pulsars which show high energy transient burst and flaring activity and persistent pulsations with luminosities higher than the spin-down luminosity. Nowadays, we know ∼24 magnetars (Olausen & Kaspi, 2014). They are characterized by having long periods ($P > 1$ s) and associated dipolar magnetic fields greater than $B_{crit} = m_e^2 c^3 / e\hbar \sim 4.4 \times 10^{13}$ G, which is the elecron critical magnetic fields at which the cyclotron energy of an electron reaches the electron rest mass energy. The latter characteristic is now misleading since, in the last years, magnetar-like behaviour has been discovered also in low-magnetic X-ray pulsars (Rea et al., 2010, 2012, 2014). Regarding the flaring and bursting activity, it might involve their emission from radio to hard X-rays, with an increase of the soft X-ray flux of a factor between 10 and 1000 with respect the flux in quiescense. The decay timescales of this flux is very varied raging from weeks to years. The same happens with the decay of the light curve, which can be characterized by an exponential or a power-law function (Rea & Esposito, 2011).

The mechanism of formation of the extremely high magnetic fields found in magnetars is still under debate. In the original idea (Duncan & Thompson, 1992; Thompson & Duncan, 1993; Duncan & Thompson, 1996), magnetars were thought to form through a magnetic amplification via an alpha-dynamo which was active during the proto-neutron star phase (lasting maximum $\sim$10 s) after the supernova explosion. For this process to operate, the proto-neutron star rotational period is required to between 0.6-3 ms (Duncan & Thompson, 1996). For a neutron star with a born period of $P \sim 1ms$, the associated free energy is $E \sim 10^{52}(P/1\ \mathrm{ms})^{-2}$ ergs and the magnetic fields could arrive to $B \sim 3 \times 10^{17}(P/1\ \mathrm{ms})^{-1}$ G as the differential rotation is smoothed by growing magnetic stresses. However, this scenario is encountering more and more difficulties: i) in recent studies on proto-neutron star formation (Buras et al., 2006b,a; Fryer & Warren, 2004), it appears very difficult to form proto-neutron stars spinning faster than $\sim$10 ms; ii) such a fast spinning proto-neutron star would require a supernova explosion one order of magnitude more energetic then normal supernovae, possibly an hypernova, which is yet not clear on whether it can indeed form neutron star instead of a black hole.

Besides the fastly spinning proto-neutron star, a further idea on the origin of these high magnetic fields is that they simply reflect the high magnetic field of their progenitor stars. Magnetic flux conservation (Woltjer, 1964) implies that magnetars must then be the stellar remnants of stars with internal magnetic fields of $B > 1$ kG, whereas normal radio pulsars must be the end products of less magnetic massive stars.

Recent theoretical studies showed that there is a wide spread in white dwarf progenitor magnetic fields (Wickramasinghe & Ferrario, 2005), which, when extrapolated to the more massive progenitors implies a similar wide spread in neutron stars progenitors (Ferrario & Wickramasinghe, 2006). Hence, apparently it seems that a fossil magnetic field might be the solution of the origin of such strongly magnetized neutron stars, without the need of invoking dynamo actions on utterly fast spinning proto-neutron stars.

However, this lead to the problem of the formation of such high B progenitor stars. The most common idea is that the magnetic field in the star reflects the magnetic field of the cloud from which the star is formed. The only known very massive stars (around $\sim$40M$_\odot$) with a directly measured magnetic field are Orion C and HD191612, with dipolar magnetic field of 1.1 kG and 1.5 kG, respectively (Donati et al., 2002, 2006). Very interestingly, the magnetic fluxes of both these stars (1.1×10^{27} G cm^2 for Orion C and 7.5×10^{27} G cm^2 for HD191612) are comparable to the flux of the highest field magnetar SGR 1806-20 (5.7×10^{27} G cm^2; Woods & Thompson 2006). Other high magnetic field stars are reported in Oskinova et al. (2011).

Recent observations of the environment of some magnetars revealed strong evidence that these objects are formed from the explosion of very massive progenitors ($M > 30\mathrm{M}_{\odot}$). In particular, a shell of HI has been detected around the AXP 1E 1048.1-5937, and interpreted by ISM displaced by the wind of a progenitor of 30-40$\mathrm{M}_{\odot}$ (Gaensler et al., 2005); SGR 1806-20 and SGR 1900+14 have been claimed to be a member of very young and massive star clusters, providing a limit on their progenitor mass of $>50\mathrm{M}_{\odot}$ (Fuchs et al., 1999; Figer et al., 2005; Davies et al., 2009) and $>20\mathrm{M}_{\odot}$ (Vrba et al., 2000). Finally, the AXP CXOU 010043-7211 it is a member of the massive cluster Westerlund 1 (Muno et al., 2006; Ritchie et al., 2010), with a progenitor with mass estimated to be $>40\mathrm{M}_{\odot}$.

In chapter 6, we study the X-ray spectrum of some SNR with an associated magnetar to check some of these statements and compare their spectra with the features found in SNRs with associated normal pulsars. Other important questions and observational properties are discussed in some reviews (Woods & Thompson, 2006; Mereghetti, 2008; Kaspi & Boydstun, 2010; Rea & Esposito, 2011; Olausen & Kaspi, 2014).

1.3 Pulsar Wind Nebulae

In addition to their electromagnetic emission, PSRs dissipate their rotational energy via relativistic winds of particles. Because the relativistic bulk velocity of the wind is supersonic with respect to the ambient medium, such a wind produces a termination shock. In turn, the wind particles, moving trough the magnetic field and the ambient photons, produce radiation that we observe as pulsar wind nebulae. As the pulsars themselves, the PWN emits at all wavelengths from radio to TeV.

1.3.1 Morphology

PWNe usually have two main X-ray morphologies, depending on the velocity of the pulsar proper motion and the ambient medium. A classic example is the Crab Nebula (see figure 1.5) For slow pulsars, images taken with the Chandra X-ray Observatory (see e.g., Kargaltsev & Pavlov 2008) show a toroidal shape around the pulsar equator, with two possible jets starting from the pulsars poles. Instead, pulsars moving with high velocity in the interstellar medium produce on average PWNe with the characteristic bullet-like or bow-shock morphology, with the tail developed along the pulsar motion. Thus, the study of PWNe can lead to knowledge of pulsar winds, the properties of the ambient medium, and the wind-medium

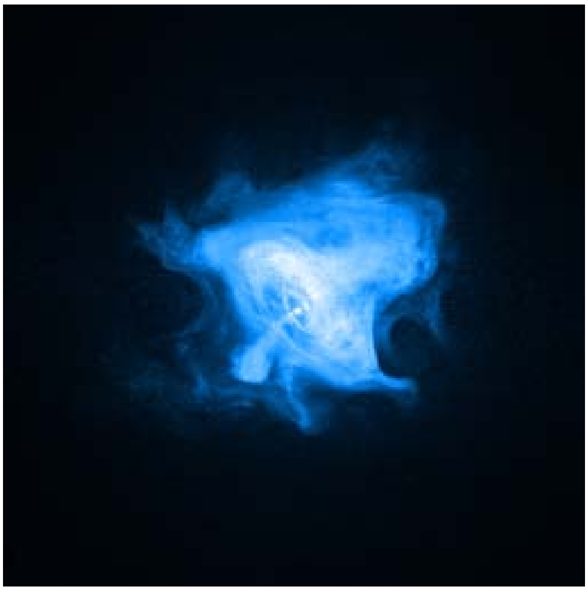

Fig. 1.5 Crab Nebula in X-rays seen by the Chandra X-ray Observatory.

interaction.

The pulsar wind expands in its wound-up toroidal magnetic fields and it is confined by the expanding shell of the SN ejecta. As the wind decelerates to match the boundary condition imposed by the slowly-expanding SN material at the nebula radius, a wind termination shock is formed with radius R_w such that (e.g., Gelfand, Slane & Zhang 2009):

$$R_w = \sqrt{\frac{E}{4 \quad c P_{PWN}}} \tag{1.23}$$

where is the equivalent filling factor for an isotropic wind. $= 1$ when the wind is isotropic. P_{PWN} is the pressure of the gas in the PWN interior. High resolution X-ray observations have shown the ring-like emission from the termination shock of the Crab Nebula, but it has not been detected in other cases as, for example, 3C 58 (Slane, Helfand & Murray, 2002), G21.5–0.9 (Camilo et al., 2006) and G292.0+1.8 (Hughes et al., 2001).

In the case of the Crab Nebula (also similar for 3C 58), the X-ray morphology consist in a tilted torus with jets along the toroid axis (see figure 1.5). The jets extend nearly 0.25 pc from the PSR (Gaensler & Slane, 2006). A faint counter-jet accompanies the structure and the X-ray emission is significantly enhanced along one edge of the torus presumably as the result of Doppler beaming of the outflowing material.

Chandra X-ray observations revealed a similar structure for G54.1+0.3 with a point-like central source surrounded by an X-ray ring with an inclination of 45° (Lu et al., 2002). In the eastern part of the ring, the X-ray emission is brighter. Jets of shocked material are also observed aligned with the projected axis of the ring (Bogovalov et al., 2005). An important difference of this case with the Crab Nebula or 3C 58 is that the X-ray flux contribution of the torus and the jets is similar, when for the latter two, the central torus is brighter by a large factor.

Some effort has been done in order to understand the formation of these structures. Modeling of the flow conditions across the shock shows that magnetic collimation produces jet-like flows along the rotation axis (Komissarov & Lyubarsky, 2004; Bogovalov et al., 2005). The collimation of the jet is highly dependent on the magnetization of the wind. For $\gtrsim 0.01$, magnetic hoop stresses are sufficient to divert the toroidal flow back toward the pulsar spin axis, collimating and accelerating the flow to speeds of $\sim 0.5c$ (Del Zanna, Amato & Bucciantini, 2004). Smaller values of the magnetization allow to increase the radius at which the flow is diverted. Near the poles, is large, resulting in a small termination shock radius and strong collimation, while near the equator, it is much smaller and the termination shock is larger (Bogovalov & Khangoulyan, 2002).

Note that all these structures and time variability is also observed at other wavelengths (radio & optical) indicating that the accelaration of the associated particles must have the same origin as for the X-ray-emitting population (Bietenholz et al., 2004).

The filaments formed by Rayleigh-Taylor instabilities are also observed in the optical for the Crab Nebula (Hester et al., 1996). MHD simulations indicates that 60–75% of the swept-up mass can be concentrated in such filaments (Bucciantini et al., 2004). These filaments compresses the expanding bubble and increases the magnetic field forming sheaths of enhanced synchrotron emission (Reynolds, 1988), but this emission is not detected in the Crab Nebula (Weisskopf et al., 2000).

Loop-like filaments are observed in 3C 58 in X-rays (Slane et al., 2004a) and coincident with those observed in radio (Reynolds & Aller, 1988). Optical fainter filaments are also observed (van den Bergh, 1978) and their origin seems similar as in the Crab Nebula, but they are not coincident with the X-ray ones, revealing that the mechanisms of formation must be different. Slane et al. (2004a) propose that the bulk of the discrete structures seen in the X-ray and radio images of 3C 58 are magnetic loops torn from the toroidal field by kink instabilities.

Finally, there are time variable structures which appear and disappear on timescales of months as the compact-knots near the PSR observed in the Crab Nebula (Tziamtzis, Lundqvist & Djupvik, 2009) and others, as for PSR B1509-58 (Gaensler et al., 2002). It is believed that they actually correspond to unstable, quasi-stationary shocks in the region just

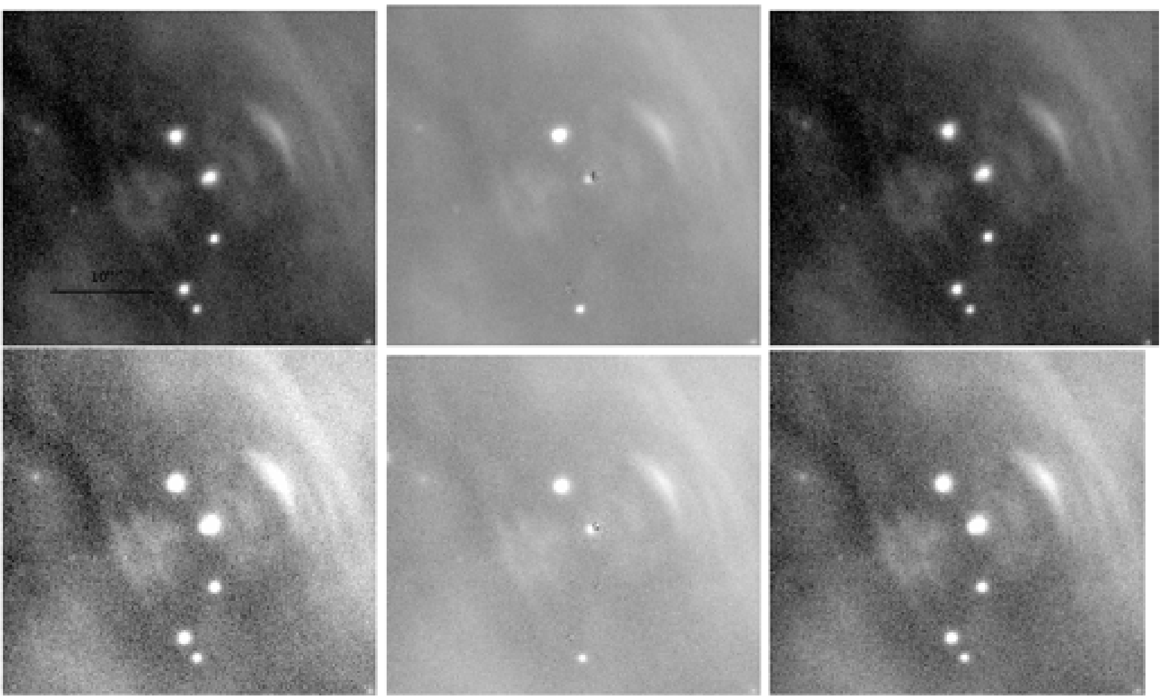

Fig. 1.6 Time variability of the knots and wisps near the Crab Nebula PSR observed in the H band (upper panel) and K_s band (lower panel) by the Nordic Optical Telescope (NOT). The images were taken December 13th 2007 and September 30th 2007 (Tziamtzis, Lundqvist & Djupvik, 2009).

outside the termination shock, at high latitudes where the shock radius is small due to larger values of (e.g., Komissarov & Lyubarsky 2004).

1.3.2 Spectrum characteristics

Pulsar wind nebulae emit radiation from ratio to TeV energies. The most observed PWN is, by far, the Crab Nebula, for which we find detailed observations in the whole electromagnetic spectrum. From radio to X-rays, the emission consist in synchrotron radiation coming from the particles accelerated by the magnetic field of the nebula. Depending on the density of the magnetic field and the lifetime of the particles, we can get an idea about the frequency where the cooling cut-off is located in the synchrotron spectrum (Ginzburg & Syrovatskii, 1965):

$$ {}_b = 10^{21} \left(\frac{B_{PWN}}{10^{-6}\,\mathrm{G}} \right)^{-3} \left(\frac{t}{1\,\mathrm{kyr}} \right)^{-2} \mathrm{Hz} \tag{1.24} $$

Using a -approximation for the synchrotron cross-section (Ginzburg, 1979), it is easy to related the energy of synchrotron photons (E_{sync}) with the energy of the electrons that produce the radiation itself (E_e)

$$E_{sync} = \frac{h \quad _c}{3}, \tag{1.25}$$

where h is the Planck constant and $\quad _c$ is the so-called *critical frequency* which depends on the magnetic field and the energy of the electrons

$$_c = \frac{3eB(t)E_e^2}{4 \quad m_e^3c^5}. \tag{1.26}$$

Particles radiating photons beyond this frequency decrease rapidly their energy before reaching the outer shell of the PWN. Observationally, we see a decreasing radius of the nebula as we increase the frequency as we observe in Crab Nebula (e.g., Hillas et al. 1998). At lower magnetic fields, this effect is less important, because the synchrotron loss time is longer. It is also detected in some PWNe, an infrared and optical excess and some recombination lines in the spectrum (Hester et al., 1996) coming from thermal radiation produced by the filament structures surrounding the PWN.

Generally speaking, the PWN radio spectra are characterized by a flat power-law index at radio wavelengths (≈ -0.3). We find an intrinsic energy break at infrared/optical frequencies and the slope changes for the X-ray emission ($\Gamma \approx 2$). The nature of this spectral shape is still not understood. Relic breaks in the spectrum can be produced by a rapid decline in the pulsar output over time, and these breaks propagate to lower frequencies as the PWN ages (Pacini & Salvati, 1973). In case where we can observe the spectrum with radial resolution, it is detected radial steepening in the spectrum (Slane et al., 2000; Willingale et al., 2001; Slane et al., 2004a). This steepening is less than expected in the outer part of the nebula (Kennel & Coroniti, 1984b; Reynolds, 2003), but diffusion processes can be involved in some mixing of electrons with different ages at each radius.

From X-rays to VHE, the radiation produced comes basically from inverse Compton (IC) interaction of the high energy pairs with the low energy photons of the ambient medium. Three main target photon fields are considered in the current spectral models: the cosmic microwave background (CMB), the far-infrared contribution coming from the galactic ISM (FIR) and the infrared/optical contribution coming from the surrounding stars (NIR). Using the aproximation done by Ginzburg (1979) for the IC cross-section in the Thompson limit, the IC photons energy (E_{IC}) and the energy of the electron is related as

$$E_{IC} = \frac{4}{3}h \quad _i \left(\frac{E_e}{m_ec^2}\right)^2, \tag{1.27}$$

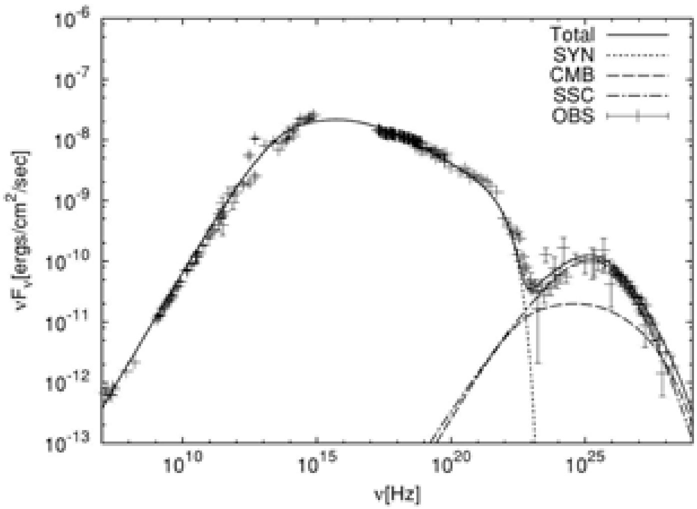

Fig. 1.7 The most complete example of PWN spectrum, the Crab PWN. From radio to X-rays, the emission is well described by synchrotron emission, and from hard X-rays to VHE, the spectrum is described by the IC scattering of the electrons with the background photon fields. Image taken from Tanaka & Takahara (2010).

where $_i$ is the energy of the target electrons. We can relate equations (1.25) and (1.27) to connect the characteristic energies of the synchrotron and IC photon produced by the same electrons. Assuming the CMB as the only contributor for the IC emission, we obtain (Aharonian, Atoyan & Kifune, 1997)

$$E_{sync} \quad 0.07 \left(\frac{E_{IC}}{1\,\mathrm{TeV}}\right)\left(\frac{B}{10\quad G}\right)\mathrm{keV}. \tag{1.28}$$

This relation is useful to obtain a first idea on the value of the magnetic field of the nebula from the spectrum. An example of a multi-wavelength spectrum of a PWN is shown in figure 1.7.

PWNe constitute the largest class of identified Galactic very high energy (VHE) -ray sources, with the number of TeV detected objects increasing from 1 to ~30. in the last years. This statistics shines in comparison with the ~30, 10, or 40 PWNe known in radio, optical/IR, or X-rays, respectively, detected in decades of observations.

Regarding the time evolution of the spectra, as the magnetic field diminishes with age, the synchrotron flux decreases and the IC component becomes more important. This is because the electrons required to emit in hard X-rays are more energetic than those necessary to emit in TeV by IC, thus when these very high energy electrons loss energy, they increase the electron population which contributes to the TeV emission via IC. This is one of the reasons we have detected middle-aged PWNe in -rays that have not been detected in other wavelengths.

1.3.3 Current models

In studying PWNe, there are two distinct theoretical approaches. On one hand, detailed magnetohydrodynamic (MHD) simulations have succeeded in explaining the morphology of PWNe. On the other hand, spherically symmetric 1D PWNe spectral models, with no energy-dependent morphological output, have been constructed since decades. We will review some of these models and others in section 1.3.

There has been a great effort trying to reproduce the spectral and morphological features of PWNe. The first model for the Crab Nebula was proposed by Rees & Gunn (1974). Ten years later, Kennel & Coroniti (1984a,b) did a further step introducing an analytical model with a magnetic field with radial dependence. The diffusion-loss equation was solved analytically by Syrovatskii (1959) applied to the distribution of relativistic electron in the Galaxy (explained in detail in section 2.1). The solution of this equation was calculated considering no time-dependence on the energy losses or the magnetic fields. Atoyan & Aharonian (1996) and Aharonian, Atoyan & Kifune (1997) applied the same equation to PWNe but neglecting the diffusion term to study the IC radiation from these sources. In the latter models, the -ray and VHE radiation is produced by pairs, but some others proposed that there could be an important contribution from ions by pion decay (Bednarek & Bartosik, 2003, 2005; Li, Chen & Zhang, 2010).

Time-dependent models has been presented lately (e.g., Bednarek & Bartosik 2003, 2005; Büsching et al. 2008; Zhang, Chen & Fang 2008; Fang & Zhang 2010a,b; Li, Chen & Zhang 2010; Tanaka & Takahara 2010; Bucciantini, Arons & Amato 2011; Tanaka & Takahara 2011; Van Etten & Romani 2011; Martín, Torres & Rea 2012; Tanaka & Takahara 2013; Torres, Cillis & Martín Rodriguez 2013; Torres et al. 2013; Vorster et al. 2013; Torres et al. 2014). Zhang, Chen & Fang (2008) integrates the energy loss equation considering only the synchrotron and Bohm diffussion lifetimes of the particles to obtain an analytical solution for the electron population varying the magnetic field with time. Fang & Zhang (2010a) extrapolates the electron injection function fitted by Spitkovsky (2008) from numerical simulations of collisionless shocks in unmagnetized plasmas. Tanaka & Takahara (2010, 2011, 2013) integrates numerically the energy loss equation for pairs taking into account the energy losses of the particles, but neglecting escape time term. The magnetic field is not time parametrized as in other works (e.g., Venter & de Jager 2007), but it is calculated by magnetic field energy conservation. Van Etten & Romani (2011) included radial dependence and the diffusion term to calculate the electron population. Vorster & Moraal (2013) also studies in detail the effect of the diffussion in the electron population in PWNe. In Martín, Torres & Rea (2012); Torres, Cillis & Martín Rodriguez (2013); Torres et al. (2013, 2014), the energy loss equation is integrated considering the energy losses and the escape terms in a time-dependent way and taking into account adiabatic losses for the magnetic field calculation as in Pacini & Salvati (1973).

Due to the complexity of the problem, the majority of these are only capable to reproduce the first stage of the evolution (i.e, free expansion phase) with high precision. Other caveat is the morphology, which is completely neglected. Some models has been more dedicated to reproduce better the dynamical evolution of the system. For example, van der Swaluw et al. (2001) proposed an analytical model to study the PWN evolution during the Sedov phase of the SNR. Chevalier (1982); Blondin, Chevalier & Frierson (2001) studied the interaction of the PWN with the reverse shock of the SNR using numerical simulations. Gelfand, Slane & Zhang (2009); Fang & Zhang (2010b); Bucciantini, Arons & Amato (2011); Vorster et al. (2013) combined the works done by Chevalier (1982); Blondin, Chevalier & Frierson (2001) with simple spectral models to study the evolution of the spectrum and applied to some particular cases.

In order to understand better the magnetic configuration of a PWN and its morphology, several works has been focused to reproduce the X-ray morphology of the Crab Nebula using MHD multidimensional time-dependent models (e.g., Del Zanna, Amato & Bucciantini 2004; Komissarov & Lyubarsky 2004; van der Swaluw, Downes & Keegan 2004; Del Zanna et al. 2006; Volpi et al. 2008).

1.4 PWN-SNR complex evolution

After the SN explosion, the ejected mass expands throught the interstellar material. The central PSR starts to accelerate particles inside the termination shock and these particles interacts with the material inside the SNR. Due to the explosion, the PSR has a certain kick velocity and will move inside its proper PWN and SNR. The typical energy that a PSR injects into the PWN during its lifetime is only $\sim$1% of the SN explosion (10^{51} erg). Therefore, the presence of an energetic PSR has little effect on the global evolution of the SNR, but the evolution of the PWN strongly depends on its interaction with the SNR. In this section we will explain briefly the different evolution stages of the system. Note that this scheme is a simplification when we study particular SNRs, since the SN explosion and the ISM density have important asymmetries and different parts of the system may be in different phases. In any case, this provides a useful framework to have a first idea on how these systems evolve.

1.4.1 Free expansion phase

At the beginning, the mass ejected by the SN explosion (M_{ej}) sweeps up the ISM (M_{sw}) like a piston with a constant velocity (Taylor, 1946). The shock wave moves at a speed of $> (5-10)\times 10^3$ km s^{-1}, while asymmetry in the SN explosion gives the pulsar a random space velocity of typical magnitude 400-500 km s^{-1} and stars to move from the center. In this phase, M_{ej} dominates over M_{sw}. As $t \ll {}_0$, we can consider that the PWN has constant energy input such that $L(t)\quad L_0$ (we recall E to $L(t)$ for convenience) (see equation 1.13). The pulsar wind is highly over-pressured with respect to its environment, and the PWN thus expands rapidly, moving supersonically and driving a shock into the ejecta. In the spherically symmetric case, the radius of the PWN evolves as (e.g., van der Swaluw et al. 2001):

$$R_{PWN} = C\left(\frac{L_0 t}{E_{SN}}\right)^{1/5} V_0 t, \tag{1.29}$$

where E_{SN} is the energy of the supernova explosion and V_0 is the velocity of the SN ejecta at the center of the explosion. V_0 is calculated assuming that the energy E_{SN} is converted into kinetic energy and a uniform density medium. Its expression is then

$$V_0 = \sqrt{\frac{10E_0}{3M_{ej}}}. \tag{1.30}$$

The numerical constant C depends on the adiabatic coefficient of the pulsar wind ${}_{PWN}$,

$$C = \left(\frac{6}{15({}_{PWN}-1)} + \frac{289}{240}\right)^{-1/5}, \tag{1.31}$$

which in this case is ${}_{PWN} = 4/3$, since the gas is relativistically hot. Because the PWN expansion velocity is steadily increasing, and the sound speed in the relativistic fluid in the nebular interior is $c/\ \overline{3}$, the PWN remains centered on the pulsar. There are some systems discovered at this stage, but a good example would be the composite SNR G21.5–0.9 with the PSR J1833-1034 (see figure 1.8).

For the SNR, as the swept-up mass becomes comparable to the ejected mass, two effects become important. The first one is that the pressure difference between the shocked ISM and the ejecta drives a shock wave into the ejecta due to the low pressure in the ejected

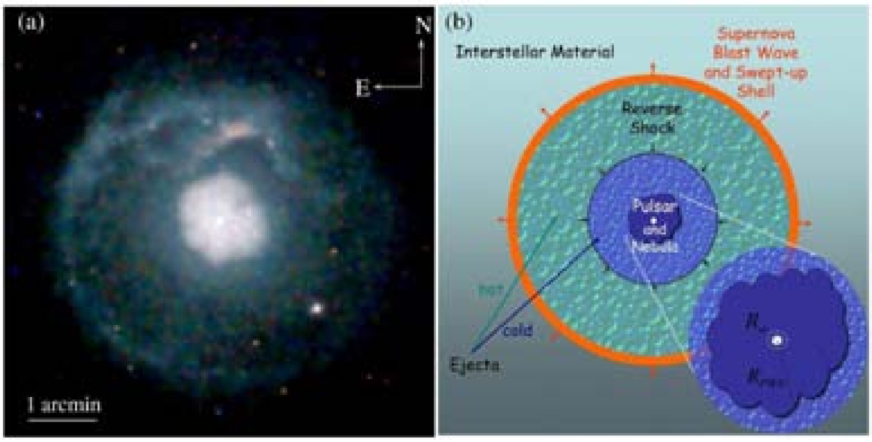

Fig. 1.8 Free expansion stage scheme (Gaensler & Slane, 2006). Left image: Composite SNR G21.5-0.9 image obtained by Chandra. This is a canonical example of a free expansion phase system. Right image: Free expansion stage scheme. The SN blast wave expands through the ISM and sweeps up the material, increasing the mass in the shock. The reverse shock heats the material of the interior of the SNR. The PWN expands supersonically inside the SNR and the PSR remains in the center due to the low kick velocity in comparison with the expansion velocity of the nebula.

material which has been adiabatically expanding. This is the so-called reverse shock. The reverse shock wave is the beginning of the deceleration of the supernova ejecta, which leads to the second effect: the Rayleigh-Taylor instability at the interface between the dense shell and the ambient medium. At this moment, significant deceleration is expected and the SNR evolution follows the self-similar adiabatic blast wave solution for a point explosion in a uniform medium described by Sedov (1959). The PWN expansion will be affected later when the reverse shock collides with the front shock of the pulsar wind.

1.4.2 Sedov phase

As we explained in the previous section, when $M_{sw} > M_{ej}$, the expansion of the SNR follows the self-similar solution given by Sedov (1959). It assumes that the energy of the SN explosion is injected into the ISM instantaneously with an uniform density $_0$. As in the free expansion phase, radiative energy losses are neglected. A simple formula for the evolution of the SNR is obtained

$$R_{SNR}(t) = \left(\frac{E_{SN}t^2}{_0} \right)^{1/5}, \tag{1.32}$$

with $= 2.026$ for a non-relativistic, monatomic gas ($_{ej} = 5/3$). The Sedov–Taylor solution can be generalized to a gas medium with a power-law density profile $(r) \propto r^{-s}$,

$R_s \propto t$, $V_s = \ R_s/t$, with the parameter $\ = 2/(5-s)$. A SNR shock moving through the progenitor's stellar wind corresponds to the case where $s = 2$ ($\ = 2/3$). A physical example would be Cas A (e.g. van Veelen et al. 2009), where the observed value in x-rays of is 0.63 ± 0.02 (Vink et al., 1998; DeLaney & Rudnick, 2003; Patnaude & Fesen, 2009).

Regarding the reverse shock, firstly it expands outwards behind the forward shock and separated by the contact discontinuity where the Rayleigh-Taylor instabilities are produced, but eventually the reverse shock moves inwards. The reverse shock reaches the center of the SNR in a characteristic timescale assuming that there is neither PWN nor PSR. This timescale is (Reynolds & Chevalier, 1984)

$$t_{Sedov} \approx 10 \left(\frac{M_{ej}}{15M_{\odot}}\right)^{5/6} \left(\frac{E_{SN}}{10^{51}\,\mathrm{erg}}\right)^{-1/2} \left(\frac{\ _0}{1\,\mathrm{cm}^{-3}}\right)^{-1/3} \mathrm{kyr} \tag{1.33}$$

At this point the SNR interior is entirely filled with shock-heated ejecta, and the SNR is in a fully self-similar state that can be completely described by a small set of simple equations (Cox, 1972). But, of course, this is not the case, and we are considering a young PWN and PSR inside the remnant. In a few thousand years, the reverse shock arrives at the PWN shell and compresses the PWN by a large factor, increasing the pressure and producing a bounce of the nebula. The magnetic field also increases and burns off the highest energy electrons (Reynolds & Chevalier, 1984; van der Swaluw et al., 2001; Bucciantini et al., 2003). Rayleigh-Taylor instabilities produces filamentary structures and mixes thermal and nonthermal material within the PWN (Chevalier, 1998; Blondin, Chevalier & Frierson, 2001). At this stage, the central PSR can move outside the PWN and re-enter afterwards due to the expansion of the PWN. After this reberveration phase, the PSR powers again the PWN (when it re-enters) and there are two solutions depending on whether $t < \ _0$ or $t > \ _0$. In the former case, $L(t) \quad L_0$ and $R_{PWN} \propto t^{11/15}$ when the braking index $n = 3$ (van der Swaluw et al., 2001) or $R_{PWN} \propto t^{3/10}$ in the latter case (Reynolds & Chevalier, 1984). When the distance traveled by the PSR is large enough, the PSR escapes from the original PWN and does not power it anymore, leaving a so-called *relic PWN*. As the PWN travels through the SNR material, it creates a new smaller PWN (van der Swaluw, Downes & Keegan, 2004). Observationally, this appears as a central, possibly distorted radio PWN, showing little corresponding X-ray emission. The pulsar is to one side of or outside this region, with a bridge of radio and X-ray emission linking it to the main body of the nebula. An example is the PWN in the SNR G327.1–1.1 (figure 1.9).

When the speed of the PSR becomes supersonic inside the SNR, it drives a bow shock (Chevalier, 1998; Van Der Swaluw, Achterberg & Gallant, 1998). The pressure produced

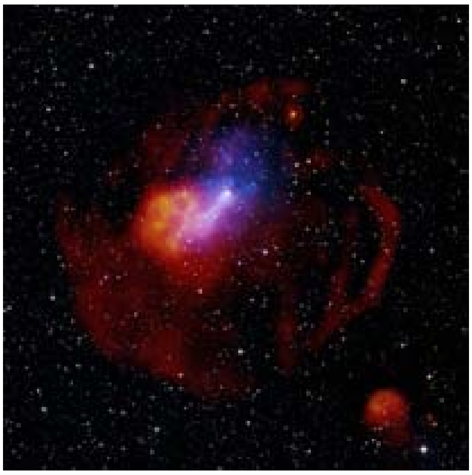

Fig. 1.9 Composite image of SNR G327.1-1.1 (Temim et al., 2009). The blue emission corresponds to the X-ray emission of the PWN and the red emission is the radio emission obtained by 843 MHz Molonglo Observatory. The peak of the X-ray emission is displaced from the center coming from the new particles injected by the pulsar. The radio emission corresponds to the original PWN (relic PWN).

by the PSR's motion confines the PWN, which is in equilibrium with the material of the SNR (for example, W44, see figure 1.10). For a SNR in the Sedov phase, the transition to a bow shock takes place when the pulsar has moved 68% of the distance between the center and the forward shock of the SNR (Van Der Swaluw, Achterberg & Gallant, 1998; van der Swaluw, 2003). At this moment, the PWN takes a comet-like shape. A pulsar will typically cross its SNR shell after ∼40000 years. If the SNR is still in the Sedov phase, the bow shock has a Mach number ~ 3.1 (van der Swaluw, 2003). After crossing the SNR shell, the PWN maintains this bow-shock, but this time it is propagating through the ISM. It can be detected from radio to X-rays. The shock driven by the PWN has H emission produced by excitation of the ISM. Finally, the spin-down luminosity of the PSR drops and it is not capable to power an observable synchrotron nebula and the PSR is surrounded by a static or slowly expanding cavity of relativistic material in equilibrium with the pressure of the ISM.

1.4.3 Later stages for SNRs

As the SNR forward shock accumulates matter form the ISM, it weakens and radiative cooling starts to be an important energy loss contribution. Generally, radiative losses become important when the post-shock temperature falls below $\sim 5\times10^5$ K, in which case oxygen line emission becomes an important coolant (e.g., Schure et al. 2009). In this moment, the

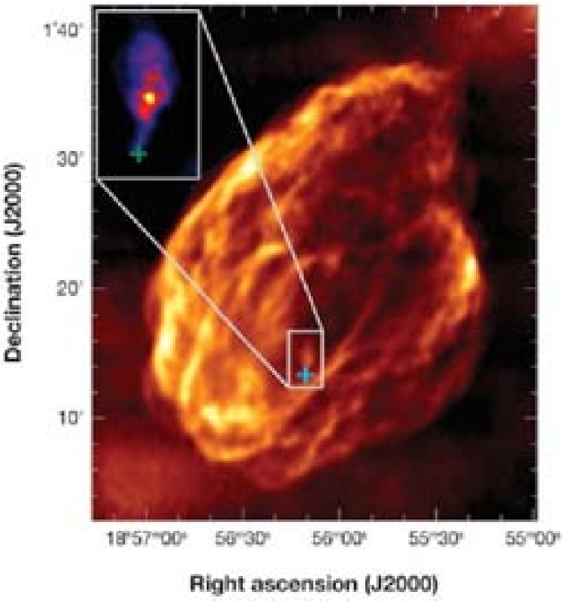

Fig. 1.10 1.4 GHz radio image of SNR W44 made by the *Very Large Array* telescope (VLA) (Giacani et al., 1997). In the upper left small panel, it is shown a 8.4 GHz VLA image of the bow-shock pulsar wind nebula powered by PSR B1853+01 (Frail et al., 1996a).

evolution of the shock radius is described using a momentum conservation law, such that

$$M_{sw}V_{SNR} = \frac{4}{3}\ \ R^3_{SNR}\ \ {}_0\frac{dR_{SNR}}{dt} = \text{const.} \tag{1.34}$$

From this conservation law, one can calculate the moment when radiative losses become important

$$t_{rad} = \frac{4\ \ R^3_{rad}}{3\ \ {}_0V_{rad}}, \tag{1.35}$$

and finally integrate to obtain an implicit function for the SNR radius (e.g. Toledo-Roy et al. 2009)

$$t = t_{rad} + \frac{R_{rad}}{4V_{rad}}\left[\left(\frac{R(t)}{R_{rad}}\right)^4 - 1\right], \tag{1.36}$$

with

$$t_{rad} = 44.6\left(\frac{E_{51}}{\ {}_0}\right)^{1/3}\text{kyr}, \tag{1.37}$$

$$R_{rad} = 23\left(\frac{E_{51}}{\ {}_0}\right)^{1/3}\text{pc}. \tag{1.38}$$

After this stage, the SNR continues to expand slowly and decreasing its temperature untill it megers completely with the ISM (merging phase).

1.5 Supernova Remnants in X-rays

Supernova remnants (SNRs) are gas and dust structures formed as a consequence of a supernova explosion. Supernovae can be produced in different ways depending on if the progenitor star is isolated or in a binary system. In the isolated case, at the beginning of its life, the star sustains the force of gravity using the radiation preassure produced by photons generated in the core which merge hydrogen atoms (H) to form helium (He) by thermonuclear reactions. This stage, which is the longest during the life of the star, is called *main sequence*. At the end of the main sequence, if the mass of the star is not very large ($M \lesssim 9M_\odot$, $M_\odot = 1.9889 \times 10^{33} g$), the density in the core is so high that the gas becomes degenerate before reaching the temperature to merge He nuclei to carbon and oxigen (C and O). For a degenerate gas, the pressure depends almost only on its density which is much higher than for an ideal gas. This makes the core stable against gravity without thermonuclear burning of C. Regarding the expanding envelope, it finally becomes unstable and the stellar winds strip the core forming a planetary nebula around it. This stripped core, with a typical mass of $1M_\odot$ and a radius of ~5000 km is called a *white dwarf*. The evolution of this white dwarf is only a thermal cooling, but if it forms a binary system with a companion star which transfers mass, depending on the transfered mass rate, we can observe sudden explosions due to H burning in the surface of the white dwarf, called *novae*, or if the transfer rate is very high, this could activate the thermonuclear burning of C of the white dwarf and explode destroying completely the star as a *thermonuclear supernovae* (or Type Ia SNe).

Stars with $M \gtrsim 9M_\odot$ pass through all the thermonuclear burning phases acquiring a burning layer structure, where lighter materials as H and He are found in the envelope surface and silicon and iron (Si and Fe) in the core. The energy to merge two atoms of Fe is higher than the nuclear potential energy released in the reaction, thus when the core burns almost all the Si, the contraction of the core becomes unavoidable. The bounce of the core creates a shock wave propagating outwards which accelerates the thermonuclear reactions of the outer layers releasing a huge amount of energy of 10^{51} erg. The star explodes as a *core collapse supernovae* (Type II and Type I SNe, with the exception of Type Ia SNe). If the mass of the surviving core has a mass of 1-2$M_\odot$, then the gas degenerates and becomes stable forming a neutron star. In this conditions, almost all the electrons has fallen into the nuclei of the atoms and formed neutrons (giving the name of neutron star). If the mass of the core is higher than ~2-3$M_\odot$ (Oppenheimer-Volkov limit), then the collapse is completely unavoidable and becomes a time-space singularity called *black hole*.

The elements created during the life of the star determine the chemical composition of the SNR. The shock wave arised from the explosion sweeps up the star envelope and the surrounding interstellar medium (ISM) and creates a thermal shell which can be visible at different wavelengths (from radio to X-rays, generally).

SNRs are objects of interest for many applications in astrophysics. They are important in the study of the local population of SNe (2 or 3 per century in a spiral galaxy like ours). In addition, they can give more information about how the explosion mechanism of the SN revealing different asymmetries and velocity distrubition of the material. SNR shocks provide the best laboratories to study high Mach number, collisionless shocks. It is thought that cosmic-rays are accelerated in these shocks. This is supported by the detection of SNRs of synchrotron emission from radio to X-rays and -ray emission from pion decay. X-ray observations and spectroscopy of these objects are essential to know more about the abundances and nucleosynthesis of the elements generated in the SN explosion and the state of the plasma. We will see some results obtained using these techniques in chapter 6.

More than 100 SNRs has been observed in X-rays (e.g., Chandra SNR catalog[1]) and many more if we take into account the rest of the electromagnetic spectrum (e.g, the Green SNR catalog[2] or the University of Manitoba SNR catalog[3]). Observations in X-rays are very important in many aspects of SNRs, and particularly, the X-ray spectroscopy. Using X-ray spectroscopy we can study the abundances of the elements created during the life of the progenitor star, the so-called *-elements* (C, O, Ne, Mg, Si, S, Ar, Ca, Fe) and other elements that can be produced during the SN explosion. The emission lines between 0.5-10 keV are very prominent for plasma temperatures between 0.2-5 keV, which are the temperatures that we usually find in the SNR shocks. The plasma in SNR is optically thin at this energy range, which makes the measurement of the abundances quite confident (Vink, 2012). Analyzing the X-ray spectra is also possible to see the existence of non-thermal emission coming from synchrotron radiation produced by cosmic-rays and inferred the magnetic field that accelerates particles.

The last generation of X-ray telescopes as XMM-Newton and Chandra and the spectrometers intalled in these observatories allowed as to do imaging spectroscopy, which is very useful to differenciate the regions in the SNR where thermal and non-thermal radiation is produced and to produce temperature maps of the plasma to understand better the dynamics of the shocks.

---

[1] `http://hea-www.cfa.harvard.edu/ChandraSNR/`

[2] Green (2009)

[3] Ferrand & Safi-Harb (2012)

In this section, we will explain the main features of the X-ray emission of SNRs (see reviews of Mewe (1999); Kaastra et al. (2008) for an detailed explanation) and which physical processes are involved, which will be useful to understand better the work done in chapter 5.

1.5.1 Thermal emission

Most of the spectral characteristics of the thermal emission, i.e. continuum shape and emission line ratios, are determined by the electron temperature. Note that this temperature is not necessarily the same as the ion temperature. SNR plasmas are optically thin in X-rays, which makes X-ray spectroscopy a very interesting tool for measuring element abundances. In the case of old SNR, this is also useful to study the abundances in the ISM (e.g. Hughes, Hayashi & Koyama 1998).

Thermal X-ray spectra has different components: continuum emission by Bremsstrahlung (free-free emission), recombination continuum (free-bound emission), which arises when an electron is captured into one of the atomic shells, and two-photon emission caused by a radiative electron transition from a metastable quantum level.

The total emissivity for a Maxwellian energy distribution of the electrons is (Vink, 2012)

$$ {}_{ff} = \frac{32\ \ e^6}{3m_e c^3}\sqrt{\frac{2}{3km_e}}g_{ff}(T_e)T_e^{-1/2}\exp\left(-\frac{h}{kT_e}\right)n_e\sum_i n_i Z_i^2 \quad (\mathrm{erg\,s^{-1}\,cm^{-3}\,Hz^{-1}}) \tag{1.39} $$

with $g_{ff} \approx 1$, the gaunt factor. The subscript i denotes the ion species with charge eZ_i. The emissivity at a given temperature is determined by the factor $n_e \sum_i n_i Z_i^2$. Collisions with H and He nuclei dominate and this is why is we usually simply this factor by taking $n_e n_H$ or n_e^2. The normalization factor fitted by spectral analysis tools (e.g., *xspec*) is $\int n_e n_H \mathrm{d}V/(4\ \ d^2)$ (alos called *emission measure*), where we integrate the emissitivy by the observed volume observed and divide by $4\ \ d^2$ factor to obtain the measured flux. This simplification of the factor $n_e \sum_i n_i Z_i^2$ may be not valid for shocked SN ejecta electrons where collisions with heavy ions can also be an important contribution. Neglecting these contributions can derive erroneous density and mass estimates from the Bremsstrahlung emissivities (e.g. Vink, Kaastra & Bleeker 1996).

The other mentioned components (recombination and two-photon emission) are normally neglected, but in some situations, they can also be important, in particular for metal-rich plasmas in young SNRs (Kaastra et al., 2008).

SNR plasmas are often out of ionization equilibrium or *non-equilibrium ionization* plasmas (NEI). Plasmas of cool stars and clusters of galaxies are referred to as *collisional ionization equilibrium* (CIE). SNR plasmas are in NEI becuase for the low densities involved, not enough time has passed since the plasma was shocked, and few ionizing collisions have occurred for any given atom (Itoh, 1977). The number fraction of atoms in a given ionization state F_i is governed by the following differential equation:

$$\frac{1}{n_e}\frac{dF_i}{dt} = \;\;_{i-1}(T)F_{i-1} - [\;\;_i(T) + R_{i-1}(T)]F_i + R_i(T)F_{i+1} \tag{1.40}$$

with $\;\;_i(T)$ being the ionization rate for a given temperature and R_i the recombination rate. For NEI plasmas, $dF_i/dt = 0$ and the ionization fractions have to be solved using equation (1.40) as a function of $n_e t$, the *ionization age*. To solve this system is CPU expensive, but fast approach were proposed by Hughes & Helfand (1985); Kaastra & Jansen (1993); Smith & Hughes (2010). The main effect of NEI in young SNRs is that the ionization states at a given temperature are lower than in CIE.

1.5.2 Non-thermal emission

X-ray synchrotron radiation has been traditionally related with composite SNRs (SNR with a PWN), but recently this kind of radiation has been also detected in young SNR shells (Koyama et al., 1997). X-ray synchrotron spectra of young SNRs have rather steep indices (Γ=2-3.5) indiating a rather steep underlying electron energy distribution. Electrons which produce X-ray synchrotron radiation are close to the maximum energy of the distribution. When this maximum is defined where the acceleration gains are comparable to the radioactive losses, we say that we are in the *loss-limited case*. When the shock acceleration process has not had enough time to accelerate particles, then we say that we are in the *age-limited case* (Reynolds, 1998). The energy cut-off in these two situations is defined differently: in the age-limited case, the energy cut-off is $\;\;\exp(-E/E_{max})$, whereas in the loss-limited case the cut-off is superexponential $\;\;\exp(-E/E_{max})^2$ (Zirakashvili & Aharonian, 2007). In the loss-limited case, the cut-off photon energy is independent of the magnetic field (Aharonian & Atoyan, 1999). Values of the shock velocity obtained through this energy cut-off are $\sim$2000 km s^{-1} only encountered in young SNRs.

Another source of non-thermal X-ray emission comes from Bremsstrahlung and IC scattering. IC scattering is for SNRs important in the GeV–TeV band (Hinton & Hofmann, 2009), but for the magnetic fields inside SNRs, $B \approx 5-500\;\;$G, it is generally not expected to be important in the soft X-ray band. Bremsstrahlung would be caused by the non-thermal

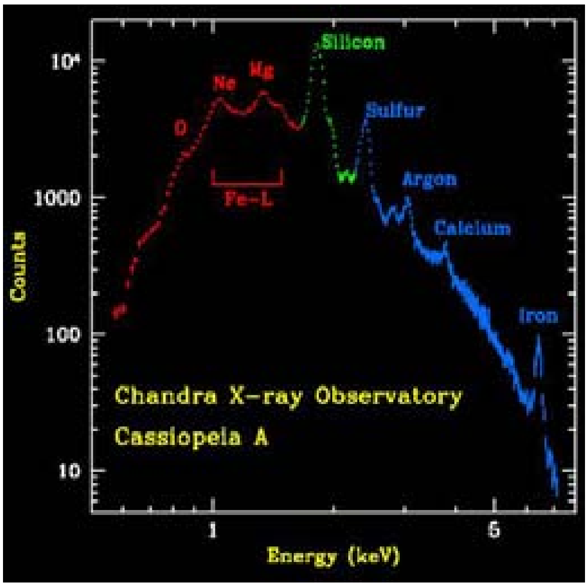

Fig. 1.11 X-ray spectrum of Tycho's SNR obtained with the *Chandra* X-ray Observatory (`http://chandra.harvard.edu`).

electron distribution. This contribution has been considered in some works (e.g., Asvarov et al. 1990; Vink, Kaastra & Bleeker 1997; Bleeker et al. 2001; Laming 2001). The electrons involved in the production of X-ray Bremsstrahlung emission have non-relativistic energies. This means that identifying non-thermal Bremsstrahlung would be useful to obtain information about the low energy end of the electron cosmic-ray distribution. However, it is unlikely that non-thermal Bremsstrahlung contributes enough to identify it with the current generation of hard X-ray telescopes.

1.5.3 Line emission

Line emission in SNR results from excitation or recombination of electrons in ions. Since density is very low, ions can be assumed to be in the ground state, and thus, collisional de-excitation or further excitation or ionization can be neglected. This also means that the ionization balance can be treated independently of the line emission properties (see Mewe 1999, for a full treatment). The spectrum of Tycho's SNR by the *Chandra* X-ray observatory is shown in figure 1.11 as an example. Tycho's SNR is the reminiscent of a Type Ia SN (e.g, Lopez et al. 2009). The most important lines in the spectrum from 0.3 to 1 keV are the oxigen (O), iron (Fe) and neon (Ne) lines. Magnesium (Mg), sulfur (S) and silicon (Si) lines dominate from 1 to 3 keV followed by the lines of argon (Ar) at 3.1 keV, calcium (Ca) at 3.8 keV and the Fe line at 6.4 keV.

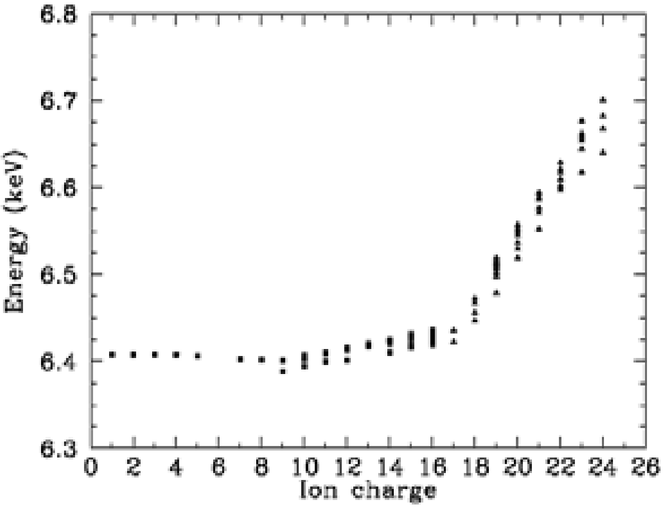

Fig. 1.12 Energy of the Fe-K shell line as a function of the ionization state (Vink, 2012). The data is given by Beiersdorfer et al. (1993); Palmeri et al. (2003); Mendoza et al. (2004). For ionization states from Fe I to Fe XVII the average Fe-K shell line is ~6.4 keV.

Fe line emission is an useful tool to characterize the state of the plasma. Fe-K shell ($n = 1$) emission can be observed for all ionization states of Fe, because of its high fluorescence yield and high abundance, provided that the electron temperature is high enough ($kT_e \gtrsim 2$ keV). The average line energy of the Fe-K shell emission provides information about the dominant ionization state. Figure 1.12 shows how the energy of the lines depends on the ionization state of the atom. For ionization states from Fe I to Fe XVII the average Fe-K shell line is ~6.4 keV.

Regarding the Fe-L shell ($n = 2$), there are prominent transitions between 0.7 and 1.2 keV. Fe-L shell line emission occurs for lower temperatures and ionization ages than the Fe-K lines ($kT_e \gtrsim$0.15 keV). The ionization state of the plasma can be also accurately determined by combining the observations of the Fe-K and Fe-L shell lines. This is especially useful in high resolution X-ray spectroscopy, where you can resolve the individual lines produced by the Fe-L shell. Fe-K emission around 6.4 keV could be caused by Fe XVII-XIX, or by lower ionization states, but in the latter case, Fe-L lines should not be detected. In higher ionization states, as Fe XXV and Fe XXVI, displace this line at 6.7 keV and 6.96 keV (see figure 1.12).

Aditional lines caused by radioactivity could be detected. During the first year after the SN explosion, the most important radioactive element is ^{56}Ni, which decays in 8.8 days into ^{56}Co, which subsequently decays into ^{56}Fe. ^{56}Fe is the most abundant isotope in the Universe. Type Ia supernovae (thermonuclear SNe) produce typically $0.6M_\odot$ per explosion, which makes the larger part of the production of this isotope. Other important element is ^{44}Ti. Its production is about 10^{-5}–10^{-4}M$_{\odot}$ per explosion (e.g. Prantzos 2011). The longer decay time makes it interesting for studying SNR in hard X-rays (85 yr, Ahmad et al. 2006). The decay chain of ^{44}Ti results in line emission at 67.9 keV and 78.4 keV, which are caused by the nuclear de-excitation of ^{44}Sc. The emission lines of this element are sensitive to the expansion speed of the inner layers of the ejecta. In addition, ^{44}Ti is sensitive to the boundary between the accreted material onto the proto-neutron star and the ejected material. Also is useful to identify and study explosion asymmetries (Nagataki et al., 1998).

1.6 This thesis

There are still many unanswered questions about how pulsars interact with the ambient interstellar medium and how these interactions affect their evolution. During their life, PSRs accelerate particles in the termination shock creating what we know as a pulsar wind nebula (PWN). Here, we explore models of spectra and magnetic field. These magnetized nebulae show spectral features which are still difficult to reproduce.

We have developed a new code to reproduce the spectra of PWNe, which we call TIDE-PWN (*TIme DEpendent-Pulsar Wind Nebulae*). This code solves the electron diffusion-loss equation as a function of time for the pairs accelerated and injected to the ambient medium from the termination shock of the PSR considering synchrotron, inverse Compton (IC), adiabatic and Bremmstrahlung energy losses. The resulting electron population is integrated in order to obtain the synchrotron, IC and Bremmstrahlung spectra of the PWN. The expansion of the nebula is considered during the free expansion. The model is described in detail in chapter 2.

We use this code to study different approximations made on the diffussion-loss equation and how they affect the spectra and their evolution. We have also performed a parameter space exploration with $\sim$100 simulations covering a wide range of ages, magnetic fractions and spin-down luminosities, in order to understand better the behavour of the spectra of Crab-like PWNe and shed some light on general issues as the dominance of the synchrotron self-Compton component at VHE for the Crab Nebula, the low magnetic fraction deduced from multiwavelength observations and some general constrains on the detectability of young PWNe at high energies. Other project in this field has been the systematic parameterization of the already detected young PWNe. We analyzed the spectra of 10 young PWNe and made a consistent comparison between the parameters obtained in each of them and looked for correlations (see chapter 3). All this work is explained in detail in chapter

4. In some cases, despite of the high spin-down power of the central pulsar, the associated PWN is not detected in TeV energies. We discuss about their detectability at TeV and magnetization state in chapter 5.

The formation mechamisms of magnetars and how it could influence the surrounding medium, i.e. the SNR is discussed in chapter 6. There are also unsolved questions about how magnetars are created after the supernova explosion. Two main models are still under debate to generate their huge magnetic fields: increase of the magnetic field of the pulsar through magnetic field conservation of the progenitor star or the alpha-dynamo process through vigorous convection of the core during the first few seconds after the supernova event. In this second process, it is expected to observe an excess of rotational energy generated during the process, but previous works done on this did not find clear evidences. Using the X-ray data available in the XMM-Newton and Chandra telescopes archive, we want to extend these works done before and look for features not only in the spectral lines, but also in the photometry and other parameters in comparison with other well studied SNRs. Finally, the conclusions of this dissertation and future projects are described in chapter 7.

Chapter 2

Time-dependent spectra of pulsar wind nebulae

In this chapter, we describe in detail the main characteristics of the 1D spectral model for PWNe that we have developed and its technical structure. We apply this model and fit the most known and complete PWN spectrum, the Crab Nebula. We also discuss about the improvements and caveats of our model and how the parameters of the Crab Nebula have changed with new implementations of physics in each version of the code. This chapter is based on the work done in Martín, Torres & Rea (2012).

2.1 Description of the code

2.1.1 The difussion-loss equation

The difussion-loss equation describes the evolution of the distribution of particles per unit energy and per unit volume in a certain time. We represent this function by $N_i(\gamma,\vec{r},t)$, where the subscript i represents the particle species, γ the energy Lorentz factor, $\vec{r}$ the position vector where we consider the distribution and t the current time. The most general form of this equation is (e.g., Ginzburg & Syrovatskii 1964)

$$\frac{\partial N_i(\gamma,\vec{r},t)}{\partial t} = \vec{\nabla}\cdot[D_i(\gamma,\vec{r},t),t] - \frac{\partial}{\partial E}[\dot{\gamma}_i(\gamma,\vec{r},t)N_i(\gamma,\vec{r},t)] + \frac{1}{2}\frac{\partial^2}{\partial E^2}[d_i(\gamma,\vec{r},t)N_i(\gamma,\vec{r},t)]$$
$$+Q(\gamma,\vec{r},t) - \frac{N_i(\gamma,\vec{r},t)}{\tau_i(\gamma,\vec{r},t)} + \sum_k \int P_i^k(\gamma,\gamma')N_k(\gamma',\vec{r},t)\mathrm{d}\gamma' . \quad (2.1)$$

The term on the left-hand side of the equation is the variation of the distribution in time. The first term on the right-hand side of the equation describes the spatial diffusion of the particles and $D_i(\,,\vec{r},t)$ is the diffusion coefficient. The space and time-dependence of the diffusion coefficient is due to changes in time in the structure and composition of the PWN (expansion and interaction with the ISM) and also changes in the magnetic field structure and density. Note that the diffusion coefficient also depends on the particle species, because the motion of particles in the magnetic field depends on their charge. The second term leads continuous change in energy of the particles due to acceleration mechanisms or energy losses in collisions. The function $_i(\,,\vec{r},t)$ is the summation of the energy losses due to all the mechanisms or collisions. The third term takes into account the fluctuations of this continuous variation of the energy of the particles. The coefficient $d_i(\,,\vec{r},t)$ is the variation in time of the mean square increment of energy of each kind of particle

$$d_i(\,,\vec{r},t) = \frac{d}{dt}(\Delta\bar{E})^2. \tag{2.2}$$

The function $Q_i(\,,\vec{r},t)$ represents the injection of particles from the termination shock per unit energy and unit volume in a certain time. The fifth term allows for the disappearance of particles due to escape from the distribution. $_i(\,,\vec{r},t)$ is the characteristic escape time of each particle. When energy losses are very important, we can consider them as an escape term defining

$$_i(\,,\vec{r},t) = \frac{\quad}{_i(\,,\vec{r},t)}. \tag{2.3}$$

Finally, the last term of equation (2.1) takes into account all the collisions which allow creation and annihilation of particles. $P_i^k(\,, \,)$ is the probability per unit time and per unit energy of the appearance of a particle of kind i with an energy produced by a collision of a particle of kind k with an energy . Note that the fluctuations in the energy variations due to the creation or annihilation of particles are not included. If the particles are atoms, $P_i^k(\,, \,)$ gives also the probability of fragmentation of the nuclei.

The solution of equation (2.1) considering all the terms is an extraordinary difficult task and it is useful to make approximations in some terms which are not important in our problem. First of all, in PWNe the spectral emission can be explain just considering electrons-positron pairs. We do not consider creation or annihilation of other particles species. Fluctuations in the variation of the energy are also neglected as we will use the mean value of the energy losses per unit energy, which typically are known and they have an analytical expressions for pairs. We assume an isotrpic injection in the whole nebula and no morphology in the magnetic field is taken into account, thus we do not consider diffusion effects.

Applying these approximations, typically found in the literature, equation (2.1) yields

$$\frac{N(\ ,t)}{t} = -\frac{}{}[\ (\ )N(\ ,t)] - \frac{N(\ ,t)}{(\ ,t)} + Q(\ ,t). \tag{2.4}$$

This equation can be solved using a Green function (see e.g., Aharonian, Atoyan & Kifune 1997). The solution is

$$N(\ ,t) = \frac{1}{(\ ,t)}\int_{-\infty}^{t} (\ _0,t_0)Q(\ _0,t_0)\exp\left(-\int_{t_0}^{t}\frac{\mathrm{d}x}{(\ _x,t_x)}\right)\mathrm{d}t_0. \tag{2.5}$$

being $_0$ the initial energy of the electron at time t_0. The initial and final energy are related by

$$t - t_0 = \int^{\ _0} \frac{\mathrm{d}}{(\ ,t\ )}. \tag{2.6}$$

To calculate these equations has a high computational cost. Because of this, we prefered to do a numerical approach using a first order approximation implicit scheme. Equation (2.4) is then

$$\frac{N(\ ,t+\Delta t)-N(\ ,t)}{\Delta t} = -\frac{(\ +\Delta\ ,t+\Delta t)N(\ +\Delta\ ,t+\Delta t) - (\ ,t+\Delta t)N(\ ,t+\Delta t)}{\Delta} - \frac{N(\ ,t+\Delta t)}{(\ ,t+\Delta t)} + Q(\ ,t), \tag{2.7}$$

where Δt and Δ are the increments in time and energy. To abbreviate the notation, we will write a superscript t or $t+1$ all those parameters which depend on the current time t or on the next time step Δt. We do the same with the energy using the subscripts g and $g+1$. Reordering the elements of the equation, we obtain the implicit scheme

$$\left(1-\frac{\Delta t}{\Delta}\,{}^{t+1}_{g} + \frac{\Delta t}{{}^{t+1}_{g}}\right)N_g^{t+1} + \frac{\Delta t}{\Delta}\,{}^{t+1}_{g+1}N^{t+1}_{g+1} = N^t_g + Q^t_g\Delta t. \tag{2.8}$$

Equation (2.8) can be written in matrix representation, such that

$$\begin{pmatrix} {}_1 & {}_2 & \cdots & \cdots & 0 \\ 0 & {}_2 & {}_3 & \cdots & \vdots \\ \vdots & \ddots & \ddots & \vdots & \vdots \\ 0 & \cdots & \cdots & {}_{M-1} & {}_M \end{pmatrix} \cdot \begin{pmatrix} N_1^{t+1} \\ N_2^{t+1} \\ \vdots \\ N_M^{t+1} \end{pmatrix} = \begin{pmatrix} N_1^t \\ N_2^t \\ \vdots \\ N_M^t \end{pmatrix} + \Delta t \begin{pmatrix} Q_1^t \\ Q_2^t \\ \vdots \\ Q_M^t \end{pmatrix} \tag{2.9}$$

where $_g = \left(1 - \frac{\Delta t}{\Delta}\ ^{t+1}_{g} + \frac{\Delta t}{^{t+1}_{g}}\right)$ and $_{g+1} = \frac{\Delta t}{\Delta}\ ^{t+1}_{g+1}$ and M is the number of points where we compute the spectrum. Solving this system of equations in each time step is needed to obtain the evolution of the pair population.

The injection $Q(\ ,t)$ acts as a source term. It is usually supplied by the user. The most typical form of injection for PWNe is a broken power law,

$$Q(\ ,t) = Q_0(t)\begin{cases}\left(\frac{}{_b}\right)^{-\ _1} & \text{for } _{min} \le\ \le\ _b,\\ \left(\frac{}{_b}\right)^{-\ _2} & \text{for } _b <\ \le\ _{max}.\end{cases} \tag{2.10}$$

where $_{min}$ and $_{max}$ are the minimum and maximum energy of particles. The energy break is represented by $_b$ and Q_0 is the normalization factor of the injection. In our model, the spin-down losses of the PSR accelerate particles (E_p) and maintain the magnetic field of the nebula (E_B), thus $E = E_p + E_B$. We define the magnetic fraction as (e.g., Tanaka & Takahara 2010)

$$= \frac{E_B}{E} = \frac{E_B}{E_B + E_p}. \tag{2.11}$$

Note that this definition is different from the magnetization factor defined in equation (1.22), where we calculate the ratio between the energy that goes to the magnetic field and the energy that goes to particles ($\ = E_B/E_p$). This implies that the relation between both factors is

$$= \frac{}{1+}. \tag{2.12}$$

We assume that is constant during the life of the PWN. We use the magnetic fraction to compute the injection normalization factor Q_0, such that

$$(1-\ )L(t) = \int_{_{min}}^{_{max}} m_e c^2 Q(\ ,t) \mathrm{d}\ . \tag{2.13}$$

In our model, $_{min}$ is a free parameter fixed by the user, but $_{max}$ is calculated demanding particle confinement into the acceleration zone, i.e. the Larmor radius of particles R_L must be smaller than the termination shock radius R_w

$$R_L = \ R_w, \tag{2.14}$$

where < 1 is the containment factor. The Larmor radius is given by $R_L = \ _{max} m_e c^2 / e B_w$, thus $_{max}$ can be written as

$$_{max} = \frac{e\ B_w R_w}{m_e c^2}. \tag{2.15}$$

The magnetic field in the termination shock B_w, in terms of the magnetic fraction , is (Kennel & Coroniti, 1984b)

$$B_w = \sqrt{\quad \frac{E}{c}}\frac{1}{R_w}, \tag{2.16}$$

where is the magnetic compression ratio which lies between 1, for Vela-like shocks, and 3, for strong shocks ($\ll 1$). Combining equations (2.15) and (2.16), we obtain

$${}_{max} = \frac{e}{m_e c^2}\sqrt{\quad \frac{E}{c}}. \tag{2.17}$$

The containment factor depends on the coherent length of the magnetic field ($= \sqrt{l_c/3R_L}$), but as our model does not take into account the magnetic field morphology, we consider as a free parameter.

Extrapolations to the PWN case of the simulations done by Spitkovsky (2008) for collisionless shock (e.g., Fang & Zhang 2010a; Holler et al. 2012). In this case, the injection function consist in a Maxwellian distribution for pairs at low energies plus a power law component only important at high energy

$$Q(\ ,t) = \begin{cases} Q_{0,1}(t)\ \exp\left(-\frac{}{\Delta {}_{1}}\right) & \text{for} \ < {}_{b}, \\ Q_{0,1}(t)\ \exp\left(-\frac{}{\Delta {}_{1}}\right) + Q_{0,2}(t)\ {}^{-} & \text{for} \ {}_{b} \leq \ < {}_{cut}, \\ Q_{0,1}(t)\ \exp\left(-\frac{}{\Delta {}_{1}}\right) + Q_{0,2}(t)\ {}^{-}\ \exp\left(-\frac{- {}_{cut}}{\Delta {}_{cut}}\right) & \text{for} \ \geq {}_{cut}, \end{cases} \tag{2.18}$$

where $\Delta {}_{1}$ is the width of the Maxwellian distribution and ${}_{cut}$ and $\Delta {}_{cut}$, the energy and the energy width of the cut-off. The index should be between 2.3–2.5 and the are ratios established between some parameters, i.e. ${}_{b}/\Delta {}_{1} \approx 7$, ${}_{cut}/ {}_{b} \approx 7.5$ and ${}_{cut}/\Delta {}_{cut} \approx 3$.

2.1.2 Magnetic field evolution

The magnetic field evolution is balance solving the differential equation (e.g., Pacini & Salvati 1973)

$$\frac{dW_B(t)}{dt} = \ E(t) - \frac{W_B(t)}{R_{PWN}(t)}\frac{dR_{PWN}(t)}{dt}, \tag{2.19}$$

where $W_B = B^2 R_{PWN}^3/6$ is the total magnetic energy. Note that the variation of the magnetic energy depends on the spin-down luminosity magnetic fraction and the adiabatic energy losses due to expansion of the nebula. Multiplying both sides of the equation and reordering, we find that

$$R_{PWN}(t)\frac{dW_B(t)}{dt}+\frac{dR_{PWN}(t)}{dt}W_B(t)=\frac{d}{dt}[W_B(t)R_{PWN}(t)]=\quad E(t)R_{PWN}(t). \tag{2.20}$$

Integrating, the equation yields

$$W_B(t)=\frac{}{R_{PWN}(t)}\int_0^t L(t\ )R_{PWN}(t\ )\mathrm{d}t\ , \tag{2.21}$$

and the magnetic field is then

$$B(t)=\frac{}{R^2_{PWN}(t)}\sqrt{6\quad\int_0^t L(t\ )R_{PWN}(t\ )\mathrm{d}t\ }\ . \tag{2.22}$$

2.1.3 Energy losses and escape

The non-thermal emission received from the PWN comes from the energy losses from pairs due to different radiative (or mechanical) processes described in many papers and books (e.g, Blumenthal & Gould 1970; Blumenthal 1971; Ginzburg & Syrovatskii 1964, 1965; Haug 2004; Longair 1994; Rybicki & Lightman 1979). We describe briefly the main energy losses taken into account in the diffusion-loss equation for leptonic models: synchrotron, inverse Compton, adiabatic and Bremsstrahlung energy losses. For more detail in the formulae derivation, see appendix A. Some particles escape from the distribution due to diffusion or catastrophic energy losses (mechanisms in which particles lose practically all the energy). In our model, we consider the escaping particles due to Bohm diffusion, which is the diffusion effect due to the presence of a magnetic field (e.g., Vorster et al. 2013)

$$_{Bohm}=\frac{eB(t)R^2_{PWN}(t)}{2\quad m_e c^3}, \tag{2.23}$$

where e is the electron charge. Note that the effect of this diffusion grows linearly with the energy as the timescale diminishes.

When particles are accelerated by a magnetic field, synchrotron radiation is emitted. The synchrotron energy losses suffered by a relativistic electron passing through a magnetic field are given by

$$_{sync}(\ ,t)=-\frac{4}{3}\frac{_T}{m_e c}U_B(t)\ ^2, \tag{2.24}$$

where $_T=(8\ /3)r_0^2$ is the Thomson cross section for electrons, r_0 is the electron classical radius, and $U_B(t)=B^2(t)/8$ is the energy density of the magnetic field. The dependence of equation (2.24) with the magnetic field and the energy is quadratic and tipically dominates in the high energy range of the pair distribution for young PWNe.

Inverse Compton interaction (IC) consist on collisions of high energy electrons with soft photons of the environment (e.g., CMB) that lend part of their energy to photons, upgrading them to -rays. For low photon energies ($h\ \ll m_e c^2$), the scattering of radiation from free charges reduces to the classical case of Thomson scattering. In the Thomson limit, the IC energy losses have the form (Blumenthal & Gould, 1970)

$$_{IC}(\ ,t) = -\frac{4}{3}\frac{_T}{m_e c}U\ \ ^2, \tag{2.25}$$

where U is the total energy density of the photon background in the PWN. Note that equation 2.25 has a similar form with equation 2.24. This means that in the Thomson limit, the synchrotron and the IC energy losses domain depending on the energy density of the magnetic field and the target photon field density rate.

Thomson approximation fails when we extrapolate it when $h\ \gg m_e c^2$. In order to take into account both regimes, we use the IC energy losses calculated using the exact Klein-Nishina cross section (Klein & Nishina, 1929). The IC energy losses in this case yield

$$_{IC}(\ ) = -\frac{3}{4}\frac{_T h}{m_e c}\frac{1}{\ ^2}\int_0^\infty {}_f \mathrm{d}\ _f \int_0^\infty \frac{n(\ _i)}{\ _i} f(q,\Gamma\ )H(1-q)H\left(q-\frac{1}{4\ ^2}\right)\mathrm{d}\ _i, \tag{2.26}$$

being H the Heaviside step function ($H(x) = \int_{-\infty}^{x}\ (y)\mathrm{d}y$) and $n(\ )$ the photon background distribution. The subscripts i and f refer to frequencies of the photons before and after scattering, respectively. The other terms are defined as

$$f(q,\Gamma\ ) = 2q\ln q + (1+2q)(1-q) + \frac{1}{2}(1-q)\frac{(\Gamma\ q)^2}{1+\Gamma\ q}, \tag{2.27}$$

$$\Gamma\ = \frac{4\ h\ _i}{m_e c^2}, \tag{2.28}$$

$$q = \frac{h\ _f}{\Gamma\ (\ m_e c^2 - h\ _f)}. \tag{2.29}$$

Bremsstrahlung radiation is caused by the deceleration of pairs due to the presence of electric fields that modifies the original trajectory. We consider two contributions: the electron-ion Bremsstrahlung and the electron-electron Bremsstrahlung. The electron-ion

Bremsstrahlung is due to the interaction of the electron with the electromagnetic field produced by the ionized nuclei of the ISM. The electron-atom bremsstrahlung energy losses have the form (Haug, 2004)

$$ {}^{e-a}_{Brems} = -\frac{3}{\ } \quad {}_{T} c S \frac{2}{{}^{2}+p^{2}} \left[\ \ln(\ +p) - \frac{p}{3} + \frac{p^{3}}{6}\left(\frac{2}{9}\ {}^{2} - \frac{19}{675}\ p^{2} - 0.06\frac{p^{4}}{\ }\right)\right], \tag{2.30}$$

with

$$ S = \sum_{Z} Z^{2} N_{Z} = N_{H}\left[1 + \sum_{Z\geq 2}\left(\frac{N_{Z}}{N_{H}}\right) Z^{2}\right]. \tag{2.31}$$

The parameter $p = \sqrt{\ {}^{2}-1}$ is the linear moment of the electron. N_H is the number density of ISM hydrogen and N_Z, the number density of the elements with atomic number Z and $\quad 1/137$ is the fine-structure constant.

For the second contribution, the electron-electron Bremsstrahlung, the energy losses are given by

$$ {}^{e-e}_{Brems} = -c\left(\sum_{Z} Z N_{Z}\right)\frac{p}{\ }(\ \ -1)\Phi^{ee}_{rad}(\ \ ). \tag{2.32}$$

It is not possible to obtain approximated formulae for the function $\Phi^{ee}_{rad}(\ \ )$, but we use function coming from fits of numerical computations (Haug, 2004)

$$ \Phi^{e-e}_{rad} \approx \frac{3}{8}\quad {}_{T}\begin{cases} \frac{\ +1}{\ }\left(0.6664+43.935p-2.272p^{2}-3.055p^{3}\right)\left(1-e^{2\ \ /p}\right), & \leq 1.02, \\ {}_{T}\frac{\ +1}{\ }\left(0.5754+1.14492\ \ -0.0665\ {}^{2}\right), & 1.02 < \ \leq 3, \\ (\ +1)\frac{4.181\ \ln(\ +p)-2.676\ \ -2.256}{{}^{2}+1.022\ \ -3.871}, & 3 < \ \leq 980, \\ 4\left[\ln(2\ \ ) - \frac{1}{3}\right], & > 980, \end{cases} \tag{2.33}$$

Note that the last term of equation (2.33) coincides with the formula given by Blumenthal & Gould (1970).

Finally, we take into account a non-radiative energy loss term, i.e the adiabatic losses. It is referred to the loss of internal energy of particles due to work applied over the ISM in the expansion of the PWN. For a relativistic gas, this term yields

$$ {}_{ad} = -\frac{1}{3}\left(\vec{\nabla}\cdot\vec{v}\right)\ . \tag{2.34}$$

In our model, we consider the PWN as an uniform expanding sphere, thus, we get the simple expression

$$_{ad}(\ ,t) = -\frac{v_{PWN}(t)}{R_{PWN}(t)} \ . \tag{2.35}$$

where $v_{PWN}(t) = dR_{PWN}(t)/dt$. Usually, adiabatic energy losses dominate in the low energy range of the pair distribution and is the most important contribution together with synchrotron losses.

2.1.4 Photon luminosity

Once we integrate the diffusion-loss equation, we obtain the energy distribution of pairs $N(\ ,t)$. To compute the spectrum luminosity, we need to multiply the pair population by the power emission of each contribution. A more detailed derivation of the formulae is given in appendix B. For synchrotron luminosity, the power emitted by each electron is given by (e.g., Ginzburg & Syrovatskii 1965; Blumenthal & Gould 1970; Rybicki & Lightman 1979)

$$P_{syn}(\ , \ ,B(t)) = \frac{\overline{3}e^3B(t)}{m_ec^2}F\left(\frac{}{_c(\ ,B(t))}\right), \tag{2.36}$$

where $_c$ is the critical function defined in equation (1.26) and the dimensionless function F is defined as

$$F(x) = x\int_x^{\infty} K_{5/3}(y)\mathrm{d}y, \tag{2.37}$$

where $K_{5/3}$ is the modified Bessel function of order $5/3$. The function F peaks near $0.29 \ _c$ as shown in figure 2.1. In the literature we find approximations to the synchrotron emission, where all the radiation at a given energy comes is concentrated at this frequency. In our code, we do not consider this monochromatic approximation and we compute numerically the function F. Some useful asymptotic expressions of F are given by Ginzburg & Syrovatskii (1965)

$$\begin{aligned}
F(x) &= \frac{4}{3\Gamma(\frac{1}{3})}\left(\frac{x}{2}\right)^{1/3}\left[1-\frac{\Gamma(\frac{1}{3})}{2}\left(\frac{x}{2}\right)^{2/3}+\frac{3}{4}\left(\frac{x}{2}\right)^2-\frac{9}{40}\frac{\Gamma(\frac{1}{3})}{\Gamma(\frac{5}{3})}\left(\frac{x}{2}\right)^{10/3}+\cdots\right] \quad \text{for } x \ll 1,\\
F(x) &= \frac{2}{3\Gamma(\frac{1}{3})}\left(\frac{x}{2}\right)^{1/3}\left[1-\frac{\Gamma(\frac{1}{3})}{\Gamma(\frac{5}{3})}\left(\frac{x}{2}\right)^{4/3}+3\left(\frac{x}{2}\right)^2-\frac{3}{5}\frac{\Gamma(\frac{1}{3})}{\Gamma(\frac{5}{3})}\left(\frac{x}{2}\right)^{10/3}+\cdots\right] \quad \text{for } x \gg 1.
\end{aligned} \tag{2.38}$$

Multiplying by the pair distribution and integrating, the synchrotron luminosity gives (in erg cm^{-2} s^{-1} Hz^{-1})

$$L_{syn}(\ ,t) = \int_{min}^{max} N(\ ,t)P_{syn}(\ , \ ,B(t))\mathrm{d} \ . \tag{2.39}$$

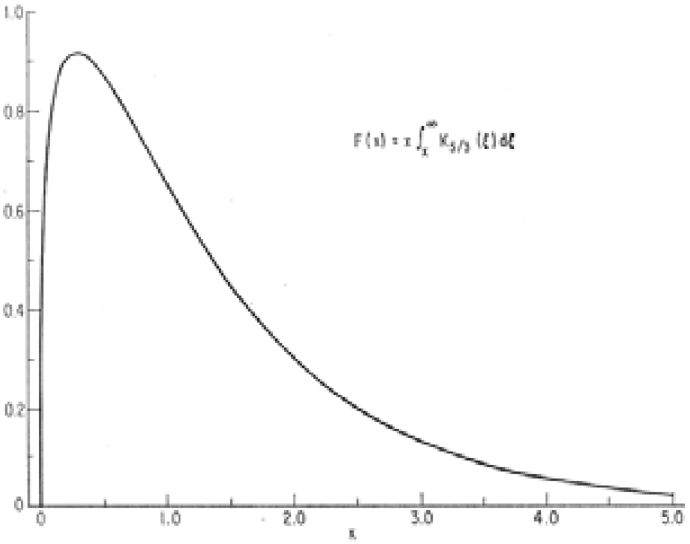

Fig. 2.1 Plot of the F function (Blumenthal & Gould, 1970). The peak of the function is near x =0.29.

Regarding the IC radiation, the power emitted by each electron is given by (Blumenthal & Gould, 1970)

$$P_{IC}(\ ,\ ,t) = \frac{3}{4}\frac{\ _T ch}{\ ^2}\int_0^\infty \frac{n(\ _i)}{\ _i} f(q,\Gamma\ )H(1-q)H\left(q-\frac{1}{4\ ^2}\right)\mathrm{d}\ _i. \tag{2.40}$$

Proceeding as for the synchrotron case, we obtain

$$L_{IC}(\ ,t) = \frac{3}{4}\ _T ch \int_{\ _{min}}^{\ _{max}} \frac{N(\ ,t)}{\ ^2}\mathrm{d}\ \int_0^\infty \frac{n(\ _i)}{\ _i}f(q,\Gamma\ )H(1-q)H\left(q-\frac{1}{4\ ^2}\right)\mathrm{d}\ _i. \tag{2.41}$$

In the code, the target photon field $n(\ )$ can be defined in two ways. One possibility is using a renormalized black body (grey body) with energy density w and temperature T for each one of the target photon fields considered, such that $n(\ ) = \sum_j n_j(\ )$, with

$$n_j(\ ) = \frac{15 w_j h^3}{kT_j^4}\frac{\ ^2}{\exp\left(\frac{h\ }{kT_j}\right)-1}. \tag{2.42}$$

The other posibility allowed by the code is to introduce a synthesized target photon distribution coming from other codes (e.g., GALPROP[1]). The code provides tools to transform the GALPROP outputs into a proper format (see section 2.1.7).

The synchrotron spectrum generated by pairs is also a target photon field for IC in-

---

[1] Porter, Moskalenko & Strong (2006)

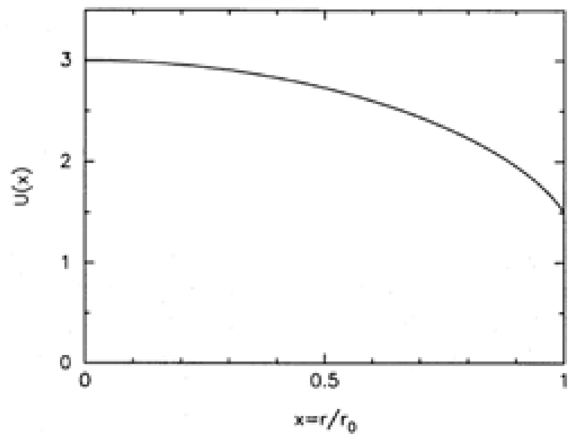

Fig. 2.2 Plot of the U function inside the spherical source, i.e. the PWN (Atoyan & Aharonian, 1996).

teraction. This process is called synchrotron self-Compton interaction (SSC). The photon distribution coming from the synchrotron spectrum is calculated assuming an homogeneous distribution of sources in a spherical volume $V_{sync} = (4/3) \quad R_{sync}^3$, such that $R_{sync} \leq R_{PWN}$ (Atoyan & Aharonian, 1996),

$$n_{SSC}(\quad ,R_{sync}(t),t) = \frac{L_{sync}(\quad ,t)}{4 \quad R_{sync}^2(t)c} \frac{\bar{U}}{h}. \tag{2.43}$$

The volume V_{sync} corresponds to the equivalent volume where the synchrotron radiation is contained. It is observed in many PWNe that the radius of the synchrotron volume varies with the frequency. For instance, the radius of the Crab PWN in radio is 2 pc, while in X-rays is only 0.6 pc. The parameter $\bar{U}$ is ~2.24 and corresponds to the spherical mean of the function $U(x)$ given by (Atoyan & Aharonian, 1996)

$$U(x) = \frac{3}{2} \int_0^{\frac{R_{sync}(t)}{R_{PWN}(t)}} \frac{y}{x} \ln \frac{x+y}{x-y} \mathrm{d}y. \tag{2.44}$$

In figure 2.2, we see that the value of $U(x)$ at $x = 0$ is 3 and decreases until 1.5 when $x = 1$. If we would consider a distribution greater than the radius of the PWN, then $U(x) \quad 1/x^2$ and $n_{SSC}(\quad ,R_{sync},t) = L(\quad ,t)/(4 \quad R_{PWN}^2 c)$, as we should expect.

Finally, Bremsstrahlung luminosity per electron has the form (Blumenthal & Gould, 1970)

$$P_{Brems}(\quad _i, \quad) = \frac{3}{2} \frac{\quad _T hcS}{\quad _i^2} \left(\quad _i^2 + \quad _f^2 - \frac{2}{3} \quad _i \quad _f \right) \left(\ln \frac{2 \quad _i \quad _f mc^2}{h} - \frac{1}{2} \right), \tag{2.45}$$

where S as defined in equation (2.31). ${}_i$ and ${}_f$ are the energy of the electron before and after interaction and are related by the kinematic condition

$${}_i - {}_f = \frac{h}{m_e c^2}. \tag{2.46}$$

For a given frequency, there is a minimum initial energy for the electron to produce the scattered photon. This minimum energy is

$${}_i^{min}(\ ) = \frac{1}{2}\left[\frac{h}{m_e c^2} + \sqrt{\left(\frac{h}{m_e c^2}\right)^2 + \frac{2h}{m_e c^2}\exp\left(\frac{1}{2}\right)}\right]. \tag{2.47}$$

With all these conditions, the total Bremsstrahlung luminosity is

$$L_{Brems}(\ ,t) = \frac{3}{2} \quad {}_T hcS \int_{{}_i^{min}(\ )}^{max} \frac{N(\ {}_i)}{{}_i^2}\left({}_i^2 + {}_f^2 - \frac{2}{3}\ {}_i\ {}_f\right)\left(\ln\frac{2\ {}_i\ {}_f mc^2}{h} - \frac{1}{2}\right) \mathrm{d}\ {}_i. \tag{2.48}$$

2.1.5 PWN expansion

The radius of the nebula is necessary not only for the calculation of the magnetic field, but also for the adiabatic losses of the nebula. The evolution is described only for the free expansion phase. For $E \quad E_0$, the expression for the radius is described by equation (1.29) and used in the first versions of the code. Currently, we do a more detailed calculus. We use the first law of the thermodynamics

$$\mathrm{d}q = E(t)\mathrm{d}t - P_{PWN}(t)\mathrm{d}V_{PWN}, \tag{2.49}$$

where q is the thermal energy of the nebula, P_{PWN} the internal pressure and V_{PWN} the volume of the nebula. The spin-down luminosity is given by equation (1.17). Equation (2.49) can be written in a more explicit way

$$\frac{d}{dt}\left[\frac{4\ P_{PWN}(t)R^3_{PWN}(t)}{3(\ {}_{PWN}-1)}\right] = E_0\left(1+\frac{t}{{}_0}\right)^{-\frac{n+1}{n-1}} - \frac{4}{3}\ R^2_{PWN}(t)P_{PWN}(t)\left(\frac{dR_{PWN}(t)}{dt}\right). \tag{2.50}$$

The internal pressure is given by (van der Swaluw et al., 2001)

$$P_{PWN}(t) = \frac{3}{25}\ {}_{ej}(t)\left(\frac{R_{PWN}(t)}{t}\right)^2, \tag{2.51}$$

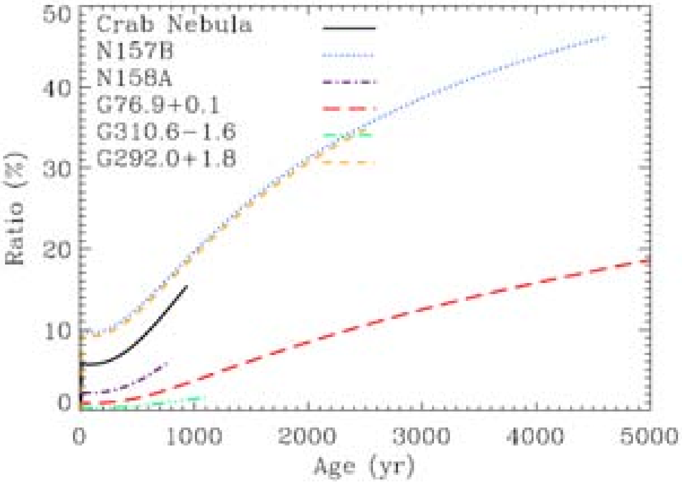

Fig. 2.3 Ratio of the PWN radii resulting from the analytical and numerical models as commented in the text for the nebulae studied in Martín et al. (2014).

being $_{ej}(t) = 3M_{ej}/(4\ \ R_{ej})$ the density of the ejecta. $R_{ej} = V_0 t$ is the radius of the SNR forward shock with V_0 defined as in equation (1.30). Equation (2.50) is integrated numerically using an first order explicit scheme, which is stable enough in this case. In figure 2.3, we show the difference as a function of time of using equation (1.29) and the numerical solution of equation (2.50) applied to the PWNe modelled in Martín et al. (2014). Note that the difference in some cases could reach more than 40%.

2.1.6 Code design

TIDE-PWN is written in FORTRAN language. It is divided in five independent executables, which compute separately the pair distribution (*nspectrum*) and the synchrotron (*synclum*), IC (*iclum*), SSC (*ssclum*), and Bremsstrahlung spectra (*bremslum*). There are also useful tools incorporated to sum up the components of the spectrum, integrate the spectra, etc. These tools are describe in section 2.1.7.

In a complete normal run of the code (see figure 2.4), the parameters of the problem are edited in the external file `parameters.txt`. The list of physical parameters is: age of the PSR (yr), braking index, distance (kpc), energy of the SN explosion (erg), ejected mass (in $M_\odot$), minimum energy of injection (Lorentz factor units), injection low and high energy indices, containment factor, magnetic fraction, temperature (K) and energy density (erg cm^{-3}) of the target photon field (up to five different target fields), hydrogen ISM density (cm^{-3}) and helium/hydrogen density ratio, the time step in the integration of the diffusion-loss equation (yr) and the number of points in energy where we compute the pair distribution.

Other important parameters in the file, but less usual to modify, are those which define the frequency range where we integrate the spectra components, the name of the output files and the path where the code has to save the outputs and read them when it is needed. Additional outputs as the magnetic field, spin-down luminosity, radius and energy losses evolution can be demanded or avoided. As we explained in section 2.1.4, the target photon field can be also provided by an external code. The TIDE-tool *gtotide* converts the target fields generated by GALPROP to TIDE-format files called `cmb.txt`, `fir.txt` and `nir.txt`, which are inputs of our simulation. As we observe in figure 2.4, *nspectrum* computes the pair distribution function at the given age of the PSR (file named by default `electron_spectrum.txt`). The file `electron_spectrum.txt` provides the pair distribution where we integrate the PWN spectrum in the rest of the codes. All the photon spectra are summed using the tool *sumspec*, which requires the additional input file `spectrum_list.txt` where we enter the list of the spectra that we want to join.

TIDE-PWN is written to have an easy interaction with the user and to allow the implementation of user-supplied routines to extend its applicability to other kind of physical problems as radiative processes in SNRs, cosmic-rays, etc. In order to get this, the code has been written using a modular structure, where the different ingredients are located in independent files. The executables work independently allows to compute only those component in which we are interested or use pair distributions given by other codes or given by analytical formulae. A brief description of each executable and their modules is explained below.

nspectrum

nspectrum is the program that we use when we want to obtain the pair distribution function solving the difussion-loss equation. The code is written in six different archives which include functions and subroutines to compute the evolution of the parameters of the diffusion-loss equation. In a complete run, *nspectrum* generates the outputs not only of the pair distribution, but also the magnetic field, energy losses, spin-down luminosity and PWN radius evolution. The code `nspectrum.f` includes the general algorithm to read the parameters, call the subroutines needed during the execution of the program and generates the output files. `injection.f` computes the particles injected into the nebula in each time step taking into account the evolution of the spin-down luminosity. The evolution of the latter is also written in the same file. The evolution of the magnetic field is performed by `magfield.f` and the PWN expansion is driven by `pwnexp.f`. The escape terms are calculated in `escape.f` and the energy losses formulae are written in `losses.f`. The main

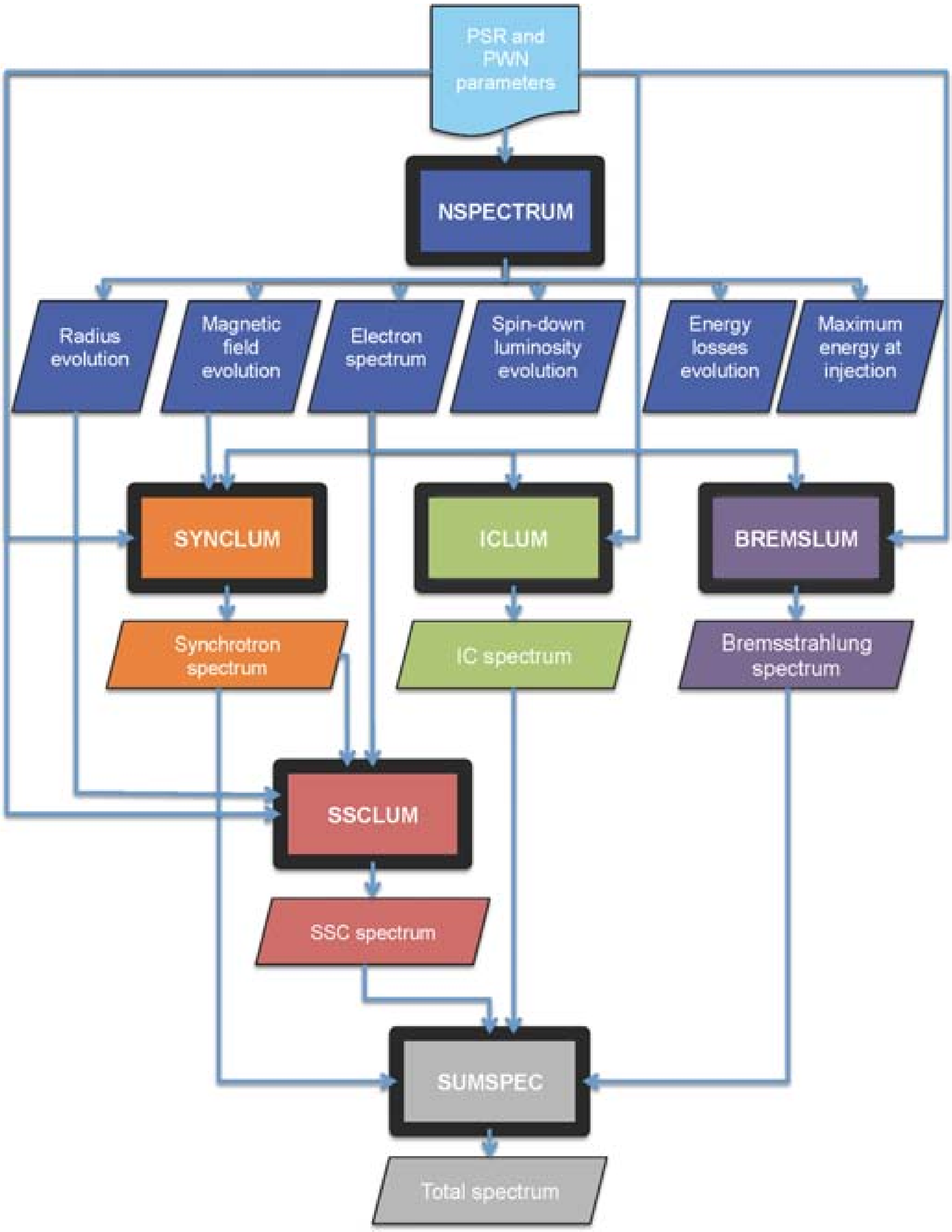
PSR and PWN parameters
NSPECTRUM
Radius evolution
Magnetic field evolution
Electron spectrum
Spin-down luminosity evolution
Energy losses evolution
Maximum energy at injection
SYNCLUM
ICLUM
BREMSLUM
Synchrotron spectrum
IC spectrum
Bremsstrahlung spectrum
SSCLUM
SSC spectrum
SUMSPEC
Total spectrum

Fig. 2.4 Flowchart for a complete run of TIDE-PWN. The parameters, modules and files involved in each program are explained in the text.

output is a three-column file called `electron_spectrum.txt` (name by default), where we keep the pair distribution as a function of the energy. The information description by columns is the following: energy (Lorentz factor units), $N(\ ,t)$ (Lorentz factor units^{-1}) and $^2 m_e c^2 N(\ ,t)$ (erg).

Apart from the file `electron_spectrum.txt`, the other generated files are: `magfield.txt` (magnetic field evolution), `linj.txt` (spin-down luminosity evolution), `rpwn.txt` (PWN expansion) and `losses(1-10).txt` (energy losses evolution). The current age (yr), magnetic field (G), spin-down luminosity (erg s^{-1}), radius of the PWN (pc) and maximum energy of the particles at injection (Lorentz factor units) is shown in the screen at the end of the run.

synclum

The synchrotron spectrum of a given pair distribution is computed by *synclum*. Apart from the parameters given in `parameters.txt`, there are two additional inputs. The first one is the pair distribution, which can be provided by *nspectrum* or an external code in a list format, or we can modify the analytical function in the module `analytic.f`. The second additional input is the current magnetic field of the nebula. We introduce it by hand in the screen. The module `synclum.f` contains the integration routine to compute equation (2.39). *synclum* generates a five-column output file called `sync_spectrum.txt` (name by default). The description of columns is: frequency (Hz), differential luminosity $L(\ )$ (erg s^{-1} Hz^{-1}), luminosity $\ L(\ )$ (erg s^{-1}), differential flux $F(\ )$ (erg s^{-1} cm^{-2} Hz^{-1}) and flux $\ F(\ )$ (erg s^{-1} cm^{-2}).

iclum

The program *iclum* computes the IC spectra coming from the target photon fields given in the file `parameters.txt` or the fields provided in a list format, i.e. `cmb.txt`, `fir.txt` and `nir.txt`. As in *synclum*, the pair distribution function is given in a list format or using the analytical defined in the module `analytic.f`. The integration routine is written in `iclum.f`. *iclum* can generate up to five output files depending on the number of the target photon fields considered for interaction (one file for each field). The format of the output files is the same as in *synclum*.

ssclum

The integration algorithm of *ssclum* is very similar as in *iclum*, but both routines has been written separately because the target photon spectrum (in this case the, synchrotron spectrum) can be treated with a greater level of complexity and include some morphology. The pair distribution input works as in the other programs already explained, but we need to introduce the current radius of the PWN (or generally, the radius of the volume where pairs are contained) as an additional input by screen. The synchrotron radiation produced by pairs is also demanded (only in list format), thus it is necessary to run first *synclum* before start *ssclum*. The output file is called `ssc_spectrum.txt` by default and has the same format as in *synclum*.

bremslum

bremslum computes the Bremsstrahlung radiation produced by the interaction with the electric field generated by pairs and the ions of the ejecta. Apart from the `parameters.txt` file, we only need the pair distribution function, which can be provided in a list format or by a function in the module `analytic.f`. The integration routine is written in `bremslum.f`. The output file is `brems_spectrum.txt` by default and has the same format as in *synclum*.

2.1.7 Other tools

TIDE-PWN provides other tools useful for the analysis of the spectra obtained. In this section we make a brief description of these supplementary codes.

- **sumspec**: it is used to sum up all the contributions of the PWN spectrum (see figure 2.4). The input file is `spectrum_list.txt`, which contains a list with the names of the files containing the spectrum information. *sumspec* generates the output file `photon_spectrum.txt` (name by default) with the same format described for *synclum*. Up to eight components can be summed at the same time.

- **lsdlum**: this program computes the total energy injected by the central pulsar during its life via spin-down luminosity. It solves the equation

$$E_{total} = \int_0^t E_0 \left(1 + \frac{t}{0}\right)^{-\frac{n+1}{n-1}} \mathrm{d}t \; . \tag{2.52}$$

The input parameters are demanded by screen: initial luminosity (erg s^{-1}), initial spin-down age (yr), braking index and age of the PSR (yr). The output is given by screen in erg.

- **nelec**: it computes the total energy contained in the electron spectrum E_p, such that

$$E_p = \int_{\gamma_{min}}^{\gamma_{max}} m_e c^2 N(\gamma, t) d\gamma . \tag{2.53}$$

  The only input is the electron spectrum in a list format, i.e. `electron_spectrum.txt`. The result is given by screen in erg.

- **luminteg**: this program integrates the photon spectrum in a given frequency range. It solves the integral

$$L = \int_{\nu_l}^{\nu_h} L(\nu) d\nu , \tag{2.54}$$

  where ν_l and ν_h are the low and high limits of the desired frequency range. These limits are introduced by screen. The photon spectrum has to be written in a list format. The output is shown by screen and gives the integrated flux (erg s^{-1} cm^{-2}) and its decimal logarithm, and the integrated luminosity (erg s^{-1}) and its decimal logarithm.

- **radiationFields**: the program *radiationFields* is written in IDL language and obtains the target photon fields calculated by GALPROP. *radiationFields* reads a fits file incorporated in the TIDE-PWN package which contains the simulation of the CMB, FIR and NIR photon fields. The input files introduced by screen are: galactic latitude and longitude (degrees), and distance from the Earth (kpc). It generates two output files called `table1.dat` and `table2.dat`. `table1.dat` is a one-column file with the wavelengths where the photon fields are computed in μm, and `table2.dat` contains the energy density distribution of the CMB, FIR and NIR fields in μm erg cm^{-3} μm^{-1}.

- **integ_ph**: it computes the energy densities of the CMB, FIR and NIR fields provided by GALPROP. There input files are `table1.dat` and `table2.dat`. In this case, there is no need to used *gtotide* previously. The energy densities are shown in the screen in eV cm^{-3}.

- **gtotide**: This program reads the files provided by GALPROP and change its format creating three new files in a tide-friendly format. The inputs are `table1.dat` and `table2.dat`. The outputs files are called `cmb.txt`, `fir.txt` and `nir.txt`. In each

Table 2.1 Summary of the physical magnitudes used or obtained for the Crab Nebula fit at the current age. A few parameters are fixed based on prior input or hypothesis.

Magnitude	Symbol	Value	Origin or Result
Age (yr)	t_{age}	940	fixed
Period (ms)	$P(t_{age})$	33.4033474094	from Taylor, Manchester & Lyne (1993)
Period derivative (s s^{-1})	$P(t_{age})$	4.209599 $\times 10^{-13}$	from Taylor, Manchester & Lyne (1993)
Spin-down luminosity now (erg s^{-1})	$L(t_{age})$	4.53×10^{38}	equation (1.6)
Moment of inertia (g cm^2)	I	10^{45}	fixed
Breaking index	n	2.509	from Lyne, Pritchard & Smith (1988)
Distance (kpc)	d	2	from Manchester et al. (2005)
Ejected mass ($M_\odot$)	M_{ej}	9.5	from Bucciantini, Arons & Amato (2011)
SN explosion energy (erg)	E_0	10^{51}	from Bucciantini, Arons & Amato (2011)
Minimum energy at injection	$_{min}$	1	assumed
Maximum energy at injection at t_{age}	$_{max}(t_{age})$	7.9×10^9	result of the fit
Break energy	$_b$	7×10^5	result of the fit
Low energy index	$_1$	1.5	result of the fit
High energy index	$_2$	2.5	result of the fit
Containment factor		0.3	result of the fit
Initial spin-down luminosity (erg s^{-1})	L_0	3.1×10^{39}	result of the fit
Initial spin-down age (yr)	$_0$	730	equation (1.19)
Magnetic field (G)	$B(t_{age})$	97	result of the fit
Magnetic fraction		0.012	result of the fit
PWN radius today (pc)	$R_{PWN}(t_{age})$	2.1	equation (1.29)
CMB temperature (K)	T_{CMB}	2.73	fixed
CMB energy density (eV/cm^3)	w_{CMB}	0.25	fixed
FIR temperature (K)	T_{FIR}	70	as in Marsden et al. (1984)
FIR energy density (eV/cm^3)	w_{FIR}	0.5	as in Marsden et al. (1984)
NIR temperature (K)	T_{NIR}	5000	as in Aharonian, Atoyan & Kifune (1997)
NIR energy density (eV/cm^3)	w_{NIR}	1	as in Aharonian, Atoyan & Kifune (1997)
Hydrogen density (cm^{-3})	n_H	1	assumed

file, we find two columns: the first one is frequency (Hz) and the second one is the photon density per unit frequency (cm^{-3} Hz^{-1}).

2.2 The Crab Nebula

We apply the model to the fit the spectrum of the Crab Nebula. The Crab Nebula is the most studied PWN in the whole electromagnetic spectrum. The distance to the Crab nebula is only 2 kpc (Manchester et al., 2005). The period of the PSR and its derivative are obtained from (Taylor, Manchester & Lyne, 1993). Assuming that the moment of inertia of the Crab PSR is $I = 10^{45}$ g cm^2, and using equation (1.6), we obtain the spin-down luminosity power today (4.5×10^{38} erg s^{-1}). The expansion of the PWN is considered using the free expansion approximation given by van der Swaluw et al. (2001) (equation 1.29). We consider a characteristic energy for the SN explosion of 10^{51} erg and an ejected mass of $9.5 M_\odot$ (Bucciantini, Arons & Amato, 2011). All the parameters used for the Crab nebula are summarized in table 2.1, including those determined by the code.

At the date of the pulsar period ephemerides (year 1994), the age of the pulsar was 940 yr. This is consistent with equation (1.6) and helps to minimize the bias produced by the non-simultaneity of the multi-wavelength data points used, obtained from ∼1970 (radio) to 2008 (VHE). We checked that changing the ephemeris to the latest one (e.g. the one used by the Fermi–LAT Collaboration[2]) introduces no visible change in the results.

In order to compute the IC energy losses and spectrum, we consider the CMB, FIR and NIR as a target photon fields. Each one of the latter two is considered as a diluted blackbody (Schlickeiser, 2002). The temperature of the FIR (NIR) is considered as 70 (5000) K. The CMB is a blackbody of temperature 2.73 K.

Regarding the magnetic field, in this fit we have assumed magnetic energy conservation as in Tanaka & Takahara (2010),

$$\int_0^t \quad L(t\ )\mathrm{d}t\ = \frac{4}{3}R^3_{PWN}(t)\frac{B^2(t)}{8}, \tag{2.55}$$

thus, using equation (1.6) and solving for the field, we obtain

$$B(t) = \sqrt{\frac{3(n-1)\quad L_0\ _0}{R^3_{PWN}(t)}\left[1-\left(1+\frac{t}{_0}\right)^{-\frac{2}{n-1}}\right]}. \tag{2.56}$$

A summary of how the parameters has changed with the new versions is done in the next section.

For the injection we use equation (2.10), where $Q_0(t)$ is calculated using equation (2.13). The final luminosity power is given by equation (1.6) and the initial spin-down power is determined using equation (1.17), since we know the luminosity power nowadays and the age of the PSR. For the ISM density in the Crab nebula, we take a fiducial value of 1 cm^{-3}. Thus, our free parameters in order to fit the spectrum are the magnetic fraction and the containment factor . For the final fit, we get $= 0.012$ and $= 0.3$. The magnetic field value we get today is 97 G, which is close to the 100 G calculated by the MHD simulations done by Volpi et al. (2008). Table 2.1 clarifies which parameters come from observations or assumptions, and which parameters are used to fit the data.

Figure 2.5 shows the magnetic field, spin-down power, lepton population and spectral energy distribution of the Crab nebula as a function of time, resulting from our code after normalization to current measurements. The current cooling times for the different processes considered are shown in Fig. 2.6, whereas the current spectrum is shown in figure 2.7.

---

[2] `http://fermi.gsfc.nasa.gov/ssc/data/access/lat/ephems/`

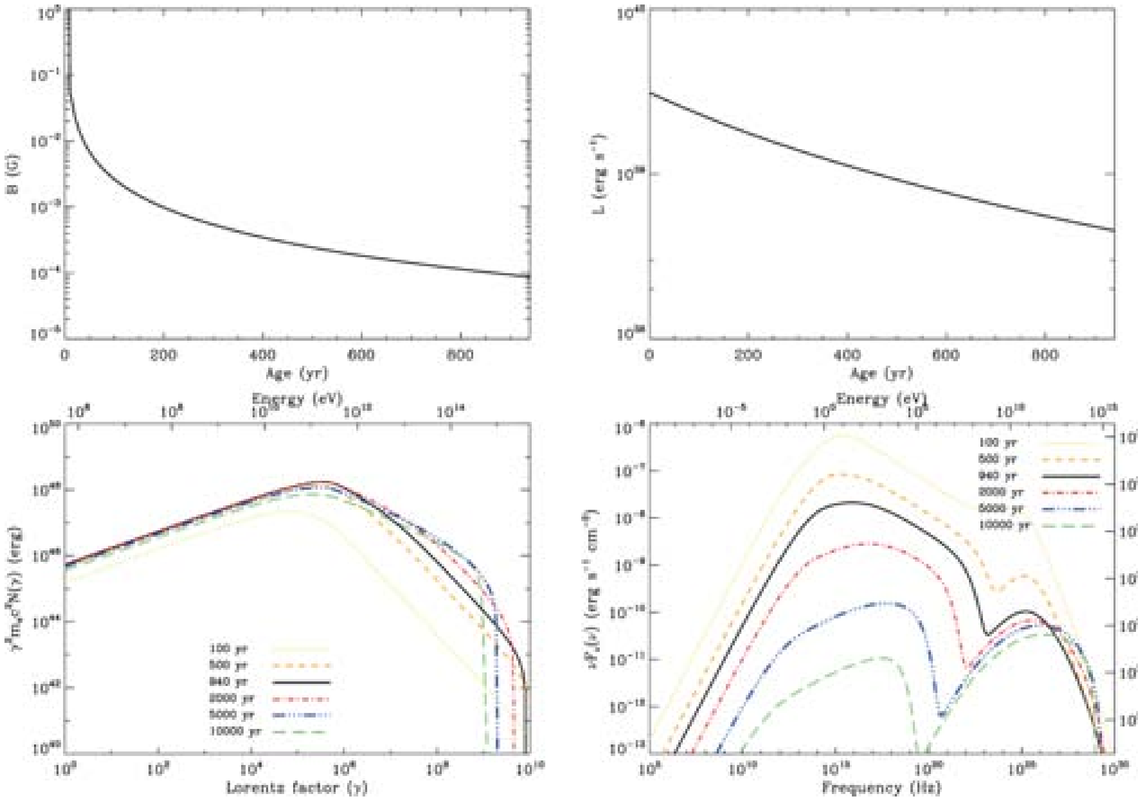

Fig. 2.5 Crab Nebula parameters and spectrum evolution. From top to bottom, left to right: Magnetic field, spin-down power, lepton population, and spectral energy distribution of the Crab Nebula as a function of time.

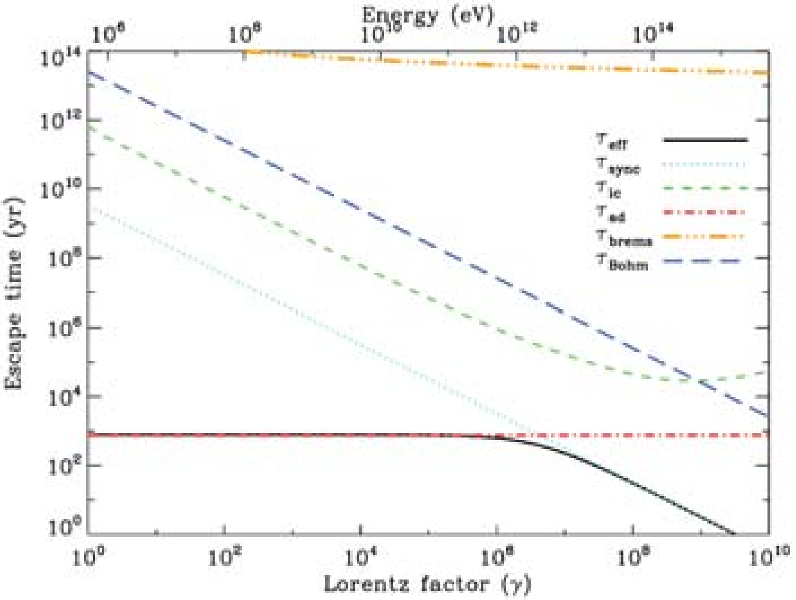

Fig. 2.6 Cooling times for the Crab Nebula at $t_{age} = 940$ yr. At low energies, the adiabatic losses are dominant because their cooling time is of the same order of the pulsar age. At high energies, synchrotron losses become the most important.

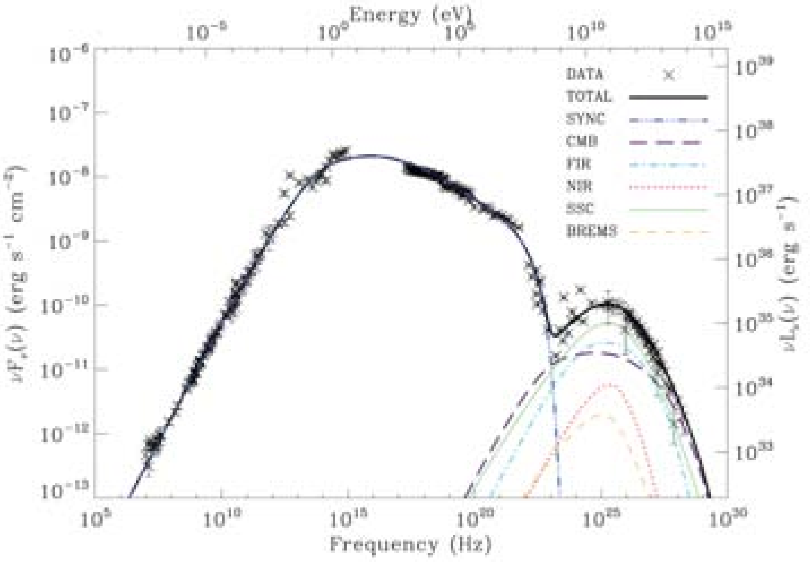

Fig. 2.7 Spectrum of the Crab Nebula fitted by our model. The data points are obtained from Baldwin (1971); Macías-Pérez et al. (2010) for the radio band; Ney & Stein (1968); Grasdalen (1979); Green, Tuffs & Popescu (2004); Temim et al. (2006) for the infrared; Veron-Cetty & Woltjer (1993) for the optical; Hennessy et al. (1992) for the ultraviolet; Kuiper et al. (2001) for the X-rays and soft -rays; and Abdo et al. (2010a); Aharonian et al. (2004, 2006a); Albert et al. (2008a) for -rays.

The SSC flux is the strongest contributor to the high-energy spectra, followed by IC with the CMB and the FIR. The Bremsstrahlung contribution is not very important, but as it is similar to the NIR radiation, we do not neglect it in favour of the other contributions. Most of the radiative considerations of Tanaka & Takahara (2010) are similarly obtained in our model, since they are driven by SSC domination. Our resulting value of the magnetic field today is lower than that used by Atoyan & Aharonian (1996) in their time-independent approach, who in turn adopted it from the Kennel & Coroniti (1984a) model, followed by an adjustment on the relativistic particle density to enable the data fitting. This value of magnetic field is unrealistically high for our time-dependent spectral model, and a lower value is preferred also by MHD simulations.

Regarding the time evolution presented in figure 2.5, it is interesting to note how the peak of the electron distribution moves from lower Lorentz factors to the energy break in the injection. This displacement of the peak is due to the high energy losses for energies lower than the break at early ages. The maximum energy of the injection is decreasing with time and the maximum energy of the electron population is decreasing also through energy losses, but at a slower rate due to the presence of high-energy electrons that were previously injected. The slope of the distribution at VHE becomes flattened with time also due to evolution in time of the dominant cooling process, increasing the power of the IC radiation. As the magnetic field falls, the synchrotron radiation diminishes with respect the IC radiation and at later ages (e.g. towards 10 kyr), the IC radiation contains most of the emitted flux. This is in agreement with the idea of older PWNe being still detectable at high energies but being devoid of lower-energy counterparts (de Jager & Djannati-Ataï, 2009). This is shown in figure 2.8. We see that the flux at energies >1 TeV and the gamma-ray flux are equal for an age of ∼5 kyr.

The radio and optical flux evolution of the Crab nebula show a decreasing-with-time behaviour. Measurements of the radio flux decrease were done by Vinyaikin (2007), using data from 1977 to 2000 at 86, 151.5, 927 and 8000 MHz. The mean flux-decrease rate averaged obtained was (-0.17 ± 0.02)% yr^{-1}. Using data obtained from our code at the same frequencies for the same time interval we obtained an averaged rate of -0.2% yr^{-1}. In optical frequencies, the continuum flux decreases 0.5±0.2% yr^{-1} at 5000 Å (Smith, 2003). In this case, we obtained directly from the model a flux decrease of 0.3% yr^{-1}. The evolution of both luminosities as extracted from our model is in agreement with observations.

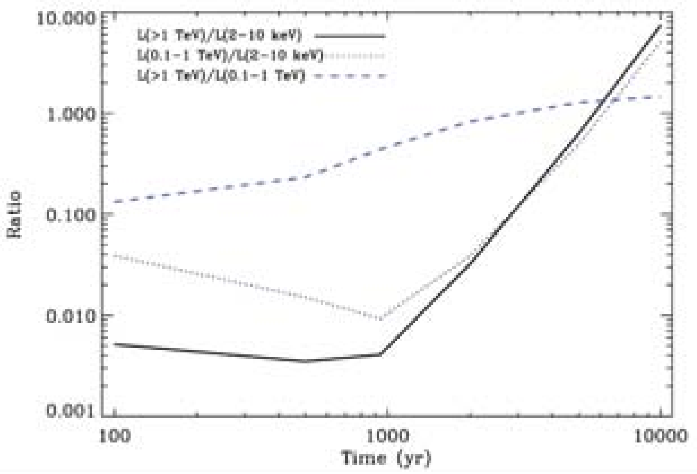

Fig. 2.8 Luminosity ratios for the Crab nebula evolution: $L(>1$ TeV)/L(2–10 KeV), L(0.1–1 TeV)/L(2–10 KeV) and $L(>1$ TeV)/L(0.1–1 KeV).

2.3 Improvements and caveats

Since the first version of the code (TIDE-PWN v0.0), where the diffusion-loss equation was solved using the time-independent analytical solution given by Aharonian, Atoyan & Kifune (1997) (equation 2.5), there has been a lot of improvements in terms of the physical assumptions, design and interaction with the user.

The time dependent code was introduced in the version v.1.0, where the spin-down luminosity varied as in equation 1.17 and the magnetic field as the prescription given by Venter & de Jager (2007)

$$B(t) = \frac{B_0}{\left(1+\frac{t}{_B}\right)}, \tag{2.57}$$

where B_0 is the initial magnetic field, $_B$ a characteristic timescale and is the index which regulates how fast the magnetic field decays. The PWN expansion was considered in a ballistic approximation ($R_{PWN}(t) = v_{PWN}t$).

The CPU time cost to solve equation (2.5) is high and it is not flexible for future versions of the code or for taking into account other similar physical problems. TIDE-PWN v1.1 solves the diffusion-loss equation in the numerical approach and the modular code struture described in section 2.1. The magnetic evolution prescription given by (Tanaka & Takahara, 2010) using the magnetic field energy conservation assumption was implemented in TIDE-PWN v1.2 (equation 2.56). In this version, we also implemented a better approximation in the expansion of the PWN and we introduced the free expansion model for constant spin-down luminosity deduced by van der Swaluw et al. (2001) (equation 1.29). The model for

Table 2.2 Physical magnitudes obtained for the Crab Nebula in the different versions of TIDE-PWN. The age considered in all cases is 940 yr.

Magnitude	TIDE-PWN v1.2	TIDE-PWN v1.3	TIDE-PWN v1.4
M_{ej} ($M_\odot$)	9.5	9.5	8.5
E_0 (erg)	10^{51}	10^{51}	10^{51}
$_{min}$	1	1	1
$_{max}(t_{age})$	7.9×10^9	9.3×10^9	8.0×10^9
$_b$	7×10^5	7×10^5	7×10^5
$_1$	1.5	1.5	1.5
$_2$	2.5	2.5	2.5
	0.3	0.25	0.25
L_0 (erg s^{-1})	3.1×10^{39}	3.1×10^{39}	3.1×10^{39}
$_0$ (yr)	730	730	730
$B(t_{age})$ (G)	97	84	80
	0.012	0.03	0.022
$R_{PWN}(t_{age})$ (pc)	2.1	2.1	2.1
T_{CMB} (K)	2.73	2.73	2.73
w_{CMB} (eV/cm^3)	0.25	0.25	0.25
T_{FIR}	70	70	70
w_{FIR}	0.5	0.23	0.23
T_{NIR}	5000	5000	5000
w_{NIR}	1	0.56	0.56
n_H (cm^{-3})	1	1	1

the Crab Nebula in the previous section was done using this version of the code (Martín, Torres & Rea, 2012).

In TIDE-PWN v1.3, we improved the estimate of the nebular magnetic field implementing the solution given in equation (2.22) proposed in Pacini & Salvati (1973). Another important implementation were the creation of the TIDE-tools. In particular, *integ_ph*, *lsdlum*, *nelec*, *radiationFields* and *sumspec*.

The rest of implementations as the tools *luminteg* and *gtotide*, the possibility to use the target photon fields generated by GALPROP, the module `analytic.f` which allows an analytic function for the pair population, the free expansion model with varying E and the current flowchart were introduce in the current version of the code presented in this chapter (v1.4).

In table 2.2, we show a summary of the parameters obtained for the Crab Nebula in different versions of the code. As we should expect, the parameters that changes are those related with the magnetic field and the expansion of the nebula. The IC target photon fields change from version 1.3 since we use the values provided by GALPROP.

Despite the improvements, there is still a lot of work to do in order to reproduce the PWN spectrum in the most complete and realistic way as possible. The first caveat of our model is that we only can reproduce the spectrum of young PWNe, i.e. PWNe which are still in its free expansion phase. We are developing a new module to reproduce the evolution of the SNR and the trajectory of the reverse shock to take into account its interaction with the PWN shell. When the reverse shock and the PWN shell collide, there is a bouncing process where the radius of the nebula is reduced and the magnetic field increases and reduces the energy of particles through synchrotron losses, increasing the emitted synchrotron radiation. After the bounce, the PWN reaches its Sedov phase, where the expansion behaves differently, as we already explaned in chapter 1. The proper motion of the PSR may be not important during the free expansion phase, but after the interaction with the reverse shock, the PSR can leave the PWN and powers it anymore (relic PWN) or re-enter in the nebula after the re-expansion. This possible discontinuity in the injection is nowadays neglected. Our code is, as all the other radiative codes we know, a 1D spectral code, thus other effects related with morphology are also neglected as injection and radiation anisotropies, magnetic field morphology, formation of the torus and jets, etc. All this phenomenology is only observed for a few relatively young PWNe, but observations with the next generation observatories (e.g., CTA) will increase, not only the number, but also the resolution of the images and morphology will be a key factor to understand the radiation and acceleration mechanisms of these objects and their evolution.

Chapter 3

Impact of approximations and effects of parameter variation in time-dependent modelling of PWNe

PWNe detected at TeV energies are associated with young ($\tau_c < 10^5$ years, here, only the very young are considered) and energetic PSRs ($E > 10^{33}$ erg s^{-1}), and usually display extended emission up to a few tens of parsecs (Rieger, de Oña-Wilhelmi & Aharonian, 2013). The majority of PWNe were observed by the H.E.S.S. experiment during the Survey of the Galactic plane performed since 2004 (see Gast et al. 2011 for the current status). Up to that time, only the Crab Nebula has been detected having a steady γ-ray flux about 1 TeV (Weekes et al., 1989). Due to the lack of a previous systematic study of the known young PWNe, some basic questions remain: How do approximations done in many radiative PWNe models affect to the spectra in a time-dependent context? Why is Crab the only PWN that is self-synchrotron (SSC) dominated? Why are the PWNe that we see at TeV energies particle dominated? Is there any observational bias behind this fact? At which sensitivity do we expect to map the whole phase space between particle and magnetic dominated nebula? What defines TeV observability of PWNe? In this chapter, we deal with these questions based on the works done in Martín, Torres & Rea (2012); Torres et al. (2013).

3.1 Impact of approximations

Apart from the approximations we focus below, one can also find many radiative approximations too in PWNe models: using a priori guesses for which field is dominant in each environment, using mono-chromatic assumptions for synchrotron and IC, or using Thompson cross-section instead of Klein–Nishina. These assumptions certainly simplify the treatment, but at the expense of assuming approximations for which their impact is usually not checked. We have not adopted any of them here.

Regarding the diffusion-loss equation, the most usual approximation is to neglect the escape term (see e.g. Tanaka & Takahara 2010, 2011) to obtain an advective differential equation (to abbreviate, we call it ADE). Using just this approximation in our complete model would lead to very similar values for the magnetic field and magnetic fraction (needed to obtain a good fit for today's Crab nebula, when imposing a correct contribution of the SSC such that it fits the high energy data today). This is because the Bohm time-scale is larger than the age of the Crab Nebula and is not affecting strongly the particles' evolution (see figure 2.6). Another common (and additional) approximation is neglecting the treatment of energy losses and instead replace it by the particle's escape time (see e.g. Zhang, Chen & Fang 2008; Qiao, Zhang & Fang 2009). In this case, equation (2.4) has the form

$$\frac{N(\ ,t)}{t} = -\frac{N(\ ,t)}{(\ ,t)} + Q(\ ,t). \tag{3.1}$$

In equation (3.1), particles are not losing energy, but they are rather removed from the distribution after a certain time. This makes equation (3.1) a partial differential equation in time (from now, TDE).

We use the fit of Crab Nebula to do the comparison between models. We include the fits in the ADE and TDE cases with the complementary approximations done by Tanaka & Takahara (2010) (hereafter ADE-T) and Zhang, Chen & Fang (2008) (hereafter TDE-Z). In ADE-T, the Bremsstrahlung energy losses and its spectrum, and the FIR and NIR contributions into the IC energy losses and their spectrum, are ignored. Also, the maximum energy at injection is fixed and the expansion of the PWN is modelled in a ballistic approximation ($R_{PWM} = v_{PWN}t$). All these approximations are not done in the full treatment presented before, against which we compare. In the TDE-Z, only the synchrotron escape time is considered (thus ignoring all other time-scales) and Bohm diffusion is used.

Table 3.1 shows the parameters for each of the models needed to obtain a good fit of the Crab nebula data at the current age. The column labelled value gives the parameters of the complete model in section 2.2.

Given that the observational parameters such as the age, the braking index, the period and the period derivative are fixed, they continue to determine $_0$ and $_c$ in all models. For the TDE model, the break energy and the containment factor (and, in consequence,

Table 3.1 Comparison of the values used or obtained in the different fits of the Crab Nebula today. We use dots for those parameters which have the same values as in the complete model. The dots appear when no change is needed from those values.

Symbol	Value	ADE-T	TDE-Z
$L(t_{age})$	4.5×10^{38}	…	2.5×10^{38}
$_{min}(t)$	1	10^2	…
$_{max}(t)$	7.9×10^9	7×10^9 (fixed)	6.5×10^9
$_b$	7×10^5	7×10^5	9×10^5
$_1$	1.5	…	…
$_2$	2.5	…	…
	0.3	…	…
L_0	3.1×10^{39}	…	1.7×10^{39}
$B(t_{age})$	97	…	93
	0.012	0.006	0.015
R_{PWN}	2.1	1.7	1.9
T_{CMB}	2.73	…	…
w_{FIR}	0.25	…	…
T_{FIR}	70	0	…
w_{FIR}	0.5	0	…
T_{NIR}	5000	0	…
w_{NIR}	1	0	…
n_H	1	0	…

the maximum energy at injection) have decreased. A smaller shock radius diminishes the number of VHE electrons, which is necessary due to the lack of energy losses affecting the population, and the smaller energy break corrects the lack of radio flux. The initial spin-down luminosity is smaller because the lack of losses makes electrons' disappearance slower. The magnetic fraction is larger to power the SSC contribution, and the energy break increases to compensate the lack of escaping particles at low energies and correct the radio flux. In the ADE-T case, we take the expansion velocity given by Tanaka & Takahara (2010) of 1800 km s^{-1}, which gives a radius for the PWN of 1.7 pc. This means that the synchrotron radiation is confined in a smaller volume, so the synchrotron photon density is larger and the magnetic energy fraction needed to obtain the correct SSC contribution is smaller than in our case. Note that the minimum and maximum energy at injection are also fixed in time according to the values used in Tanaka & Takahara (2010).

It is clear that at the current age, and particularly due to the fact of the strong SSC domination of the Crab nebula, one can find acceptable sets of parameters in both approximated models that fit the data well. However, this does not mean that the time evolution of these models would be similarly close to the complete analysis. Figures 3.1 and 3.2 compare the evolution of the results of the complete model and the approximate ones for the electron population and photon spectra, respectively. Differences increase with the time elapsed off the normalization age (the current Crab nebula), and are clear at a few hundred and a few thousand years. To have a better idea on how the spectra are changing, we use our model as reference data and calculate the relative theoretical distance of the ADE-T and TDE-Z models with respect to it as a function of frequency, both for the electron population and spectrum. We thus compute the theoretical distance D as $D = \ F_{comp} - F_{approx} \ /F_{comp}$, so that distance times 100 per cent is the percentile value of the deviation. F_{comp} and F_{approx} are the fluxes obtained by the complete and approximated model, respectively. These results are given in figures 3.3 and 3.4. The dips visible in these figures correspond to the crossing of the curves (lepton Lorentz factors or photon energies where both the approximate and complete models, as plotted in figures 3.1 and 3.2, coincide). The recovering of the curves after these dips correspond to the use of the absolute value in the Distance definition. Visually removing these dips gives an idea of the average deviation between the approximate and complete models across all energies. Note that the peaks in the relative distance evolution are broader, and represent bona fide increases in the deviation of the approximate results.

Regarding the underlying electron population, we see that differences among models range from 10 to 100 per cent and beyond. The TDE-Z models have a more deviating behaviour than the ADE-T models at later ages. Regarding the photon spectrum deviation, we find that for ages close to $t_{age} = 940$ yr and lower, the relative distance of all models with respect to the complete one is below 40 per cent with the exception of the frequency range between 10^{22} and 10^{23} Hz, where there is a transition between the synchrotron and IC dominated radiation. At larger times, deviations can be larger than 100 per cent. From 2 to 10 kyr, the relative distance in the optical range and in gamma-rays increases with age. As soon as the Crab nebula is let to evolve beyond a few thousand years, and consistently with the results found for the electron population, the relative distance between the spectra of the complete and the approximate models goes up to a factor of a few (i.e. percentile distance is a factor of a few 100 per cent) over large portions of the electromagnetic spectrum. These changes in the nebula evolution are only the by-product of the approximations used in the models and do not represent the expected behaviour of the source.

In conclusion, the time-evolution of the electron population and the photon spectrum deviation from the complete analysis are larger than 100 per cent, when they evolve in time off the normalization age. This puts in evidence the risks of considering approximations when studying time evolution, as well as, equivalently, when members of a population observed at different ages are analysed with the intention of extracting statistical conclusions.

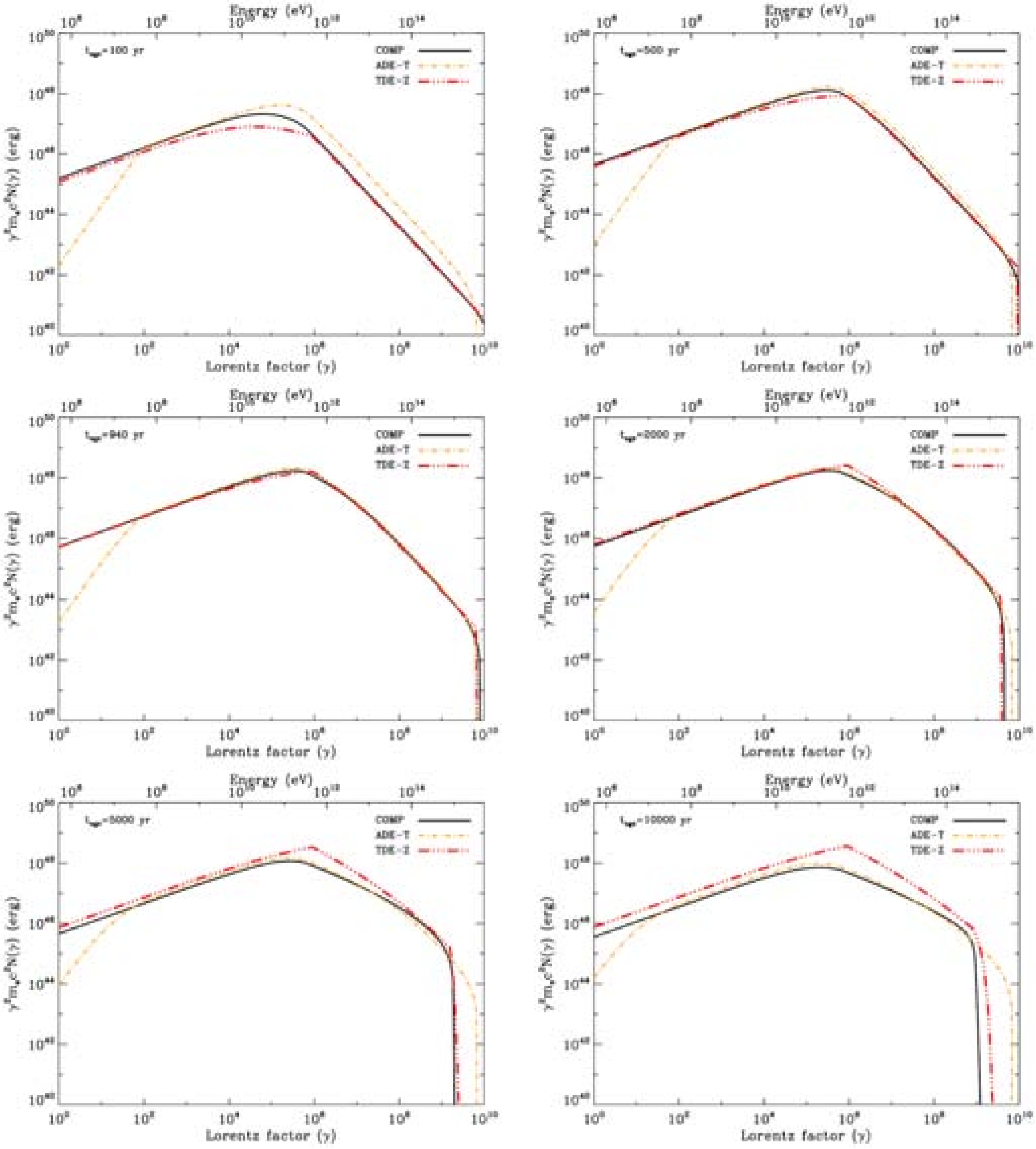

Fig. 3.1 Electron distribution of the Crab Nebula computed for different ages using the complete model together with the obtained results under the ADE-T and TDE-Z approximations.

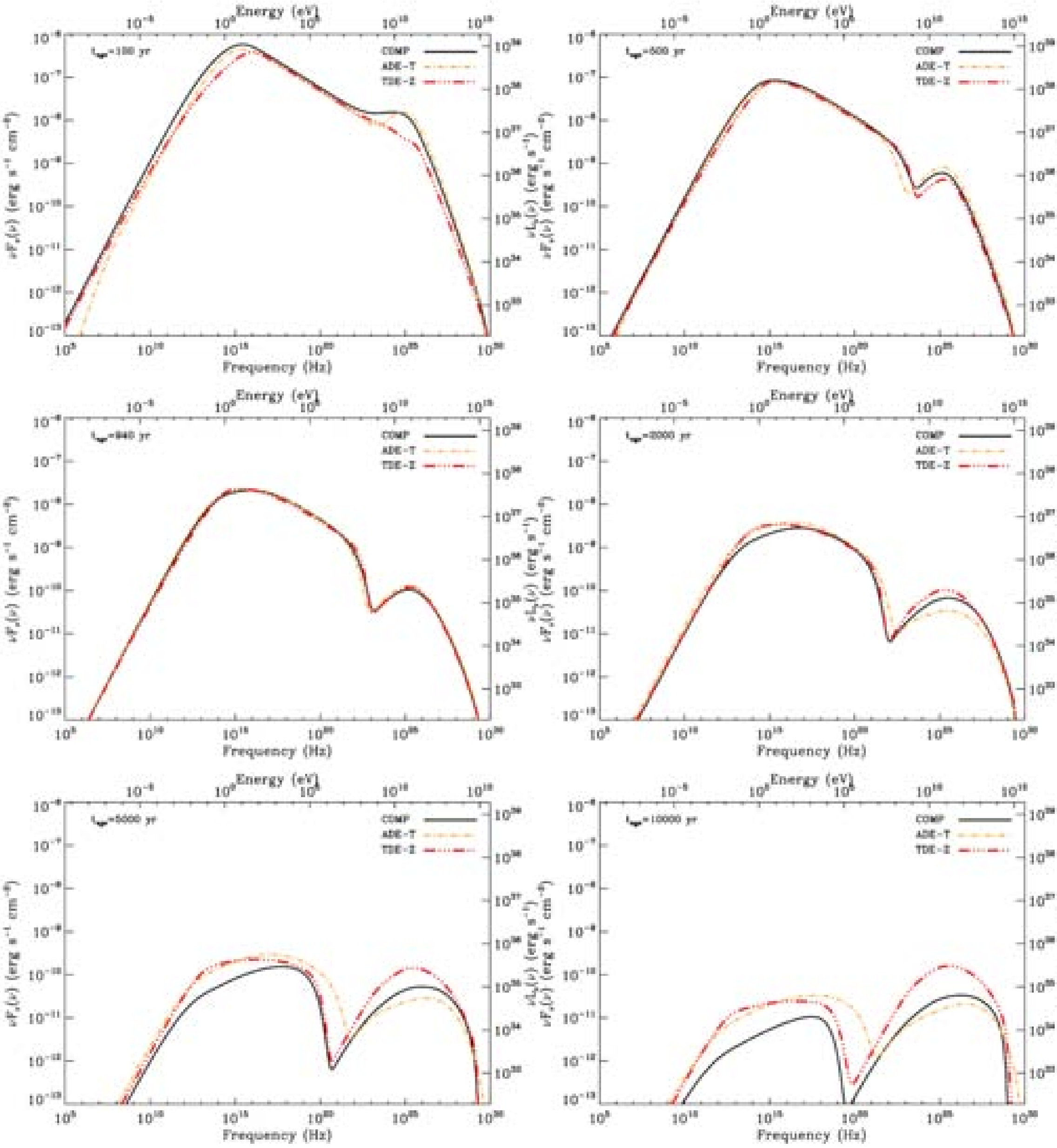

Fig. 3.2 Photon spectrum of the Crab Nebula computed for different ages using the complete model, together with the obtained results under the ADE-T and TDE-Z approximations.

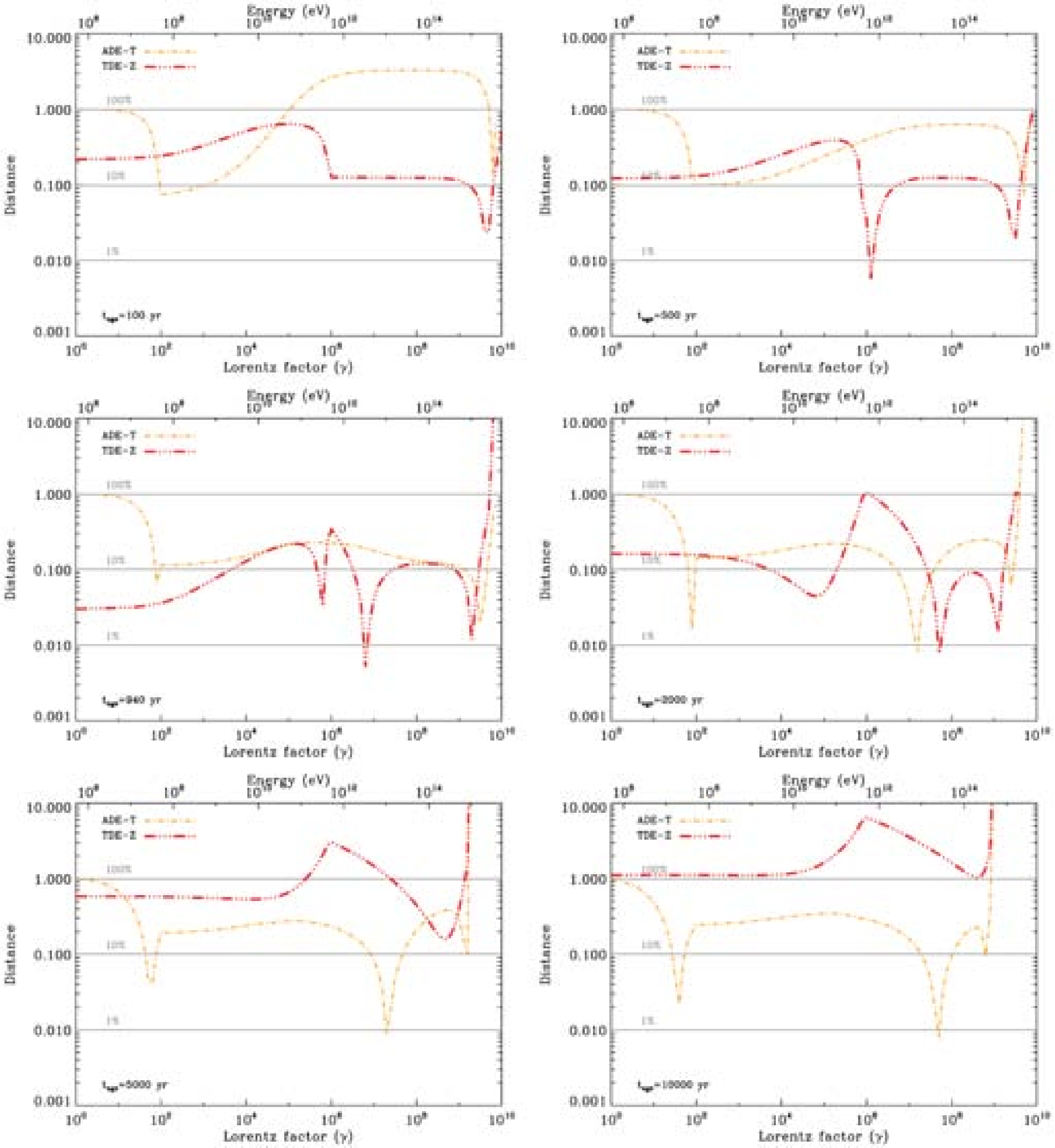

Fig. 3.3 Relative distance of the results for the electron distribution between the complete model, the ADE-T and TDE-Z approximations for the Crab Nebula at different ages.

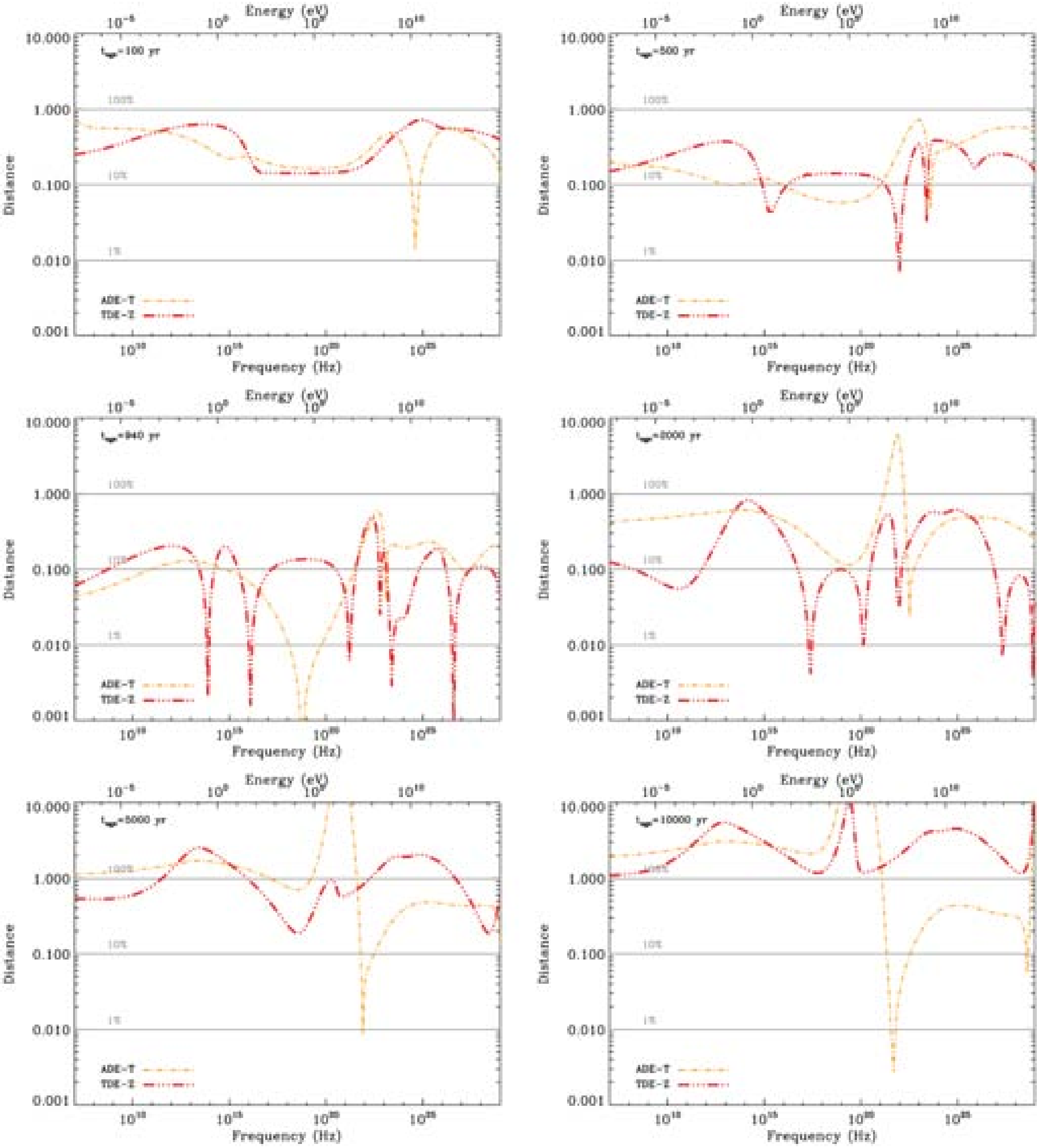

Fig. 3.4 Relative distance of the results for the photon spectrum between the complete model, the ADE-T and TDE-Z approximations for the Crab Nebula in different ages.

Table 3.2 Properties of the fake PSRs considered for the study, at an age of 940 years.

L_0 ($L_{0,Crab}$)	P (s)	P (s s^{-1})
1	0.0334	4.2×10^{-13}
0.1	0.1048	1.3×10^{-12}
0.01	0.3314	4.2×10^{-12}
0.001	1.0479	1.3×10^{-11}

3.2 Effects of magnetic field, age and intrinsic luminosity on Crab-like PWNe

To investigate the behavior of a Crab-like PWNe with different parameters, we generated a set of fake (i.e. synthetic) PWNe-models using the Crab Nebula as starting scaling. The Crab Nebula model we adopt is the one obtained with version 1.3 of TIDE-PWN (see table 2.2).

We consider 4 different intrinsic luminosities with respect to the Crab one (E_0= 1, 0.1, 0.01, 0.001 $\times E_{0,\mathrm{Crab}}$). Additionally, we require $_0$ and $_c$ to be the same as those of Crab, as well as we take the same moment of inertia and braking index. All pulsars which have a braking index measurement show an n-value smaller than 3 (Espinoza et al., 2011), like Crab. These requirements sets the properties of the fake pulsars, as well as define that all of them are young. We use equation (1.19) and the definition of $_c$ to derive, e.g., P as a function of P, and equation (1.17) to derive P as a function of the chosen E_0. The definition of n can then be used to define $\ddot{P}$. Using this approach, and an initial spin-down power equaling that of Crab, 10%, 1%, and 0.1% of the latter, we have defined the properties of 4 fake pulsars, which we show in table 3.2 at an age of 940 years (the first row in that table is Crab's observational data). Their position in the PP-diagram is shown in figure 3.5. These 4 simulated PSRs cover a wide range of young systems putatively powering a nebula, from the powerful Crab, to a magnetar-like case with 0.1% of its power (i.e. like PSR J1550-5418). The two intermediate cases, with luminosities of 10% and 1% of Crab are similar to, e.g., PSR J1124-5916 or J1930+1852, and J1119-6127, respectively.

The spectral energy distribution (SED) of the nebulae (consisting of synchrotron and inverse Compton (IC) radiation) is determined by several factors, including the magnetic field strength, the age of the system, and the background photon fields. To account for the PWNe phase space, we considered 8 values of magnetic fraction (0.001, 0.01, 0.03, 0.1,

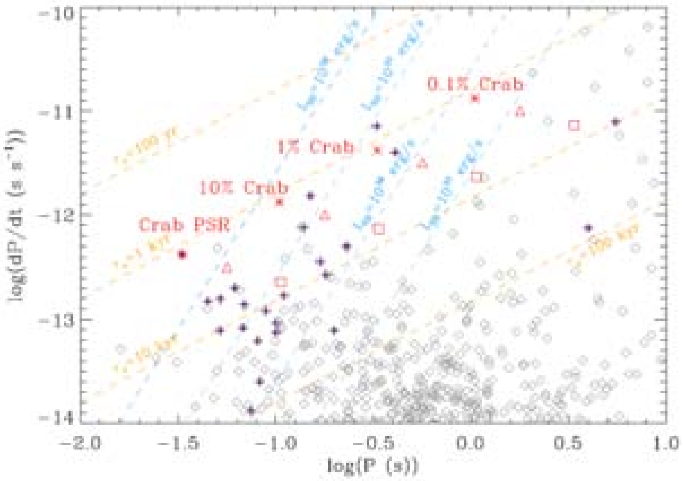

Fig. 3.5 *PP*-diagram of ATNF PSRs (in grey), together with the TeV detected PWNe (in violet), and the 4 fake PSRs adopted for this study (in red). The latter are shown at three different ages. See the text for a discussion.

0.5, 0.9, 0.99, and 0.999, from fully particle dominated to fully magnetically dominated nebulae), and 3 distinctive ages: 940, 3000, and 9000 years, in addition of the 4 values of L_0. Therefore, the explored phase space of PWNe models is constructed by $8 \times 4 \times 3 = 96$ cases. The supernova (SN) explosion energy is fixed in our models, as is the ejected mass, the injection parameters, and the environmental variables. It should be noted that these assumptions (particularly, to assume the same injection or environmental parameters than those in the Crab Nebula) will not necessarily reflect the reality of a particular PWN (below we present a discussion on how the photon field and injection spectrum would affect the results). Here, we are not looking for fits of the multiwavelength emission of a particular source, but rather searching for common trends in the phase-space of PWN models. For the study we are doing, maintaining these parameters fixed is essential to shed light on the behavior of the generated luminosities and SEDs as a function of the initial spin-down power and the magnetic fraction.

For instance, the contribution of the IC yield on the far infra-red (FIR) background (T∼70 K) would increase with respect to the cosmic microwave background (CMB) if we consider a steeper spectrum of electrons than the one in the Crab Nebula. In such a case, more electrons (with energies of a few TeV) are able to generate TeV photons via interacting with the FIR background, increasing its contributions relatively to the one from the CMB (Aharonian, Atoyan & Kifune, 1997). On the contrary, the optical / near infra-red (NIR) background (T∼5000 K) hardly plays any role. Assuming the Thompson limit, the IC emissivity $q(E) \propto wT^{(\ -3)/2}E^{-(\ +1)/2}$, where w is the energy density and T is the temperature of the photon background, and is the slope of the electron distribution (Blumenthal & Gould, 1970). It is possible to compare the two contributions by estimating the ratio $q_1/q_2 = (w_1/w_2)(T_1/T_2)^{(\ -3)/2}$. Supposing $\sim$1.5, then the ratio between the IC contribution of NIR (T$\sim$5000 K) to FIR (T$\sim$70 K) is about 0.045 (for equal energy densities; and as per the quoted formula). In addition, the Klein-Nishina effect, operative for VHE production with NIR photons, would reduce the IC-NIR yield significantly. If we use the ratio above to compare the IC-FIR with the IC-CMB yield, the contribution of dust with T$\sim$70 K interacting with electrons distributed with a slope of =2.5 will be similar to that of the CMB when $w_{FIR} \sim 2.2 w_{CMB} \sim 0.5$ eV cm^{-3}. The fixed values of the photon backgrounds on our Crab-like models are close to the Galactic averages (see Porter, Moskalenko & Strong 2006) and should be enough to gather general trends, which is the aim of this exercise. Finally, the distance to Crab is taken as fiducial. Given the relatively short distance to the Crab Nebula ($D = 2$ kpc), the conclusions reached on the lack of detectable TeV emission for some configurations will hold for pulsars located farther away. In any case, we provide both, luminosities and fluxes, when showing SEDs.

Table 3.3 shows the results for the scaled models for the different parameters considered. The results varying the total luminosity from the largest to the smallest are listed from top to bottom, each one considering three evolutionary ages (940, 3000 and 9000 years), and different magnetic fractions, increasing from left to right. Table 3.3 also quotes the intrinsic sizes of the simulated nebulae, magnetic fields, and maximum energy at the selected age, for the different models. A systematic comparison among the different results will be done in the following.

3.2.1 IC contributions for different age and PSR spin-down power

To compare the TeV luminosities, we integrated the simulated gamma-ray emission between 1 and 10 TeV. For comparison, we have also computed the synchrotron luminosity integrated between 1 and 10 keV. We compare the contributions of different photon backgrounds, namely SSC, FIR, NIR, and CMB, to the total IC yield of each of the nebulae. The results for the luminosity as a function of age are shown in figure 3.6 (for fixed LSD=0.1, 1, 10, and 100% of the Crab, from top to bottom, and a magnetic fraction of 0.001, 0.03, 0.5 & 0.999, from left to right). The results for the luminosity as a function of spin-down power are shown in figure 3.7 (for fixed increasing age, from top to bottom, and a magnetic fraction of 0.001, 0.03, 0.5 & 0.999, from left to right).

The IC components have a very similar behavior one to another, with the exception of

Table 3.3 Physical magnitudes for the fake PWNe sets. The symbol “…" stands for the same value shown in the column to the left.

$E_0 = E_{0,Crab}$=3.1×10^{39} erg s^{-1}							
Magnitude	Symbol	=0.001	=0.03	=0.1	=0.5	=0.9	=0.999
Age (yr)	t_{age}	940					
Spin-down luminosity at t_{age} (erg/s)	$E(t_{age})$	4.5×10^{38}	…	…	…	…	…
Maximum energy at injection at t_{age}	$_{max}(t_{age})$	2.3×10^{9}	1.2×10^{10}	2.3×10^{10}	5.1×10^{10}	6.8×10^{10}	7.2×10^{10}
Magnetic field (G)	$B(t_{age})$	15.4	84.2	153.8	343.8	461.3	486.0
PWN radius today (pc)	$R_{PWN}(t_{age})$	2.1	…	…	…	…	…
Age (yr)	t_{age}	3000					
Spin-down luminosity at t_{age} (erg/s)	$E(t_{age})$	7.0×10^{37}	…	…	…	…	…
Maximum energy at injection at t_{age}	$_{max}(t_{age})$	9.0×10^{8}	4.9×10^{9}	9.0×10^{9}	2.0×10^{10}	2.7×10^{10}	2.8×10^{10}
Magnetic field (G)	$B(t_{age})$	1.7	9.3	17.0	38.0	50.9	53.7
PWN radius today (pc)	$R_{PWN}(t_{age})$	8.5	…	…	…	…	…
Age (yr)	t_{age}	9000					
Spin-down luminosity at t_{age} (erg/s)	$E(t_{age})$	7.5×10^{36}	…	…	…	…	…
Maximum energy at injection at t_{age}	$_{max}(t_{age})$	2.9×10^{8}	1.6×10^{9}	2.9×10^{9}	6.6×10^{9}	8.8×10^{9}	9.3×10^{9}
Magnetic field (G)	$B(t_{age})$	0.2	0.9	1.7	3.8	5.1	5.4
PWN radius today (pc)	$R_{PWN}(t_{age})$	31.6	…	…	…	…	…
$E_0 = 0.1\,E_{0,Crab}$=3.1×10^{38} erg s^{-1}							
Age (yr)	t_{age}	940					
Spin-down luminosity at t_{age} (erg/s)	$E(t_{age})$	4.5×10^{37}	…	…	…	…	…
Maximum energy at injection at t_{age}	$_{max}(t_{age})$	7.2×10^{8}	3.9×10^{9}	7.2×10^{9}	1.6×10^{10}	2.2×10^{10}	2.3×10^{10}
Magnetic field (G)	$B(t_{age})$	9.7	53.1	97.0	216.9	291.0	306.6
PWN radius today (pc)	$R_{PWN}(t_{age})$	1.3	…	…	…	…	…
Age (yr)	t_{age}	3000					
Spin-down luminosity at t_{age} (erg/s)	$E(t_{age})$	7.0×10^{36}	…	…	…	…	…
Maximum energy at injection at t_{age}	$_{max}(t_{age})$	2.8×10^{8}	1.6×10^{9}	2.8×10^{9}	6.3×10^{9}	8.5×10^{9}	9.0×10^{9}
Magnetic field (G)	$B(t_{age})$	1.1	5.9	10.7	23.9	32.1	33.9
PWN radius today (pc)	$R_{PWN}(t_{age})$	5.3	…	…	…	…	…
Age (yr)	t_{age}	9000					
Spin-down luminosity at t_{age} (erg/s)	$E(t_{age})$	7.5×10^{35}	…	…	…	…	…
Maximum energy at injection at t_{age}	$_{max}(t_{age})$	9.3×10^{7}	5.1×10^{8}	9.3×10^{8}	2.1×10^{9}	2.8×10^{9}	2.9×10^{9}
Magnetic field (G)	$B(t_{age})$	0.1	0.6	1.1	2.4	3.2	3.4
PWN radius today (pc)	$R_{PWN}(t_{age})$	19.9	…	…	…	…	…
$E_0 = 0.01\,E_{0,Crab}$=3.1×10^{37} erg s^{-1}							
Age (yr)	t_{age}	940					
Spin-down luminosity at t_{age} (erg/s)	$E(t_{age})$	4.5×10^{36}	…	…	…	…	…
Maximum energy at injection at t_{age}	$_{max}(t_{age})$	2.3×10^{8}	1.2×10^{9}	2.3×10^{9}	5.1×10^{9}	6.8×10^{9}	7.2×10^{9}
Magnetic field (G)	$B(t_{age})$	6.1	33.5	61.2	136.9	183.6	193.5
PWN radius today (pc)	$R_{PWN}(t_{age})$	0.8	…	…	…		
Age (yr)	t_{age}	3000					
Spin-down luminosity at t_{age} (erg/s)	$E(t_{age})$	7.0×10^{35}	…	…	…	…	…
Maximum energy at injection at t_{age}	$_{max}(t_{age})$	9.0×10^{7}	4.9×10^{8}	9.0×10^{8}	2.0×10^{9}	2.7×10^{9}	2.8×10^{9}
Magnetic field (G)	$B(t_{age})$	0.7	3.7	6.8	15.1	20.3	21.4
PWN radius today (pc)	$R_{PWN}(t_{age})$	3.4	…	…	…	…	…
Age (yr)	t_{age}	9000					
Spin-down luminosity at t_{age} (erg/s)	$E(t_{age})$	7.5×10^{34}	…	…	…	…	…
Maximum energy at injection at t_{age}	$_{max}(t_{age})$	2.9×10^{7}	1.6×10^{8}	2.9×10^{8}	6.7×10^{8}	8.8×10^{8}	9.3×10^{8}
Magnetic field (G)	$B(t_{age})$	0.07	0.4	0.7	1.5	2.0	2.1
PWN radius today (pc)	$R_{PWN}(t_{age})$	12.6	…	…	…	…	…
$E_0 = 0.001\,E_{0,Crab}$=3.1×10^{36} erg s^{-1}							
Age (yr)	t_{age}	940					
Spin-down luminosity at t_{age} (erg/s)	$E(t_{age})$	4.5×10^{35}	…	…	…	…	…
Maximum energy at injection at t_{age}	$_{max}(t_{age})$	7.2×10^{7}	3.9×10^{8}	7.2×10^{8}	1.6×10^{9}	2.2×10^{9}	2.3×10^{9}
Magnetic field (G)	$B(t_{age})$	3.8	21.2	38.6	86.4	115.9	122.1
PWN radius today (pc)	$R_{PWN}(t_{age})$	0.5	…	…	…	…	…
Age (yr)	t_{age}	3000					
Spin-down luminosity at t_{age} (erg/s)	$E(t_{age})$	7.0×10^{34}	…	…	…	…	…
Maximum energy at injection at t_{age}	$_{max}(t_{age})$	2.8×10^{7}	1.6×10^{8}	2.8×10^{8}	6.3×10^{8}	8.5×10^{8}	9.0×10^{8}
Magnetic field (G)	$B(t_{age})$	0.4	2.3	4.3	9.5	12.8	13.5
PWN radius today (pc)	$R_{PWN}(t_{age})$	2.1	…	…	…	…	…
Age (yr)	t_{age}	9000					
Spin-down luminosity at t_{age} (erg/s)	$E(t_{age})$	7.5×10^{33}	…	…	…	…	…
Maximum energy at injection at t_{age}	$_{max}(t_{age})$	9.3×10^{6}	5.1×10^{7}	9.3×10^{7}	2.0×10^{8}	2.8×10^{8}	2.9×10^{8}
Magnetic field (G)	$B(t_{age})$	0.04	0.2	0.4	1.0	1.3	1.4
PWN radius today (pc)	$R_{PWN}(t_{age})$	7.9	…	…	…	…	…

the SSC, which has a similar slope as the synchrotron contribution. This slope similarity between the synchrotron and the SSC luminosity is seen for most of the plots in this section. There are some particular cases in which this is not the case, though. In the top-left panel of figure 3.6, the CMB contribution decays with age much more steeply than the FIR contribution to the total yield. This is the result of cutting the energy range in a small band, from 1 to 10 TeV, where, in this case, the IC contribution off the CMB is falling. The latter dominates the FIR contribution at 1 TeV in this case, where it starts to fall steeply; due to the value of $_{max}$ (see table 3.3), there are not enough electrons to generate higher energy photons interacting with the CMB background.

If we consider the SSC contribution, depicted by the blue-dashed line, we note it is only visible in the y-axis scale of the different panels of figure 3.6 in only a few occasions. It is irrelevant for $E =$0.1, 1, and 10% of the Crab power, disregarding the age and the magnetic fraction of the nebulae. On the contrary, it only becomes relevant for highly energetic (Crab-like) particle dominated nebulae at low ages (of less than a few thousand years). The Crab Nebula today corresponds to the bottom row, second column plot of figure 3.6 when the age (in the x-axis) is taken as 940 years. It is seen there how uncommon the SSC domination is: A lower or higher magnetic fraction (left or right panels), or a higher age (movement along the x-axis), and the SSC contribution would quickly be sub-dominant to the IC-FIR or even to the IC-CMB components.

Figure 3.7 shows the IC contributions of the spectrum as a function of spin-down. As we increase the spin-down power, all the IC contributions increase their luminosity due to the presence of additional high-energy electrons, but the SSC depends also on the power of the synchrotron emission, which is increasing too due to the higher magnetic field. This effect makes the SSC a steeper function of *E* compared to the other contributions. Consistently with the results of figure 3.6, the SSC contribution requires a young age and $\sim$70% of the Crab's power to become relevant. Fully magnetized nebulae ($= 0.999$), if they exist, are never SSC-dominated no matter the age or pulsar spin-down power. This is partly also a result of the increased synchrotron losses produced by the very high magnetic field, which diminishes the relative importance of all IC components. Finally, we note that –mimicking the SSC behaviour– for lower *E* and older ages than that of the Crab Nebula, the synchrotron luminosity falls down very quickly. This is partly because the energy range where we are integrating the luminosity is in the synchrotron cutoff regime produced by the electron population cut at high energies. The former results clarify why the Crab Nebula, and only it, is SSC dominated: There are no other PSRs we know, young and powerful enough so that SSC could play any role against the comptonization of FIR, or CMB photons.

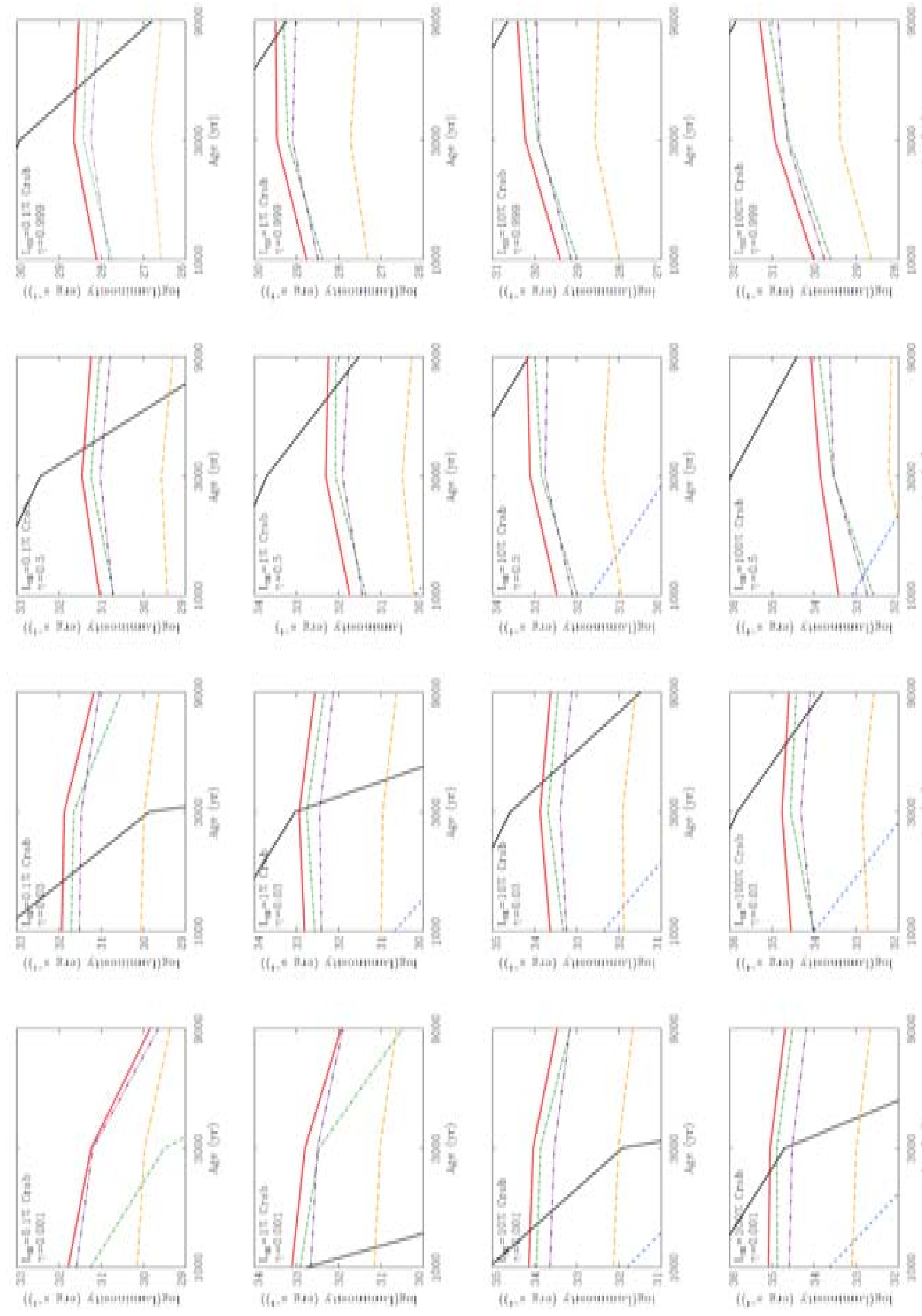

Fig. 3.6 Luminosities between 1 and 10 TeV of the IC contributions of the spectrum as a function of age. We fix $E = 0.1$, 1, 10, and 100% of the Crab Nebula (from top to bottom) and a magnetic fraction of 0.001, 0.03, 0.5 & 0.999 (from left to right). The black solid line is the synchrotron luminosity calculated between 1 and 10 keV. The other components are: total IC (red solid line), IC-CMB (green dot-dashed line), IC-FIR (purple triple dotted-dashed line), IC-NIR (orange dashed line) and SSC (blue-dashed line).

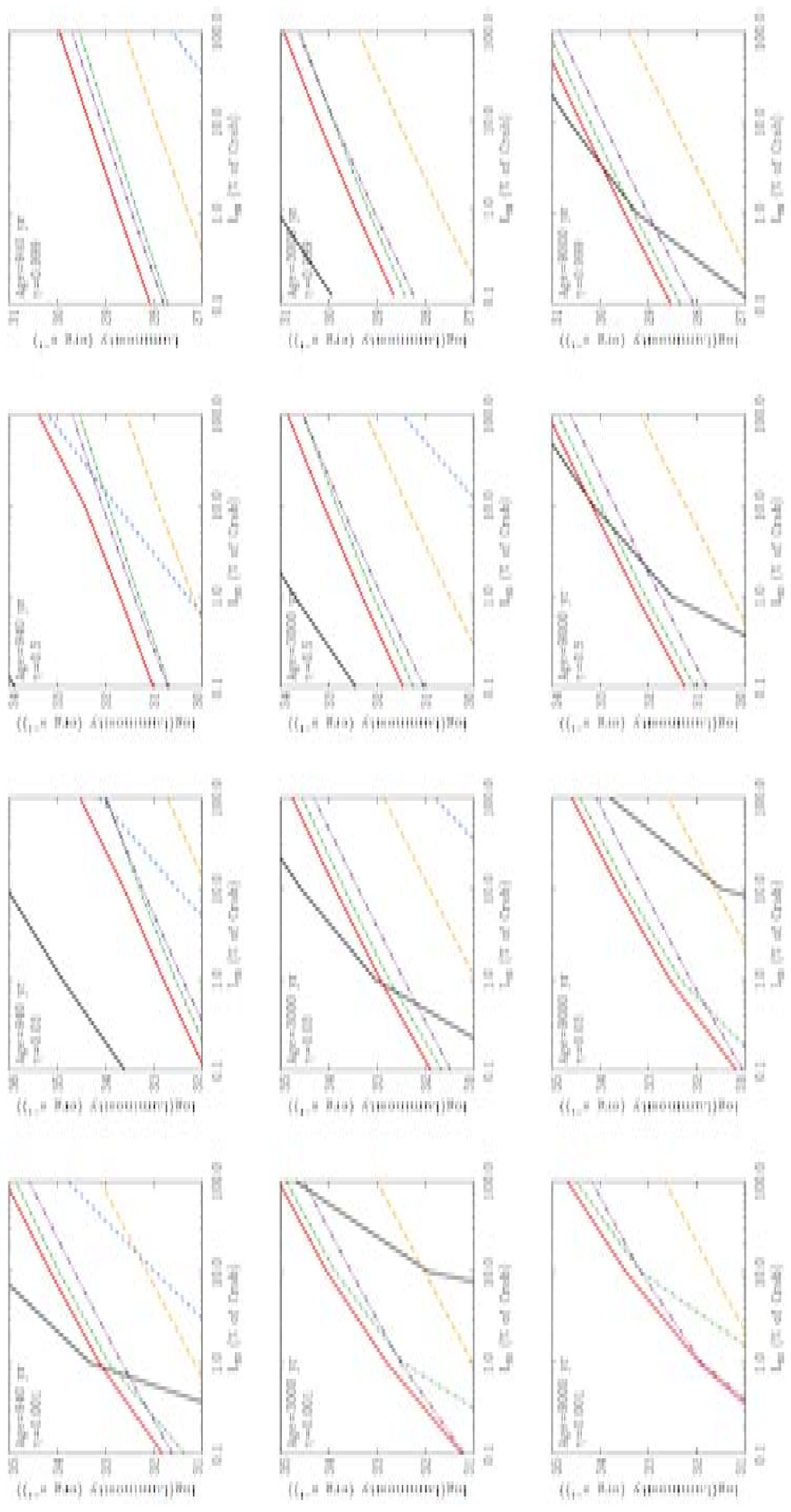

Fig. 3.7 Luminosities between 1 and 10 TeV of the contributions of the spectrum as a function of the spin-down luminosity. We fix an age of 940, 3000, and 9000 years (from top to bottom) and a magnetic fraction of 0.001, 0.03, 0.5 & 0.999 (from left to right). The color coding is as in figure 3.6

Similar considerations can be done by inspecting the SED as a function of age and spin-down power (figure 3.8 and 3.9). In each Figure, the SED showed in the left panel is calculated for a particle-dominated nebula ($= 0.03$) whereas the right one is computed for a nebula in equipartition ($= 0.5$). The shadowed areas correspond to the frequency intervals in radio, X-rays, GeV, and TeV bands where we integrate the luminosity to compare their ratios (see below). Several instrument sensitivities (in survey mode) are also shown, corresponding to the NVSS and EMU in radio[1], e-Rosita and ROSAT in X-rays[2], Fermi (3-yr Galactic) in the GeV band[3], and the current (H.E.S.S.) and future (CTA) experiments in the TeV band (for 50 hours and 5 detection) (e.g., Gast et al. 2011; Actis et al. 2011).

It is interesting to note that, for the considered sensitivities, no young PWN at TeV energies (for any age or magnetic fraction, top row in figure 3.8) would be detectable if the pulsar's spin-down power is 0.1% Crab or lower (and under the caveats of the assumptions discussed in the previous section, e.g., assuming the same spectral slope in the injection than those in the Crab Nebula). This conclusion is particularly stable for H.E.S.S.-like telescopes; the youngest of the pulsar's considered is more than one order of magnitude below the sensitivity considered. The effect of using different injection or FIR energy density to this conclusion is discussed below.

For more energetic pulsars (1% of Crab, middle row) distinctions in age and magnetic fraction appears to reflect strongly on the TeV flux and therefore on the detectability of the nebulae. For instance, only low magnetic fraction, i.e., particle dominated nebulae, can be detected by H.E.S.S.-like telescopes if young enough (a few thousand years). If the same nebulae were in equipartition, the TeV luminosity would be very much suppressed and the detection even with CTA would require a deep observation. Which exact ages of the nebulae will CTA detect in these conditions will ultimately depend on the injection and environmental parameters. For the ones we have assumed, larger ages are preferred, when enough electrons are available for interaction. On the contrary, nebulae powered by pulsars with spin-down of 10% Crab or more are all detectable by H.E.S.S.-like telescopes if they are particle dominated, no matter the age (bottom-left panel of figure 3.8). The possibility of detection is less clear in case of larger magnetic fractions (bottom-right panel, same figure). We recall that 2 kpc is assumed for the distance in the scale of the left-axis of figures 3.8 and 3.9, but the general trend of these conclusions should scale with it, worsening the chances of detection the farther the nebula is located. This already points to an interesting observational

---

[1] See for instance `http://askap.pbworks.com/w/page/14049306/RadioSurveys`

[2] See `http://www.mpe.mpg.de/455799/instrument`

[3] From the Fermi-LAT performance `http://www.slac.stanford.edu/exp/glast/groups/canda/lat_Performance.htm`

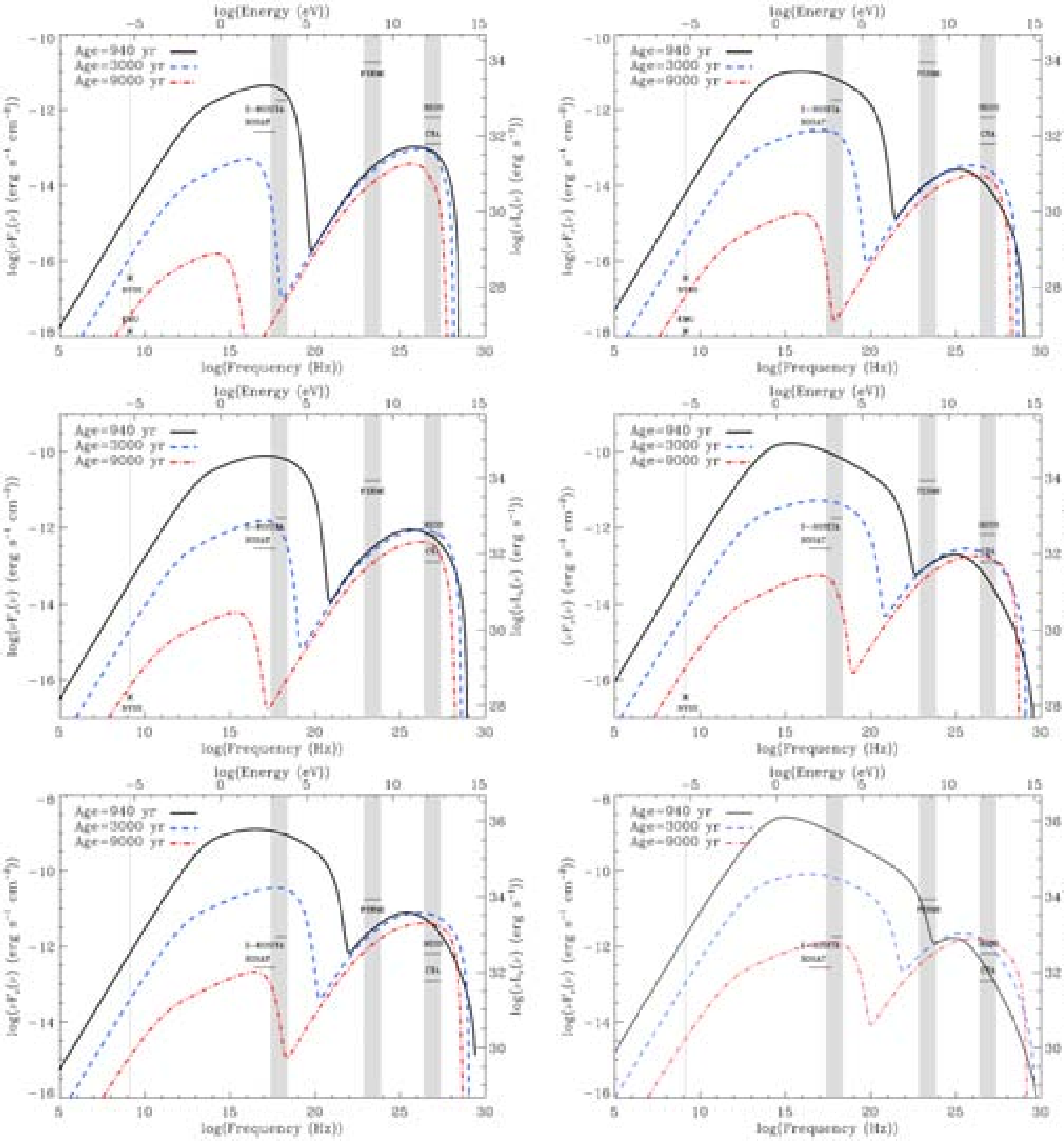

Fig. 3.8 Comparison of the SEDs for *E*=0.1, 1, and 10% of the Crab (from top to bottom) as a function of the age. The magnetic fraction is fixed at 0.03 (left) and 0.5 (right). The shadowed columns correspond to the frequency intervals in radio, X-rays, the GeV, and the TeV bands where we have integrated the luminosity. The sensitivity of some surveys and telescopes in these energy ranges are shown by thin black lines.

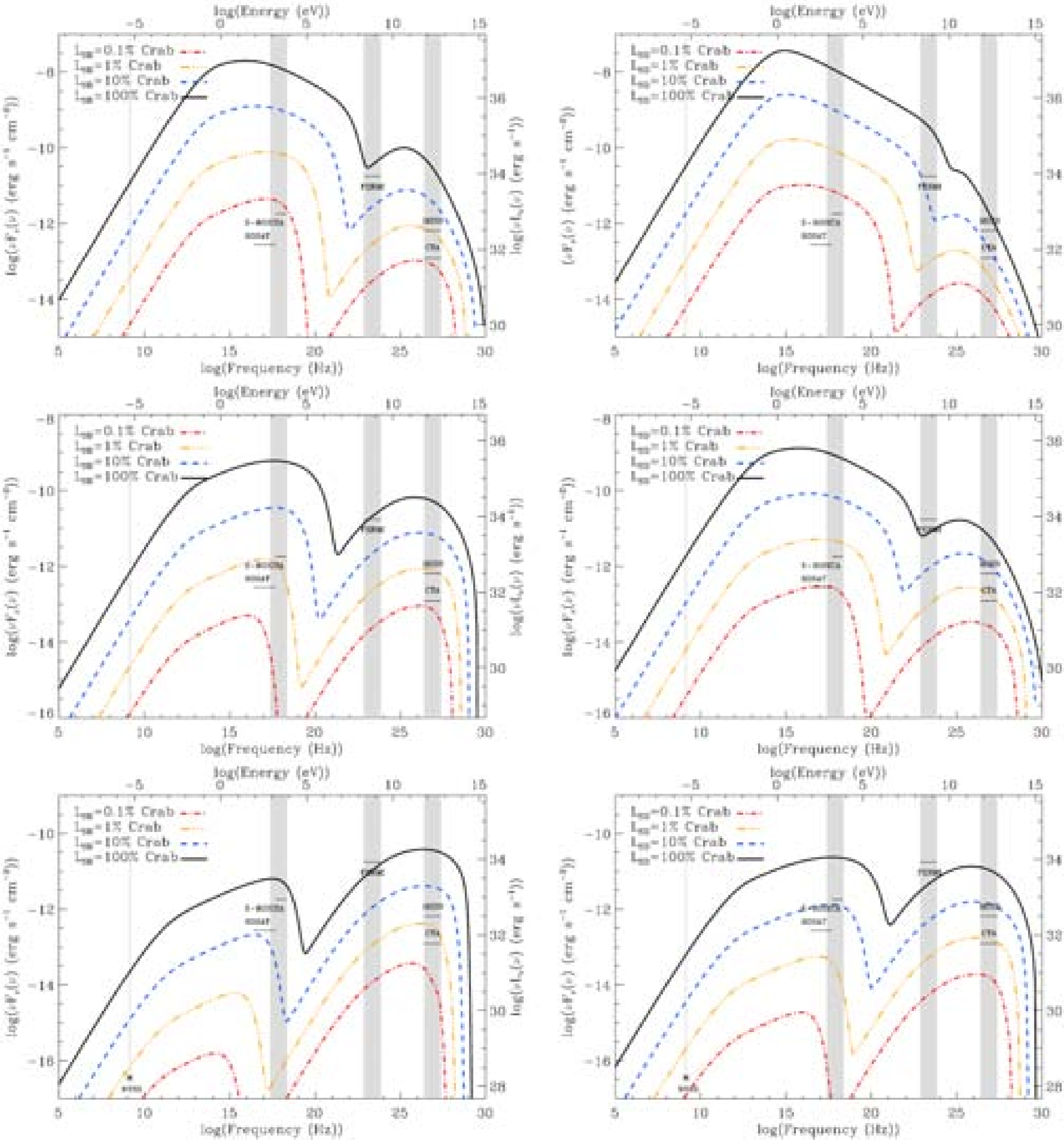

Fig. 3.9 Comparison of the SEDs for an age of 940, 3000, and 9000 years (from top to bottom) as a function of the spin-down luminosity. The magnetic fraction is fixed at 0.03 (left) and 0.5 (right).

bias, which we discuss further below: if there are magnetically dominated PWNe, similar to the ones simulated here, it would be hard to detect them with the current generation of TeV telescopes.

To illustrate the effect of the initial spin-down power injected, the SED is shown in figure 3.9 for each of the 4 E_0 proposed. Similarly to figure 3.8 the figures on the left panels are calculated for a particle dominated nebula ($= 0.03$) and the right ones for equipartition ($= 0.5$). The trends noted above are more clearly shown here. In particular, for relatively old PWNe, at ages of 9000 years (bottom row), the increase of the X-ray nebula to detectable levels with the current instruments has a strong dependence on the magnetic fraction considered. For instance, a relatively bright pulsar with a spin-down energy of 10% of the Crab, at 9000 years would be detectable by ROSAT if in equipartition, but not for smaller magnetic fields.

3.2.2 The effect of magnetic fraction on the X-ray and TeV luminosity

Generally, magnetic equipartition is assumed when discussing X-ray nebulae, but recent TeV observations have shown that many (if not all) of these PWNe are particle dominated. To analyze in more detail the impact of the magnetic fraction parameter on the detectability of the nebulae (or on their flux level), we represent the IC contribution to the spectral flux between 1 and 10 TeV as a function of the magnetic fraction (figure 3.10). As discussed before, large spin-down and very young ages (top right panels) are required to observe a relevant contribution of SSC. The rightmost top panel corresponds to a pulsar such as Crab, having its age but different magnetic fraction. The contribution of SSC dominates for > 0.02 whereas for lower -values the total luminosity would be dominated by FIR even for a 940 years pulsar.

Figure 3.10 shows the corresponding SEDs for the three ages under consideration, and three spin-down powers (1, 10, and 100% of Crab's). The impact of the magnetic fraction on the final SED is large, generating orders of magnitude variations in the luminosity even when keeping all other system's parameters fixed (same spin-down, P, P, injection, and environment). At TeV energies, the simulations show (for Crab-like photon field background and injection parameters) that H.E.S.S.-like telescopes would not be sensitive enough to fully explore the > 0.5 regime, independently from the pulsar age (when lower than 10^4 years) or spin-down power. Even for CTA, a complete coverage of the phase space of young nebulae (assuming that strongly magnetic field-dominated nebulae exist, of course) can only be partially achieved for up to < 0.9 and $E_0 >$10% Crab, for near PWNe. Below, we give

Table 3.4 Ratio of the bolometric radiated power (erg s^{-1}) of the spectra in figure 3.11 divided by the spin-down power (erg s^{-1}) at the given age. Two examples are shown for 1% and 10% of Crab's spin-down.

	940 yr	3000 yr	9000 yr
1% Crab			
0.001	0.00580	0.00471	0.01480
0.01	0.04356	0.00794	0.01880
0.03	0.09022	0.01350	0.02013
0.1	0.16356	0.02757	0.02000
0.5	0.18889	0.04229	0.01480
0.9	0.04733	0.01169	0.00292
0.99	0.00491	0.00123	0.00030
0.999	0.00049	0.00012	0.00003
10% Crab			
0.001	0.01689	0.00640	0.01960
0.01	0.08822	0.01457	0.02280
0.03	0.15733	0.02800	0.02320
0.1	0.25778	0.05443	0.02307
0.5	0.26667	0.07157	0.01747
0.9	0.06467	0.01900	0.00427
0.99	0.00667	0.00199	0.00044
0.999	0.00067	0.00020	0.00004

details on the impact that a different injection or a different FIR background energy density have on this conclusion.

Finally, we calculate the total bolometric power integrating the total luminosity $L(\ )$, corresponding to the spectra in figure 3.10. The results for 1% and 10% of the Crab luminosity are shown in table 3.4. The total radiated power is in all cases less than the injected spin-down (see table 3.3) at the age considered, amounting a few percent for young PWNe (with $\ \sim$0.01 - 0.1). Equipartition naturally produces the maximum of the radiated power in all cases. The integrated-in-time spin-down power ranges from $\sim 4 \times 10^{47}$ erg, for 1% of Crab, to $\sim 5 \times 10^{48}$ erg, for 10% of Crab.

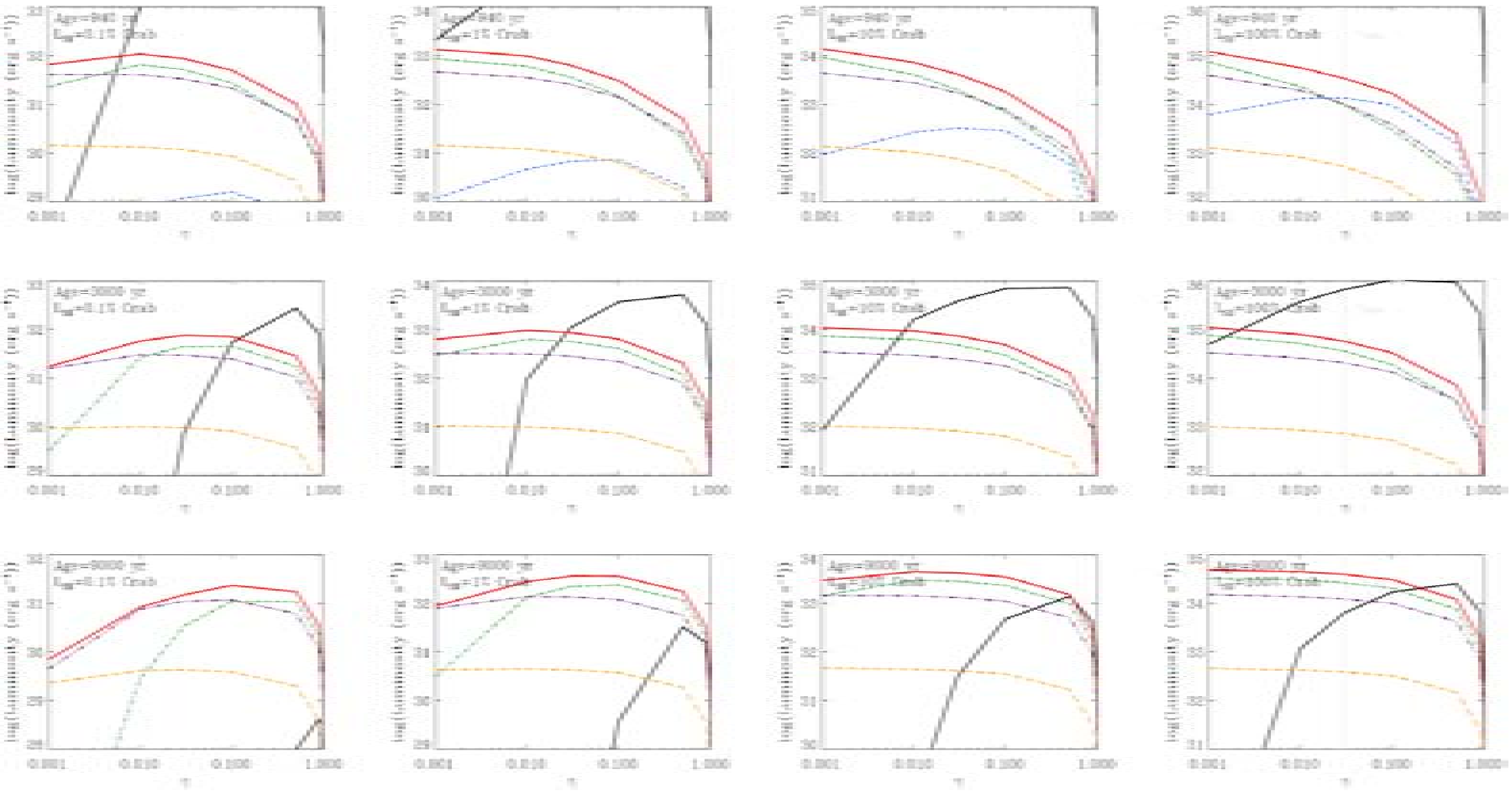

Fig. 3.10 Luminosities between 1 and 10 TeV of the IC, and between 1 and 10 keV of the synchrotron contributions to the spectrum as a function of the magnetic fraction. We fix an age of 940, 3000, and 9000 years (from top to bottom) and vary the spin-down luminosity (0.1%, 1%, 10% & 100% of Crab, from left to right). The color coding is as in figure 3.6.

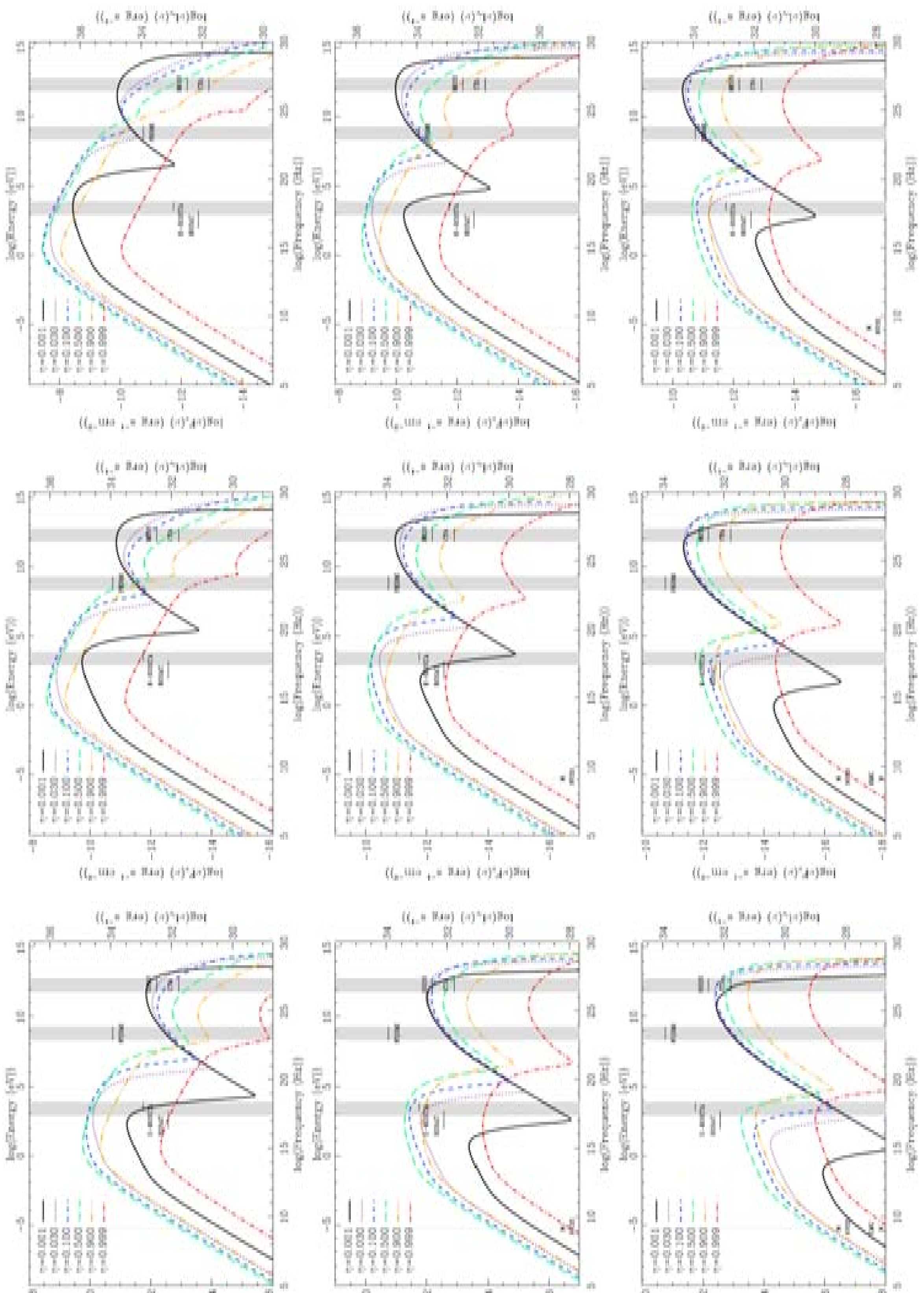

Fig. 3.11 Comparison of the SEDs for an age of 940, 3000, and 9000 years (from top to bottom) as a function of the magnetic fraction. The spin-down luminosity is fixed at 1% 10%, and 100% (panels from left to right) of Crab.

3.2.3 Luminosity ratios for different wavelengths

Figure 3.12 represents the distance-independent luminosity ratios at 940, 3000, and 9000 years (from top to bottom) as a function of the magnetic fraction; for different spin-down powers. All the ratios can, of course, be directly measured if such pulsars exist. As an example, the vertical line in the rightmost panels shows the ratios from the spectrum of the Crab Nebula along time (the right-top panel corresponds to the values of the ratios as measured today). They correspond to one and the same magnetic fraction (in the framework of the model assumptions), at $= 0.03$. Note that the ratios are, mostly, monotonic functions of , and thus, a measurement or upper limits on the luminosities of a PWN can be used to estimate a value of the magnetic fraction. Exceptions to the monotonic character of the ratios happen. Examples of those are the VHE/X-ray ratio (represented by the black dashed line) of pulsars having 1 to 10% of the Crab's spin down and ages of 9000 years (the two bottom-middle panels). If we are to measure a VHE/X-ray ratio only, there could be two magnetic fractions corresponding to it and its value is then degenerate. However, not all ratios are, and measurements of other luminosity ratios would break the degeneracy and inform on a plausible value of .

One can also consider that the ratios between luminosities can be ideally measured even if we do not know the P and P of the corresponding pulsar, say, after a blind discovery of a PWN in the foreseen CTA Galactic Plane survey. Having several luminosity ratios, if they correlate with a single value of would inform of a plausible value not only of the magnetic fraction, but also of the age and power (always under the assumption of Crab-like injection and environmental variables, which we challenge below). The efficiencies of the radiative power at each of the bands play a similar role to figure 3.12 when P and P are known quantities.

The caveat is that for particular PWNe, neither the injection parameters, nor the densities of the background photons will be exactly as assumed here. Thus, there is no escape from individual modeling; figure 3.12 can only be taken as an approximation if we are to compare with directly measurable quantities. However, we can imagine having a set of figures 3.12 and/or the efficiencies at each of the bands, spanning different assumptions for the injection or the environmental parameters. Using such expanded phase space, an automatic procedure of interpolation could inform on plausible values of , age, and luminosity starting only from observational data, like the ratios of luminosities or efficiencies. This is to be considered at CTA times, when hundreds of PWN are expected to be discovered blindly.

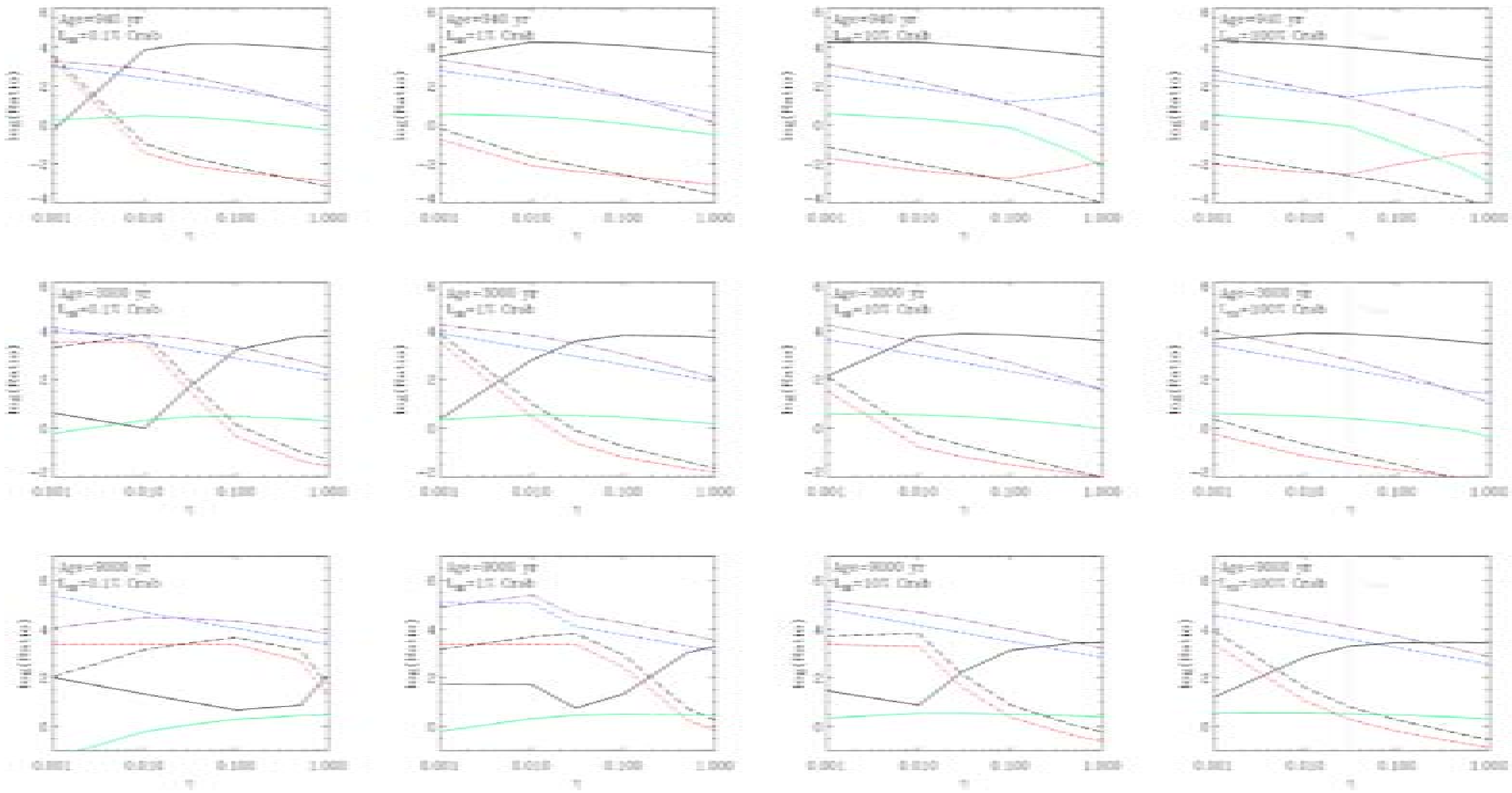

Fig. 3.12 Luminosity ratios at 940, 3000, and 9000 years (from top to bottom) as a function of the magnetic fraction. We show the cases for E=0.1, 1, 10, and 100% of Crab (from left to right) and depict the following ratios: X-ray/radio: black solid line, -ray/radio: blue dashed line, VHE/radio: purple triple-dot-dashed line, -ray/X-ray: red dot-dashed line, VHE/X-ray: black dashed line, VHE/ -ray: green solid line. The bands used for defining the ratios corresponds to the shaded regions in previous figures. For further details, see text.

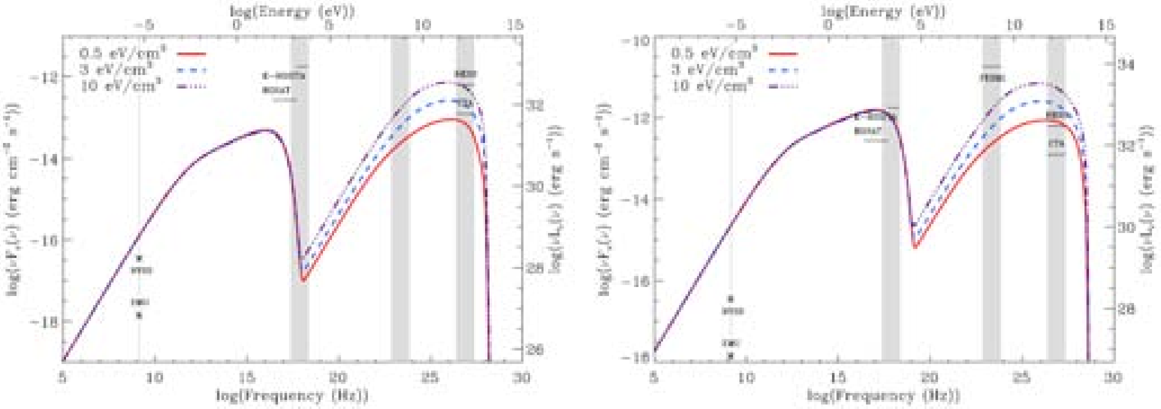

Fig. 3.13 SEDs for Crab's injection parameters and different FIR photon density, from 0.5 to 10 eV cm^{-3}. The left panel shows the results for 0.1% of Crab's energetics, at an age of 3000 years. The right panel shows the same analysis for 1% of Crab's energetics. A low magnetization of 0.03 is assumed.

3.2.4 Discussion and conclusions

After considering a phase space of $\sim$ 100 Crab-like PWNe of different magnetization, spin-down power, and age we concluded that:

- The SSC contribution to the total IC yield is irrelevant for *E*=0.1, 1, and 10% of the Crab power, disregarding the age and the magnetic fraction of the nebulae. It only becomes relevant for highly energetic ($\sim$ 70% of the Crab) particle dominated nebulae at low ages (of less than a few thousand years).

- No young (rotationally powered) PWN would be detectable at TeV energies if the pulsar spin-down power is 0.1% Crab or lower. For 1% of the Crab spin-down, only particle dominated nebulae can be detected by H.E.S.S.-like telescopes if young enough (with the detail of the detectability analysis depending on the precise injection and environmental parameters). Above 10% of the Crab's power, all PWNe are detectable by H.E.S.S.-like telescopes if they are particle dominated, no matter the age.

- The magnetic fraction is an important order parameter in the TeV observability of nebulae, and induces orders of magnitude variations in the luminosity output for systems that are otherwise the same (same spin-down, *P*, *P*, injection, and environment). For Crab-like photon field background and injection parameters, H.E.S.S.-like telescopes would not be sensitive enough to fully explore the >0.5 regime, independently from the pulsar age (when lower than 10^4 years) or spin-down power.

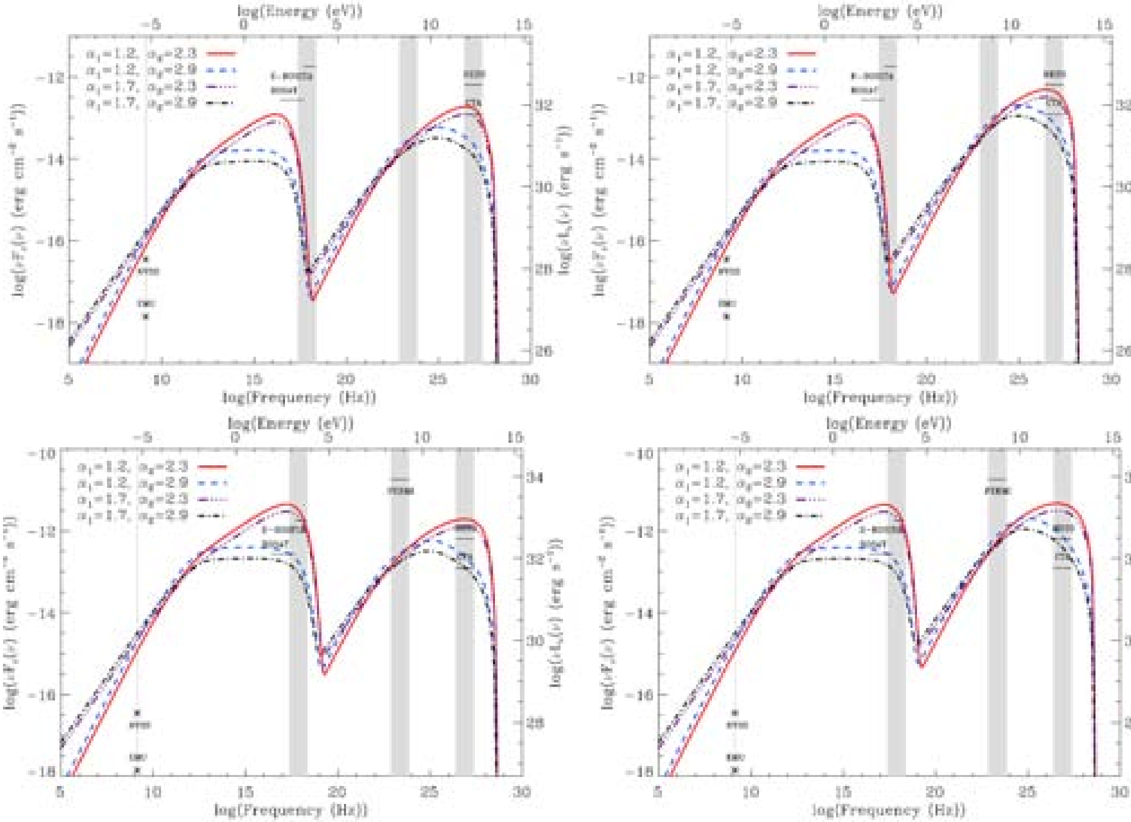

Fig. 3.14 SEDs for different injection parameters (as detailed in the legend) and different FIR photon density (0.5 eV cm^{-3} in the left panel, and 3 eV cm^{-3} in the right one) for a pulsar with 0.1% (top row) and 1% (bottom row) of Crab's energetics. A low magnetization of 0.03 is assumed.

Based on the above results, we pose that if extreme differences between the environmental or injection variables do not occur (in comparison with the Crab Nebula's) it is the magnetic fraction what decides detectability of TeV nebulae. It is thus important to analyze the impact that a different injection or environmental parameters have on our conclusions. Here we specify on the stability of the results against changes on α_1, α_2, and w_{FIR}. The IR energy density in specific regions of the Galaxy can well exceed the 0.5 eV cm^{-3} considered, for instance close to star formation sites.

Figure 3.13 (left) compares the results for 0.1% of Crab's energetic, at an age of 3000 years. It can be seen that even in the extreme case of 10 eV cm^{-3}; a factor of 20 in excess of Crab's energy density, a H.E.S.S.-like telescope will not detect this PWN. The conclusion is thus stable for the current generation of telescopes. CTA detectability, instead, will depend on the FIR density. We recall that the distance assumed for the flux-sensitivity comparison is that of Crab, and thus, that for farther PWNe, the ability of the telescope for detection will

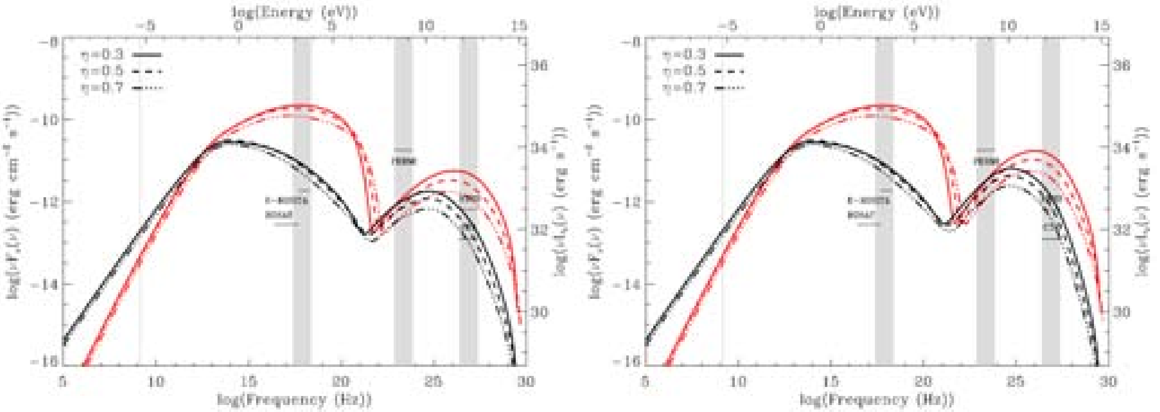

Fig. 3.15 SEDs for different magnetic fraction (as detailed in the legend) and different FIR photon density (0.5 eV cm^{-3} in the left panel, and 3 eV cm^{-3} in the right one) for a pulsar with 10% of Crab's energetics. In red, a hard spectrum of particles with $_1 = 1.2$, $_2 = 2.3$ is assumed, whereas the black curves stand for a steep case with $_1 = 1.7$, $_2 = 2.9$.

be diminished further. The right panel of figure 3.13 shows the same analysis but for 1% of Crab's energetics. As stated above, the FIR energy density (and distance, of course) is the decisive parameter concerning the detectability of PWNe in H.E.S.S.-like telescopes in this case. Note that the extreme case of 10 eV cm^{-3} , which at 2 kpc produces about one order of magnitude in excess of a H.E.S.S.-like telescope sensitivity, would be invisible when the pulsar that drives the nebula is located instead at 5 kpc or beyond. Thus, if having the same injection parameters, most of of the PWNe with 1% of the Crab's energetics would not be seen by the current generation of instruments.

The detectability of PWNe with 0.1% of Crab's energetics in H.E.S.S.-like telescopes is not affected either by changes in the injection parameters. The top row of figure 3.14 shows such changes together with an increased FIR background. Four different pairs of injection slopes are assumed and results are shown for an age of 3000 years. The differences produced by the the changes in injection are indeed large, as expected, but still, a low FIR background would preclude most of these PWNe having 0.1% of Crab's energetics to be detected even by CTA. The bottom row of 3.14 shows the same results for the case of 1% of Crab. Note that for an average value (0.5 eV cm^{-3} in the left example) or even a significantly increased value (3 eV cm^{-3} in the right example) of FIR photon density, only hard spectra will lead to a clear detection in the current generation of instruments. None of these pulsars featuring 1% Crab's energetics, if located at 5 kpc instead of 2 kpc, would be detected by H.E.S.S.-like instruments.

We also consider how stable is the assertion that at 10% of Crab's spin down, a H.E.S.S.-like instrument needs < 0.5 for detecting PWNe, against variations of injection or FIR background. To do that we consider a PWN of a pulsar with 10% of Crab's energetics, subject to two energy densities, 0.5 and 3 eV cm^{-3}, with electron distributions having slopes of $_1 = 1.2$, $_2 = 2.3$ and $_1 = 1.7$, $_2 = 2.9$ represented in red and black in figure 3.15, respectively. Obviously, the most favorable cases for detection are given by the harder slopes of injection and the largest FIR densities. In those particular cases with w_{FIR}=3 eV cm^{-3} (0.5 eV cm^{-3}) H.E.S.S.-like instruments could detect the PWNe up to a magnetic fraction of 0.7 if located closer than $\sim$5 kpc ($\sim$3.5 kpc). Results for pulsars with 10% of Crab's energetic uniformly produce detectable PWNe for magnetization parameters lower than 0.5. The fact that most of the PWNe detected have strong particle dominance is thus not affected by observational biases when their spin-down exceeds 10% of the Crab.

Chapter 4

Systematic modeling of young PWNe

PWNe constitute the largest class of identified Galactic sources at VHE. Since the observation of the first unidentified TeV -ray source (Aharonian et al., 2002; Albert et al., 2008b), more than 20 PWNe have been identified at very-high-energies (VHE; $E > 100$ GeV) by the current generation of Cherenkov telescopes. With the forthcoming generation of Cherenkov telescopes as CTA, the number of these objects will increase to hundreds (de Oña-Wilhelmi et al., 2013), providing an unprecedented database to study the fraction of the pulsar energy that is transferred to the particles, or the magnetic field in the nebula, or what rules the injection power in the surroundings of the pulsar.

In this chapter, we present a systematic study of the Galactic TeV-detected young PWNe. There are previous systematic studies with other models (see e.g., Bucciantini, Arons & Amato 2011; Tanaka & Takahara 2011, 2013), but they are partial. We have modelled the spectra of all the known objects of this kind consistently and search correlations between parameters, extending the work done previously by Mattana et al. (2009). We also compare the results with the predictions extracted form the parameter space exploration done in Torres et al. (2013).

This chapter is based on the work done in Torres et al. (2014).

4.1 Characteristics of the sample

A compilation of PSRs with known rotational parameters and characteristic age of $_c < 10^4$ years is presented in table 4.1, which is obtained from the updated ATNF catalog (Manchester et al., 2005) and includes the recently detected magnetar close to the Galactic Center (Mori et al., 2013; Rea et al., 2013). The value of the period P, period derivative P, distance D, characteristic age $_c$, dipolar field B_d, spin-down power E, and E/D^2 is listed. Their definitions are given below. These values are obtained directly from the catalog, neglecting some better estimations on the distances, such as those of e.g., G0.9+0.1 or pulsars at the LMC, in favor of uniformity when compiling the table. According to their position in the sky, we added the label H, M or V (for H.E.S.S., MAGIC or VERITAS respectively) to indicate the visibility from different Cherenkov telescopes. The names of the TeV putative PWNe (or at least co-located TeV sources even if the TeV source is likely not associated to the pulsar in some cases) are also included. The majority of these pulsars, located in the inner part of the Galaxy, were in the reach of the H.E.S.S. Galactic Plane Survey (GPS), which attains a roughly uniform sensitivity of 20 mCrab (Gast et al., 2011). Some of the pulsars in the northern sky have been observed by either MAGIC or VERITAS, with comparable sensitivity.

To compare the pulsar sample in table 4.1 we consider their characteristic ages. Even if this is not the pulsar real age, which is usually uncertain, it can be considered a good approximation when the pulsar braking index is $n \sim 3$ and the initial pulsar spin-down period is much shorter than the current one. In order to give an idea of relative strength, the E of any pulsar is compared to that of the Crab extrapolated to the corresponding characteristic age. The last three columns in table 4.1 represent, respectively, the age of Crab (assuming no change in braking index) at which it would have the same characteristic age as the corresponding pulsar (T_c^{Crab}), the Crab's spin-down power at that age ($E^{Crab}(T_c^{Crab})$), and the E of the pulsar in terms of percentage of $E^{Crab}(T_c^{Crab})$, which we refer to as CFP (or Crab fractional power). When looked in this way, the Crab PSR is no longer special.

Considering the characteristic ages provides the possibility of assessing the total power input into the nebula. Take as an example PSR J1617-5055 and J1513-5908, and assume for the sake of the argument that both generate TeV emission via a PWN. Both pulsars have essentially the same, and relatively high spin-down power, 1.7×10^{37} erg s^{-1}. However, one has likely been injecting this power for a much longer time, since the characteristic age of PSR J1617-5055 is a factor of 5 larger. The electrons that populate the nebulae will sustain energy losses and live, in most conditions, for more than 10^4 years. Thus, it is reasonable to suppose that there will be more high-energy electrons with which generate TeV radiation in the older pulsar than in the younger one. The differences between PSR J1617-5055 and J1513-5908 are reflected in the comparison with Crab at the moment when its characteristic age is correspondingly the same to the pulsar in question. PSR J1617-5055 is approximately three times as luminous than Crab will be at the same ${}_c$. Instead PSR J1513-5908 spin-down corresponds to only a few percent of the Crab will have at its ${}_c$. Thus, even when both have the same E we are speaking of very different nebulae.

Table 4.1 Pulsars in the ATNF catalog with known period P, and period derivative P, and less than 10 kyr of characteristic age ($_c$). The first few columns are taken from ATNF data. The column "TeV Obs.?" answers whether the pulsar has been observed in TeV range, and, if so, by which telescope (noting H for H.E.S.S., M for MAGIC, and V for VERITAS). The column "TeV PWN?" indicates whether there has been a detection of a PWN or in general a TeV source spatially co-located with the pulsar. This information comes from published literature. The last three columns represent, respectively, the age of Crab (assuming today's braking index) at which it would have the same characteristic age than the corresponding pulsar (T^{Crab}), the Crab's spin-down power at that age ($E^{Crab}(T^{Crab})$), and the spin-down power of the pulsar in terms of percentage of $E^{Crab}(T^{Crab})$, which we refer to as CFP (Crab fractional power). Sources maked with † are magnetars, which low rotational power is not expected to contribute significantly to the corresponding TeV sources (marked in red). Names of the TeV sources shown in blue are the ones studied in this work.

Name	P (s)	P (s s^{-1})	D (kpc)	$_c$ (yr)	B_d (G)	E (erg s^{-1})	E/D^2 (erg s^{-1} kpc^{-2})	TeV Obs.?	TeV source	T_c^{Crab} (yr)	$E^{Crab}(T_c^{Crab})$ (erg s^{-1})	CFP (%)
J1808−2024 †	7.5559	5.49×10^{-10}	13.0	218	2.0×10^{15}	5.0×10^{34}	3.0×10^{32}	H	J1809-194/G11.0+0.08	…	…	…
J1846−0258	0.3265	7.10×10^{-12}	5.8	728	4.9×10^{13}	8.1×10^{36}	2.4×10^{35}	H	Kes 75	238	1.6×10^{39}	0.5
J1907+0919 †	5.1983	9.20×10^{-11}	…	895	7.0×10^{14}	2.6×10^{34}	…	H	J1908+063/G40.1-0.89	459	1.0×10^{39}	0.003
J1714−3810 †	3.8249	5.88×10^{-11}	…	1030	4.8×10^{14}	4.1×10^{34}	…	H	J1718–385/CTB37A	638	7.2×10^{38}	0.006
J0534+2200	0.0334	4.21×10^{-13}	2.0	1258	3.8×10^{12}	4.5×10^{38}	1.2×10^{38}	HMV	Crab nebula	940	4.5×10^{38}	100
J1550−5418	2.0698	2.32×10^{-11}	9.7	1410	2.2×10^{14}	1.0×10^{35}	1.1×10^{33}	H	…	1141	3.5×10^{38}	0.03
J1513−5908	0.1512	1.53×10^{-12}	4.4	1560	1.5×10^{13}	1.7×10^{37}	9.0×10^{35}	H	J1514–281/MSH 15–52	1340	2.8×10^{38}	6
J1119−6127	0.4079	4.02×10^{-12}	8.4	1610	4.1×10^{13}	2.3×10^{36}	3.3×10^{34}	H	J1119-6127/G292.1–0.54	1406	2.6×10^{38}	0.9
J0540−6919	0.0504	4.79×10^{-13}	53.7	1670	5.0×10^{12}	1.5×10^{38}	5.1×10^{34}	H	…	1486	2.4×10^{38}	63
J0525−6607	8.0470	6.50×10^{-11}	…	1960	7.3×10^{14}	4.9×10^{33}	…	…	…	1871	1.6×10^{38}	0.003
J1048−5937	6.4520	3.81×10^{-11}	9.0	2680	5.0×10^{14}	5.6×10^{33}	6.9×10^{31}	H	…	2825	7.8×10^{37}	0.007
J1124−5916	0.1354	7.52×10^{-13}	5.0	2850	1.0×10^{13}	1.2×10^{37}	4.8×10^{35}	H	…	3050	6.8×10^{37}	18
J1930+1852	0.1368	7.50×10^{-13}	7.0	2890	1.0×10^{13}	1.2×10^{37}	2.4×10^{35}	V	J1930+188/G54.1+0.3	3103	6.6×10^{37}	18
J1622−4950	4.3261	1.70×10^{-11}	9.1	4030	2.7×10^{14}	8.3×10^{33}	9.9×10^{31}	H	…	4614	3.0×10^{37}	0.03
J1841−0456	11.7789	4.47×10^{-11}	9.6	4180	7.3×10^{14}	1.1×10^{33}	1.2×10^{31}	H	…	4813	2.8×10^{37}	0.004
J1023−5746	0.1115	3.84×10^{-13}	8.0	4600	6.6×10^{12}	1.1×10^{37}	1.7×10^{35}	H	J1023+575	5370	2.2×10^{37}	50
J1833−1034	0.0618	2.02×10^{-13}	4.10	4850	3.6×10^{12}	3.4×10^{37}	2.0×10^{36}	H	J1833–105/G21.5–0.9	5701	2.0×10^{37}	170
J1838−0537	0.1457	4.72×10^{-13}	…	4890	8.4×10^{12}	6.0×10^{36}	…	H	J1841–055	5754	1.9×10^{37}	32
J0537−6910	0.0161	5.18×10^{-14}	53.7	4930	9.2×10^{11}	4.9×10^{38}	1.7×10^{35}	H	N157B (in the LMC)	5807	1.9×10^{37}	2579
J1834−0845 †	2.4823	7.96×10^{-12}	…	4940	1.4×10^{14}	2.1×10^{34}	…	H	J1834–087/W41	5820	1.9×10^{37}	0.1
J1747−2809	0.0521	1.55×10^{-13}	17.5	5310	2.9×10^{12}	4.3×10^{37}	1.4×10^{35}	H	J1747–281/G0.9+0.1	6311	1.6×10^{37}	269
J0205+6449	0.0657	1.94×10^{-13}	3.2	5370	3.6×10^{12}	2.7×10^{37}	2.6×10^{36}	MV	…	6390	1.6×10^{37}	169
J1813−1749	0.0446	1.26×10^{-13}	…	5600	2.4×10^{12}	5.6×10^{37}	…	H	J1813–178/G12.8–0.02	6695	1.4×10^{37}	400
J0100−7211	8.0203	1.88×10^{-11}	62.4	6760	3.9×10^{14}	1.4×10^{33}	3.7×10^{29}	…	…	8233	9.1×10^{36}	0.02
J1357−6429	0.1661	3.60×10^{-13}	4.1	7310	7.8×10^{12}	3.1×10^{36}	1.9×10^{35}	H	J1356–645/G309.9–2.51	8962	7.6×10^{36}	41
J1614−5048	0.2316	4.94×10^{-13}	7.2	7420	1.1×10^{13}	1.6×10^{36}	3.0×10^{34}	H	…	9107	7.3×10^{36}	22
J1734−3333	1.1693	2.28×10^{-12}	7.4	8130	5.2×10^{13}	5.6×10^{34}	1.0×10^{33}	H	…	10048	5.9×10^{36}	0.9
J1617−5055	0.0693	1.35×10^{-13}	6.4	8130	3.1×10^{12}	1.6×10^{37}	3.8×10^{35}	H	J1616-508	10048	5.9×10^{36}	271
J2022+3842	0.0242	4.32×10^{-14}	10.0	8910	1.0×10^{12}	1.2×10^{38}	1.2×10^{36}	…	…	11082	4.8×10^{36}	2500
J1708−4009 †	11.0013	1.93×10^{-11}	3.8	9010	4.7×10^{14}	5.7×10^{32}	4.0×10^{31}	H	J1708-443/G343.1–2.69	11215	4.7×10^{36}	0.01
J1745−2900 †	3.76356	6.5×10^{-12}	8.0	9170	1.6×10^{14}	4.8×10^{33}	7.5×10^{31}	HM	(in the Galactic Center)	11427	4.4×10^{36}	0.99

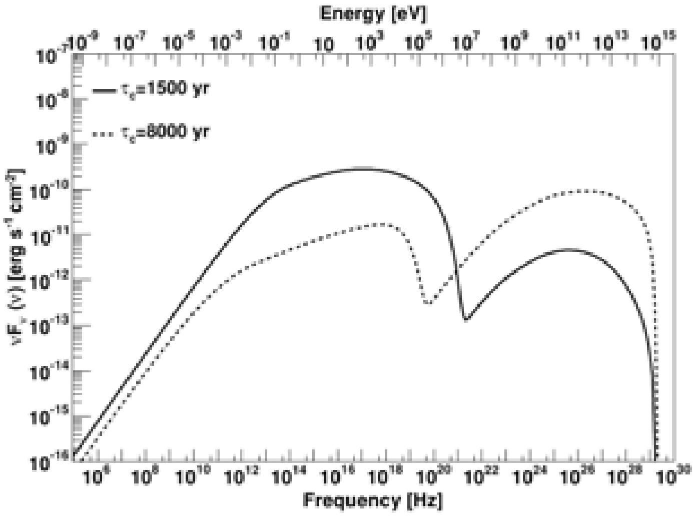

Fig. 4.1 Comparing two PWNe models that differ only in age. Parameters of these models are as those used for the Crab nebula, and both have the same spin-down power.

To exemplify further this point, consider two mock pulsars having the same spin-down evolution, magnetic fraction, injection spectrum, and photon background parameters than Crab (see below for precise definition of all these quantities) and both having also the same spin-down power, 1.7×10^{37} erg s^{-1}, but two different characteristic ages of 1500 and 8000 years, respectively. The modeled PWNe (details of the model itself are discussed below) when every parameter is the same but just the $_c$ and the corresponding real age vary turn out to be different: For instance, the resulting magnetic field varies from 1 to 30 G. The SEDs shown in figure 4.1 show that the spin-down power E, or the parameter E/D^2 (which is the same for the SEDs in the figure), unless of course when E is extremely low, cannot by themselves blindly define dectectability of PWNe, and further considerations about the PWNe age, injection, and environment have to be taken into account. This conclusion is emphasized when the photon background, the injection, and the magnetic fraction, among other key parameters, may vary from one pulsar to the next.

Table 4.1 shows that most of the young pulsars we know of were indeed surveyed for TeV emission. This has motivated developing detailed radiative models to tackle the complexities in each of the PWNe. However, whereas some of these models are time-dependent, which is essential for a proper accounting of the nebula evolution and electron losses as per the discussion above, they are different to one another, and are constructed under different approximations and assumptions (see section 1.6 for a summary). The magnitude of spectral results introduced by different underlying assumptions has been quantified only in some cases (e.g., see section 3.1 or Martín, Torres & Rea 2012)). Having a clear conversion of

Table 4.2 Examples of radiative time-dependent models used to fit observations of young PWNe.

	Tanaka & Takahara 2011	Zhang et al. 2008	Bucciantini et al. 2011	Fang & Zhang 2010	Qiao, Zhang, & Fang 2009	Li, Chen, & Zhang 2010	Venter & de Jager 2007	This work
Crab nebula	X	X	X	–	–	–	–	X
G54.1+0.3	X	–	–	–	–	X	–	X
G0.9+0.1	X	–	X	X	X	–	X	X
G21.5–0.9	X	–	–	–	–	–	–	X
MSH 15–52	–	X	X	X	–	–	–	X
G292.2–0.5	–	–	–	–	–	–	–	X
Kes 75	X	X	X	–	–	–	–	X
HESS J1356–645	–	–	–	–	–	–	–	X
CTA-1	–	–	–	–	–	–	–	X
HESS J1813–178	–	–	–	–	–	–	–	X

results from one model to another, in order to generate a uniform theoretical setting where PWNe fittings can be compared, is simply impossible. In addition, apart from the obvious mismatches in the models per se, the nebulae that have been studied with each of them are scarce. Table 4.2 gives some examples using a certainly incomplete span of the literature. Our interpretation of observations is based on uncommon modeling, undermining our conclusions.

In this work, we put at least a partial remedy to this situation, and provide a study of several young, TeV detected PWN. In order to do that we have used version 1.3 of TIDE-PWN. Our sample is formed by 10 TeV detected, possibly Galactic PWNe, taken from table 4.1 plus the recently detected CTA-1, which has a characteristic age slightly larger than 10^4 years. We comment also on why we do not consider in our study the cases of HESS J1023–575, J1616–508, J1834–087/W41, and J1841–055 (in most cases, the information gathered on them imply that the TeV emission is not univocally associated with a PWN) as well as Boomerang and HESS J1640–465. We find that not all of the 10 cases studied are best interpreted with a PWN. In particular, we conclude that the case of HESS J1813–178 is most likely related to the SNR rather than to the PWN.

4.2 Individual modelling of young PWNe

Table 4.3 presents all the fit parameters and assumed physical magnitudes for all the models fitted, including the Crab nebula. We introduce below each of the TeV detections in our

Table 4.3 Physical magnitudes obtained for the young PWNe in our study. The dot symbols are used to represent the same value of the corresponding left column.

	Crab nebula	**G54.1+0.3**	**G0.9+0.1**	. . .	**G21.5−0.9**	**MSH 15–52**	. . .
			Model 1	Model 2		Model 1	Model 2
Pulsar & Ejecta							
$P(t_{age})$ (ms)	33.40	136	52.2	. . .	61.86	150	. . .
$P(t_{age})$ (s s^{-1})	4.2×10^{-13}	7.5×10^{-13}	1.5×10^{-13}	. . .	2.0×10^{-13}	1.5×10^{-12}	. . .
$_c$ (yr)	1296	2871	5305	. . .	4860	1600	. . .
$E(t_{age})$ (erg s^{-1})	4.5×10^{38}	1.2×10^{37}	4.3×10^{37}	. . .	3.4×10^{37}	1.8×10^{37}	. . .
n	2.509	3	3	. . .	3	2.839	. . .
t_{age} (yr)	940	1700	2000	3000	870	1500	. . .
D (kpc)	2.0	6	8.5	13	4.7	5.2	. . .
$_0$ (yr)	730	1171	3305	2305	3985	224	. . .
E_0 (erg s^{-1})	3.1×10^{39}	7.2×10^{37}	1.1×10^{38}	2.3×10^{38}	5.0×10^{37}	1.3×10^{39}	. . .
M_{ej} ($M_\odot$)	9.5	20	11	17	8	10	. . .
$R_{PWN}(t_{age})$ (pc)	2.1	1.4	2.5	3.8	0.9	3	. . .
Environment							
T_{FIR} (K)	70	20	30	. . .	35	20	20
w_{FIR} (eV/cm^3)	0.5	2.0	2.5	3.8	1.4	5	4
T_{NIR} (K)	5000	3000	3000	. . .	3500	3000	400
w_{NIR} (eV/cm^3)	1.0	1.1	25	. . .	5.0	1.4	20
n_H	1.0	10	1.0	. . .	0.1	0.4	. . .
Particles and field							
$_{max}(t_{age})$	7.9×10^9	7.5×10^8	1.3×10^9	1.9×10^9	2.4×10^9	1.9×10^9	2.3×10^9
$_b$	7×10^5	5×10^5	1.0×10^5	0.5×10^5	1.0×10^5	5.0×10^5	. . .
$_1$	1.5	1.20	1.4	1.2	1.0	1.5	. . .
$_2$	2.5	2.8	2.7	2.5	2.5	2.4	. . .
	0.2	0.3	0.2	. . .	0.2	0.2	. . .
$B(t_{age})$ (G)	84	14	14	15	71	21	25
	0.03	0.005	0.01	0.02	0.04	0.05	0.07

sample, proppse a PWN model, and discussiong the complexities of each case, surfacing caveats of our model when appropiate.

VER J1930+188 (G54.1+0.3)

The central pulsar in G54.1+0.3 (PSR J1930+1852) is observed in radio and X-rays to have a period of 136 ms, and a period time derivative of 7.51×10^{-13} s s^{-1}, implying a characteristic age of $_c$ $\sim$2.9 kyr (Camilo et al., 2002). The braking index is unknown, we assume it to be 3. Considering a possible range of braking indices and initial spin periods, Camilo et al. (2002) estimated the age of G54.1+0.3 to be between 1500 and 6000 yr.

The PWN was first discovered by Reich et al. (1985) in radio wavelengths. The later observation by Lu, Aschenbach & Song (2001); Lu et al. (2002) reveals the X-ray non-thermal spectrum and the ring and bipolar jet morphology confirmed the source as a PWN. From the equations describing the PWN evolution in the model by Chevalier (2005), Camilo et al. (2002) calculated an age of 1500 yr and an initial spin period of 100 ms. Based on HI line emission and absorption measurements, the distance to G54.1+0.3 was reported to be in the 5–9 kpc range (Weisberg et al., 2008; Leahy, Tian & Wang, 2008), while the pulsar

Continued.

	G292.2–0.5	**Kes 75**	…	**HESS J1356–645**	…	**CTA 1**
		Model 1	Model 2	Model 1	Model 2	
Pulsar & Ejecta						
$P(t_{age})$ (ms)	408	324	…	166	…	316.86
$P(t_{age})$ (s s^{-1})	4.0×10^{-12}	7.1×10^{-12}	…	3.6×10^{-13}	…	3.6×10^{-13}
$_c$ (yr)	1610	724	…	7300	…	13900
$E(t_{age})$ (erg s^{-1})	2.3×10^{36}	8.2×10^{36}	…	3.1×10^{36}	…	4.5×10^{35}
n	1.72	2.16	…	3	2	3
t_{age} (yr)	4200	700	800	6000	8000	9000
D (kpc)	8.4	6	10.6	2.4	…	1.4
$_0$ (yr)	270	547	447	1311	6622	4901
E_0 (erg s^{-1})	9.3×10^{40}	7.7×10^{37}	1.3×10^{38}	9.6×10^{37}	3.3×10^{37}	3.6×10^{36}
M_{ej} ($M_\odot$)	35	6	7.5	10	12	10
$R_{PWN}(t_{age})$ (pc)	13	0.9	1.0	9.5	9.9	8.0
Environment						
T_{FIR} (K)	70	25	…	25	…	70
w_{FIR} (eV/cm^3)	3.8	2.5	5.0	0.4	…	0.1
T_{NIR} (K)	4000	5000	…	5000	…	5000
w_{NIR} (eV/cm^3)	1.4	1.4	1.4	0.5	…	0.1
n_H	0.02	1.0	…	1.0	…	0.07
Particles and field						
$_{max}(t_{age})$	8.0×10^{8}	5.2×10^{8}	4.9×10^{8}	8.8×10^{8}	1.5×10^{9}	8.6×10^{8}
$_b$	5.0×10^{6}	2.0×10^{5}	1.0×10^{5}	3.0×10^{5}	–	0.8×10^{5}
$_1$	1.5	1.4	1.6	1.2	–	1.5
$_2$	4.1	2.3	2.1	2.52	2.6	2.2
	0.3	0.2	0.1	0.2	0.3	0.2
$B(t_{age})$ (G)	4	19	33	3.1	3.5	4.1
	0.03	0.008	0.03	0.06	0.08	0.4

dispersion measure implied a distance less than or equal to 8 kpc (Camilo et al., 2002; Cordes & Lazio, 2003). Leahy, Tian & Wang (2008) suggested a morphological association between the nebula and a CO molecular cloud at a distance of 6.2 kpc. However, the absence of X-ray thermal emission and the lack of evidence for an interaction of the SNR with the cloud are caveats in this interpretation. According to Temim et al. (2010), who also assumes a distance of 6 kpc, the size of the PWN is 2 × 1.3 arcmin. Extrapolating these magnitudes to the spherical case by matching the projected area of the nebula to that of a circle, the radius for the nebula assumed in our model is ∼1.4 pc at 6 kpc. We also assume Temim et al. (2010) estimation of the mass of the ejecta (∼20M$_\odot$). Since the SNR shell has not been detected, the particle density in the nebula is more uncertain. Temim et al. (2010) have derived a density of 30 cm^{-3} at one IR knot that appears to be interacting with one of the jets of the PWN. To be conservative (see the discussion on the influence of the bremsstrahlung component in the SED below) we will adopt a lower, average density of 10 cm^{-3}.

The observations against which we fit the theoretical model are collected from different works. Radio observations are obtained from Altenhoff et al. (1979); Reich et al. (1984, 1985); Caswell & Haynes (1987); Velusamy & Becker (1988); Condon, Broderick & Seielstad (1989); Griffith et al. (1990); Hurley-Walker et al. (2009). X ray data come from Temim et al. (2010), where we have considered the fluxes given in their table 2 except the one corresponding to the central object. For the spectral slope span, we have adopted the limiting cases of -1.8 and -2.2, also from Temim et al. (2010). We note that the X-ray observations of Lu, Aschenbach & Song (2001); Lu et al. (2002) (used for instance in Lang et al. 2010; Li, Chen & Zhang 2010; Tanaka & Takahara 2011) also took into account the central source (region 1 of Temim et al. 2010; leading to a higher flux, and did not account for pileup effects (see Temim et al. 2010 for a discussion). Use of these X-ray flux values are thus disfavored for modeling the PWN. Finally, TeV observations represent the results of the VERITAS array (Acciari et al., 2010). Fermi-LAT did not detect G54.1+0.3 (Acero et al., 2013).

For the ISRF, the region around G54.1+0.3 has been observed in the infrared by Koo et al. (2008), and Temim et al. (2010). These observations suggest that the ISRF around G54.1+0.3 is larger than that resulting from Galactic averages as obtained, for instance, from CR propagation models. We concur (see table 4.3). Considering further additional components in the ISRF, as for instance Li, Chen & Zhang (2010) did with the optical/UV contribution from nearby YSOs, does not yield to any significant changes in the fit.

YSOs, does not yield to any significant changes in the fit. Table 4.3 and figure 4.2 present the fitting result of our model of G54.1+0.3. Radio and X-ray data can be fitted very well with a synchrotron component driven by a low magnetic field of only 14 G. We found a very small parameter dependence for differences in the value of the containment factor; for instance for values of =0.5, 0.3, 0.2, other parameters are only slightly changed. The magnetic fraction in our model is 0.005 (half of a percent). This turns out to be a factor of 6 smaller than that of Crab nebula. Clearly, G54.1+0.3 is a particle dominated nebula.

At high energies, the influence of the SSC, and the NIR-IC contribution is negligible, with the FIR-IC contribution clearly dominating and the CMB-IC and Bremsstrahlung contributing at the same level at $\sim$100 GeV (albeit both do so at one order of magnitude lower than the dominant component). The Bremsstrahlung contribution is linear with the uncertain particle density. Then, the selection of 10 cm^{-3} as the average particle density against which we compute the bremsstrahlung contribution may be subject to further discussion. We note that it is a factor of 3 lower than that measured in the IR knots (see, e.g., Temim et al. 2010). However, the average density of the medium is probably lower than that found in such IR enhancements, and in addition, relativistic electrons may not be able to fully penetrate into the knots. Other authors, e.g., Lu, Aschenbach & Song (2001), used the IR-knot measured 30 cm^{-3} as average particle density, but did not compute the bremsstrahlung luminosity in his leptonic models. For such densities, the bremsstrahlung would overcome the IC-CMB contribution to the SED in a narrow range of energies. In agreement with observations, G54.1+0.3 should not be seen by Fermi-LAT in the framework of this model.

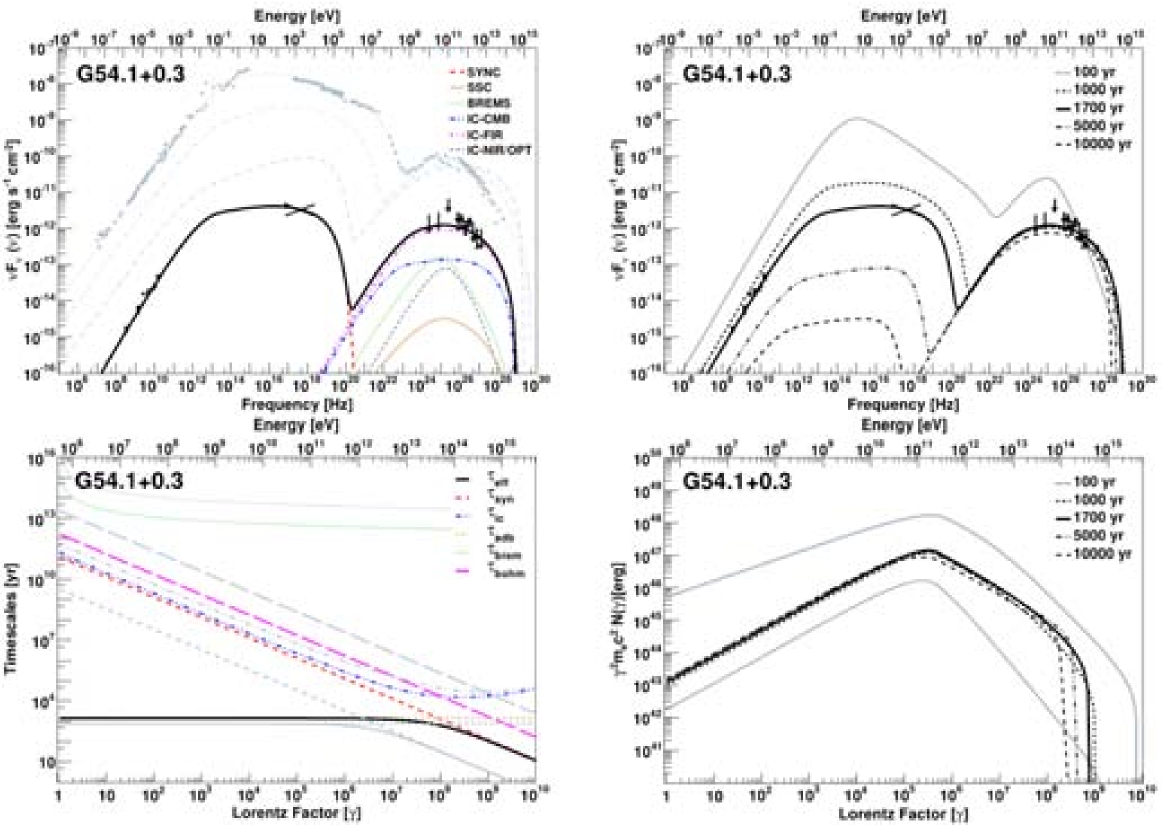

Fig. 4.2 Details of the SED (black bold line) of G54.1+0.3 as fitted by our model. The top left panel shows the SED at the adopted age (i.e., today), whereas the top right panel does it along the time evolution. The bottom panels represent the timescales for the different losses today (the effective timescale for the losses is represented with bolder curves, both for G54.1+0.3 and the Crab nebula) and the evolution of the electron spectra in time. Here and in the figures that follow, we use the results of the Crab nebula model as a comparison. In the top-left panel, we plot (in grey, from top to bottom) three curves corresponding to the Crab nebula's SED at 940, 2000, and 5000 years. In the bottom left panel we compare the losses of G54.1+0.3 to each of the processes with those of Crab (in grey). In the case of the electron distribution we compare with the electron population resulting from the Crab nebula model at its current age. For details regarding the observational data and a discussion of the fit, see the text.

One interesting difference with the results of the work by Tanaka & Takahara (2011) is the value of the high-energy index ($_2$). In our model, it results in 2.8 where it is 2.55 for Tanaka & Takahara (2011). Contributing to this difference is likely the fact that in the latter model the maximum energy of electrons is fixed all along the evolution of the nebula, whereas in ours it evolves in time in agreement with the rest of the physical magnitudes. Having a fixed maximal electron energy hardens the needed slope to fit the data.

Li, Chen & Zhang (2010) have argued for a lepto-hadronic origin of the TeV radiation from G54.1+0.3. The main reason argued for this case is that a leptonic-only model would produce a low magnetic field, as indeed we find. This would result, these authors claim, very low in comparison with estimates of an equipartition magnetic field of 38 G, obtained from the radio luminosity of the PWN or a magnetic field of 80–200 G from the lifetime of X-ray emitting particles as discussed by Lang et al. (2010). But there is no indication that the PWN is in equipartition (in fact, models such as ours, including a proper calculation of losses) show that it is not necessary to include any significant relativistic hadron contribution to fit the SED.

Finally, we have also considered uncertainties in parameters that lead to degeneracies in the fit quality. One such is the age. Indeed, considering ages around 1700 years would still make possible to produce a good fit to the spectral data if changes to the photon backgrounds are allowed. For instance, the FIR energy density would need to shift from 2 to 3 eV cm^{-3} in order to have a good fit when the age is 1500 yrs. Another aspect of note is the degeneracy in $_{b}$, which, within a factor of a few, can lead to equal-quality fits requiring a smaller magnetic field (and magnetic fraction) or small changes in the FIR density.

HESS J1747-281 (G0.9+0.1)

The PWN G0.9+0.1 was first identified in radio emission (Helfand & Becker, 1987), and then detected in X-rays (Mereghetti, Sidoli & Israel, 1998; Sidoli et al., 2000). Its central pulsar, PSR J1747-2809, was detected years later (Camilo et al., 2009). The period of this pulsar is 52.2 ms, with a period derivative of 1.56×10^{-13} s s^{-1}, leading to a characteristic age $_{c}$=5300 kyr, and a spin-down luminosity of 4.3×10^{37} erg s^{-1} (Camilo et al., 2009), one of the largest among Galactic pulsars. The braking index of PSR J1747-2809 is unknown, and we assume $n = 3$. The actual age of G0.9+01 is also unknown. Camilo et al. (2009) estimated an age between 2000 and 3000 yr, which is compatible with the properties of the composite SNR in radio and in X-rays (Sidoli et al., 2000). The average radius of the PWN in radio is $\sim$1 arcmin (Porquet, Decourchelle & Warwick, 2003). G0.9+01 is close to the Galactic Center. Because of that a distance of 8.5 kpc is usually adopted (Aharonian et al., 2005a; Dubner, Giacani & Decourchelle, 2008). Camilo et al. (2009) estimated a distance of 13 kpc according to the dispersion measure and the NE2001 electron model (Cordes & Lazio, 2003), but this estimation can be especially faulty towards the inner Galactic regions, and only a range between 8 and 16 kpc can be reliably suggested.

The observational data against which we fit the theoretical models come from different sources. We use new high-resolution radio images from observations at 4.8 GHz and at 8.4 GHz carried out with the Australia Telescope Compact Array, and from reprocessed archival

VLA data at 1.4 GHz (Dubner, Giacani & Decourchelle, 2008). The X-rays observations we use were done by XMM (Porquet, Decourchelle & Warwick, 2003), and have an unabsorbed flux in the range 2–10 keV of 5.78×10^{-12} erg s^{-1} cm^{-2}, with a power-law index 1.99±0.19. This corresponds to an X-ray luminosity of $\sim 5 \times 10^{34}$ erg s^{-1}, if located at 8.5 kpc. The lack of non-thermal X-ray emission from the shell of G0.9+0.1 argue against the TeV radiation being leptonically originated there. TeV observations are as in figure 3 of Aharonian et al. (2005a).

The values needed of FIR and NIR energy densities for the nebula to be detected in the TeV range, which we found by fitting -see table 4.3-, are higher than what is found in the model by GALPROP (Porter, Moskalenko & Strong, 2006). This discrepancy is not surprising at the central Galactic region.

It is interesting to note that different authors have used alternative set of observations for their fits. Aharonian et al. (2005a) used the XMM data. Porquet, Decourchelle & Warwick (2003) like us, but for the radio data they used the work by Helfand & Becker (1987) since their paper is prior to that of Dubner, Giacani & Decourchelle (2008). The latter authors argue for an overestimation of the radio flux of the PWN given by Helfand & Becker (1987). On the other hand, Tanaka & Takahara (2011) used the data by Dubner, Giacani & Decourchelle (2008) for radio, but Chandra observations for X-ray data (Gaensler, Pivovaroff & Garmire, 2001), a choice making the X-ray spectrum higher in the SED, see the discussion in (Porquet, Decourchelle & Warwick, 2003). These differences in the assumed multi-wavelength spectra of the PWN reflect in the fits, and have to be taken care of when analyzing results.

Due to the uncertainties in the distance, age, and ejected mass, we consider two cases in our fit: In Model 1 (to which the plots in figure 4.3 correspond) we assume a distance of 8.5 kpc, and an age of 2000 yrs. We consider that the PWN is a sphere with a physical radius of 2.5 pc. In Model 2 we assume a larger distance of 13 kpc, and an age of 3000 yrs, leading to a physical radius of 3.8 pc. We assume a value of 11M$_\odot$ (Model 1) and 17M$_\odot$ (Model 2) for the ejected mass. In both models we assume a density of 1 cm^{-3}. There are no significant differences (beyond the defining values for the dynamics and location) between these two models. The magnetic field obtained from our fits is low $\sim$15 G, and the magnetic fraction is in the order of 1–2%. The spectral break in the electron distribution is equal to 10^5 for Model 1 and 0.5×10^5 for Model 2. The spectral indices for the two cases are given in table 4.3 and they are very similar for the two models as well. This similarity gives an idea of the importance of knowing the age and distance of the PWN in fixing model parameters.

We have also analyzed the case in which the injected spectrum is a single power-law; but

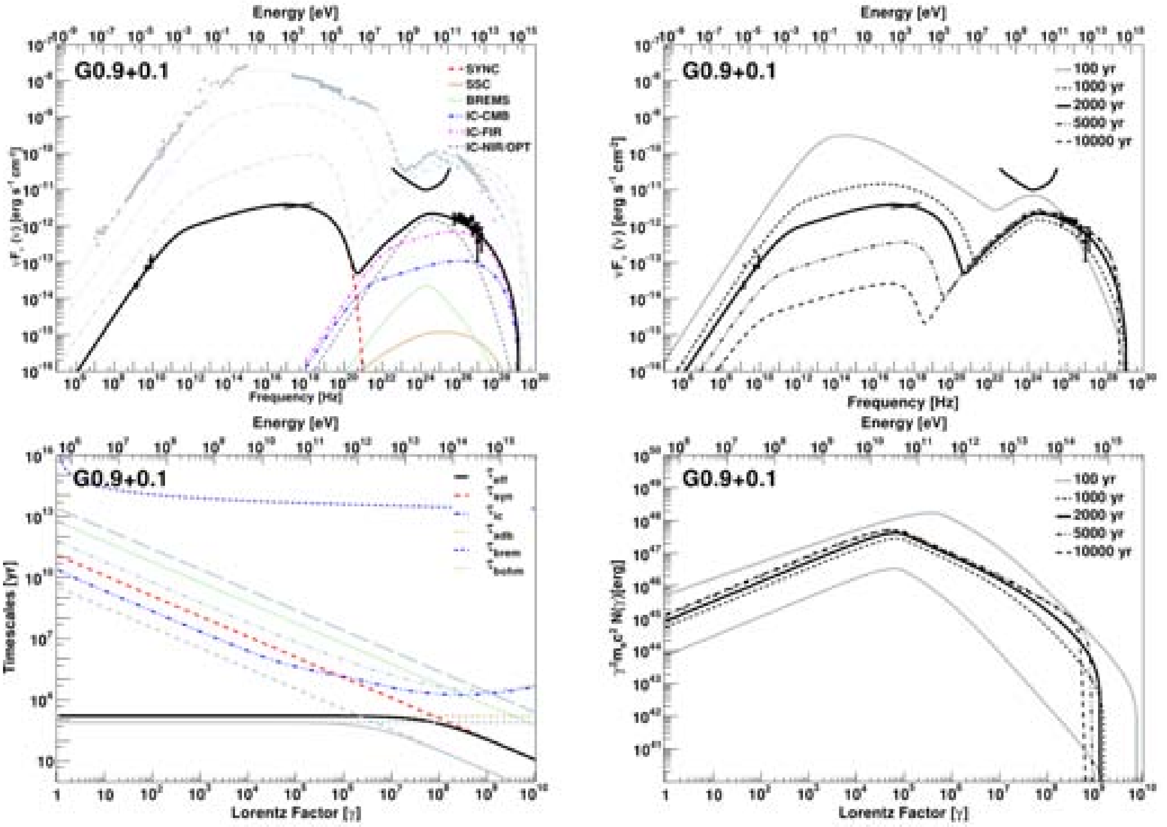

Fig. 4.3 Details of the SED of G0.9+0.1 as fitted by our model. The panels are as in figure 4.2. For details regarding the observational data and a discussion of the fit, see the text.

in practice, this required increasing the minimum energy of the electrons in the nebula up to the break energy. The values obtained for the energy densities in FIR and NIR in order to fit the data change accordingly. The SED distribution of all of these models (Models 1 and 2, both described in table 4.3, and their analogous with a single power-law) is essentially exactly the same as the one plotted in figure 4.3, implying that the degeneracy will be hard to break without precise measurements or modeling of the ISRF backgrounds.

In order to reduce the FIR and NIR densities the only solution is of course to have more high-energy electrons in the nebula. This can be achieved for instance assuming an injection of electrons in the form of a single power-law with a fixed maximum and minimum energy, as in the case of Tanaka & Takahara (2011). However, there are no particular reasons to choose given values for the latter parameters. Other differences with the assumptions in the Tanaka & Takahara (2011) model is that their nebula is 4500 years-old (instead of 2000–3000 yrs) and located slightly closer, at 8 kpc (instead of 8.5 kpc). At this adopted age/distance, which seems not particularly preferred by any observation, the total power would be $\sim$1 order of magnitude larger than that in our Model 1; what explains the lesser need of target photon backgrounds to achieve the same TeV fluxes. This set of assumptions for the injection and age does not appear preferable or particularly justifiable when confronted with the possibility of having larger local background in the Galactic Center environment. Fang & Zhang (2010a) also studied the spectral evolution of G0.9+0.1; but under the assumption that the particle distribution at injection is given by a relativistic Maxwellian distribution plus a single power-law distribution. The latter produces a distinctive feature in the SED at about 10^{-9} MeV for which there is no observational need yet. Even when different assumptions and modeling techniques are used, a low magnetic field is also singled out by their study.

In agreement with our prediction in all the models analyzed, Fermi-LAT did not detect this PWN, and because of the Galactic Center location, it has been impossible to impose useful upper limits either (Acero et al., 2013). The SED fit in figure 4.3 shows only a guiding-curve for the 3-years Fermi-LAT sensitivity.

HESS J1833-105 (G21.5-0.9)

G21.5-0.9 is a plerionic SNR with an approximately circular shape having a radius of ∼40” in radio, infrared and X-ray. The pulsar is at its center. The central pulsar of G21.5-0.9, PSR J1833-1034, was observed in radio having a period of 61.8 ms, and a period derivative of 2.02×10^{-13} s s^{-1}, yielding a characteristic age τ_c=4860 yr (Camilo et al., 2006). It was not possible to measure the braking index, and we take $n = 3$. PSR J1833-1034 was also observed pulsating in GeV by Fermi-LAT (Abdo et al., 2010b), but not in X-rays (see for example, Camilo et al. 2006).

The pulsar is one of the youngest in the galaxy. A recent age estimate based on measuring the PWN expansion rate in the radio band gives an age of 870 yr Bietenholz & Bartel (2008). In case of decelerated expansion, this real age could be even lower. However, Wang et al. (1986) suggested that G21.5-0.9 might be the historical supernova of 48 BC. Uncertainty remains in this point. We assume the 870 years of age in our model. The distance to the system was estimated, based on HI and CO measurements, to be 4.7±0.4 kpc (Camilo et al., 2006). The same value (within errors) was obtained by other authors (Tian & Leahy, 2008b). We approximate the nebula as an sphere of radius ∼1 pc. We assumed a mass of 8$M_\odot$ for the ejected mass. Matheson & Safi-Harb (2005) derived an upper limit for the upstream density of ∼0.1–0.4 cm^{-3}. For our fitting procedure, then, we assumed that the PWN expands in a low density media with a value of 0.1 cm^{-3}.

G21.5-0.9 has been observed at different frequencies. In our analysis we have used the radio data obtained in the works by Salter et al. (1989); Morsi & Reich (1987); Wilson

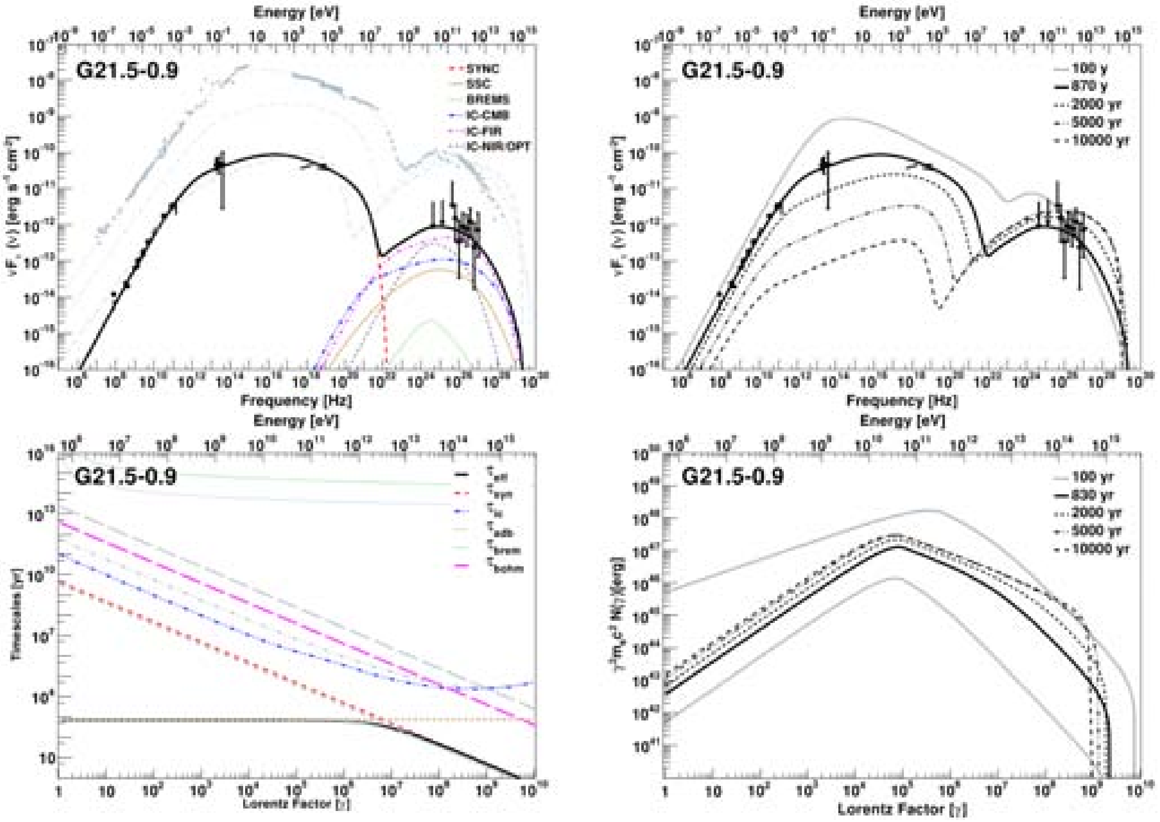

Fig. 4.4 Details of the SED model of G21.5-0.9. The panels are as in figure 4.2. For details regarding the observational data and a discussion of the fit, see the text.

& Weiler (1976); Becker & Kundu (1976). We have also used the infrared observations performed by Gallant & Tuffs (1998, 1999). There are additional X-ray and IR data that we are not using in the fit (Zajczyk et al., 2012) and corresponding to the compact nebula only, a region of 2 arcsec surrounding the central pulsar.

G21.5-0.9 is usually taken as a calibration source for X-ray satellites, see for example the works by Slane et al. (2000); Warwick et al. (2001); Safi-Harb et al. (2001); Matheson & Safi-Harb (2005, 2010); de Rosa et al. (2009). We have used the joint calibration of Chandra, INTEGRAL, RXTE, Suzaku, Swift, and XMM-Newton done by Tsujimoto et al. (2011) when considering the X-ray spectrum. The latter shows an spectral softening with radius (Slane et al., 2000; Warwick et al., 2001). Chandra data showed for the first time evidence for variability in the nebula, a similar behavior that occurs in Crab and Vela (Matheson & Safi-Harb, 2010). Fermi-LAT data come from Acero et al. (2013). Finally, at TeV energies, the data comes from H.E.S.S. observations, which detected the PWN as the source HESS 1833-105 (Gallant et al., 2008; H. E. S. S. Collaboration et al., 2007).

G21.5-0.9 was the first PWN discovered to be surrounded by a low-surface brightness

X-ray halo that was suggested to be associated with the SNR shell; its spectrum being non-thermal (Slane et al., 2000). The halo was not observed in radio wavelengths. Slane et al. (2000) argued that the halo may be the evidence of the expanding ejecta and the blast wave formed in the initial explosion. Warwick et al. (2001) posed that the halo may be an extension of the central synchrotron nebula. But deep Chandra observations revealed limb-brightening in the eastern portion of the X-ray halo and wisp-like structures, with the photon index being constant across the halo (Matheson & Safi-Harb, 2005). Another interpretation of the origin of the halo is that it could be composed by diffuse extended emission due to the dust scattering of X-ray from the plerion (Bocchino et al., 2005). Spectroscopy analysis done by Matheson & Safi-Harb (2010) with Chandra data revealed a partial shell on the eastern side of the SNR. Safi-Harb et al. (2001) could not find evidence for line emission in any part of the remnant.

Table 4.3 summarizes the values of the parameters and the result of the fit. The latter is shown in figure 4.4, which has the same panels as in the previously analyzed PWNe. It is particularly interesting to note that the electron losses in our model (see bottom left panel of figure 4.4) are almost exactly the same as those of Crab, and has ∼10% of its spin-down power. Table 4.3 gives further account of this similarity as regards of age and energy densities of the photon backgrounds. G21.5-0.9 is a particle dominated nebula, with a magnetic fraction of 0.03–0.04. This value is higher than the one obtained by Tanaka & Takahara (2011), in correspondence with the different equation used for the definition of magnetic field. Otherwise, the resulting model parameters are very similar, which is probably due to a significant domination of the FIR component, almost one order of magnitude above the CMB contribution to the inverse Compton yield at 1 TeV. We fixed the temperature of FIR and NIR photon distributions at the same values obtained from GALPROP. In order to be detected in the TeV range as has been, the value for the energy density in the FIR is ∼1.4 eV cm^{-3}. The Comptonization of these photons dominates the spectrum at the highest energies. There is some degeneracy in the precise determination of the FIR and NIR densities and temperatures. For instance, we have checked that our fits would be very similar with temperature of 70 and 5000 K, and densities of 2 eV cm^{-3} in the FIR and NIR, respectively. We have analyzed the impact of having a smaller braking index (e.g., 2.5), and a different containment factor (from 0.1 to 0.3), but did not find any significant differences in our fits due to the change in these parameters.

HESS 1514–591 (MSH 15-52)

The composite SNR G320.4-1.2/MSH 15-52 (Caswell, Milne & Wellington, 1981) is associated with the radio pulsar PSR B1509-58. This pulsar is one of the youngest and most energetic known, with a 150 ms rotation period. It was discovery by the Einstein satellite (Seward & Harnden, 1982), and was also detected at radio frequencies by Manchester, Tuohy & Damico (1982). It has a period derivative of 1.5×10^{-12} s s^{-1}, and a characteristic age of $\sim$1600 yr, leading to a spin-down power of 1.8×10^{37} erg s^{-1}. It is one of the pulsars with measured braking index (Kaspi et al., 1994; Livingstone et al., 2005); and we adopt for it the value of 2.839. The pulsar was detected also in gamma-rays using Fermi-LAT (Abdo et al., 2010b). The central non-thermal source of the system has been interpreted as a PWN powered by the pulsar (Seward et al., 1984; Trussoni et al., 1996). The distance to the system was estimated using HI absorption measurements (Gaensler et al., 1999) to be 5.2±1.4 kpc, which is consistent with the value obtained by Cordes & Lazio (2003) from dispersion measure estimates, 4.2±0.6 kpc.

The dimension of the PWN as observed by ROSAT (Trussoni et al., 1996) and H.E.S.S. (Aharonian et al., 2005b) are 10×6, and 6.4×2.3 arcmin respectively. The dimensions obtained in the TeV data, corresponds to a radius of a circle of $\sim$3 pc, at a distance of 5.2 kpc.

The measured braking index of the pulsar implies a young age, lower than $\sim$1700 yr. According to the standard parameters of the ISM, the age of the system was estimated to be in the range 6-20 kyr, an order of the magnitude larger than the age estimated by the pulsar parameters. A plausible explanation for this discrepancy is that the SNR has expanded rapidly into a low-density cavity, what can also explain the unusual SNR morphology, the offset of the pulsar from the apparent center of the SNR, and the faintness of the PWN at radio wavelengths (Gaensler et al., 1999; Dubner et al., 2002). The south-southeastern half of the SNR seems to have expanded across a lower density environment of $\sim$0.4 cm^{-3}. And the north-northwestern radio limb has instead encountered a dense HI filament. In our models we adopt a density of 0.4 cm^{-3}. However, the morphology of MSH 15–52 is complex and not taken into account in our model (similarly to other analysis alike e.g., Tanaka & Takahara 2011; Abdo et al. 2010b; Zhang, Chen & Fang 2008; Nakamori et al. 2008).

To perform our multi-wavelength fit we acquired the observational data as follows: Radio observations were obtained from Gaensler et al. (1999, 2002). Observations of the nebula in the hard X-rays come from Beppo-SAX (Mineo et al., 2001), and INTEGRAL-IBIS telescopes (Forot et al., 2006). COMPTEL and EGRET measurements (Kuiper et al.,

1999) combine the pulsar and the PWN measurement, so we did not consider them in our fit. The PWN was detected and its spectral distribution in GeV energies was obtained by Fermi-LAT during the first year of operation of this instrument (Abdo et al., 2010b). Fermi-LAT observations used in our work come from subsequent work by Acero et al. (2013). At even higher energies, Cangaroo III observations are in agreement with the previous H.E.S.S. observations. Both data sets were used below. In the models presented here an ejected mass of $10M_\odot$ is assumed.

We consider different scenarios to fit the multiwavelength data. In the model presented in figure 4.5 we assume that the age of the system is 1500 yrs, close to the characteristic age of the pulsar. We also assume a broken power-law injection. In order to fit the measured GeV and TeV data we use a FIR photon field of 5 eV cm^{-3}, at a temperature of 20 K. This component is dominating the IC yield, while the contribution of the optical photon field is much lower in comparison (see table 4.3). The other parameters resulting from the fit are $_1$=1.5, $_2$=2.4, a break Lorentz Factor of 5×10^5, a maximum Lorentz Factor of 1.9×10^9, a nebula magnetic field of 21 G, and a magnetic fraction of 0.05. It would seem that the Fermi-LAT data is not perfectly well reproduced. This can be cured by choosing higher densities and temperatures of the photon backgrounds, but we have not been able to find a perfect match in these conditions.

It was already proposed that the local photon background for this PWN could be higher than the average Galactic value, in particular in the FIR (Aharonian et al., 2005b). Nakamori et al. (2008); Du Plessis et al. (1995) suggested that the SNR itself could be the origin of the excess of the IR photon field. As in the work of Bucciantini, Arons & Amato (2011), we have also investigated the possibility of performing our fit assuming a contribution of a local IR photon field with a temperature of ∼400 K. This possibility is presented in our Model 2. Indeed, we have found that we could fit the observational data with a temperature (energy density) of the IR photon field of 20 K (4 eV cm^{-3}), and local IR photon field with a temperature (energy density) of 400 K (20 eV cm^{-3}). The quality and final SED corresponding to these assumptions (leaving all other parameters unscathed) is better matching also to the Fermi-LAT data, and both M1 and M2 models are compared in figure 4.5. As the result of the M2 fit we obtained $_1$=1.5, $_2$=2.4, a break Lorentz Factor of 5×10^5, a maximum Lorentz Factor of 2.3×10^9, a nebula magnetic field of 25 G, and a magnetic fraction of 0.07.

Previous to Fermi-LAT observations, Aharonian et al. (2005b) presented a fit of the X ray and VHE data using a static IC model (Khelifi, 2002). Using this model they reproduced the VHE spectrum of the whole nebula assuming a power-law energy spectrum for

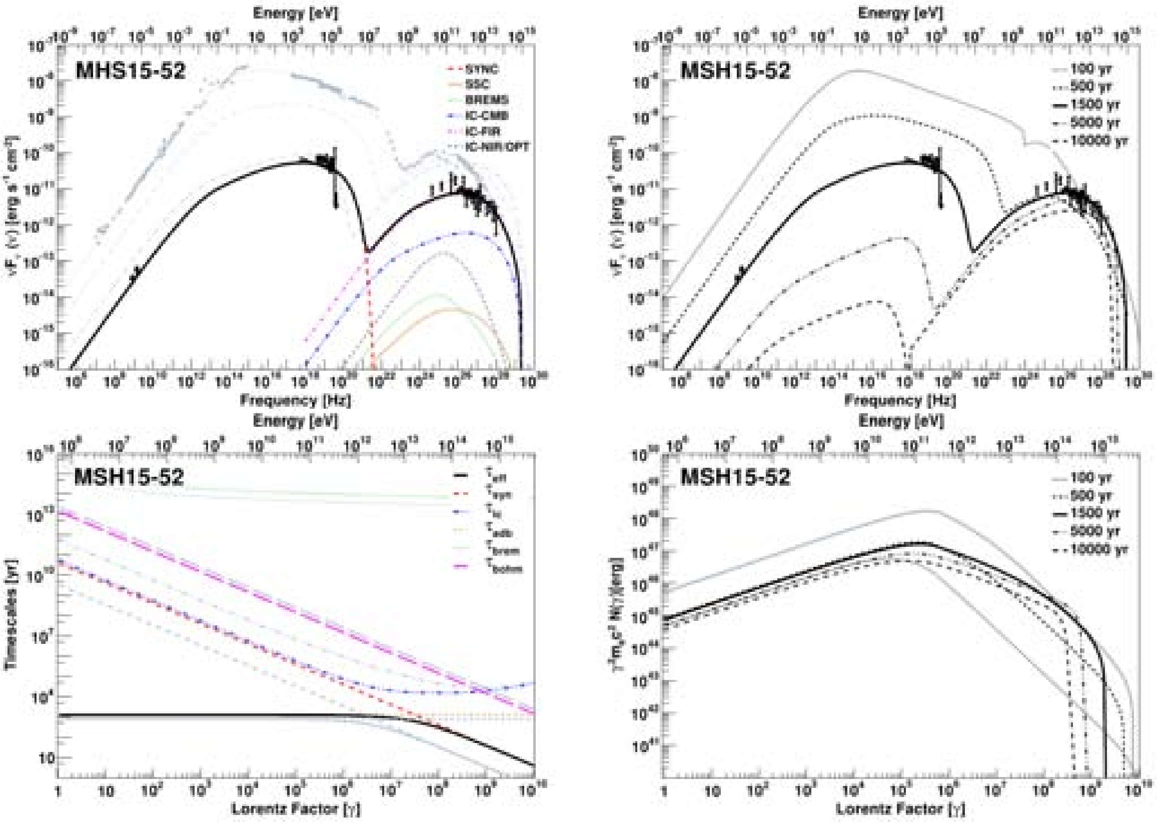

Fig. 4.5 Details of the SED model of MSH15–52. The panels are as in figure 4.2. For details regarding the observational data and a discussion of the fit, see the text.

the population of the accelerated electrons with an spectral index of 2.9. The energy density of the dust component is more than a factor of 2 higher than the nominal value given by GALPROP, similar to ours. Abdo et al. (2010b) also performed a fit of the observational data, including radio, X-ray, Fermi-LAT, and TeV observations using the one-zone, static model described by Nakamori et al. (2008). According to their model the gamma-ray emission is dominated by the IC of the FIR photons from the interstellar dust grains with a radiation density fixed at 1.4 eV cm^{-3} which actually is the nominal value of GALPROP at the position of MSH 15-52. The energy densities in the model by Aharonian et al. (2005b) are similar to those assumed by Abdo et al. (2010b) when presenting Fermi-LAT results. In these works, no time evolution is considered in any of the quantities. We tried performing a fit with the same parameters used in Abdo et al. (2010b); i.e., assuming their spectral indeces, break in the spectrum of the injected particles, magnetic field, and energy densities of the photon fields (see table 4 of the mentioned paper). We compare the results of the fits of Model 1 and 2 with the resulting model having the same parameters of Abdo

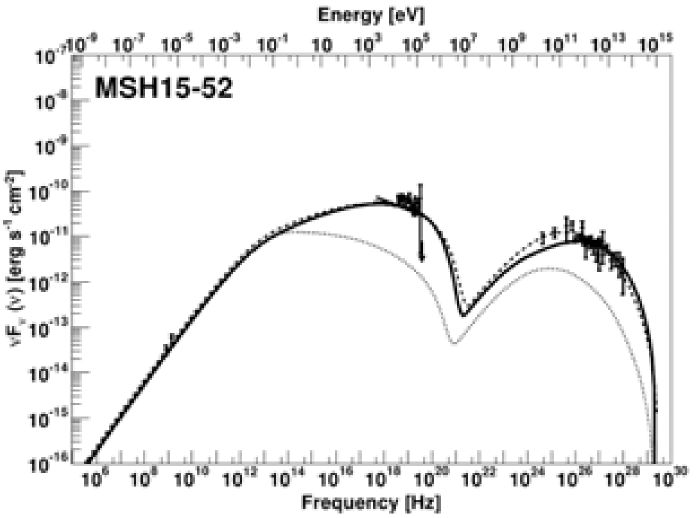

Fig. 4.6 SED of MSH 15–52 fitted with the parameters of the model described in table 4.3 (solid line), together with a comparison with the resulting fit using as photon temperatures and corresponding energy densities (20 K and 4 eV cm^{-3} for the FIR, and 400 K and 20 eV cm^{-3} for the NIR; leaving all other parameters the same, dashed line). We also compare with the current SED results if the parameters of Abdo et al. (2010b) are assumed (dotted line).

et al. (2010b) in figure 4.6. The main difference between Abdo et al. (2010b) model and ours reside, apart that the latter is static, is the assumed lower photon field densities and the steeper high-energy slope of the injected electrons. These changes make for a significant underestimation of the TeV emission. The nebula magnetic field obtained in our model (of the order of 20–25 G) is however similar to the one obtained by Aharonian et al. (2005b); Abdo et al. (2010b) (17 G). Previous estimations Gaensler et al. (2002) gave a lower limit of the field (8 G), which is also compatible.

HESS J1119-614 (G292.2-0.5)

G292.2-0.5 is a SNR associated with the high-magnetic field radio pulsar J1119-6127, which was discovered in the Parkes multibeam pulsar survey (Camilo et al., 2000). The pulsar was also detected in X-rays (Gonzalez et al., 2005) and -rays (Parent et al., 2011). It has a rotational period of 408 ms, and a period derivative of 4×10^{-12} s s^{-1}, leading to a characteristic age of ∼1600 yr, and a spin-down luminosity of 2.3×10^{36} erg s^{-1}. The braking index was measured for the first time by Camilo et al. (2000), but this value was recently refined using more than 12 years of radio timing data to 2.684±0.002 (Weltevrede, Johnston & Espinoza, 2011). The high value of the pulsar magnetic field, $\sim 4.1 \times 10^{13}$ G places PSR J1119-6127 between typical radio pulsars and usual magnetars.

A faint PWN surrounding the pulsar was detected in X-rays (Gonzalez & Safi-Harb, 2003; Safi-Harb & Kumar, 2008). The X-ray unabsorbed flux between 0.5 and 7 keV was measured to be 1.9×10^{-14} erg s^{-1} cm^{-2} for the compact nebula, and 2.5×10^{-14} erg s^{-1} cm^{-2} for the associated jet, with spectral indices of $1.1^{+0.9}_{-0.7}$ and $1.4^{+0.8}_{-0.9}$ respectively. These are extremely low values in comparison to other PWNe, G292-0.5 is a very faint PWN in X-rays, which remains so even in the case of adding the southern jet flux. The PWN was also detected at high energies by Fermi-LAT (Acero et al., 2013) and at very high energies by H.E.S.S. (Mayer, 2010; Djannati-Ataï, 2009)[1]. TeV measurements have shown a flux of 4% of the Crab nebula and a steeper spectrum (with slope larger than 2.2) compared with other young PWNe. The luminosity in TeV gamma-rays (at 8.4 kpc, see below) is 3.5×10^{34} erg s^{-1} which makes for an efficiency of 1.5% in comparison of the current pulsar spin-down. Thus, the ratio of L_X/L is $\sim 10^{-3}$, which would imply a low magnetic field.

The mass of the progenitor of the SN explosion is large (Kumar, Safi-Harb & Gonzalez, 2012); these authors inferred that the expansion occurred in a very low-density medium. We assumed in our calculations that the ejected mass had a value between 30 and $35 M_\odot$, and that the density of the medium was 0.02 cm^{-3}. The kinematic distance to the system was suggested to be 8.4±0.4 kpc based on HI absorption measurements (Caswell, McClure-Griffiths & Cheung, 2004). According to Safi-Harb & Kumar (2008), the size of the compact PWN in X-rays is 6×15 arcsec, with the jet corresponding to a faint structure of 6×20 arcsec. For a distance of 8.4 kpc, this size corresponds to ~0.5 pc. In the TeV range, the source is extended and the size is larger, its diameter is of the order of ~30 pc (Kargaltsev & Pavlov, 2010; Djannati-Ataï, 2009).

Kumar, Safi-Harb & Gonzalez (2012) estimated the age of the SN in a range between 4200 yr (for a free expansion phase, assuming an expansion velocity of 5000 km s^{-1}) and 7100 yr (for a Sedov phase). This estimation is larger than the one obtained using the pulsar parameters, of 1900 yr. In our model we propose a fit of the data assuming an age of 4200 yr (and $n = 1.7$), and compare it with the results of assuming an age of 1900 yrs (and $n = 2.7$) in alternative fittings.

To compute the fit we then consider the H.E.S.S. measurements (Kargaltsev & Pavlov, 2010; Djannati-Ataï, 2009); together with the X-ray flux quoted above Safi-Harb & Kumar (2008). These are both crucial assumptions, which, as we shall see, reflect in a very steep injection at high energies. We comment more on them below. ATCA deep measurements revealed only a 15 arcmin SNR shell (Crawford et al., 2001), but no radio emission from the PWN. The latter authors interpreted the absence of a radio PWN as being the result of the pulsar's high magnetic field; which would lead to a short time of high energy electron injection (due to a large spin-down). What they see is a limb brightening elliptical shell (in fact designated thereafter as G292-0.5) of dimensions 14 × 16 arcmin with a 1.4 GHz flux density of 5.6±0.3 Jy. At 2.5 GHz, the measured flux density of G292.2-0.5 is 1.6±0.1 Jy (but this should likely be taken as a lower limit since the shell is larger than the largest scale to which the interferometer used is sensible). We shall take this SNR flux measurement at 1.4 GHz as a safe upper limit for the PWN radio emission.

---

[1] We remark that these are not official claims of the H.E.S.S. collaboration; they are not confirmed, but not ruled out either. We entertain the possibility that the final TeV data may differ from the current available spectrum.

We consider first an age of 4200 years, as derived by Kumar, Safi-Harb & Gonzalez (2012) based on SNR properties. To reconcile the pulsar age with the supernova, Kumar, Safi-Harb & Gonzalez (2012) suggested that the braking index has to be smaller than 2 for most of the pulsar lifetime. We assume it to be 1.7. With this age, a fit can be obtained with the FIR dominating the IC yield, with relatively low energy densities. However, the injected electron spectrum at high energy needs to be steep (4.1) to achieve good agreement with observational data. This is an interesting result, since it is by far steepest $_2$ we shall see in the whole sample, and it is quite constrained by the observations of both GeV and TeV emission from this source. Another interesting difference in this case is that the spectral break of the injected electron is higher, in the three models, that the one obtained for other PWNe. However, the extra degree of freedom given by the lack of a detection of the synchrotron at low frequencies peak is a caveat. The resulting model parameters under this age assumption are given in table 4.3 and figure 4.7.

We have also explored models in which the age of the PWN is lower, as resulting from the estimate of the pulsar period, period derivative, and braking index (Weltevrede, Johnston & Espinoza, 2011). We have found that it is especially difficult to find models that could consistently fit the whole set of observations, with the more constraining range being the GeV gamma-rays. In order to fit the MW observational data for lower pulsar ages, either we assume that the energy densities of the FIR and NIR components are significantly larger (10 and 130 eV cm^{-3}, respectively), or we assume that there is a contribution of a local IR field at 400 K, similar to the alternative model considered above for MSH 15-52; which, in any case, would need a large energy density (33 eV cm^{-3}). These values of NIR densities would make the corresponding IC component to significantly contribute, or overcome the FIR-IC yield. Both of these models take the measured value of $n \sim 2.7$, show a radius of about 6 pc, and similar magnetic field, magnetization, injection slopes, and break energies that the corresponding ones shown in table 4.3, but are less satisfying due to the large en-

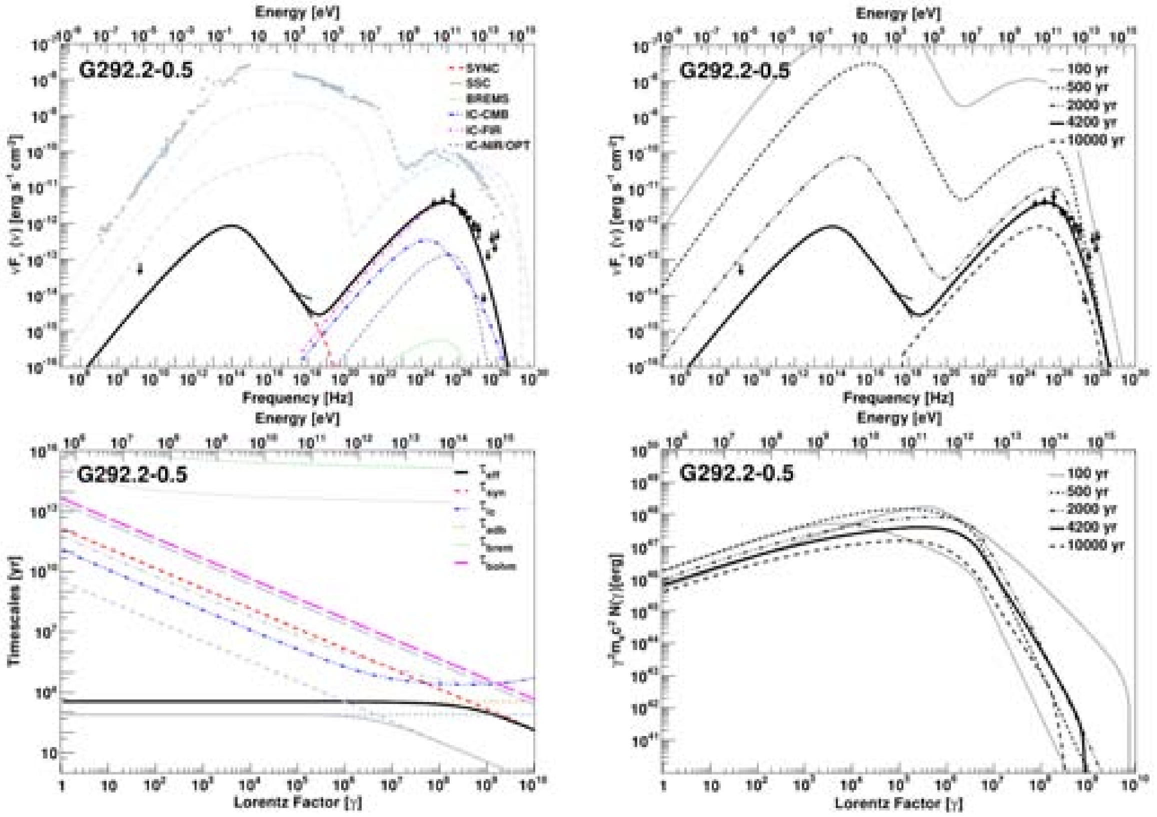

Fig. 4.7 Details of the SED model of G292.2-0.5. The panels are as in figure 4.2. For details regarding the observational data and a discussion of the fit, see the text.

ergy densities involved without a clear a priori justification. In any case, degeneracies in modeling can be broken at radio and optical frequencies (see figure 4.8).

Interestingly, the three models show a very low magnetic field for the nebula, which is consistent with the expectations coming from the extremely low value of the ratio of X-ray and gamma-ray luminosities, and about one order of magnitude lower than the one estimated earlier by Mayer (2010), of 32 G. A lower ejected mass or a higher energy explosion (that can make the size of the nebula larger) will make the magnetic field even lower than the ones obtained in the models presented here.

Another point of discussion in this case is the size of the nebula. Whereas the different sizes could be explained due to the larger losses of X-ray generating electrons, this PWN has one of the largest mismatches. Electrons generating keV photons have, for the resulting B field, a very high energy, in excess of 70 TeV, much larger than the energy of electrons generating TeV photons. In the model of table 4.3, we obtain a radius of ∼13 pc and use it for all frequencies. However, the X-ray and TeV emission regions are probably not the same, and a more detailed model could be needed for a more proper accounting.

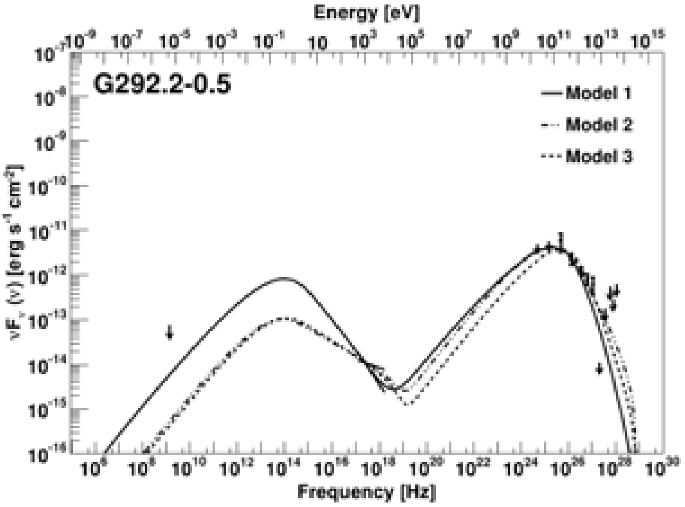

Fig. 4.8 Spectrum of the three different models for G292.2–0.5. See the text for a discussion of the differences and caveats underneath each of these models.

HESS J1846-029 (Kes 75)

Kes 75 (also known as G29.7-0.3) is a shell-type supernova remnant with a central core whose observed properties suggest an association with a PWN. The pulsar associated with this system, PSR J1846-0258, was discovered in a timing analysis of the X-ray data from RXTE and ASCA (Gotthelf et al., 2000). The pulsar has not been detected in the radio band, perhaps due to beaming. Fermi-LAT did not detect the pulsar at high energies either. PSR J1846-0258 has a spin period of ∼324 ms, and a spin-down age of 7.1×10^{-12} s s^{-1}, implying a large spin-down luminosity of 8.2×10^{36} erg s^{-1}, a high surface magnetic field of $\sim 5 \times 10^{13}$ G, and a small characteristic age ∼720 yr (Kuiper & Hermsen, 2009). This pulsar exhibited a magnetar-like outburst with a large glitch in 2006 (Gavriil et al., 2008; Kumar & Safi-Harb, 2008; Livingstone et al., 2011). The pulsar's braking index was measured using RXTE observations (Livingstone et al., 2006). The latter authors found a value of 2.65±0.01, which implies a spin-down age of 884 years, placing this pulsar among the youngest in the Galaxy. During the magnetar-like outburst and the large glitch of 2006, the pulsar presented 5 very short X-ray bursts, changes in the spectra, timing noise, increase in the flux (6 times larger than in the quiescent state), and softening of the spectral index (Ng et al., 2008; Gavriil et al., 2008; Kumar & Safi-Harb, 2008). After that episode the braking index decreased, and has now a value of 2.16±0.13 and the pulsar and the PWN came back to the previous flux and spectral index (Livingstone et al., 2011). It was proposed that the PWN variability observed in 2006 is most likely unrelated to the outburst and is probably similar in origin to the variation of small-scale features seen in other PWNe (Livingstone et al., 2011). Detailed studies of the variability of the PWN using deep Chandra observations were also presented by Ng et al. (2008). While fitting the multiwavelength emission from Kes 75, we have assumed a value of 2.16 for the braking index, and analyzed the differences in the predictions entailed by changing the value of n to that valid before the outburst.

The morphology of the nebula in X-rays is similar to the one observed in radio wavelengths. It is highly structured and it has a dimension, according to high-resolution Chandra images, of 26×20 arcsec. A detail of the complex morphology of the nebula according to Chandra observations is presented by Ng et al. (2008). The first estimation of the distance to the system based on neutral hydrogen absorption measurements was 19 kpc (Becker & Helfand, 1984). More recently Leahy & Tian (2008) estimated a new distance between 5.1 and 7.5 kpc from HI and ^{13}CO maps. However, Su et al. (2009) also estimated a new distance to the system of 10.6 kpc based on the association between the remnant and the molecular shells. There is then a significant uncertainty in the distance to this PWN, and thus we have assumed two different models; with a distance of 6 kpc in our Model 1 and a distance of 10.6 kpc in our Model 2.

To perform the multiwavelength fit presented below, we took radio observations (Salter et al., 1989; Bock & Gaensler, 2005), and infrared upper limits (Morton et al., 2007). The X-ray spectra, resulting from Chandra observations, was taken from Helfand, Collins & Gotthelf (2003). Fermi-LAT upper limits in the photon flux corresponding to three energy bands are presented in Acero et al. (2013). In all of these energy bins, the significance (TS value) is very low (5 in the range 10–31 GeV, and 0 in the ranges of 31–100 GeV and 100–316 GeV). To obtain the upper limits in energy we multiplied the photon flux in each bin by the energy of the center of the bin. At very high energies the nebula was detected by H.E.S.S. (H. E. S. S. Collaboration et al., 2007) with an intrinsic extension compatible with a point-like source and a position in good agreement with the pulsar associated to the nebula.

We present the results of our fit to the multiwavelength observations of Kes 75 assuming that the age and distance to the system are 700 yr and 6 kpc for Model 1, and 800 yr and 10.6 kpc for Model 2. In both models, we have assumed a braking index of 2.16 (Livingstone et al., 2011) and a density of the medium of 1 cm^{-3} (Safi-Harb & Kumar, 2013). The ejected mass for Model 1 was assumed to be 6M$_\odot$ and 7.5M$_\odot$ for Model 2. These models span the range of the uncertainties in distance.

To fit the TeV data we assume a temperature (energy density) of 25 K (2.5 eV cm^{-3}) for the FIR and 5000 K (1.4 eV cm^{-3}) for the NIR photon field in Model 1. In Model 2 (corresponding to the slightly larger age and farther distance) we need to double the energy

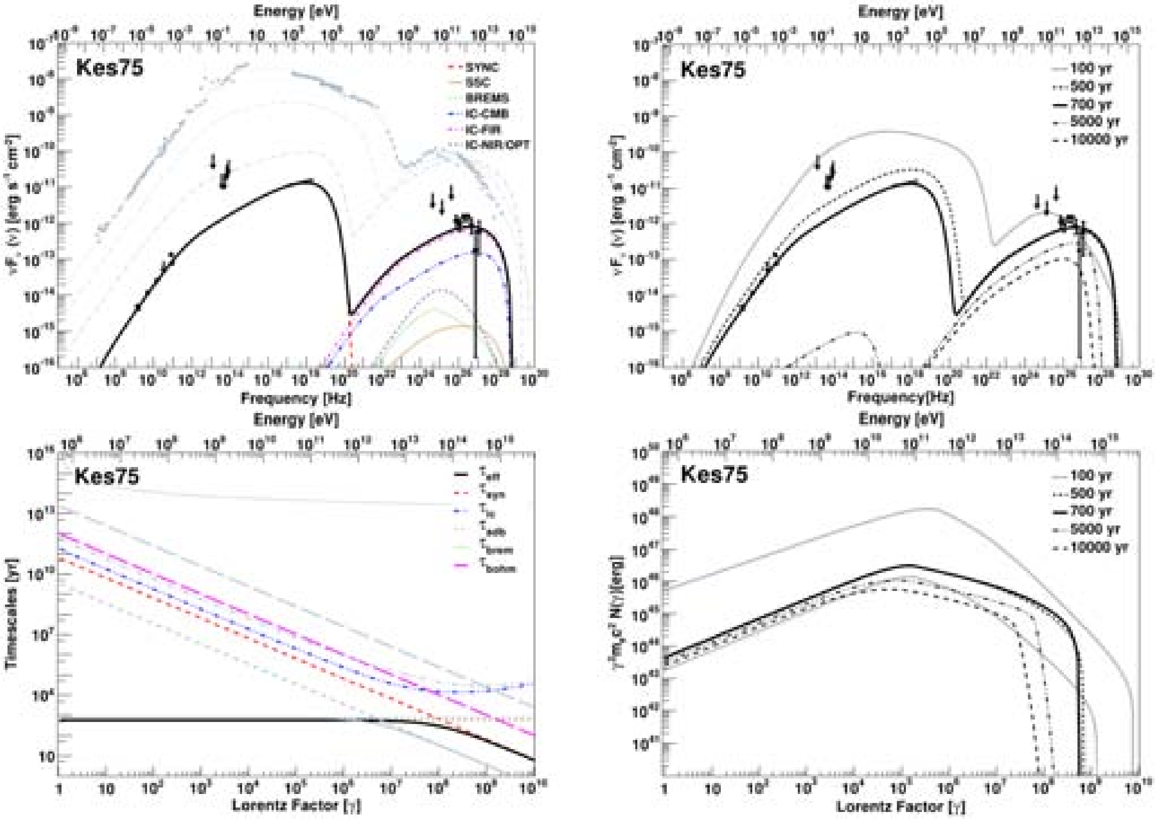

Fig. 4.9 Details of the SED of Kes 75 as fitted by our model. The panels are as in figure 4.2. For details regarding the observational data and a discussion of the fit, see the text.

density in the FIR to fit the observational data. We comment more on this below. In both of these models, the IC with the FIR photon field is the most important component, being the IC with CMB the second contributor to the total yield. The full set of assumed and fitted parameters are shown in table 4.3, whereas the results for Model 1 are presented in figure 4.9.

The Spitzer upper limits do not constrain the parameters of the models in any significant way. The break in the spectrum between the radio and X-ray bands appears at ∼100 GeV for Model 1 and ∼50 GeV for Model 2 in our fit. These low breaks are in agreement with the results presented by Bock & Gaensler (2005). The average magnetic field obtained for the nebula was 19 G in Model 1 and 33 G in Model 2. In both cases the magnetic fraction is low and comparable to other PWNe. The average magnetic field obtained are similar to the ones obtained by Tanaka & Takahara (2011). H. E. S. S. Collaboration et al. (2007) also suggested a low magnetic field for this nebula of the order of ∼10 G. The first spectral index, $_1$, of the injected spectrum are both also in agreement with the ones obtained by Tanaka & Takahara (2011), but as in other cases, our second spectral index, $_2$

are lower than the ones obtained in their fits; which may result from a different treatment of the radiative losses. The final SED results for Models 1 and 2 are quite similar, showing a problematic degeneracy which cannot be broken by the data now at hand. In fact, other degeneracies resulting from the uncertainty in age can be accommodated by modifying the high energy slope of the injected power law, or the magnetic field. Changes are not severe, though, and do not affect the main conclusions.

We could also fit the observational data assuming a braking index of 2.65 (with an age of 700 yrs). For instance, for an ejected mass of 6$M_\odot$, at a distance of 10.6 kpc, a nebula magnetic field of 40 μG with a magnetic fraction of 0.055, and spectral indices of 1.4 and 2.2 for the injected particle spectrum with a break Lorentz factor at 2×10^5 would fit the spectrum equally well, for energy densities and temperatures of photon backgrounds similar to those assumed in Models 1 and 2 presented in table 4.3.

All in all, Kes 75 is a difficult case to model in detail: in particular, we find difficult to provide an overall (along all frequencies) significantly better fit than the one we show in figure 4.9, which we see a bit dissatisfying at the largest energies. There, the fall out of the TeV emission is plausibly steeper than in the model we show, what should be studied with future datasets. The VHE energy data seems to peak around 1 TeV. However, since this is not clear within the reach of the present dataset, we have not tried to model a peak. We have considered models with larger break energies, different photon background and injection parameters, but they do not provide significant improvements. We explored increasing the NIR density, i.e., increasing the IC contribution at energies of 10^{11} eV so that the curve at the highest energies flattens. With w_{FIR}=2 eV cm^{-3} at a central temperature of 100 K and w_{NIR}=20-25 eV cm^{-3} at 3000 K the contribution of IC-NIR becomes comparable to that of IC-FIR but peaking at lower energies, thus flattening or even steppening the high-energy yield.

HESS J1356-645 (G309.9-2.5)

HESS J1356-645 is localized at $\sim$5 pc from the pulsar PSR J1357-6429, if at the same distance, and has an intrinsic Gaussian width of (0.2±0.02) deg (H.E.S.S. Collaboration et al., 2011a). PSR J1357-6429 is a young pulsar with a τ_c=7.3 kyr, a spin-down luminosity of 3.1×10^{36} erg s^{-1}, and a period of 166 ms. It was discovered during the Parkes multibeam survey of the Galactic Plane (Camilo et al., 2004). Lemoine-Goumard et al. (2011) detected pulsations using data from Fermi-LAT and XMM-Newton observations. A possible optical counterpart was also reported (Danilenko et al., 2012). Several authors pointed out the similarities of this pulsar with Vela (Esposito et al., 2007; H.E.S.S. Collaboration et al., 2011a; Acero et al., 2013). Particularly, they both have a low X-ray efficiency, presence of thermal X-ray photons, and a similar ratio of the compact to diffuse sizes of the nebula. The distance to the pulsar was estimated, based on its dispersion measure, to be 2.4 kpc (Camilo et al., 2004).

The first upper limit of the X-rays emission of the PWN of this pulsar was established by Esposito et al. (2007). Later, the H.E.S.S. collaboration studied ROSAT and XMM-Newton images and reported the X-ray spectra of the nebula (H.E.S.S. Collaboration et al., 2011a). Radio and X-ray data, although faint, are coincident in extension with the VHE emission, which provides arguments for the association between the HESS source and the nebula (H.E.S.S. Collaboration et al., 2011a). The morphology of the PWN was also recently studied in detail by (Chang et al., 2012), who also arrived to the same conclusion about the possible association of the nebula with the very high energy source. Fermi-LAT detected a faint counterpart to the nebula after 45 months of observations (Acero et al., 2013). The spatial and spectral coincidences between Fermi-LAT and HESS emission also suggests that they are coming from the same source.

To perform our fit we then take the radio, X-ray, and TeV data as quoted in the discovery paper by H.E.S.S. (H.E.S.S. Collaboration et al., 2011a): Radio data comes from the Molonglo Galactic Plane Survey at 843 MHz, Parkes 2.4 GHz, and Parkes-MIT-NRAO (PMN) at 4.85 GHz. The X-ray spectral shape comes from XMM-Newton observations. Fermi-LAT observations were taken from Acero et al. (2013).

To fit the observational data, we have assumed an age of 6000 years, a braking index of 3, an ejected mass of 10M$_\odot$, and a distance of 2.4 kpc (see table 4.3). We could fit the data with a broken power-law injection having a hard low-energy spectral index $_1$=1.2, and a high-energy slope of $_2$=2.52. We found no need of adding a constraint on $_{min}$ in this model. The break in the spectrum happens at a Lorentz factor of 3×10^5. We found HESS J1356-645 to be a particle dominated nebulae too, with a magnetic fraction of 0.06. The FIR and NIR photon fields of the model have temperatures of 25 K and 5000 K, and energy densities of 0.4 and 0.5 eV cm^{-3}, respectively. These values are quite low in comparison with other PWNe we have studied, and near the estimations obtained from GALPROP (see below). The average magnetic field we obtain is also very low $\sim$3.1 G. A magnetic field higher than $\sim$4 G would make it impossible to fit the data, even varying other parameters. The SED today, its evolution over time, the electron population, and the losses are plotted in figure 4.10. At high and very high energies, the most important contributions are coming from the IC with the CMB and FIR, almost in an equal extent, being the contributions to the IC coming from the NIR photons, as well as from Bremsstrahlung, negligible in comparison. For

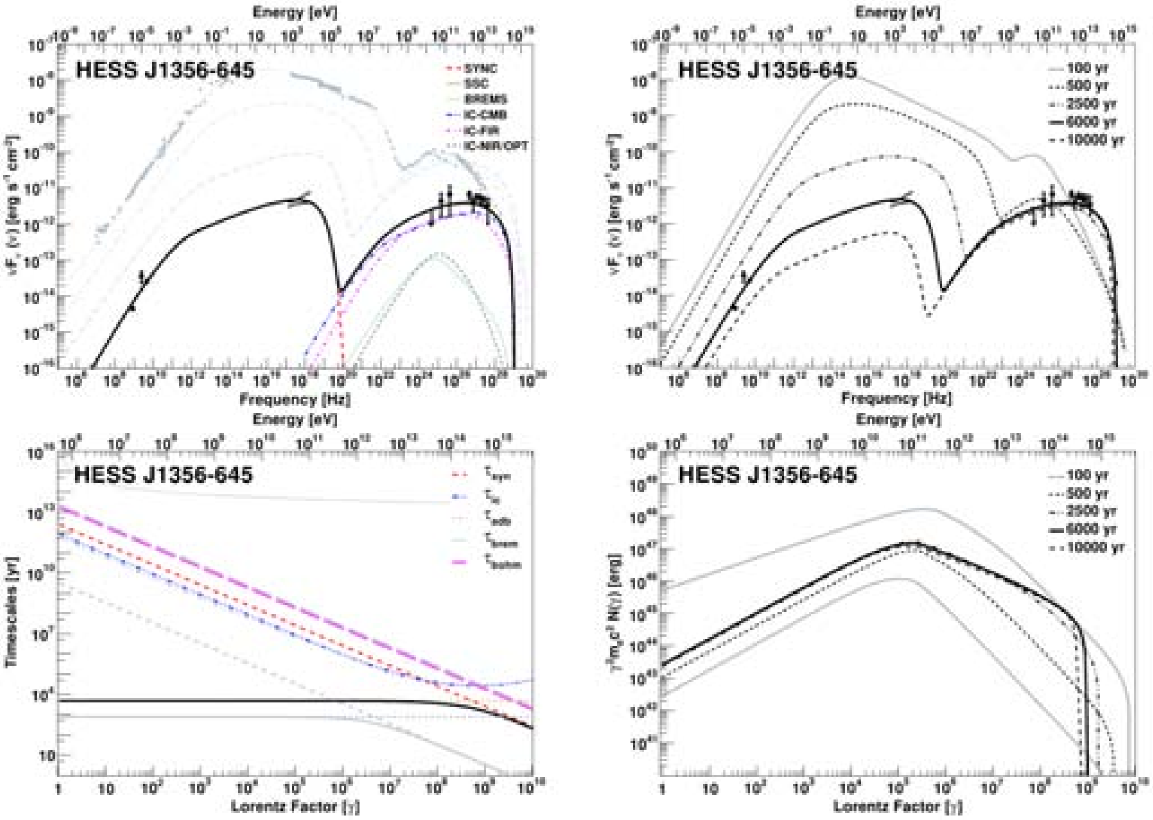

Fig. 4.10 Details of the SED model of HESS J1356-645. The panels are as in figure 4.2. For details regarding the observational data and a discussion of the fit, see the text.

comparison, the HESS Collaboration (H.E.S.S. Collaboration et al., 2011a) have modeled the source assuming a static one-zone leptonic scenario, with an electron population injected with an exponential cutoff power-law of index 2.5 and cutoff energy of 350 TeV. They also assumed photon fields with temperatures of ~35 K and 350 K and optical photon field of temperature of ~4600 K. We do not find the need of incorporating an additional component to the IR distribution at 350 K in order to fit the data.

We have found that it is also possible to have a good fit to the data with a single power law in the spectrum of injected electrons (with slope 2.6), if electrons are energetic enough. To allow for this possibility the braking index is reduced to 2, so that the initial spin-down age is increased by about a factor of ~5 (up to 6622 years). With such an spin-down age, the pulsar is injecting more electrons along most of its lifetime. An slightly larger age (assumed to be 8000 years) and magnetic fraction (0.08) would allow for an equally good SED fit. Finally, the $_{min}$ value is here constrained to be larger than 105. In practice, electrons injected are assumed to be above the break energy of the prior model, and losses populate lower levels in electron energy. These parameters are summarized in table 4.3, quoted as

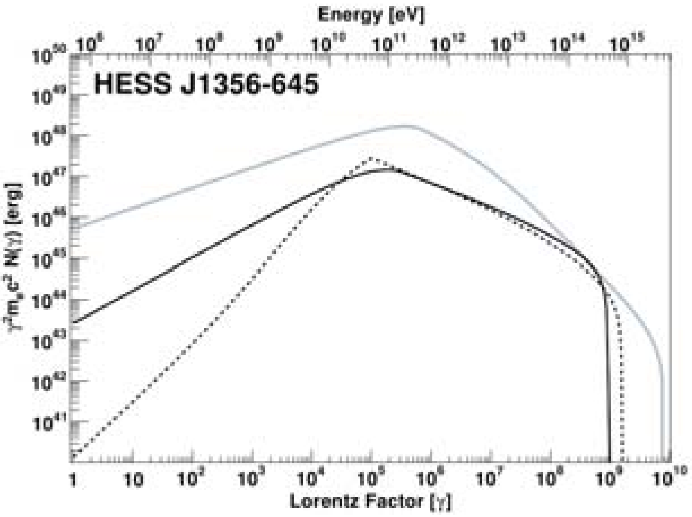

Fig. 4.11 Comparison of the electron distributions for the two models considered for HESS J1356–645. The solid (dashed) line corresponds to Model 1 (2), with the parameters given in table 4.3. Recall that the age in these two models is different. The grey solid line is the Crab nebula electron distribution today.

Model 2. Figure 4.11 compares the two resulting electron distribution at the corresponding current age. By compensating with a longer injection age and more energetic electrons, the electron distribution can be made similar in both models, leading to equally acceptable SEDs. This degeneracy still remains, although preference for model 1 can be argued: the alternative model 2 referred above requires more contrived assumptions to work and would make the nebula an outlier in comparison with others.

VER J0006+727 (CTA 1)

The extended radio source CTA 1 (G119.5+10.2) was first proposed as a SNR by Harris & Roberts (1960). The SNR was first detected in X-rays by ROSAT by Seward, Schmidt & Slane (1995). The authors also reported the presence of a faint compact source, RXJ 0007.0+7302, located within the central region. Slane et al. (1997) confirmed the non-thermal nature of the central emission using ASCA data. These early detections were indicative of the presence of a synchrotron nebula powered by an active neutron star, for which the most plausible candidate was the source RX J0007.0+7302. Further studies performed with the XMM-Newton and ASCA satellites towards RX J0007.0+7302 have resolved the X-ray emission into a point-like source and a diffuse nebula of 18 arcmin in size (Slane et al., 2004b). Using the Chandra observatory, Halpern et al. (2004) have found a point source, RX J0007.0+7302, embedded in a compact nebula of 3” in radius, and a jet like extension.

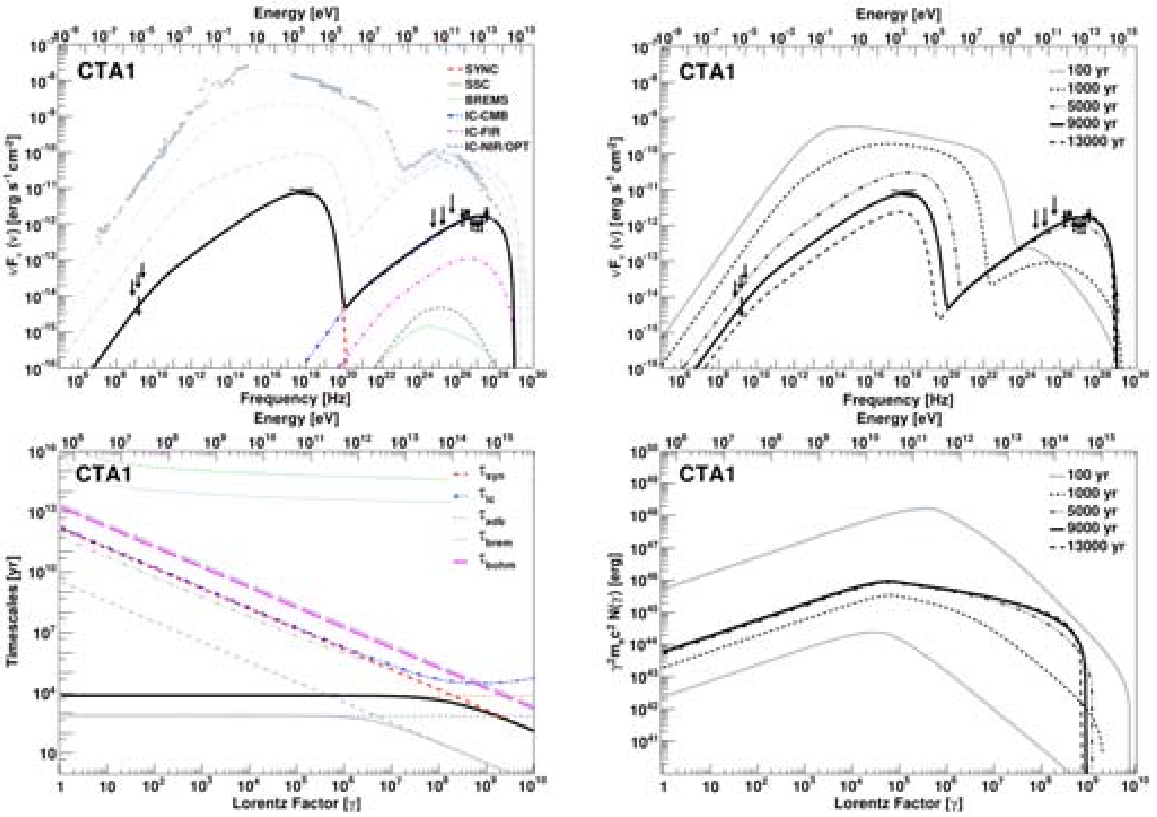

Fig. 4.12 Details of the SED model of CTA 1. The panels are as in figure 4.2. For details regarding the observational data and a discussion of the fit, see the text.

At high energies, Mattox et al. (1996) proposed that the EGRET source 3EG J0010+7309 (which lies in spatial coincidence with RX J0007.0+7302), was a potential candidate for a radio-quiet gamma-ray pulsar. Brazier et al. (1998) also pointed out that this source was pulsar-like, but a search for -ray pulsation using EGRET data failed (Ziegler et al., 2008). During the commissioning phase of the Fermi satellite, a radio-quiet pulsar in CTA 1 was finally discovered (Abdo et al., 2008). X-rays pulsations from this source were finally detected by XMM-Newton (Lin et al., 2010; Caraveo et al., 2010). The pulsar in CTA 1 has a period of $\sim$316 ms and a spin-down power of $\sim 4.5 \times 10^{35}$ erg s^{-1} counterpart. No radio to RX J0007.0+7302 was identified, most likely due to beaming. No optical counterpart is known either (Mignani et al., 2013).

Abdo et al. (2012) reported the detection of an extended source in the off-pulse emission at ~ 6 level using 2 years of Fermi/LAT data. Acero et al. (2013) improved on this result (which we use for modeling). The VERITAS Collaboration also detected an extended source of 0.3×0.24 deg at 5 min from the Fermi gamma ray pulsar PSR J0007+7303 (Aliu et al., 2013).

CTA 1 characteristics in radio and X-rays suggest an age between 5000 and 15000 yrs (Pineault et al., 1993; Slane et al., 1997, 2004b) for the SNR, which is in agreement with the spin-down age of the pulsar (∼14000 yr). Pineault et al. (1993) derived a kinematic distance of 1.4±0.3 kpc based on associating an HI shell found north-western part of the SNR. In order to perform our fit we take the radio upper limits from Aliu et al. (2013), where the authors have used a 1.4 GHz image to estimate the flux upper limit within 20 arcmin radius around the pulsar and extrapolated this upper limit to lower and higher frequencies assuming respectively a radio spectral index of 0.3 and 0. The other UL we use, at 1.5 GHz, was obtained from a new VLA image (Giacani et al., 2013) considering a size for the nebula of 20 arcmin in radius.

We performed our fit considering a distance to the system of 1.4 kpc, an ejected mass between 6 and 10$M_\odot$, a braking index equal to 3, and a density of the media of 0.07 similar to the one proposed by the VERITAS Collaboration (Aliu et al., 2013). We explored the possibility of different ages for the nebula, between 9000 and 12000 yrs. The best fit of the data was obtained with an age of 9000 yr and 10$M_\odot$ of ejected mass. The injected spectrum was assumed to follow a power-law with slopes α_1=1.5 and α_2=2.2. The magnetic field obtained for the model presented in table 4.3 was of 4.1 μG, with an extension of the nebula of 8 pc in radius. For this nebula the main contribution to the flux at high and very high energies comes from the IC with the CMB, being the IC with the FIR and NIR components almost negligible. Compared to the other PWNe analyzed in this work, the magnetic fraction of this nebula is much higher, $\eta = 0.4$. A low η value, like the one obtained with our model for Crab nebula ($\eta = 0.03$), overestimates the flux values at TeV energies compared to the observations of VERITAS.

Previous to Veritas observations, Zhang, Jiang & Lin (2009) over-predicted the value of the flux at high energies. To model the radio upper limits these authors assumed that all the emission obtained from the images of Pineault et al. (1997) was coming from the PWN, which caused also an over-estimation of the radio flux. In the model presented in figure 4.12, Fermi upper limits are higher (by about a factor of 8) than the predictions of our model at those energies.

4.3 Other cases

HESS J1813-178 (G12.8-0.0)

HESS J1813-178 is a TeV source discovered at high energies in the inner galaxy survey done by H.E.S.S. (Aharonian et al., 2006b). It was also observed by MAGIC (Albert et al., 2006a), obtaining its differential γ-ray spectrum as $(3.3 \pm 0.5) \times 10^{-12} (E/\mathrm{TeV})^{2.1 \pm 0.2}$ s^{-1} cm^{-2} TeV^{-1}. The angular extension of the source is 2.2'. With a distance of 4.8 kpc (Halpern, Gotthelf & Camilo, 2012), this gives 3.1 pc of diameter. The associated central source is the pulsar PSR J1813-1749, which has a period of 44.6 ms (Gotthelf & Halpern, 2009) and a period derivative of 1.26×10^{-13} s s^{-1} (Halpern, Gotthelf & Camilo, 2012). The spin-down power nowadays is 5.59×10^{37} erg s^{-1}, and its characteristic age is 5600 yr.

Brogan et al. (2005) discovered a radio shell (SNR G12.8-0.0) coincident with the position of HESS J1813-178, having an angular diameter of $\sim$2.5'. The flux density spectrum was fitted with a power law with an index of 0.48 between 3 cm to 90 cm wavelength. In X-rays, ASCA detected the source AX J1813-178 also coincident with the position of the SNR and the H.E.S.S. source, but the pointing uncertainty was too large to distinguish if the origin of the emission is the center of the remnant or from the shell. Helfand et al. (2007) resolved the X-ray central source and the PWN using observations from Chandra. The flux of the PWN was fitted with a power law with an index of 1.3 and an absorbed flux of 5.6×10^{-12} erg s^{-1} cm^{-2} between 2 and 10 keV. A distance of 4.5 kpc was assumed and they inferred a luminosity for the PWN of 1.4×10^{34} erg s^{-1}. The pulsations of the central source in X-rays were discovered two years later using data from XMM-Newton (Gotthelf & Halpern, 2009). Concerning the age of the system, if the SNR shell were expanding freely, the dynamic age of the system would be about 285 yr whereas in a Sedov expansion, the age increases until 2520 yr (Brogan et al., 2005). We adopt an intermediate case of $\sim$1500 yr here, similarly to other analysis. XMM-Newton also observed this source and could resolve the PWN with an spectral index of 1.8 and a flux between 2 and 10 keV of 7×10^{-12} erg s^{-1} cm^{-2} (Funk et al., 2007a), which is similar to the one obtained by Helfand et al. (2007), but softer. Ubertini et al. (2005) observed a soft gamma source with INTEGRAL with an spectral index between 20 and 100 keV of 1.8, as in the XMM-Newton data. They inferred a luminosity of 5.7×10^{34} erg s^{-1} assuming a distance of 4 kpc.

The origin of the emission in the TeV energy range is not clear and we shall use our model to assess the possibility that a PWN produces it. Other authors have considered this problem before. For instance, Funk et al. (2007a) considered two scenarios, one in which the VHE and the X-ray emission are produced leptonically, by electrons in a PWN;

and another, in which the VHE and the radio emission are generated in the SNR shell. They considered two alternatives for the leptonic scenario producing both the X-ray and the VHE photons: a normal FIR and NIR background with a single power law (with slope 2.4) electron spectrum (model 1); and a significant excess of NIR photons (a factor of 1000 beyond the expected from GALPROP) subject to an injection spectrum described by a hard, single power law (model 2). In both of these alternatives one is forced to require that the maximal energy of the electrons is beyond 1.5 PeV, that the minimal energy is also high ($_{min}$ of the order of 5×10^4) and that the magnetic fields are low (a few G). The high value needed for $_{min}$ would convert this PWN in an outlier with respect to the rest of the population. In any case, these models are both unsatisfying. Model 1 is barely a good fit to the TeV data, significantly overproducing the measurements at the highest energies. Model 2 has an extremely high photon background, even considering the contribution of the nearby star forming region W 33 (Funk et al., 2007a). We have built similar models, and whereas the results cannot be directly compared due to the different treatments, we essentially find the same trends in the case $_{max}$ is indeed allowed to reach high values. PWN are capable of accelerating electrons to PeV energies (see table 4.3). However, in the framework of our model (and in a real physical situation), the maximum Lorentz factor that electrons can achieve is not a free parameter. Here it is set by requesting that the Larmor radius be smaller than the termination shock (equation 2.17). Even assuming that the containment factor is 1, we would attain lower values than 1 PeV, leading –leaving all other parameters the same– to a bad fitting in both alternatives presented by Funk et al. (2007a). For our analogous to their model 1, the redistribution of the power to lower electron energies would not allow for a good fit to the X-ray peak and the radio emission will increase, being close or beyond the upper limits. For our analogous to their model 2, we would significantly overproduce the spectral points at all energies. We need a much lower NIR density of about 55 eV cm^{-3}, nevertheless very high, to match the spectrum better. However, particularly at high TeV energies, it would become impossible to comply with all observational constraints in the case $_{max}$ is allow to reach a high value and the slope of the injection power-law is 2, so as to provide a good fit to the X-ray part: the electrons interacting with the CMB would already overproduce the highest energy data. Fang & Zhang (2010b) also studied models for HESS J1813–178, and although the injection is different from a simple power-law, the general trend is maintained: they cannot attain a good fit to the VHE and X-ray part of the SED with a PWN model either.

Taking into account all of the former, it seems more natural to suppose that HESS J1813–178 VHE emission is generated at the shock of a SNR, or in the interaction of accelerated protons with the environment (as in Gabici, Aharonian & Casanova 2009; Torres, Marrero & de Cea Del Pozo 2010). We shall not consider this source further in our sample.

HESS J1023-575

HESS J1023-575 was discovered by H.E.S.S. (Reimer et al., 2008). Its spectrum is fitted by a power law of the form $dN/dE = 4.5 \times 10^{-12}(E/\mathrm{TeV})^{-2.53}$ s^{-1} cm^{-2} TeV^{-1}, which implies an integrated flux above 380 GeV of 1.3×10^{-11} s^{-1} cm^{-2}. The closest central source is PSR J1022-5746, but the association of these two objects is uncertain due to the large distance between them, 0.28 degrees, assuming 8 kpc, and the proximity to Westerlund 2, which provides other candidates for the origin the radiation (H.E.S.S. Collaboration et al., 2011b). As far as we are aware there is no synchrotron PWN detected for PSR J1022-5746, leaving any possible fit of the TeV emission quite unconstrained.

HESS J1616-508

HESS J1616-508 is one of the brightest sources in the HESS catalog (Aharonian et al., 2006b). It is located near RCW 103 (SNR G332.4-0.4) and Kes 32 (G332.4+0.1) and has an extension of 16 arcmin. Its spectrum is fitted by a power-law with an index of 2.35±0.06 and its flux between 1 and 30 TeV is 2.1×10^{-11} erg s^{-1} cm^{-2}. PSR J1617-5055 was discovered as a radio pulsar by Kaspi et al. (1998). This pulsar was also detected with INTEGRAL (Landi et al., 2007), and it was argued that PSR J1617-5055 was the power engine of HESS J1616-508 (e.g., Mattana et al. 2009). However, there is still some controversy due to the lack of detection in other wavelengths and the position of the PSR in later observations with Chandra (Kargaltsev, Pavlov & Wong, 2009). The latter authors discovered an X-ray PWN surrounding PSR J1617-5055, with a total luminosity between 0.5 and 8 keV of 3.2×10^{33} erg s^{-1} assuming a distance of 6.5 kpc. The X-ray efficiency is very low for a young PWN ($L_{PWN}/\dot{E} \sim 2 \times 10^{-4} d^2_{6.5\ \mathrm{kpc}}$) as is also for the ratio between luminosities ($L_{PWN}/L_{PSR} \sim 0.18$). When compared with the TeV source, the size of the putative X-ray nebulae and the TeV emission has one of the largest mismatches. Due to the controversy in the connection with HESS J1616-508 and the lack of data in the multiwavelength spectrum for the X-ray underluminous PWN, we do not include this source in our study.

HESS J1640-465

HESS J1640-465 is one of the sources discovered by H.E.S.S. during its Galactic Plane survey (Aharonian et al., 2006b). The source is extended with a width of 2.7±0.5 arcmin. Its spectrum is well fitted with a power-law with an index of ∼2.4 and a total integral flux above 200 GeV of 2.2×10^{-11} erg s^{-1} cm^{-2}. The source is partially coincident with the known radio SNR G338.3-0.0 (Whiteoak & Green, 1996). XMM-Newton observations (Funk et al., 2007b) showed a hard-spectrum X-ray emitting object at the center of the HESS source, within the shell of the SNR, most likely a PWN associated with G338.3-0.0 and the counterpart of HESS J1640-465. Chandra observations (Lemiere et al., 2009) constraint the distance and age of the system between 8 and 13 kpc and 10 and 30 kyr, respectively. For a distance of 10 kpc, the luminosity of the pulsar and PWN in the range 2-10 keV were estimated as $L_{PSR} \sim 1.3 \times 10^{33} d_{10}^2$ erg s^{-1} and $L_{PWN} \sim 3.9 \times 10^{33} d_{10}^2$ erg s^{-1} ($d_{10} = d/10$ kpc), respectively. The region of HESS J1640-465 was also detected in Fermi data (Slane et al., 2010). No pulsations were found in the Chandra data of this system. Multifrequency radio continuum observations toward SNR G338.3-0.0 were not able to detect pulsed emission up to a continuum flux density of 2.0 and 1.0 mJy at 610 and 1280 MHZ, respectively; no PWN was detected in the region of the X-ray PWN was detected (Castelletti et al., 2011). The lack of the observational data of the period and period derivative of the pulsar that could be associated with the PWN makes not possible to perform the fit in our model in the same setting as the others PWNe considered, and thus we do not consider this source in our analysis.

HESS J1834-087

The pulsar we quote being positionally correlated in table 4.1 is a magnetar and unlikely related to the TeV emission unless having an unusually high spin-down power conversion into TeV photons, of the order of 10% (orders of magnitude larger than typical values we found in Table 4.4). HESS J1834-087 is spatially coincident with the supernova remnant (SNR) G23.3-0.3 (W41) and was detected in the Galactic Plane survey (Aharonian et al., 2006b). The MAGIC telescope also observed the source, confirming these results (Albert et al., 2006b). The TeV emission seems to have two components, a central source and an extended region surrounding it (see Méhault 2011; Castro et al. 2013). The latter authors have also reported the GeV detection of this region, with a comparable intrinsic extension and a hard SED between 1 and 100 GeV, of 2.1±0.1, somewhat atypical for a PWN spectrum, which smoothly join with the TeV detection. Only a single component is found at GeV energies; the compact TeV emission is not separately seen by Fermi-LAT. The TeV emission region correlates with a local enhancement of molecular material of about 10^5 M$_\odot$ (see Albert et al. 2006a; Tian et al. 2007), what makes possible that TeV emission is in fact hadronically produced in this cloud, similarly to the models explored in Gabici, Aharonian

& Casanova (2009) or Torres, Marrero & de Cea Del Pozo (2010). However, details of the comparison between the CO intensity tracing the mass and the TeV morphology are not perfectly matching. A new pulsar candidate has been identified by Misanovic, Kargaltsev & Pavlov (2011), CXOU J183434.9–084443, but its P and P, if indeed a pulsar, are unknown. These uncertainties suggest that we could not consider this source on a par with the others in our sample.

HESS J1841-055

This source is one of the largest and most complex detected by H.E.S.S., with an extension of approximately 1 degree (Aharonian et al., 2008). It would appear that there are several emission peaks within the detection, and thus it is likely that HESS J1841–055 could have multiple origins. In particular, SNR Kes 73, the pulsar within Kes 73, 1E 1841-45, and also the High Mass X-Ray Binary AX 184100.4–0536 could all plausibly play in a role in partially generating the TeV emission (see e.g., Sguera et al. 2009). In addition, the pulsar we have proposed in table 4.1 as a plausible connection to HESS J1841-055. PSR J1838-0537, was discovered by Fermi (Pletsch et al., 2012), and can also play a role in producing the TeV source, particularly when a PWN was detected in GeV gamma-rays (Acero et al., 2013). However, the plethora of possible origins of the TeV emission, the difficulty in separating the possible contributors if more than one, and the lack of multiwavelength detections of the PSR J1838-0537 nebula at lower frequencies preclude us to consider it further in our analysis.

Boomerang

The Boomerang PWN (G106.6+2.9) is associated with the pulsar PSR J2229+6114. This pulsar is surrounded by an incomplete radio shell (Halpern et al., 2002) and it is unique due to its extremely flat spectrum in radio ($= 0.0$). Its distance is not clear, and estimates range from 3, e.g. see Pineault & Joncas (2000) or Abdo et al. (2009a), to only 0.8 kpc, see e.g., Kothes, Reich & Uyaniker (2006). The period of the central source is 51.6 ms and the period derivative is 7.8×10^{-14} s s^{-1} (Halpern et al., 2001). The inferred characteristic age is thus 10460 yr, and the spin-down luminosity is 2.2×10^{37} erg s-1. The PWN seems to have been displaced by the reverse shock of the SNR already. Kothes, Uyaniker & Pineault (2001) observed that the forward shock of the SNR has been expanding to the north-east where there is a dense HI medium. As a result of the interaction of the forward shock with the dense medium, a strong reverse shock was created and crushed with the PWN. After the passage of the reverse shock, the pulsar created another PWN with less luminosity than the first one, explaining the low radio flux of the nebula considering the spin-down power of the pulsar. The south-west area is almost empty and the PWN is expanding freely. Kothes, Reich & Uyanıker (2006) have also studied the nature of the break in the spectrum at radio frequencies and inferred an age of 3900 yr since the crush with the reverse shock and a magnetic field of 2.6 mG from the lifetime of the electrons. Due to the interaction with the reverse shock, we do not consider this PWN in our analysis.

4.4 Discussion

SED component dominance

Table 4.4 shows which components dominate the SED at TeV energies (the first and second contributors are given in the first two columns). It also provides the ratio (integrating our models in the range 1-10 TeV) between the two largest contributions to the SED at very high energies (third column). The radio (at 1.4 GHz), X-ray (1-10 keV), and gamma-ray luminosities (1-10 TeV), and their corresponding efficiencies (when compared with the pulsar spin-down), f_r, f_X, and f_γ, are also shown in table 4.4. To obtain the luminosities we use the distances to each nebulae according to table 4.3, and obtained them from an integration on our fits. This allows to uniformize the energy range, introducing no change in the conclusions given that all fits are reasonably good descriptions of the observational data when such exist.

We first see that for all the sources studied, only the Crab nebula is SSC dominated. Given the age, power, and photon backgrounds of the PWNe studied, this is an expected result (Torres et al., 2013). It is interesting to see that in the setting of a leptonic model, all the remaining PWNe except for HESS J1356-645 and CTA 1 are IC-FIR dominated. The dominance of the FIR contribution to IC is always large in these cases, and the ratio with the second contributor to the SED at 1 to 10 TeV energies spans from 1.3 to $\sim$10, with the outlying PWN G292-0.5, for which the ratio is 31. The efficiencies of emission are consistently grouped as follows: $\sim 10^{-6\div7}$ in radio, $\sim 10^{-2\div3}$ in X-rays, and $\sim 10^{-3\div4}$ in gamma-rays, except for G292.2-0.5, which shows a very low X-ray efficiency in comparison with the others.

Table 4.4 Properties of the fitted models. For an explanation of all the columns, see the text.

PWN	1st cont.	2nd cont.	ratio (1–10 TeV)	L_r (1.4 GHz)	L_X (1–10 keV)	L (1–10 TeV)	f_r	f_X	f
Crab nebula	SSC	IC-FIR	1.3	1.3×10^{33}	1.4×10^{37}	3.4×10^{34}	2.8×10^{-6}	3.2×10^{-2}	7.5×10^{-5}
G54.1+0.3	IC-FIR	IC-CMB	5.3	5.0×10^{30}	3.0×10^{34}	6.4×10^{33}	4.2×10^{-7}	2.5×10^{-3}	5.3×10^{-4}
G0.9+0.1 (M1)	IC-FIR	IC-NIR	4.1	5.0×10^{31}	6.9×10^{34}	1.4×10^{34}	1.2×10^{-6}	1.6×10^{-3}	3.2×10^{-4}
G0.9+0.1 (M2)	IC-FIR	IC-CMB	6.6	1.2×10^{32}	1.6×10^{35}	3.0×10^{34}	2.9×10^{-6}	3.7×10^{-3}	7.1×10^{-4}
G21.5–0.9	IC-FIR	IC-CMB	3.6	5.1×10^{31}	3.9×10^{35}	2.0×10^{33}	1.5×10^{-6}	1.2×10^{-2}	5.8×10^{-5}
MSH 15–52 (M1)	IC-FIR	IC-CMB	10.1	2.8×10^{31}	3.9×10^{35}	5.0×10^{34}	1.5×10^{-6}	2.2×10^{-2}	2.7×10^{-3}
MSH 15–52 (M2)	IC-FIR	IC-NIR	1.3	3.4×10^{31}	3.8×10^{35}	5.2×10^{34}	1.9×10^{-6}	2.1×10^{-2}	2.9×10^{-3}
G292.2–0.5	IC-FIR	IC-NIR	31.1	1.1×10^{31}	1.1×10^{32}	8.4×10^{33}	5.0×10^{-6}	4.8×10^{-5}	3.7×10^{-3}
Kes 75 (M1)	IC-FIR	IC-CMB	4.1	4.2×10^{30}	1.3×10^{35}	7.4×10^{33}	5.1×10^{-7}	1.5×10^{-2}	9.0×10^{-4}
Kes 75 (M2)	IC-FIR	IC-CMB	8.5	1.3×10^{31}	3.7×10^{35}	1.5×10^{34}	1.5×10^{-6}	4.5×10^{-2}	1.8×10^{-3}
HESS J1356–645 (M1)	IC-CMB	IC-FIR	1.3	1.6×10^{30}	7.1×10^{33}	5.7×10^{33}	5.0×10^{-7}	2.3×10^{-3}	1.8×10^{-3}
HESS J1356–645 (M2)	IC-CMB	IC-FIR	1.3	1.6×10^{30}	6.0×10^{33}	4.0×10^{33}	5.2×10^{-7}	1.9×10^{-3}	1.3×10^{-3}
CTA 1	IC-CMB	IC-FIR	14.2	2.7×10^{29}	4.1×10^{33}	8.6×10^{32}	6.1×10^{-7}	9.1×10^{-3}	1.9×10^{-3}

Slopes of injection & electron population

We have considered a broken or a single power law for the injection distribution of electrons. Other injections can be tried. However, if we use, e.g., the injection model based on the particle in cell (PIC) simulations done by Spitkovsky (2008), we would have several additional –and observationally unconstrained– parameters. This kind of injection is not devoid of significant extrapolations when considered in a PWN setting (e.g., the maximal PIC simulated Lorentz factor is far from the maximal electron energies considered in the PWNe). Thus a priori it would seem that the power-law distributions are a more reasonable choice for the time being, due to their simplicity. Their ability to produce good fits in all cases give a posteriori support.

We have found that the energy distribution of the electron population is well described almost in all cases by a broken power law. The high energy slope is found to be in the range 2.2–2.8 except for one outlier, G292.2-0.5, for which $_2$= 4.1. The low energy part is instead much harder, in the range 1.0–1.6. These results are consistent with previous studies of part of the sample we have treated, see, for instance, Bucciantini, Arons & Amato (2011). The breaks, on the other hand, appear at a Lorentz factor in the range $10^5 - 10^{6.7}$, and for most of the models are actually concentrated in a narrower range around 5×10^5. These very small ranges of values of the slopes and break energies for modeling sources that appear so different at first sight suggests that the processes at the pulsar wind termination shock are common. The only models that are exceptional to these trends are G292.2-0.5, and the Model 2 of HESS J1356–645. For the PWN likely associated with HESS J1356-645, a broken power law with parameters in agreement with the previous trends produces a good fit to the data; and the single power law was explored only as an alternative to give account of ignorance or degeneracies in parameters such as age and pulsar braking index.

G292.2-0.5 is also outlier to other phenomenology discussed in this section. The spectral break of the injected electron needed in G292.2-0.5 is the highest of all PWNe studied. Despite the obvious caveats in trying to model a spatially complex region with a one zone radiative model, we note that we are also uncomfortable with the large ejected mass that would be needed in our model to have a good fit to G292.2-0.5 radiative data. It may well be the case that this PWN is just different in their acceleration properties (the pulsar has one of the largest magnetic field in our sample, in excess of 10^{13}, the other one being Kes 75), or that the model fails due to a large influence of more advanced dynamical states. In fact, the PWN is offset with respect to the position of the pulsar, what could be originated if the nebula has been displaced after being crushed by an asymmetric reverse shock caused by the presence of the dark cloud in the vicinity. Finally, it may also be that the steepness of the G292.2-0.5 spectrum points towards an alternative origin, related to the SNR, a possibility discussed, but not favored, by Kumar, Safi-Harb & Gonzalez (2012). All in all, due to the more uncertain origin of the radiation at the highest energies, the case of G292.2-0.5 requires special attention when looking at the overall properties of the population. We also note that G292.2-0.5 and the Model 2 of HESS J1356-645 are the only two cases in which we have braking indices of 2 or lower.

Pair multiplicity and bulk Lorentz factor

We now consider the PWN injection rates resulting from our models. We will compare the injection rate with the electrodynamics minimum suggested by Goldreich & Julian (1969),

$$N = \sqrt{\frac{cI\Omega\Omega}{e^2}} = 7.6 \times 10^{33} \sqrt{\frac{I_{45}P}{P_{33}^3 4 \times 10^{-13}}}\ \mathrm{s}^{-1}, \tag{4.1}$$

where P and P of Crab have been used for normalizing ($P_{33} = P/33$ ms, $I_{45} = I/10^{45}$ g cm^2). We can directly compute the injection rate by integrating $Q = \int Q(\ ,t)\mathrm{d}\ $, from where the multiplicity follows

$$= \frac{Q}{N}. \tag{4.2}$$

The values of   for all the PWNe in our sample are shown in table 4.5. Multiplicities are large in all cases, although they should be taken as upper limits. We have found that at the level of the SED, the lower limit value of $_{min}$ (critical in defining the value of) remains unconstrained in most cases. For instance, for the Crab nebula, $_{min}$ values larger than 10^4 would make very difficult to realize a proper description of the synchrotron part of the SED,

Table 4.5 Goldreich & Julian (1969) estimation and multiplicity computed from our models (an upper limit). See the description in the text.

PWN	N s^{-1}	Q s^{-1}		$_{w}$
Crab nebula	7.6×10^{33}	3.2×10^{41}	4.2×10^{7}	1.7×10^{3}
G54.1+0.3	1.2×10^{33}	7.4×10^{38}	6.2×10^{5}	2.0×10^{4}
G0.9+0.1 (M1)	2.3×10^{33}	4.0×10^{40}	1.8×10^{7}	1.3×10^{3}
G0.9+0.1 (M2)	2.3×10^{33}	1.3×10^{40}	5.6×10^{6}	4.0×10^{3}
G21.5–0.9	2.1×10^{33}	1.7×10^{39}	8.0×10^{5}	2.4×10^{4}
MSH 15–52 (M1)	1.5×10^{33}	1.3×10^{40}	8.6×10^{6}	1.6×10^{3}
MSH 15–52 (M2)	1.5×10^{33}	1.3×10^{40}	8.7×10^{6}	1.6×10^{3}
G292.2–0.5	5.5×10^{32}	9.8×10^{38}	1.8×10^{6}	2.8×10^{3}
Kes 75 (M1)	1.0×10^{33}	3.5×10^{39}	3.5×10^{6}	2.9×10^{3}
Kes 75 (M2)	1.0×10^{33}	1.4×10^{40}	1.4×10^{7}	7.2×10^{2}
HESS J1356–645 (M1)	6.4×10^{32}	2.2×10^{38}	3.4×10^{5}	1.6×10^{4}
HESS J1356–645 (M2)	6.4×10^{32}	1.3×10^{37}	2.1×10^{4}	2.7×10^{5}
CTA 1	2.4×10^{32}	3.8×10^{38}	1.6×10^{6}	8.8×10^{2}

but instead, the SED is essentially unchanged for lower values. The same happens in other cases, for instance, with a $_{min} = 10^5$ it is already difficult to fit well the radio spectrum of G0.9+0.1 and G21.5-0.9. The same happens with G54.1+0.3 for which $_{min}$ values up to 1000 would require no change in any of the parameters, and up to 5×10^4, similarly good fits can be obtained with slight variations of the injection slopes. The only case in which we need a large value of $_{min}$ is in fact in the Model 2 of HESS J1356-645, the particularities of which were discussed above.

If the wind is characterized by a single value of the Lorentz factor $_{w}$, we may write the average energy per particle in the spectrum as

$$< E >= \frac{(1- \quad)E(t)}{\int Q(\quad,t)\mathrm{d}} \equiv \;_{w}m_e c^2. \tag{4.3}$$

The values of $_{w}$ are given in table 4.5. To compute these values we have used the $_{min}$, $_{max}$, and $_{b}$ values, as well as the slopes $_{1}$ and $_{2}$ when broken power-laws are a good representation of the electron spectra, for each of the nebulae. We see that in all cases, $_{b}$ is larger than $_{w}$ by up to several orders of magnitude. This can be understood from the mean energy definition above, which can be analytically computed. This formula is time-independent and $_{w}$ is fully characterized by 5 parameters: $_{min}$, $_{max}$, and $_{b}$, $_{1}$ and $_{2}$. To get a better idea on the dependence of $_{w}$ on each parameter, we can simplify the expression taking into account that normally $1 < \;_{1} < 2$, $_{2} > 2$ and $_{min} < \;_{b} < \;_{max}$. With

Table 4.6 Comparison between modeled (w,T) and GALPROP (w^G,T^G) energy densities and temperatures. When the parameters (w,T) in the model are the same as the extracted from GALPROP we quote . . .

PWN	w_{FIR} (eV cm^{-3})	T_{FIR} (K)	w_{NIR} (eV cm^{-3})	T_{NIR} (K)	w^G_{FIR} (eV cm^{-3})	T^G_{FIR} (K)	w^G_{NIR} (eV cm^{-3})	T^G_{NIR} (K)
Crab nebula	0.5	70	1.0	5000	0.2	25	0.6	3500
G54.1+0.3	2.0	20	1.1	3000	0.8	25	1.1	3000
G0.9+0.1 (M1)	2.5	30	25	3000	1.4	35	10.5	3500
G0.9+0.1 (M2)	3.8	30	25	3000	1.7	30	3.4	3200
G21.5–0.9	. . .	. . .	. . .	. . .	1.4	35	5.0	3500
MSH 15–52 (M1)	5	20	1.4	3000	1.2	30	2.2	3000
MSH 15–52 (M2) Ê	4	20	20	400	1.2	30	2.2	3000
G292.2–0.5	3.8	70	1.4	4000	0.3	25	0.7	3300
Kes 75 (M1)	2.5	25	1.4	5000	1.5	30	4.4	3500
Kes 75 (M2)	5.0	25	1.4	5000	1.6	30	2.2	3000
HESS J1356–645 (M1)	0.4	25	0.5	5000	0.6	25	1.2	3100
HESS J1356–645 (M2)	0.4	25	0.5	5000	0.6	25	1.2	3100
CTA 1	0.1	70	0.1	5000	0.3	25	0.6	3000

this assumptions, we can simplify it to yield,

$$w \quad \left[\frac{\frac{1}{2-\ _2} - \frac{1}{2-\ _1}}{\frac{1}{1-\ _1}\left(\frac{_b}{_{min}}\right)^{_1-1} + \frac{1}{1-\ _2}} \right] \ _b, \tag{4.4}$$

with the order of magnitude being $_w \sim \ _b(\ _b/\ _{min})^{(1-\ _1)}$. Physically, the population of low energy electrons is more numerous, and it is responsible for the radio to IR emission of the nebulae.

ISRF values compared with a Galactic model

Table 4.6 compares the energy densities used to fit the observational data of each of the PWNe studied with those obtained from the GALPROP code (Porter, Moskalenko & Strong, 2006). In order to do this, we have obtained the ISRF from GALPROP and fitted three diluted blackbodies, for which the energy densities and temperatures are referred to as w^G and T^G, respectively. As shown in table 4.6, the values of the FIR energy densities obtained from GALPROP are generally lower (by up to a factor of a few) than what we found is needed to fit the PWN high-energy emission. Figure 4.13 shows four examples.

The use of GALPROP ISRFs all along the Galaxy is known to be subject to local uncertainties. Galactic locations in which freshly accelerated electrons target overdensities of FIR photons contributed by nearby stars, star-forming regions, or the supernova remnants themselves, could produce these local variations. As mentioned above in some of the individual PWNe studied, the need of larger energy densities than those found in GALPROP

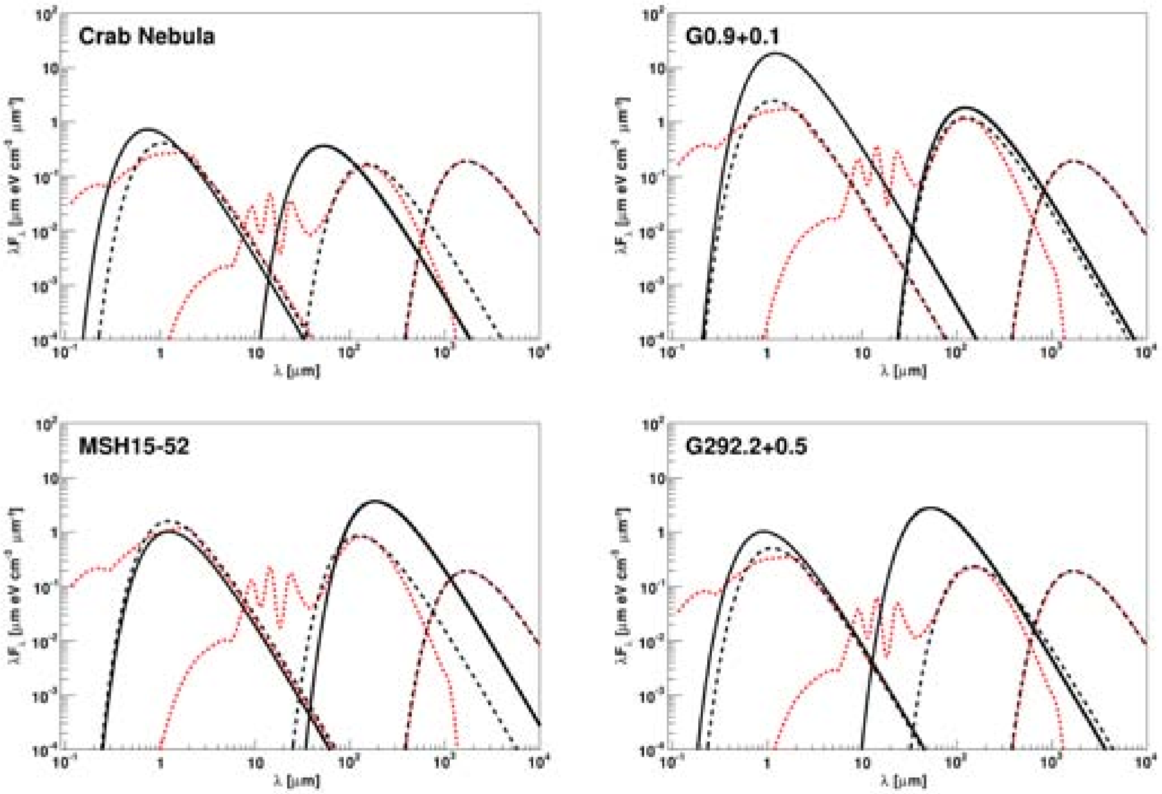

Fig. 4.13 Example of the comparison between the ISRF obtained from the GALPROP code (Porter, Moskalenko & Strong, 2006) and the assumptions made to fit the PWNe models. We show the FIR and NIR diluted blackbodies (with the parameters of table 4.3 in bold black curves), in comparison with the GALPROP raw results (in red) and fits to these results using diluted blackbodies (in black thin lines, and as given in table 4.6.) The rightmost component stands for the CMB in all panels.

when time-dependent models have been used has been spotted in the past, but for scattered PWN. The possibility of finding relatively high energy densities in the background photon fields nearby PWNe is interesting from a couple of perspectives: On the one hand, it would imply that CTA could be mapping PWNe also at averaged (and thus lower) Galactic photon backgrounds, ultimately helping determine the latter. On the other hand, detailed studies of the IR emission around PWNe should reveal significant sources. This is in general true, as examples, one could quote the case of G54.1+0.3 in which Temim et al. (2010) proposed that the SN dust is being heated by early-type stars belonging to a cluster in which the SN exploded; or MSH 15-52 where there is an O star 13 arcsec away from the corresponding pulsar (Arendt, 1991; Koo et al., 2011). A statistical study of the correlation between mass (traced by CO and dust) and TeV sources has been recently performed by Pedaletti, de Oña Wilhelmi & Torres (2014), finding that there are hints of a positive correlation with IR

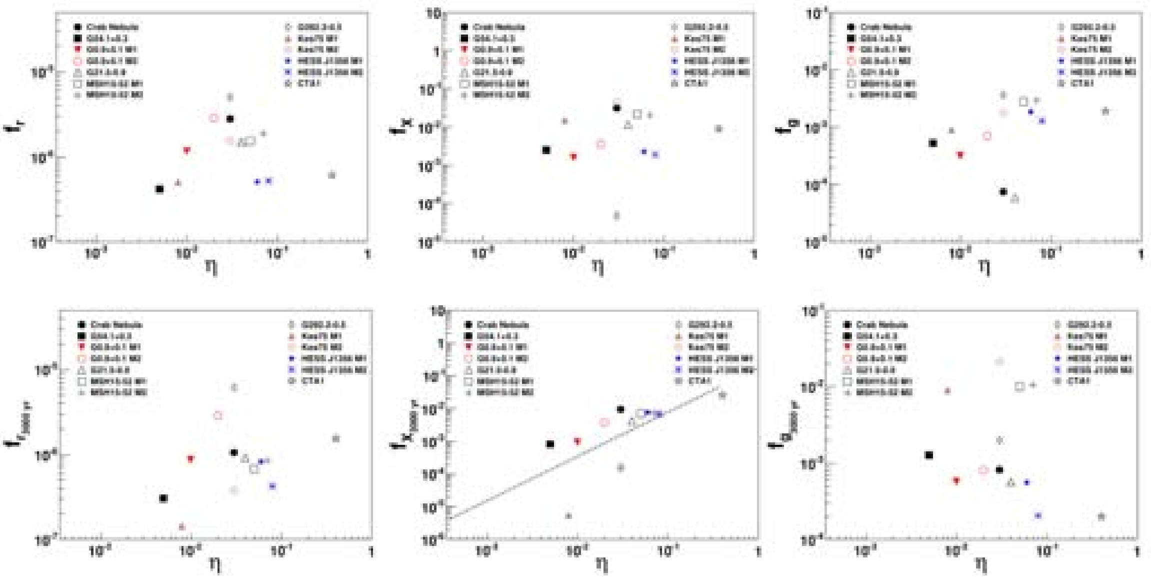

Fig. 4.14 Magnetization of PWNe as a function of the radio, X-ray, and γ-ray efficiency. In the first row, all luminosity fraction values correspond to those today; in the second row, to the values they have from the evolution of each of the PWN when considered at 3000 years.

excess at the level of 2–3 σ, which still needs to be confirmed.

Magnetization of the nebulae

From table 4.3 we see that all young nebulae detected at TeV are particle dominated, with magnetic fractions that in all cases except CTA 1, never exceed a few percent. Figure 4.14 shows the values of the obtained radio, X-ray, and γ-ray efficiencies as a function of the magnetic fraction of the nebulae (which in our model is constant along the evolution). The two sets of panels distinguish the values of the efficiencies obtained today (at different ages for each of the nebulae considered) from those obtained at the same age, fixed at 3000 years.

To consider whether there is a correlation in any of these (and subsequent) magnitudes we use a Pearson test. The Pearson *r* estimator is computed using 9 PWN models (unless otherwise clarified). When more than one model was considered plausible for a given PWN we use M1, although we have verified that considering the alternatives would not introduce a significant change to the results. We do not emphasize here the search for precise fit parameters (unless an obvious connection would appear), but of plausible correlations. The latter will be hinted in those cases in which the Pearson coefficient for the pair of magnitudes considered yields to a non-directional probability of incorrectly rejecting the null hypothesis (i.e., no correlation) smaller than 0.05. In these cases, we quote the fit parameters in table

Table 4.7 Correlation fits shown in the figures. We use $y = p_1 x + p_0$, where variables can be in logarithmic scale, as shown in the corresponding figures. Numbering of panels goes alphabetically, from left to right and top to bottom. Unless otherwise clarified we used all PWNe for fitting (in cases where we have two models, we use Model 1). We show the Pearson's correlation coefficient r and the non-directional significance implied by it.

x-Magnitude	y-Magnitude	Fig.	p_0	p_1	Pearson's r	P
	f_X	Fig. 4.14 - panel e	-0.75 ± 0.89	1.35 ± 0.55	0.68	4.3×10^{-2}
E	L_r	Fig. 4.17 - panel a	-11.50 ± 5.67	1.15 ± 0.15	0.94	1.4×10^{-4}
E	L_X	Fig. 4.17 - panel b	-17.67 ± 12.78	1.41 ± 0.34	0.84	4.5×10^{-3}
$_c$	L	Fig. 4.17 - panel f	36.95 ± 1.31	-0.88 ± 0.38	-0.67	4.8×10^{-2}
E	$L\ /L_r$	Fig. 4.17 - panel h	30.20 ± 7.69	-0.74 ± 0.21	-0.80	9.6×10^{-3}
E	$L\ /L_X$	Fig. 4.17 - panel i	36.38 ± 15.76	-1.00 ± 0.42	-0.67	4.8×10^{-2}
E	$_{max}$	Fig. 4.18 - panel a	-2.85 ± 3.53	0.32 ± 0.10	0.79	1.0×10^{-2}
B_{LC}	$_{max}$	Fig. 4.18 - panel c	7.31 ± 0.47	0.37 ± 0.10	0.82	6.8×10^{-3}
ΔV	$_{max}$	Fig. 4.18 - panel d	-1.16 ± 3.03	0.65 ± 0.19	0.78	1.3×10^{-2}
E	B	Fig. 4.18 - panel p	-18.13 ± 4.28	0.52 ± 0.11	0.86	2.9×10^{-3}
B_{LC}	B	Fig. 4.18 - panel r	-1.51 ± 0.70	0.55 ± 0.14	0.83	6.0×10^{-3}
ΔV	B	Fig. 4.18 - panel s	-15.40 ± 3.68	1.04 ± 0.23	0.86	2.9×10^{-3}

4.7, as well as we show the fit in the corresponding figure.

There is no apparent correlation of the efficiencies with the magnetization except when we consider the X-ray efficiency f_X of the nebulae normalized at the same age. In that case, the Pearson coefficient yields to a probability of 0.043 of incorrectly rejecting the null hypothesis, but the coefficients of a linear fit are poorly determined because of the dispersion of the data. The significance of the correlation barely meets our cut. The radio and -ray efficiencies computed at the same age present significances of the order of 10%. The fact that we do not see a correlation of the gamma-ray efficiency with the magnetization implies that is neither the only nor the dominant order parameter to impact the luminosities. The fact that we see essentially very similarly magnetized PWNe from a magnetic point of view reduces the -distinguishing power further.

Is there a low-magnetization observational bias?

The only high-magnetization nebula we found in the sample we study is CTA 1, for which $= 0.4$, is close to equipartition. Should be much lower than this value we would find TeV fluxes in excess of what has been detected. The possibility that CTA 1 is beyond free expansion could play a role here; a compression of the nebula due to reverberation could lead to an increase of the magnetization. Note that in the model of CTA 1 by Aliu et al. (2013), where a reverberation has been taken into account, the magnetization was also found to be in the high end, more than an order of magnitude larger than in Crab nebula. It is to note that the highest magnetized nebula in the sample is showing one of the lowest magnetic fields (see table 4.3), something which has also been found with other models (e.g., Aliu et al.

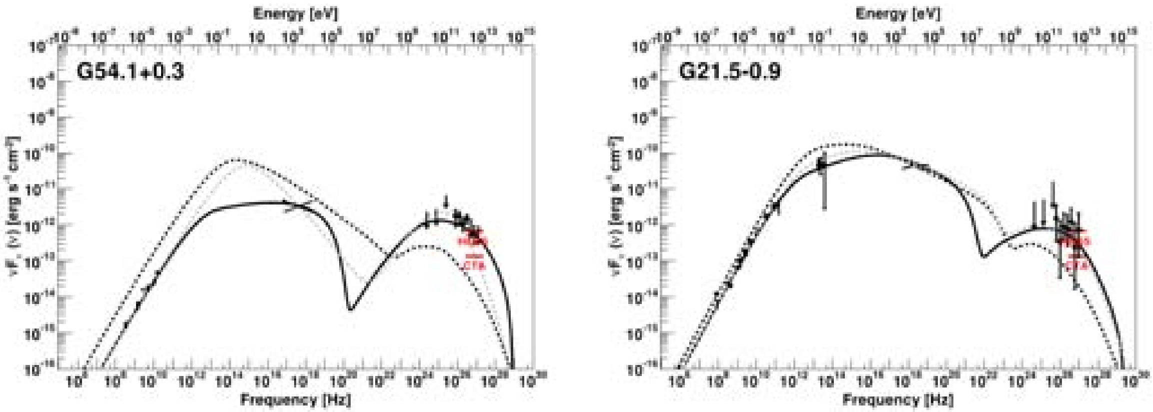

Fig. 4.15 G54.1+0.3 (left) and G21.5-0.9 (right) modeled with an imposed equipartition of the energetics ($= 0.5$) as compared with the adopted (particle dominated) models. The solid line represents the fitted model of table 4.3, the dashed black line represents a model with $= 0.5$ and no changes in other parameters with respect to the fitted model of table 4.3, and the dashed grey line stands for an equipartition model where other parameters are adjusted ad-hoc so that a relatively good fit is attained. For a discussion of the caveats of latter models see the text. The sensitivity of a H.E.S.S.-like telescope and of CTA are marked by the horizontal lines.

2013). However, the conclusion that all the other nebulae are heavily particle-dominated is not affected by uncertainties in the modeling. To prove this we have tried to fit these nebulae data with an ad-hoc increase of up to 0.5 (equal distribution of the power between particles and field) and explored the range of parameters, if any, which would allow for a good fit. Models with larger allow us to investigate whether we would have detected the nebulae should they have an increased magnetic fraction. Earlier, we have concluded that if the injection and environment of PWNe were as those of Crab, only in the case of a large, Crab-like, spin-down power feeding into a nebula located at 2 kpc or less, a H.E.S.S.-like telescope would detect magnetically-dominated nebula beyond ~ 0.5 (Torres et al., 2013). Different to our earlier study, we here consider the injection and environmental properties specifically derived for each nebulae.

Figure 4.15 shows two examples, for PWN G54.1+0.3 and G21.5-0.9, when modeled with imposed equipartition of the energetics keeping other parameters the same (e.g., with the same FIR/NIR densities). The increase in implies enlarging it by a factor of $\sim$100 and $\sim$10 in the fitted -value, respectively. The predicted TeV emission fits the data badly, and the TeV fluxes are below the sensitivity of CTA.

We have also searched for a fit in case the PWNe are in equipartition but all other parameters are allowed to vary. The solutions we found require extreme values of other parameters and are thus not preferred. For instance, in the case of G21.5-0.9, a relatively good fit (albeit of poorer quality than the one we show in figure 4.4) can be found by increasing the FIR density to 6 eV cm^{-3} (a factor of 6 larger than the GALPROP outcome at the position) and reducing the ejected mass by a factor of 2 (what enlarges the nebula size in our model and contributes to dilute the magnetic field energy). It is clear that there is no preference for these stretched parameters over the ones shown in our earlier fit. The case of G54.1+0.3 is similar, although requires even larger changes in the FIR and NIR densities, and the ejected mass in order to yield to a fit which is not even close to all data points, particularly those at high energies. In particular, figure 4.15 shows a model with $= 0.5$ a FIR (NIR) density of 4 (40) eV cm^{-3}, and an ejected mass more than a factor of 3 smaller implying a factor of $\sim$2 larger nebula. It is clear that no equipartition model can be sustained in this case either. These conclusions are similarly obtained in the analysis of other PWNe. The finding of CTA 1, however, shows that the fact that most of the PWNe we see are particle dominated cannot be fully ascribed to an observational bias; at least in some cases (but not in the majority) we would be able to detect them with the current generation of telescopes.

Searching for a more meaningful SEDs and electron population comparison

Figure 4.16 put together the currently observed SEDs, the corresponding electron losses, and the electron populations. Whereas this is an interesting figure to gather the variety of the sources detected, a direct comparison of the multi-frequency emission (as it is usually done) has to be taken with care: we are looking at objects at different ages and powered by pulsars of different spin-down. The variety we found at the SED level (top left panel) contrasts with the little dispersion (one order of magnitude) in the timescales for the losses that are operative in all the PWN. From the SED results today, the two outliers from the bulk of models are the Crab nebula and G292.2-0.5. Whereas the former can be understood due to the large difference in spin-down power, the reason for the latter discrepancy is less clear (see the discussion above).

In order to search for a more meaningful comparison we explore two normalizations of the SEDs. On the one hand, we normalize the SED of each PWN by its corresponding spin-down flux ($F_{sd} = E/4\ D^2$, as obtained from table 4.3) each pulsar has at its current age. On the other hand, we compute the SEDs at the same age (arbitrarily chosen to be 3000 yr) for all pulsars, and normalize them with the spin-down flux that each pulsar would have at that age (E(3000 yr)/4 D^2). These normalized SEDs are shown in the right panels of figure 4.16. The bottom-right panel of figure 4.16 shows the electron populations of all PWNe at the same age (3000 yr).

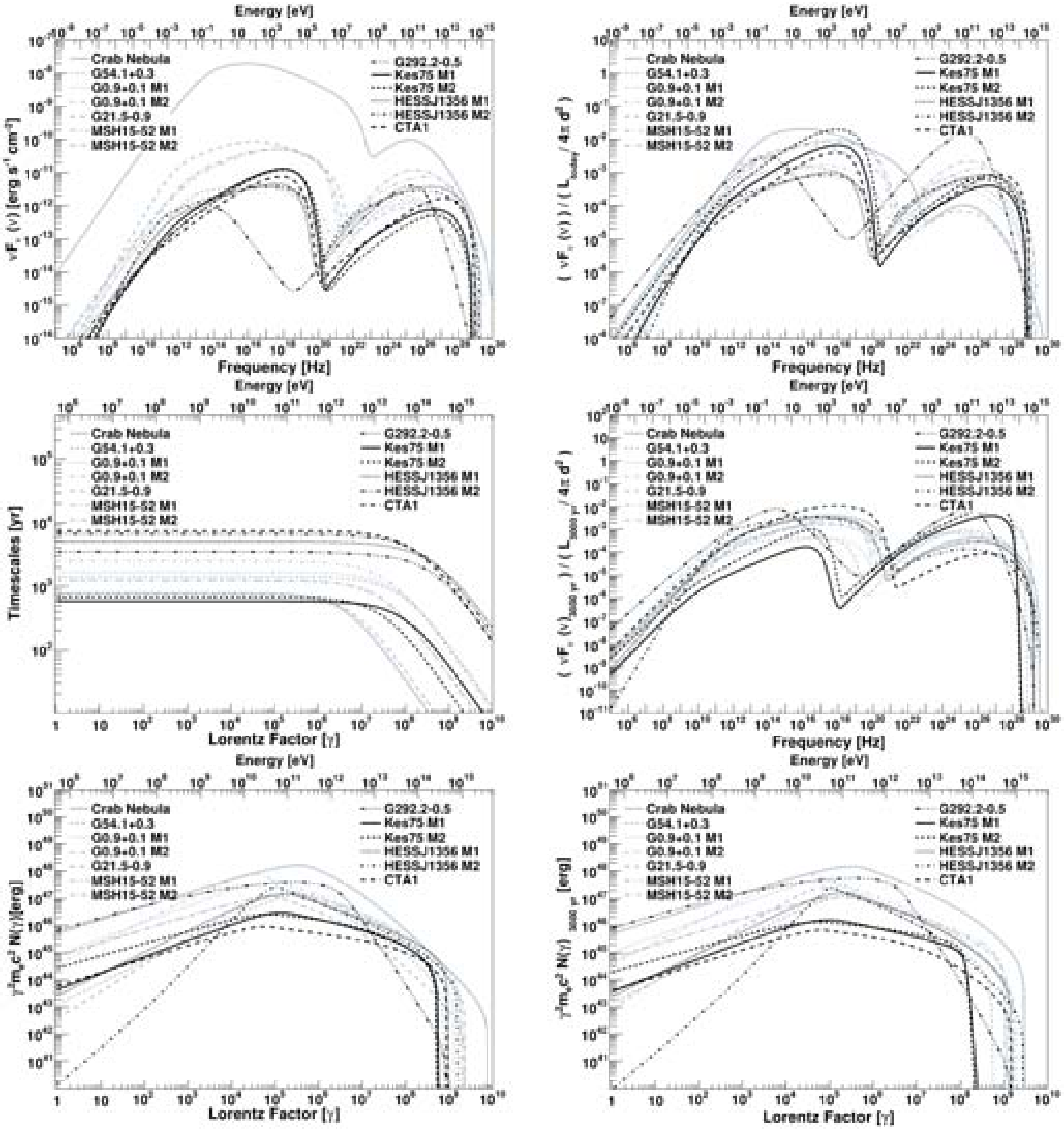

Fig. 4.16 Comparison of PWNe results. Left panels: from top to bottom, SEDs, electron losses, and electron distributions today. Right panels: from top to bottom, SEDs normalized by the corresponding spin-down flux ($E/4\ \ D^2$, as obtained from table 4.3), SEDs at 3000 yr normalized with the spin-down flux that each pulsar would have at that age, and electron populations at 3000 yr.

It is interesting to compare the Crab nebula's SED with respect to the others when one normalize it with the corresponding spin-down power and/or look at all PWNe at the same age: the Crab nebula becomes an unnoticeable member of the same population of sources. It is also interesting to notice that the other outlier, G292.2-0.5, is now also in the bulk of models (see second panel, right column). The population is only distinguished by differences in the electron content, where slight variations in the position of the breaks and cutoffs is retained even when looked at the same age.

PWN versus PSR properties: E and $_c$

Possible correlations between the luminosities obtained from our models and two of the main features of the central pulsars, their spin-down power and characteristic age, are explored in figure 4.17. It shows the distribution of radio, X-ray, and gamma-ray luminosities, and their ratios (see table 4.4) as a function of spin-down power and characteristic ages. A line is added (and parameters are shown in table 4.7) when the Pearson coefficient is such that the correlation is significant to better than 95% of confidence, as above. A red line is added to those panels for which Mattana et al. (2009) provided a fit when considering observational values of TeV-detected PWNe up to 10^5 yr of age.

The possible correlation of the PWN luminosities with the PSR characteristic ages (second row in figure 4.17) is not clear for young PWNe; for L_r and L_X we actually do not find them at the confidence cut imposed. At the latter case, however, the fit by Mattana et al. (2009) is in agreement with the overall (visual) trend of our sample. The only correlation barely surviving our 95% confidence cut is the one between $_c$ and L (see table 4.7), which Mattana et al. (2009) did not find. We see that the larger the characteristic age the lower the -ray luminosity. This trend is opposite to the example made in the introduction, where we find more -ray luminosity for pulsars with larger $_c$ when all other parameters were the same, and thus requires a careful look. On the one hand, we have in our sample cases of similar spin-down power and $_c$, for G21.5-0.9 and G0.9+0.1; but different real (or assumed real) age (the age assumed for G0.9+0.1 is a factor of 2 to 4 larger than that of G21.5-0.9). In this case, one should also expect variance in L (being smaller for the youngest, as found) even if all other parameters influencing the gamma-ray production are the same (which usually are not). On the other hand, CTA 1 (at the extreme of the distribution) has the largest magnetization and lowest spin-down power of the sample, what reduces its -ray luminosity despite its larger $_c$.

The possible correlation of the luminosities with the spin-down power is visually apparent for all three luminosities considered (see top row of figure 4.17 and table 4.7), although

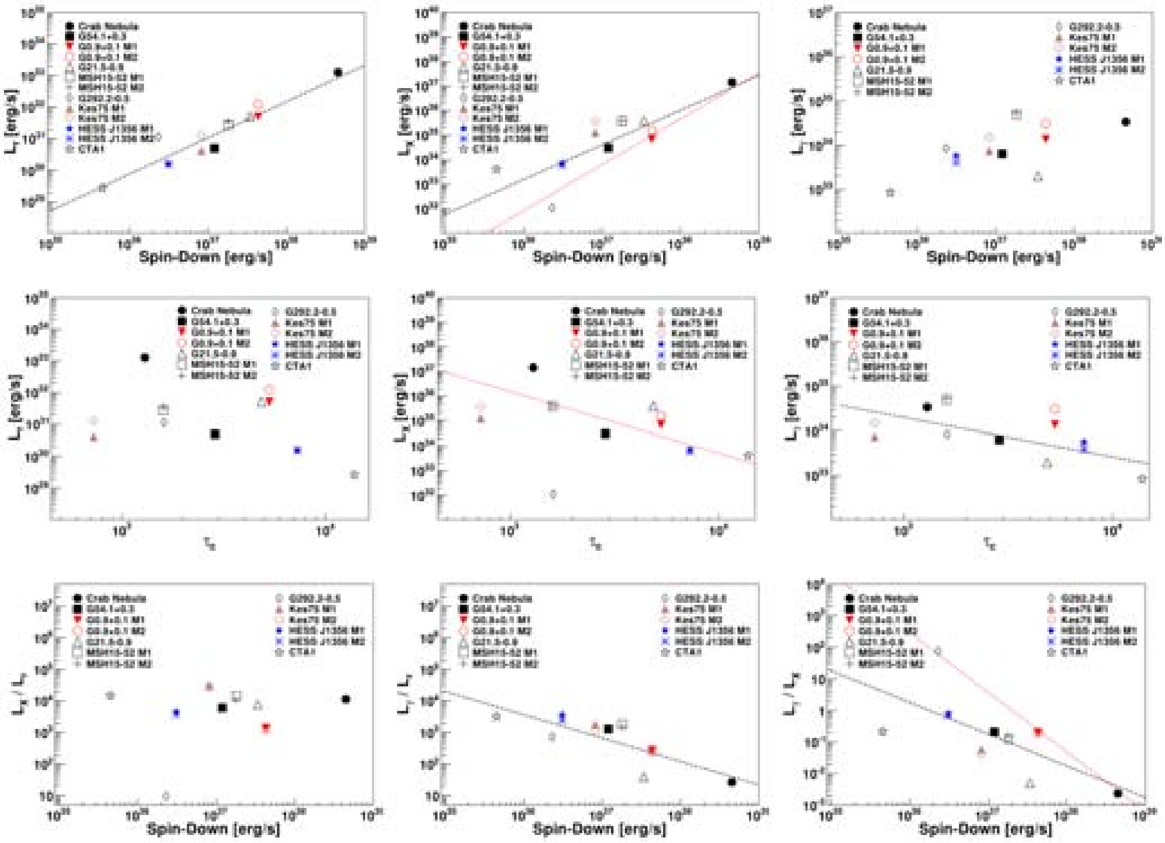

Fig. 4.17 Radio, X-ray, and γ-ray luminosities of young, TeV-detected PWNe as a function of spin-down power and characteristic ages of their pulsars. Linear fits to the data (black dashed lines) are also shown for magnitudes with a high Pearson coefficient (see text for details). Red dashed lines stand for fits presented in Mattana et al. (2009) using observational data on pulsars of up to 10^5 years of age. The bottom row shows the ratios between the X-ray and radio, gamma-ray and radio, and gamma-ray and X-ray luminosities.

in the case of the γ-ray luminosity the confidence cut is not met (the resulting probability for no correlation is 6.2×10^{-2}). This is compatible with Mattana et al. (2009) results. The scaling between X-ray luminosities and spin-down power was also noted by Seward & Wang (1988) and Becker & Truemper (1997); in the form $L_X \sim 10^{-3}\dot{E}$, see also Kargaltsev, Pavlov & Wong (2009). The radio luminosity/spin-down power correlation is the best in the sample we study.

We have also found correlations in two of the ratios of luminosities explored, L_γ/L_r and L_γ/L_X. That is, when we compare the IC γ-ray luminosity with the synchrotron generated ones, we find that the larger the spin-down, the smaller their ratio. We have seen above that all three luminosities apparently increase with the spin-down, with the luminosity of the synchrotron components increasing faster. The larger the spin-down power, the more

Table 4.8 Parameters used in search of correlations, as a function of *P* and *P* and values for the pulsars associate with the PWNe considered in the study.

PSR associated with	Surface Magnetic field	Light Cylinder Radius	Magnetic field at Light Cylinder	Electric Potential
	Equation (1.20)	$R_{LC} = 4.77 \times 10^9 (P/\mathrm{s})$ cm	$B_{LC} = 5.9 \times 10^8 (P/\mathrm{s})^{-5/2} \sqrt{(P/\mathrm{s\,s^{-1}})}$ G	Equation (1.21)
Crab	7.58×10^{12}	1.59×10^{8}	1.88×10^{6}	4.46×10^{16}
G54.1+0.3	2.04×10^{13}	6.49×10^{8}	7.49×10^{4}	7.25×10^{15}
G0.9+0.1 (M1/M2)	5.66×10^{12}	2.49×10^{8}	3.67×10^{5}	1.36×10^{16}
G21.5–0.9	7.12×10^{12}	2.95×10^{8}	2.77×10^{5}	1.22×10^{16}
MSH 15–52 (M1/M2)	3.04×10^{13}	7.16×10^{8}	8.29×10^{4}	8.85×10^{15}
G292.2–0.5	8.18×10^{13}	1.95×10^{9}	1.11×10^{4}	3.22×10^{15}
Kes 75 (M1/M2)	9.71×10^{13}	1.55×10^{9}	2.63×10^{4}	6.07×10^{15}
HESS J1356–645	1.56×10^{13}	7.92×10^{8}	3.15×10^{4}	3.73×10^{15}
CTA 1	2.16×10^{13}	1.51×10^{9}	6.27×10^{3}	1.41×10^{15}

particles are in the nebulae and the larger is the maximum energy they attain. However, the timescale for cooling of electrons via radiating synchrotron emission is faster than for IC, and whereas the radio emission is greatly enhanced, the -ray emission grows at slower rate.

We have considered what happens to these correlations when all the systems are evolved to the same pulsar age, at 3000 yr. We see that the correlations between the luminosities and the spin-down power (both at 3000 yr of age) still appear at our confidence cut level, but their significances worsen with respect to the one pointed out above. This worsening makes for the correlation of the ratio of the luminosities to disappear in this case.

PWN versus PSR properties: other parameters

We now consider possible correlations between other PWN properties resulting from our fits and those of the central pulsar. We compute for each pulsar the surface magnetic field, the potential difference at the polar cap, the light cylinder, and the magnetic field at the light cylinder (assuming the neutron star is a dipole). The definitions used for these quantities are summarized in table 4.8, as well as the values obtained for all pulsars in our study. These quantities relate to each other and to the spin-down power, all being functions of P and *P*; thus, it is to expect that if we find a correlation of any magnitude with the spin-down power, we would also find it with the potential difference at the polar cap, and the magnetic field at the light cylinder. The spin-down–surface magnetic field dispersion can introduce different correlations, depending on the values of P and *P*.

The first four rows of figure 4.18 plot the spectral parameters of the injected electrons as a function of the pulsar properties. We find no correlation of the slopes $_1$ and $_2$, or $_b$ with the pulsar properties. In the case of $_2$, this is true even disregarding the outlier, G292.2-0.5.

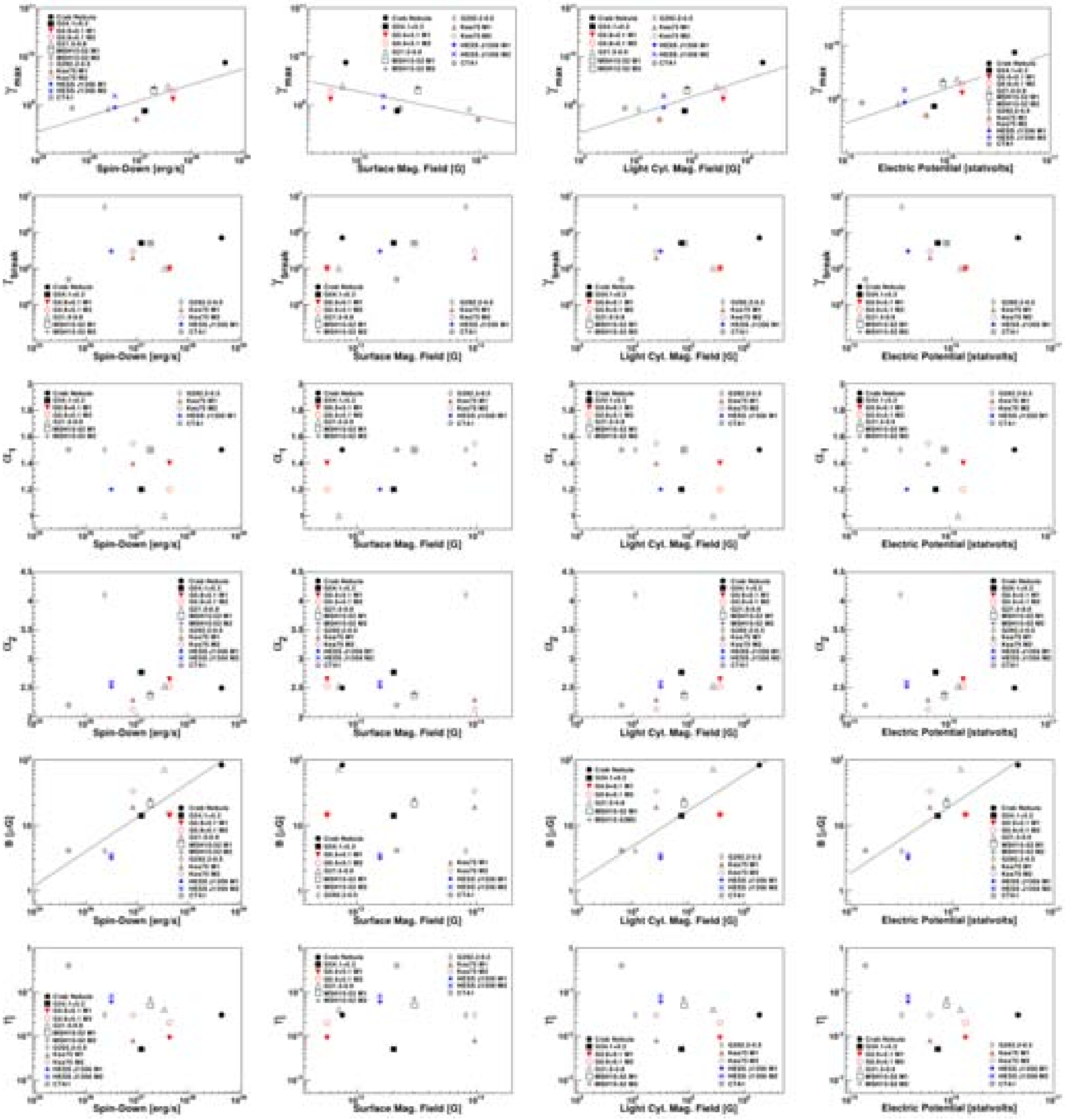

Fig. 4.18 PWNe properties in the y-axis of all plots as a function of pulsar properties in the x-axis of all plots. The values of all magnitudes refer to the current time. From left to right, we plot the obtained values of $_{max}$, $_{b}$, $_{1}$, $_{2}$, $B(t_{age})$, and , as a function of (from top to bottom) spin-down, surface magnetic field, light cylinder magnetic field, and potential.

We do find a correlation of the the maximum Lorentz factor with the spin-down power (and thus the magnetic field at the light cylinder, and the pulsar electric potential). The significance of the correlation surpasses 95% CL. For the surface magnetic field, the significance we obtain is the level of 94%, and this is why we do not quote this fit in table 4.7 although we show it in the corresponding plot for visual inspection. If this trend is considered, the $_{max}$ value is anti-correlated with the surface B field of the pulsar. On the contrary, the larger is the spin-down power (or the magnetic field at the light cylinder or the electric potential), the larger is the Lorentz factor of electrons in the nebulae. The maximum energy to which electrons are accelerated in the nebulae depends on the injected electrons at the bottom of the wind zone. This correlation is to be expected via equation 2.17 and the fact that the dispersion that we find in the two other free parameters appearing in there, and , is relatively not large for most of the sample.

Looked at the same age (at 3000 years) the $_{max}$–surface magnetic field anti-correlation is confirmed better than the 95% level, whereas the results for the other parameters are very similar.

The magnetic field in the nebulae is also correlated with the pulsar properties. Also here, the larger the spin-down power (or the magnetic field at the light cylinder or the electric potential) the larger the nebula magnetic field, but this too can be ascribed to the way we define the magnetic field in the model. The magnetization, however, is a free parameter in the fit, and with the confidence cut imposed, we see no relation between and any of the pulsar characteristics. Take as an example the Crab Nebula: it is the pulsar with the largest spin-down power and nebular B (today magnitudes) but its magnetization is similar to that of the remaining PWNe.

Taking the PWNe at the same age of 3000 years, we find that the PWN magnetic field correlation with the spin-down power (or the magnetic field at the light cylinder or the electric potential) is lost. The nebular magnetic field and the spin-down power are both decreasing with the age of the system, thus looking for its relationship at the same age increases the dispersion.

The multiplicity of the models studied is correlated (but only better than 94% of CL) with the pulsar parameters, presenting positive correlations with the spin-down power (or the magnetic field at the light cylinder or the electric potential) and negative correlation with the surface magnetic field (albeit the scatter of the data points in this latter case seems to be worse). A caveat in this case is that the parameter is already making use of the P and P values to normalize the injected electrons (see equation 4.2), and in fact, because of its definition Q itself is obviously correlated with the spin-down.

4.5 Concluding remarks

The aim of this study was to present numerical models of the TeV-detected, young PWNe along more than 20 decades of frequencies; using a radiatively complete, time-dependent numerical approach. For the first time, we have a coverage of many such PWNe analyzed under the same framework, adopting similar assumptions, which allows for a more meaningful parameter comparison. Despite the caveats of the model used, we find that one-zone, leptonic-only generated radiation provides a reasonably good fit to the multifrequency data for PWNe detected at TeV. Here we summarize our findings.

- We favor a non-PWN origin for the radiation detected from HESS J1813–178. For the remaining 9 TeV sources studied, we find a plausible PWN origin of the mutiwavelength emission.

- For all the TeV sources plausibly related with a PWN, only the Crab nebula is SSC dominated. All the remaining PWNe except for HESS J1356–645 and CTA 1 are IC-FIR dominated. The dominance of the FIR contribution to IC is always significant.

- The FIR energy densities that we found is needed to fit the PWN high-energy emission are generally larger than what is obtained from GALPROP (usually by up to a factor of a few).

- The efficiencies of emission are $\sim 10^{-6\div7}$ in radio, $\sim 10^{-2\div3}$ in X-rays, and $\sim 10^{-3\div4}$ in -rays, with only one outlier in the sample presenting very low X-ray fluxes (G292.2–0.5).

- The electron population can be described by a broken power law in all cases. The parameters of the injection cluster in relatively narrow ranges, especially, the break Lorenz factor, which is around 5×10^5. The high energy spectral slope is found to be in the range 2.2–2.8 (except for the steeper case of G292.2–0.5, which also present a higher energy break). The low energy part is instead much harder, with the low energy index in the range 1.0–1.6.

- All PWNe have large multiplicities, in general in excess of 10^5. The population of low-energy electrons is large by number, and generate a low medium energy per particle in the spectrum in all cases.

- All the nebulae except CTA 1 have low values of magnetization, of only a few percent. CTA 1 presents the largest magnetization of our sample, and reaches almost to equipartition. All the other PWNe are heavily particle dominated. This result is found to be stable against uncertainties.

- We do not find significant correlations between the efficiencies of emission at different frequencies and the magnetization, implying that the specific environment and the injection effects play a dominant role in determining, e.g., the -ray luminosity.
- Comparing SEDs of the PWNe as observed today mixes pulsars of different spin-down power and age, and generates a variety of distributions. A normalized comparison of the SEDs (e.g., with the corresponding spin-down flux) at the same age significantly reduces the dispersion.
- We do not find clear correlations between the pulsar's characteristic ages and the radio and X-ray luminosities. The gamma-ray luminosity seems to be anti-correlated with the characteristic age. On the other hand, we do find correlations of the radio and X-ray (and at a slightly lower confidence also -ray luminosities) with the spin-down, and an anti-correlation of the ratios of IC to synchrotron luminosities with the spin-down.
- The injection parameters do not appear to be correlated with the pulsar properties, except for the maximum Lorentz factor and the magnetic field in the nebula which are correlated with the spin-down power (or the magnetic field at the light cylinder or the electric potential), but these cases can be ascribed to the model properties.
- We do not find a significant correlation of any PWN parameter with the surface magnetic field of the pulsars.

Chapter 5

Is there room for ultra-magnetized PWNe among those non-detected at TeV?

The spectral energy distribution (SED) of the pulsar wind nebulae (PWNe) of the highest spin-down powered pulsars are varied. In particular, luminous pulsars such as Crab ($E = 4.5 \times 10^{38}$ erg s^{-1}) and the Large Magellanic Cloud (LMC) J0537-6910 in N157B ($E = 4.9 \times 10^{38}$ erg s^{-1}) are TeV detected, as are others with spin-down power in the order of several 10^{37} erg s^{-1}. However, several PWNe with pulsars similarly luminous, are not. Why? Do they have significantly different interstellar environment, injection, or nebular magnetization?

The X-ray luminosity efficiency of these high-spin down pulsars also presents a large range. A notable case is G76.9+1.0 for which the X-ray efficiency is $L_X/E \sim 2.4 \times 10^{-4} D_{10}^2$, where D_{10}^2 is the distance in units of 10 kpc (Arzoumanian et al., 2011)[1]. This and similar cases are challenging for PWNe spectral models since they imply an inefficient acceleration of high energy electrons in order to fit the X-ray luminosity. For these cases, Arzoumanian et al. (2008) suggested that the pulsar wind has a high magnetization factor, speculating that because particle-dominated winds are necessary for efficient conversion of wind to synchrotron power, PWNe with high magnetization would lead to dim X-ray PWNe. This was confirmed by the phase space exploration of Crab-like nebulae done by Torres et al. (2013): the magnetization of the nebulae, all other parameters being the same, can decide on TeV detectability. Thus, high- models point to an interesting alternative for the interpretation of PWNe, which, despite their high spin-down, lack TeV emission and have weak X-ray counterparts. These PWNe would be different to TeV detected ones. Except CTA 1, for which the magnetization reaches almost to equipartition, all TeV-PWNe with characteristic ages of 10 kyr or less can be described with an spectral model with low , and are thus strongly particle dominated (Torres et al., 2014).

---

[1] The spin-down of the pulsar in G76.9+1.0 has been recently re-assessed due to a new measurement of the period (see section 5.1), and while it is now lower than earlier claimed, it still qualifies as one the most energetic pulsars we know.

An interesting case is that of G292.0+0.18, for which the central powering pulsar, J1124-5916, has essentially the same P, P (up to three significant decimal places) than J1930+1852, which powers G54.1+0.3. The distance for both nebulae is also similar ($\sim$6 kpc). Whereas the latter is a TeV source, and modeled as particle dominated PWN (e.g., Tanaka & Takahara 2011; Torres et al. 2014), the former is not (at least at the level in which it has been coveredin the Galactic Plane observations by H.E.S.S. (Carrigan et al., 2013). With the same spin-down power and located at a similar Galactic distance, it seems that the flux at TeV energies depends on other factors such the environment (the FIR density, for instance) or the nebula magnetization. Is then G292.0+0.18 simply like G54.1+0.3 but subject to a stronger magnetization?

Tanaka & Takahara (2013) have also analyzed several PWNe which have been undetected at TeV[2]. However, they assumed a fixed low magnetization (3×10^{-3}) compatible with usual particle dominated nebulae that have been detected at TeV to describe them.

In this chapter, we propose models for the non-detected PWNe at TeV with $E > 10^{37}$ erg s^{-1} and we explore the phase space of PWNe models also in magnetization, in order to distinguish whether there is preference for the existence of highly magnetized nebulae (or at least, for nebula with magnetization close to equipartition) among those not yet seen at TeV.

5.1 Non-detected PWNe at TeV energies with high spin-down pulsars

G310.6+1.6

G310.6-1.6 (IGR J14003-6326) was discovered as a soft -ray source in a deep mosaic of the Circinus region done by INTEGRAL (Keek, Kuiper & Hermsen, 2006). It was also

---

[2] For differences between their model and ours see the discussion in Martín, Torres & Rea (2012); Torres et al. (2014). Their magnetic field evolution does not consider losses in magnetic energy due to expansion, and thus their magnetization values are lower than ours typically by a factor 2-3.

Table 5.1 Model parameters for 3C 58, N157B, N158A, G76.9+1.0, G310–1.6 & G292.0+1.8.

Magnitude	3C 58	N157B	N158A[†]	G76.9+1.0[‡]	G310.6–1.6	G292.0+1.8
Pulsar magnitudes						
P (ms)	65.7	16.12	50.50	48	31.18	135.48
P (s s^{-1})	1.93×10^{-13}	5.18×10^{-14}	4.79×10^{-13}	8.64×10^{-14}	3.89×10^{-14}	7.53×10^{-13}
$_c$ (yr)	5397	4936	1670	8970	12709	2854
t_{age} (yr)	2500	4600	760	5000	1100	2500
$L(t_{age})$ (erg s^{-1})	2.7×10^{37}	4.9×10^{38}	1.5×10^{38}	2.96×10^{37}	5.1×10^{37}	1.2×10^{37}
L_0 (erg s^{-1})	9.3×10^{37}	1.1×10^{41}	3.3×10^{38}	1.5×10^{38}	6.1×10^{37}	7.8×10^{38}
n	3	3	2.08	3	3	3
$_0$ (yr)	2897	336	2340	3970	11609	354
d (kpc)	3.2	48	49	10	7	6
M_{ej} ($M_\odot$)	8	20	25	20	9	9
R_{PWN} (pc)	3.7	10.6	0.7	4.7	1.3	3.5
Photon environment						
$T_{FIR}^{(1)}$ (K)	20	80	80	25	25	25
$w_{FIR}^{(1)}$ (eV cm^{-3})	5 (0.75)	0.7	5 (0.2)	0.13	0.62	0.42
$T_{FIR}^{(2)}$ (K)	-	88	-	-	-	-
$w_{FIR}^{(2)}$ (eV cm^{-3})	-	0.3	-	-	-	-
T_{NIR} (K)	-	-	-	3200	3300	2800
w_{NIR} (eV cm^{-3})	-	-	-	0.33	1.62	0.70
Injection parameters						
$_{max}(t_{age})$	7.3×10^{9}	3.8×10^{8}	9.8×10^{8}	5.7×10^{8}	5.7×10^{8}	2.4×10^{9}
$_{min}$	1	1	1	1	1	1
$_b$	7.8×10^{4}	10^{6}	3×10^{7}	10^{3}	2×10^{6}	10^{5}
$_l$	1.05	1.5	1.8	1.5	1.5	1.5
$_h$	2.91	2.75	2.6	2.7	2.5	2.55
	0.3	0.02	0.3	0.25	0.3	0.3
Magnetic field						
$B(t_{age})(\quad G)$	35	13	32	3.5	8.2	21
	0.21	0.006	0.0007	0.0017	0.0007	0.05

Some alternative models are commented in the text.

[†] The FIR energy density in the table is the one required for the PWN to be detected by H.E.S.S. (CTA) in 50 hours.

[‡] These parameters correspond to model 1 in figure 5.2, other models are described in the text.

observed in the Swift survey of INTEGRAL sources, but without conclusions about its origin (Malizia et al., 2007). With Chandra observations, Tomsick et al. (2009) fitted the spectrum (0.3 and 10 keV) of the source with a power-law with a photon index of $\Gamma = 1.82 \pm 0.13$. Renaud et al. (2010) discovered 31.18 ms pulsations using RXTE, as well as reported the radio detection of PSR J1400-6325 and its nebula. From the RXTE timing analysis, they obtained a period derivative for PSR J1400-6325 of 3.89×10^{-14} s s^{-1}, which implies an spin-down luminosity of 5.1×10^{37} erg s^{-1} and a characteristic age of 12.7 kyr. There are several estimations of the PWN distance, covering a range between 6 and 10 kpc. We adopt the value of 7 kpc given in Renaud et al. (2010).

Renaud et al. (2010) have studied the spectrum of G310.6-1.6, PSR J1400-6325 and its PWN from 0.8 to 100 keV. The spectrum is highly dominated by the PWN and it is fitted with a broken power-law. The energy break is located at 6 keV and it is probably produced by the synchrotron cooling of the particles. The spectral index for energies lower (higher) than the energy break is 1.90 ± 0.10 (2.59 ± 0.11). The total flux for the PWN at 20-100 keV is 5.3×10^{-12} erg s^{-1} cm^{-2}. The PWN flux in radio frequencies has also been measured, using data from the Molonglo Galactic Plane Survey (Murphy et al., 2007) at 843 MHz, as 217 ± 9.4 mJy, as well as from the Parkes-MIT-NRAO (PMN) survey (Griffith & Wright, 1993; Condon, Griffith & Wright, 1993) at 4.85 GHz, as 113 ± 10 mJy. An upper limit of 0.6 mJy at 2.4 GHz is also established by the Parkes telescope (Duncan et al., 1995). At TeV energies, G310.6-1.6 was observed by H.E.S.S. (Chaves, de Oña Wilhemi & Hoppe, 2008), but only an upper limit of 4% of the Crab Nebula was established (Khélifi et al., 2008).

The spectrum of G310.6-1.6 PWN has been previously studied by Tanaka & Takahara (2013). They assumed a magnetic fraction of 0.003, an age of 600 yr and a distance of 7 kpc. For these parameters, they obtained an injection with a low (high) energy spectral index of 1.4 (3.0) with an energy break of $\gamma_b = 3 \times 10^6$ and a magnetic field of 17 μG. They assumed a 0.3 eV cm^{-3} energy density for the FIR and NIR target photon fields.

In our case, we firstly propose a low magnetized model (model 1), where we assume that the age of the PWN is 1.1 kyr, which is consistent with the upper limit of 1.9 kyr established by Renaud et al. (2010), but older than the one considered in Tanaka & Takahara (2013). This assumption has been done also taking into account the size of the nebula and a reasonable ejected mass of 9$M_\odot$ with a SN energy of 10^{51} erg. Renaud et al. (2010) proposed a subenergetic SN of 5×10^{48} erg setting an ISM density of 0.01 cm^{-3}. This implies an ejected mass of 3$M_\odot$ to explain the size of the nebula. This mass is very low for the ejecta of a star that explodes as a SN. We also prefer to consider the canonical value for the SN explosion energy.

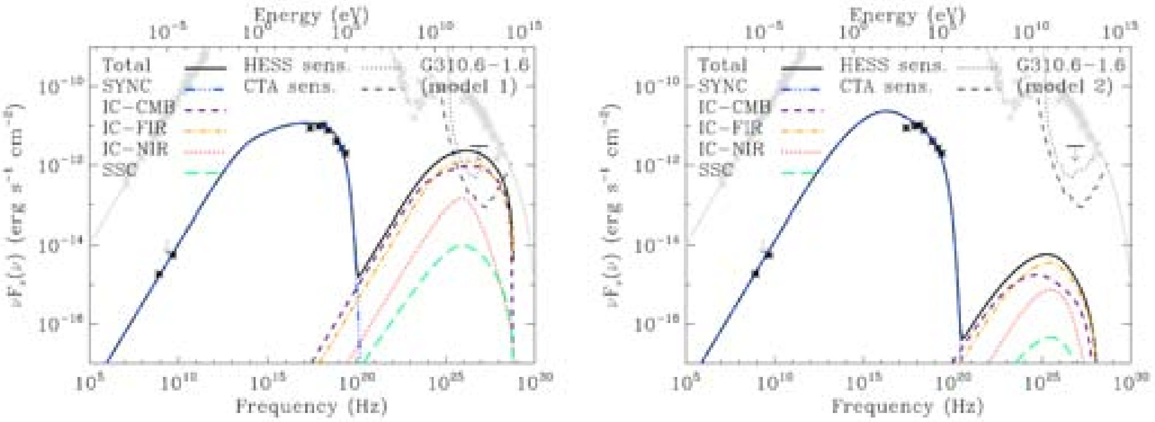

Fig. 5.1 Spectral fits for G310.6-1.6 PWN. Data points are extracted from Renaud (2009).

The target photon fields are obtained from those computed by GALPROP. The fitted black bodies of these photon fields have a temperature of 25 K and 3300 K and an energy density of 0.63 eV cm^{-3} and 1.62 eV cm^{-3} for FIR and NIR, respectively. The obtained magnetic field is 8.2 μG and $\eta = 0.0007$. The latter is the same value we find for the particle dominated models of N158A. The value of the magnetic field agrees with the lower limit of 6 μG given by Renaud et al. (2010). The intrinsic energy break of the injection in this model is located at $\gamma = 2 \times 10^6$ ($\sim$1 TeV). The injection index at low (high) energies is 1.5 (2.5).

The flux of G310.6-1.6 is a factor $\sim$4 over the H.E.S.S. sensitivity flux at 50 h of exposure time. Even with only the CMB contribution, this sensitivity is surpassed by a factor $\sim$2. If this low-η model is right, its detection is expected in a moderate exposure time with the current Cherenkov telescopes.

G76.9+1.0

G76.9+1.0 hosts the pulsar PSR J2022+3842. The period and the period derivative of this pulsar was firstly determined by Arzoumanian et al. (2011). They obtained a period of 24 ms and a period derivative of 4.3×10^{-14} s s^{-1}, which implies a spin-down luminosity of 1.2×10^{38} erg s^{-1}. This made PSR J2022+3842 the third pulsar with the highest spin-down known. In later observations with XMM-Newton, Arumugasamy, Pavlov & Kargaltsev (2013) discovered a factor 2 error in the determination of the pulsar period and period derivative. The new period is then 48 ms and the spin-down luminosity reduces to 2.96×10^{37} erg s^{-1}.

The remnant was observed in radio using the Very Large Array telescope (VLA) (Lan-

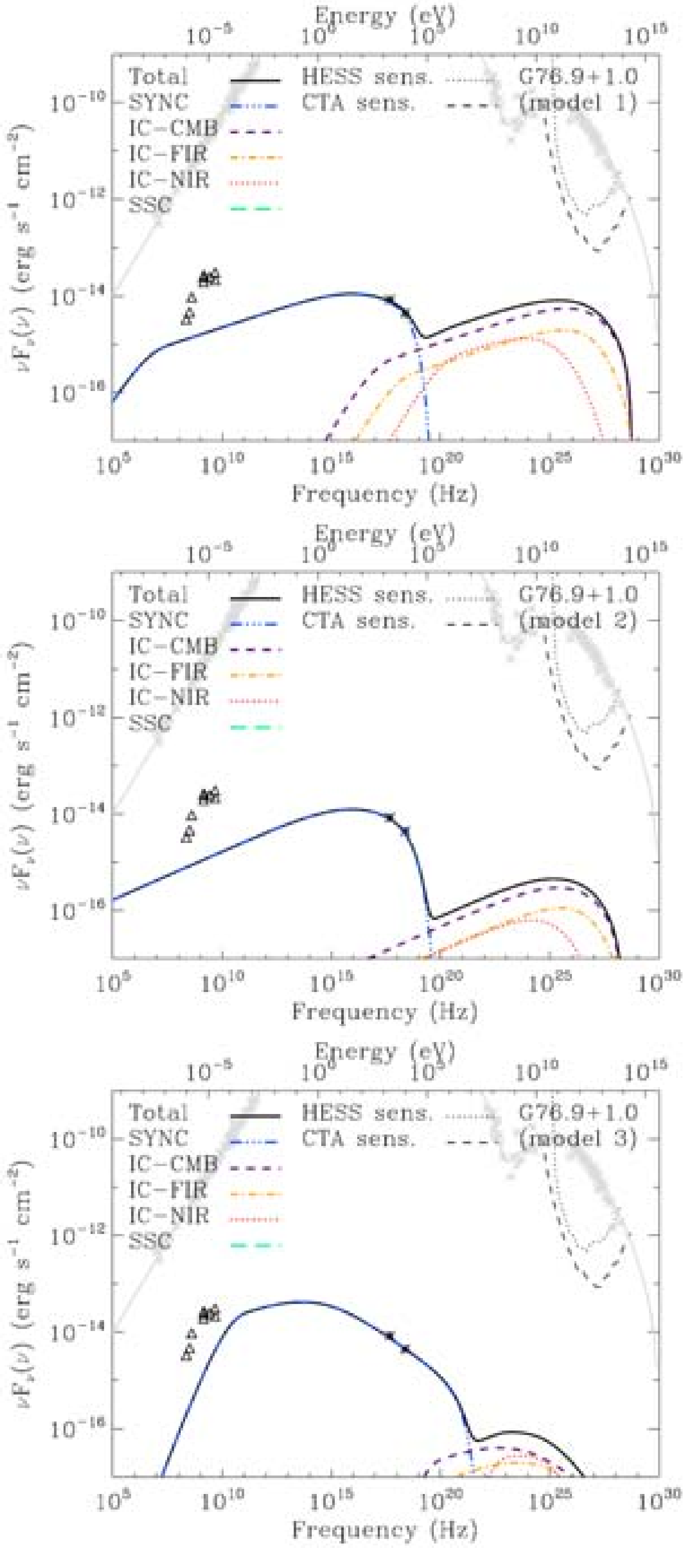

Fig. 5.2 Spectral fits for G76.9+1.0 PWN (models 1 to 3, top to bottom). The triangle data points correspond to the radio flux of the radio shell given in Landecker, Higgs & Wendker (1993), here used as upper limits. The X-ray data is obtained from Arzoumanian et al. (2011).

decker, Higgs & Wendker, 1993). These authors assume a distance of 7 kpc, which implies a size of 18×24 pc. The structure of the SNR is dominated by two lobes oriented in the north-south direction separated by 3 arcmin. The spectral index is 0.62 ± 0.04. They looked for an infrared counterpart using IRAS data but none was found. Arzoumanian et al. (2011) observed PSR J2022+3842 in X-rays using Chandra, obtaining an absorbed X-ray flux (2–10 keV) of 5.3×10^{-13} erg s^{-1} cm^{-2} and detecting a very weak PWN with an absorbed flux of 4×10^{-14} erg s^{-1} cm^{-2}. In this case, there is no TeV detection either, and we only have information about the spectrum in X-rays and upper limits in radio using the flux observed for the SNR radio shell.

We adopted an age of 5 kyr, which implies a reasonable ejected mass of 20M$_\odot$, also proposed by Arzoumanian et al. (2011). There are no estimations of the age of the remnant and of the ejected mass. Arzoumanian et al. (2011) has established an upper limit on the true age of the pulsar depending on the braking index of ∼40 kyr, which is unconstraining.

We use the data simulated by GALPROP (Porter, Moskalenko & Strong, 2006) for the energy densities and temperatures for the FIR and NIR photon fields, essentially, diluted black bodies with a temperature of 25 K and an energy density of 0.13 eV cm^{-3} for the FIR field, and a temperature of 3200 K and an energy density of 0.33 eV cm^{-3} for the NIR field. As the PWN in X-rays is very diluted, its shell cannot be distinguished. For this reason, to simulate the expansion of the nebula, we assumed a ballistic expansion of the SNR radio shell ($R_{SN} = V_0 t$) and compute the necessary ejected mass. In this case, we obtain a value of ∼20M$_\odot$, which implies a radius of ∼6.3 pc. We assume a braking index of 3, which implies a reasonable value for the initial period for PSR J2022+3842 of 32 ms.

In model 1, see table 5.1, we assume a broken power-law injection with a low-energy (high-energy) spectral index of 1.5 (2.7). The resulting energy break is at $\gamma_b = 10^3$. The magnetic field (3.5 μG) is close to the average ISM value. The magnetic fraction is 0.0017. The low value of the injection energy break in this model argues for a possible simple power-law injection. This is assumed in model 2. In this case, the spectral index is 2.6 and the magnetic field is 16.6 μG, with a magnetic fraction of 0.038. The resulting fits of these models are shown in figure 5.2.

The lack of observational data to put sufficient constrains to differenciate the models proposed. In any case, its detection at TeV energies seems unexpected.

3C 58

Our study of 3C 58 is based on the work done in Torres, Cillis & Martín Rodriguez (2013) where we have analyzed the detectability at TeV energies of this source. It was suggested to be plausibly associated with the 831-year-old supernova SN 1181 (see, e.g. Stephenson (1971); Stephenson & Green (2002)). However, recent investigations of dynamical models for the PWN (Chevalier, 2005) and the velocities of both the expansion rate of the radio nebula (Bietenholz, 2006) and the optical knots (Fesen et al., 2008) imply an age of several thousand years. This is closer to the characteristic age of the pulsar in the nebula, PSR J0205+6449 Murray et al. (2002). A recent rekindling of the low age has been put forward by Kothes (2010), based on a new estimation of the nebula distance.

3C 58 has a flat-radio spectrum with a spectral break between the radio and IR bands (Green & Scheuer, 1992). X-ray observations reveal a non-thermal spectrum that varies with radius, becoming steeper toward the outer regions (Slane et al., 2004a). PSR J0205+6449 is one of the most energetic pulsars known in the Galaxy. The pulsar powers a faint jet and is surrounded by a toroidal structure apparently associated with flows downstream of the pulsar wind termination shock (Slane et al., 2004a). The shell of the thermal X-ray emission that was seen in 3C 58, e.g., by Gotthelf, Helfand & Newburgh (2007), is smaller than the maximum extent of the PWN. Therefore, this emission is likely associated with supernova ejecta swept up by the expanding PWN rather than the original forward shock from the supernova. The pulsar has been recently detected at high-energy gamma-rays by Fermi, but only upper limits were imposed for the nebula emission (Abdo et al., 2009b). Similarly, Whipple (Hall, Wakely & VERITAS Collaboration, 2001), and both MAGIC (Anderhub et al., 2010) and VERITAS (Konopelko, 2008) observed the nebula, but only upper limits were imposed at TeV energies.

3C 58 and the Crab Nebula differ significantly both in luminosity and size. 3C 58 is larger, but less luminous, e.g., its TeV luminosity is at least $\sim$100 (Anderhub et al., 2010), its X-ray luminosity is $\sim$2000 (Torii et al., 2000), and its radio luminosity is $\sim$10 times smaller than Crab. The similarity in fact comes from morphology (e.g., Slane et al. 2004a).

PWN models for 3C 58 have been presented before by a few authors, e.g., Bednarek & Bartosik (2003, 2005); Bucciantini, Arons & Amato (2011), with some disparity in the results, particularly at the high-energy end of the spectrum. These studies use different assumptions for the primary particles assumed to populate the wind, and differ also in the treatment of the radiative physics. With 3C 58 being a candidate for observations in the current or forthcoming generation of Cherenkov telescopes, it is interesting to study under what conditions 3C 58 is observable at high energies.

We adopt a mass of the ejecta comparable to that of Crab, motivated by estimates of the total mass of the precursor (Rudie & Fesen, 2007). Not all estimates for the age and distance of 3C 58 (see Fesen et al. (2008) for a summary) can be consistently encompassed within the expansion model of the nebula. Consider first an age of $\sim$5000 years or more (as in Murray et al. (2002); Bietenholz (2006); Slane, Helfand & Murray (2002)) and a distance of 3.2 kpc (as in Roberts et al. (1993)). Following Fesen et al. (2008) for the angular size of the nebula, its physical size at that distance is 6×9.5 pc. We can extrapolate these magnitudes to the spherical case by matching the projected area of the nebula to that of a circle, and so we obtain a radius of 3.7 pc. Using the observational parameters in table 5.1 and using equation 1.29, we would, however, obtain a physical size of about 18 pc, a result that worsens for larger ages. On the contrary, if we assume the observed size and compute the ejected mass needed to have a radius of $\sim$3.7 pc, we would find an inconsistently large value. The scenario where we change the initial spin-down power is similarly problematic, since it would be impossible to reach the current $\dot{E}$, being the initial one smaller than the current power. Such innuendos are not solved by assuming a different value of braking index and are also stable (producing sizes in excess of 10 pc) for up to one order of magnitude variations in the moment of inertia I. If 3C 58 is closer to Earth, the mismatch would be larger, given that the physical size of the nebula would be smaller than at 3.2 kpc.

Consider next an 830-year-old nebula (as in Stephenson 1971; Stephenson & Green 2002) and a distance of 2 kpc (as in Kothes 2010). Geometry implies that the physical size of the nebula should be around 2.3 pc, but using the observed, derived, and assumed parameters of table 5.1 we obtain a size of 0.8 pc, a factor of three smaller. This result, similar to the larger age case above, is stable against changes in n, I, or other parameters. The only way to recover a larger nebula would be to assume a mass of the ejecta of the order of 1 $M_\odot$, but this would be inconsistent with estimates based on the observed filamentary knots (which already account for a large fraction of 1 $M_\odot$) or with evolutionary models (e.g., Rudie & Fesen (2007); Fesen et al. (2008); Bocchino et al. (2001); Slane et al. (2004a)). A larger distance to 3C 58 would imply a larger physical size of the nebula, making the mismatch more severe.

We are a priori favorable to the case of an age of 2500 years and a distance of 3.2 kpc. For this set of parameters, the size of the nebula can be easily accommodated within the model described in the previous section. Variations of the parameters in a reasonable manner maintain this conclusion stable. In addition, the shock velocity agrees with estimates coming from the thermal X-ray emission (e.g., Bocchino et al. 2001) and at the same time the swept-up mass resulting from these model parameters $M_{sw} = M_{ej}(R_{PWN}/V_0 t)^3 \sim 0.26 M_\odot$ is in line with the measurements of the mass contained in filaments (Bocchino et al., 2001; Slane et al., 2004a); i.e., we assume that the filamentary structure roughly corresponds to the swept-up shell of the ejecta. Similar conclusions have been reached by Chevalier (2004, 2005); Bucciantini, Arons & Amato (2011) with others arguments.

Multi-frequency results of our model for a 3C 58 age of 2500 years located at 3.2 kpc are shown in figure 5.3. We also show for comparison the results corresponding to the Crab Nebula at different ages, i.e., 940 (where the data points are fit with a corresponding model; see e.g. Martín, Torres & Rea 2012), 2000, and 5000 years. The differences in the data of Crab and that of 3C 58 are evident. Figure 5.3 shows results for three different assumptions regarding the dominance of the IC contribution. In the first panel, only the CMB is assumed as background for IC. The resulting parameters are given in table 5.1, and they show that a broken power law fits the current radio to X-ray data. The magnetic field of the nebula results in 35 G. The contribution of SSC to IC is sub-dominant to Bremsstrahlung under the assumption of a low medium density of 0.1 cm^{-3}. As there is no clearly detected supernova remnant shell, we cannot reliably estimate the interstellar medium density. It is impressive how low the prediction in the GeV and TeV regimes is, far beyond the reach of Fermi-LAT and Cherenkov telescopes.

Taking into account that the IR/FIR background is uncertain, we consider two limiting situations by exploring how large the energy density at 20 K should be for its corresponding IC contribution to reach the sensitivity of CTA; (Actis et al., 2011) and of the currently operating MAGIC II (Aleksić et al., 2012). The energy densities used in each panel of figure 5.3 are shown in table 5.1. The FIR energy densities range from 3 to 20 times that of the CMB. These can be compared with the typical background at that frequency from, e.g., GALPROP models to see that the case where 3C 58 appears as an in-principle-observable nebula in MAGIC II or VERITAS would be highly unexpected. In both of these cases, still, the GeV emission would be far below the Fermi-LAT upper limit.

We have explored models having different braking indices (keeping age and distance fixed at 2500 years and 3.2 kpc, respectively, as the test bed). For these models, the overall quality of the fit is unchanged; some of the fit parameters are slightly modified, however. Lower values of n imply changes in the initial spin-down power (from 9.3, to 7.3, to 5.9 × 10^{37} erg s^{-1} for n=3, 2.5, and 2, respectively), initial spin-down age (from 2897, to 4696 to 8294 years), and the PWN radius today (from 3.7 to 3.5 to 3.4 pc). The magnetic fraction changes from 0.23, for n=2, to 0.22, for n=2.5, to 0.21, for n=3. The magnetic field today has a value between 35 and 37 G in all these cases. Letting the parameter vary allows us to explore the ability of the fit to adapt to the X-ray-measured spectra better. But again we find a very small parameter dependence.

The total energetics is conserved in our model, since particles have a fraction (1-), and the magnetic field a fraction , of the total power. 3C 58 features a 21% magnetic

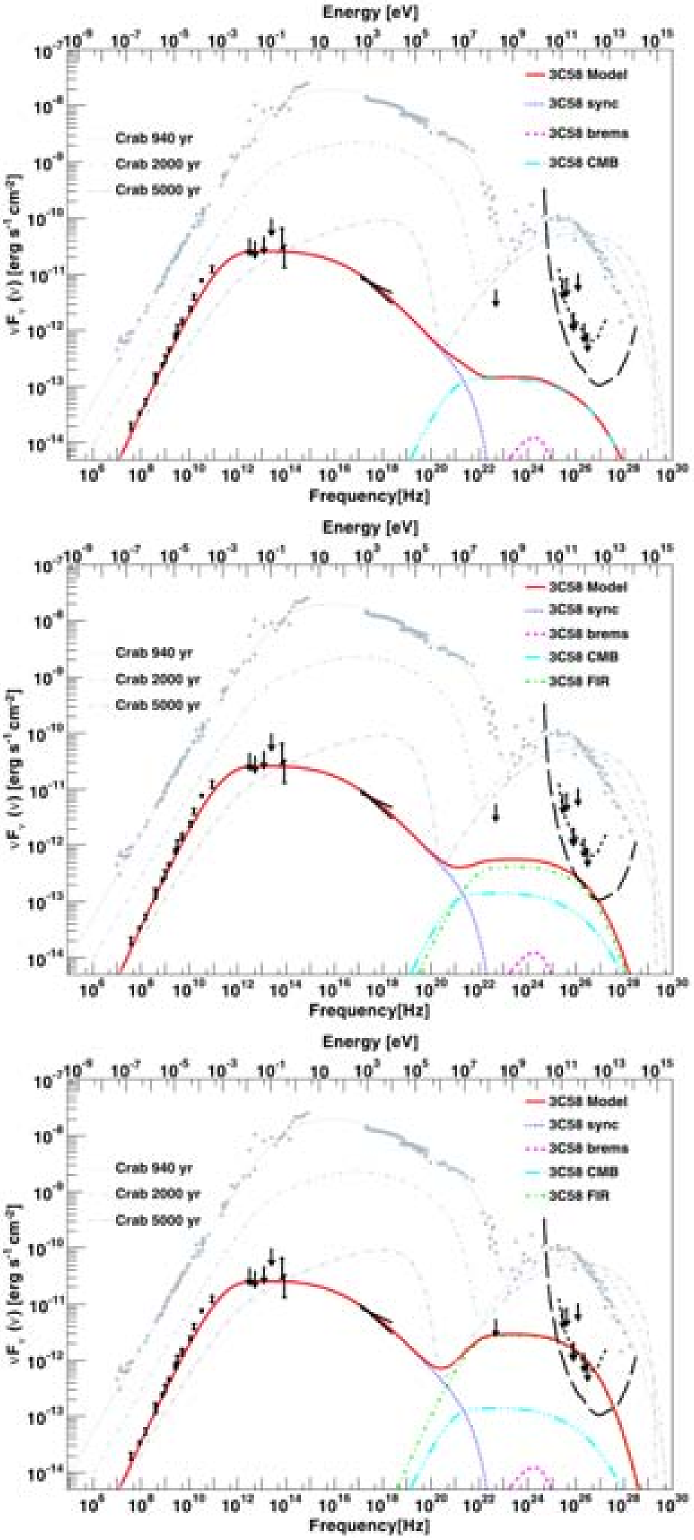

Fig. 5.3 Multi-frequency models of the PWN 3C 58 under different assumptions for the background photon fields. Top: CMB only. Middle: IR energy density up to the level where the emission of 3C 58 reaches the CTA sensitivity. Bottom: same as the middle panel, for the MAGIC sensitivity. The SSC contribution is not visible in this scale. Observational data comse from Green (1986); Morsi & Reich (1987); Salter et al. (1989) (radio); Green (1994); Slane et al. (2008) (infrared); Torii et al. (2000) (X-rays); Abdo et al. (2009b) (GeV); and Hall, Wakely & VERITAS Collaboration (2001); Konopelko (2008); Anderhub et al. (2010) (TeV).

Table 5.2 New parameters proposed for 3C58 with the TeV flux given by MAGIC.

Magnitude	Model 1	Model 2
t_{age} (yr)	2500	2000
$P(t_{age})$ (ms)	65.7	⋯
$P(t_{age})$ (s s^{-1})	1.94×10^{-13}	⋯
$_c$ (yr)	5378	⋯
$L(t_{age})$ (erg s^{-1})	2.7×10^{37}	⋯
n	3	⋯
d (kpc)	3.2	2
$_{min}$	1	⋯
$_{max}$	7.3×10^9	2.5×10^9
$_b$	8×10^4	⋯
$_l$	1.05	⋯
$_h$	2.91	3
L_0 (erg s^{-1})	9.4×10^{37}	6.8×10^{37}
$_0$ (yr)	2878	3378
$B(t_{age})$ (G)	36	22
	0.21	0.025
	0.3	⋯
$R_{PWN}(t_{age})$ (pc)	3.7	2.3
T_{CMB} (K)	2.73	⋯
w_{CMB} (eV/cm^3)	0.26	⋯
T_{FIR} (K)	25	⋯
w_{FIR} (eV/cm^3)	0.8	0.2
T_{NIR} (K)	2800	⋯
w_{NIR} (eV/cm^3)	4	1.8
n_H (cm^{-3})	0.1	⋯
E_0 (erg)	10^{51}	⋯
M_{ej} (M$_\odot$)	6	9

fraction in our model, significantly higher than the one we obtain for Crab ($\sim$3%). It is still a particle-dominated nebula. These results differ from those in Bucciantini, Arons & Amato (2011) work, where the total energy was not conserved by $\sim$30%, leading to a nebula in equipartition, and where it was said that models with energy conservation would always underpredict the radio flux.

Note the two contiguous IR measurements around 10^{14} GHz. Because of their location, it is nearly impossible to fit them both at once. Indeed, there appears to be two subsequent steepening of the spectrum, one just beyond the radio band and one additional in the IR band (see Slane et al. 2008). We have explored an injection containing another break, but results do not improve the fit significantly. We also tried to improve the fit using an injection model based on the particle in cell (PIC) simulations done by Spitkovsky (2008) keeping the ratios of the additional parameters as in Holler et al. (2012). These are not devoid of significant extrapolations and include a number of additional parameters for which we have no constraints. We used a value for the energy break of $_b = 2 \times 10^4$ to have an acceptable fit of the radio points, but it is not possible to fit the IR and X-ray points correctly, even changing the ratios of the parameters. In all these cases for the injection, the fits are of similar (two breaks power law) or lower (PIC motivated) quality than the ones presented above; and in none, the high-energy yield is significantly affected.

Recently, Aleksić et al. (2014) have claimed the detection at TeV of 3C 58 by the MAGIC telescopes. The detection has a significance of 5.7 and the flux between 400 GeV and 10 TeV is well described by a power law such that $F(E) = F_0(E/1\ \text{TeV})^{-\Gamma}$ with

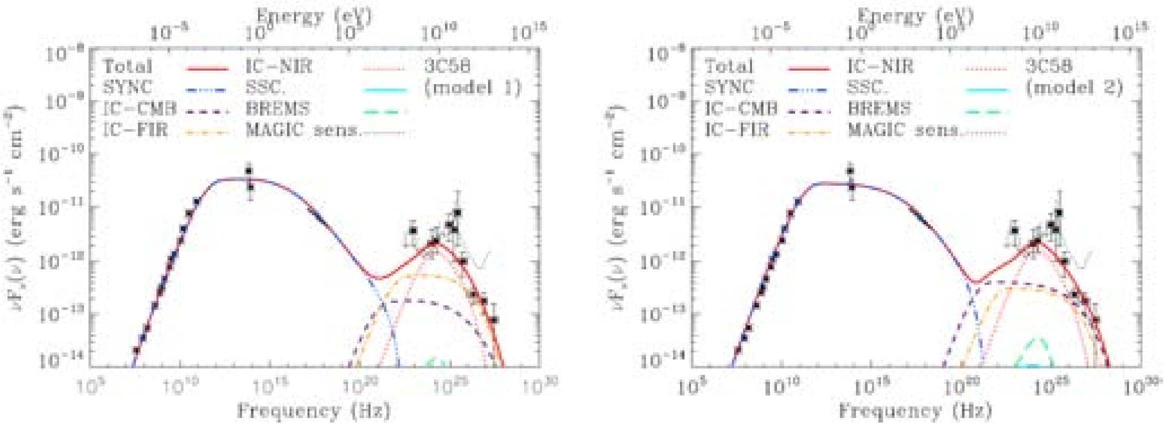

Fig. 5.4 New models for 3C 58 using the TeV flux detection by MAGIC. We include also the flux points and upper limits given by Fermi in Abdo et al. (2013).

$F_0 = 2 \times 10^{-13}$ TeV^{-1} cm^{-2} s^{-1} and $\Gamma = 2.4$. Considering this result, we propose two new models for 3C 58 in table 5.2 and show the fits in figure 5.4. In model 1, we assume the same values for distance and age as in table 5.1. Note that the ejected mass changes, because in these new fits we are taking into account spin-down luminosity variation during the expansion. We get similar values as those obtained in Torres, Cillis & Martín Rodriguez (2013), but the target photon field energy densities are readjusted to the new TeV flux. We have included a NIR contribution with an energy density of 4 eV cm^{-3} and the FIR energy density is 0.8 eV cm^{-3}, close to the energy density limit to be detected with CTA in Torres, Cillis & Martín Rodriguez (2013) (0.75 eV cm^{-3}). In model 2, we use the distance of 2 kpc given by Kothes (2010), but assuming an age of 2 kyr. In this case, the physical radius of the nebula is 2.3 pc. The magnetic field obtained to fit the synchrotron spectrum is 22 μG and the magnetic fraction is 0.025. This latter value for the magnetic fraction fits better with the trend of low-magnetized nebula observed in Torres et al. (2014). The energy densities for the FIR and NIR photon fields are lower than in model 1 (0.2 and 1.8 eV cm^{-3}, respectively). We have assumed the fiducial value of 0.1 cm^{-3} for the ISM density to compute the Bremsstrahlung contribution, but it is neglectable in both models.

G292.2+1.8

As stated in the introduction, the pulsars related with G54.1+0.3 and G292.0+0.18 both have a period of ~135 ms, period derivative of $\sim 7.5 \times 10^{-13}$, a spin-down power of 1.2×10^{37} erg s^{-1}, a characteristic age of ~2900 years and a distance of ~6 kpc. For both pulsars, the braking index is unknown.

The radius of G292.0+0.18 is based on the SNR size of 8' diameter (Gaensler & Wallace, 2003), which means a physical radius of 3.5 pc. The distance estimate is based on the HI absorption profile given by Winkler et al. (2009). Based on measurement of the transverse motions of the filaments of the SNR and assuming that the shell is expanding with transverse expansion velocity, Winkler et al. (2009) estimated an age between 3000 and 3400 years, concurring with Gaensler & Wallace (2003). The ejected mass of the SN explosion was estimated as $\sim$6 $M_\odot$ (Gaensler & Wallace, 2003).

Radio observations for the nebula were obtained from the work of Gaensler & Wallace (2003). The flux of the nebula in X-rays was measured by Chandra (Hughes et al., 2001). The photon index of the X-ray spectra, as it is suggested in Hughes et al. (2001), is considered the same as that of the pulsar. At GeV energies, we only have upper limits from Fermi-LAT (Ackermann et al., 2011). Optical and near infrared observations were obtained for the torus of the nebula, by Zharikov et al. (2008) and Zharikov et al. (2013), respectively, but these are not considered in our fits, since do not include the entire system. The background energy densities are unknown. We assume those given by GALPROP, for which the equivalent temperatures and densities of the representing blackbodies are $T_{FIR} = 25$ K, $w_{FIR} = 0.42$ eV cm^{-3}, and $T_{NIR} = 2800$ K, $w_{NIR} = 0.70$ eV cm^{-3}.

Figure 5.5 shows two models that fit the radio and the X-ray data for this nebula. In both cases the age of the system is 2500 years, and the ejected mass is 9 $M_\odot$. In model 1 (see figure 5.5), we consider a low magnetic fraction model with =0.05, which is 10 times larger than the magnetic fraction obtained in our model for G54.1+0.3 in Torres et al. (2014). This model predicts that the nebula will be seen by CTA, and it would reach H.E.S.S. sensitivity if the FIR energy density reaches 2 eV cm^{-3}. The TeV flux would be only a factor $\sim$2 lower than the H.E.S.S. sensitivity limit in 50 h exposure time. We obtain a magnetic field of 21 G with an injection intrinsic break of $_b = 10^5$ ($\sim$51 GeV), with a low (high) energy index of 1.5 (2.55). These parameters differ from the ones obtained for G54.1+0.3 in Torres et al. (2014) (B=14 G, $_b = 5 \times 10^5$, $_1 = 1.2$, $_2 = 2.8$). With this model, the difference in the magnetic fraction, the energy densities of the IC target photon fields and the age of the system explain why we observe G54.1+0.3 and not G292.0+1.8, even when both are particle dominated.

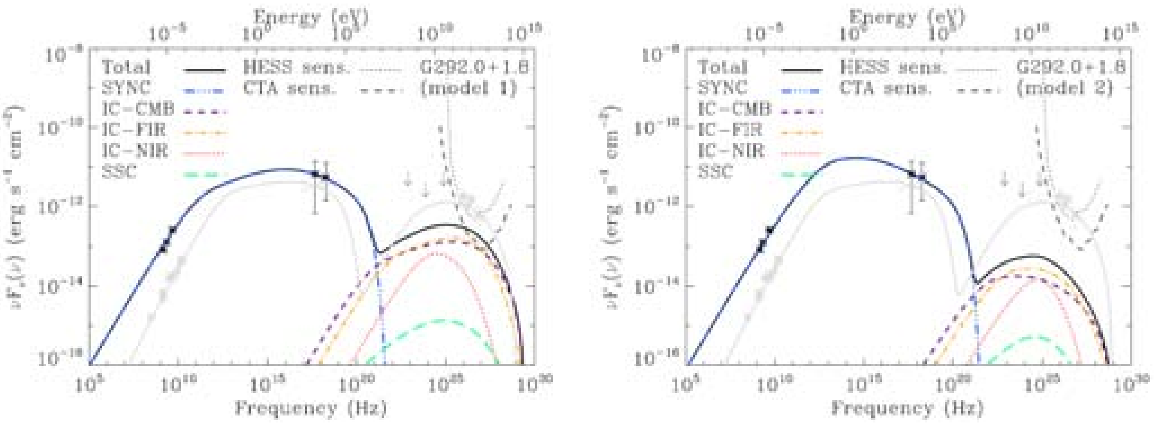

Fig. 5.5 Spectral fits for G292.0+1.8 PWN. Data points for G292.0+1.8 are obtained from Gaensler & Wallace (2003) (radio), Hughes et al. (2001) (X-rays) and Ackermann et al. (2011) (Fermi upper limits). In grey, we show the model and data for G54.1+0.3 extracted from Torres et al. (2014) (also shown in chapter 4).

5.2 Non-Galactic PWNe at TeV energies

N157B

N157B is located in the LMC and it was the first extragalactic PWN detected in gamma rays (H.E.S.S. Collaboration et al., 2012). Its pulsar, PSR J0537-6910, has a spin-down power of 4.9×10^{38} erg s^{-1} (Manchester et al., 2005). Lazendic et al. (2000) did radio observations of this PWN using the Australia Telescope Compact Array (ATCA), obtaining a spectral index of ∼0.19. Micelotta, Brandl & Israel (2009) did infrared observations using the Spitzer telescope but reported no infrared counterpart (no bright SNR). Studying the gas and dust properties of the vicinity, they deduced that the mass of the progenitor star should not be higher than 25M$_\odot$. In X-rays, N157B was observed with ASCA and ROSAT (Wang & Gotthelf, 1998), and4 (Wang et al., 2001) detected the PWN with Chandra. Chen et al. (2006) analyzed the spectrum of N157B and the pulsar PSR J0537-6910 in X-rays. The spectrum of the entire remnant is fitted with a dominant non-thermal component (a power-law with a spectral index of 2.29 and an unabsorbed flux of 1.4×10^{-11} erg s^{-1} cm^{-2}) and a thermal component (a NEI model with a temperature of 0.72 keV and an unabsorbed flux of 7×10^{-12} erg s^{-1} cm^{-2}).

In our study, we use the estimated distance of 48 kpc, see H.E.S.S. Collaboration et al. (2012). There are two gas bubbles in the vicinity of N157B which contribute to the far-infrared (FIR) photon fields: 30 Doradus complex and the OB association LH99. From the infrared observations done by Indebetouw et al. (2009), H.E.S.S. Collaboration et al. (2012)

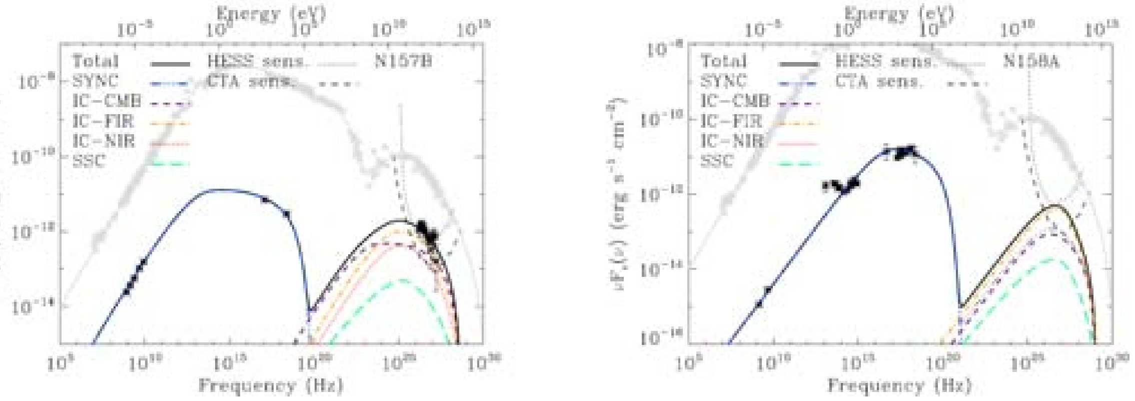

Fig. 5.6 PWNe in the LMC. Right panel: Spectral fit for the N157B PWN. The fluxes and the fit of the Crab Nebula are overplotted in grey for comparison. We plot also the sensitivity curves of H.E.S.S. and CTA for an exposure time of 50 hours. The data points are obtained from: Lazendic et al. (2000) (radio), Chen et al. (2006) (X-rays), H.E.S.S. Collaboration et al. (2012) (VHE). Left panel: Spectral fit for the N158A PWN to reach H.E.S.S. (in solid black) and CTA (in triple-dot dashed grey) sensitivities. The data points are obtained from: Manchester, Staveley-Smith & Kesteven (1993) (radio), Mignani et al. (2012) (infrared & optical), Kaaret et al. (2001); Campana et al. (2008) (X-rays).

modelled the infrared emission as a black body with energy density of 8.9 eV cm^{-3} and a temperature of 88 K for the LH99 association, and 2.7 eV cm^{-3} and 80 K for 30 Doradus. They consider these values as an upper limit since the unprojected distance between these objects is unknown.

Figure 5.6 (left panel) shows the fit we obtain for N157B. We assume the radius for the PWN given by Lazendic et al. (2000), i.e., 10.6 pc for a distance of 48 kpc. The PWN shell is not very well defined and some small contribution of the SNR could be included. In this first model, we assumed an age of 4600 yr, which is consistent with the Sedov age of the SNR given by Wang & Gotthelf (1998) ($\sim$5 kyr) and an ejected mass of 20M$_\odot$, corresponding to the lower limit in the ejected mass given by Chen et al. (2006). The electron injection has a low (high) energy index of 1.5 (2.75) and the energy break is located at $= 10^6$ ($\sim$511 GeV). From the synchrotron part of the spectrum, we inferred a magnetic field of 13 G and a magnetic fraction of 0.006. The energy density of the target photon fields, enhanced due to the near presence of LH99 and 30 Doradus, results in our fits much below the upper limits given by H.E.S.S. Collaboration et al. (2012), i.e., 0.7 and 0.3 eV cm^{-3}, respectively.

If instead we assume the energy densities given by H.E.S.S. Collaboration et al. (2012), we need to consider a lower age of 2.5 kyr to fit the TeV data. Considering the lower limit on the ejected given by Chen et al. (2006), then the radius decreases until 3.7 pc. Regarding the synchrotron spectrum, the magnetic field reaches 35 G and =0.01. The intrinsic energy break changes to $_b = 2 \times 10^5$ ($\sim$102 GeV) and the injection slopes change slightly ($_1$=1.5, $_2$=2.6). The value obtained for the radius in the latter model is only $\sim$50% higher than the radius observed in X-rays. This difference is small in comparison with other cases. For example, for the Crab nebula, we see that the radius in the radio band is $\sim$2 pc and in X-rays $\sim$0.6 pc. As the shell is not well defined, the radius measured by Lazendic et al. (2000) could include parts of the remnant, but the relation between the PWN radius in X-rays and the radius in the radio band seems to be more similar to the Crab nebula case. van der Swaluw (2004) suggested that N157B PWN could be interacting with the reverse shock of the SNR in a very initial phase, explaining its elongated morphology. In any case, we find that N157B is a luminous particle dominated nebula.

N158A

N158A, known as the Crab twin, is also located in the LMC but has not been detected at TeV yet. This PWN is powered by the pulsar PSR B0540-69, which has been observed in radio, infrared, optical and X-ray bands. The period of this pulsar is 50.5 ms (Seward, Harnden & Helfand, 1984) and the period derivative is 4.7×10^{-13}s s^{-1} (Livingstone, Kaspi & Gavriil, 2005). The resulting spin-down luminosity is then 1.5×10^{38} erg s^{-1}. The diameter of N158A is 1.4 pc, as obtained from radio observations (Manchester, Staveley-Smith & Kesteven, 1993). The distance to PSR B0540-69 has been estimated as $\sim$49 kpc (Seward, Harnden & Helfand, 1984; Taylor & Cordes, 1993; Slowikowska et al., 2007). An age of 760 yr is deduced through measurements of the expansion velocity of the SNR shell in the optical spectral range (Reynolds, 1985; Kirshner et al., 1989). There is no observational measurement of the ejected mass in N158A, and we have left this parameter free in our model. The resulting ejected mass in our fits is 25M$_\odot$. According to Heger et al. (2003), this mass is at the limit for neutron star creation, which can grow with the quantity of helium in the core of the star and the energy of the supernova explosion. In the infrared, Caraveo et al. (1992) did a high-resolution observation of N158A using the European Southern Observatory New Technology Telescope (ESO-NTT) and concluded that the progenitor of the SNR could have belonged to the same generation of young stars in 30 Doradus (Caraveo et al., 1992; Kirshner et al., 1989). Williams et al. (2008) did not find evidence of infrared emission from the SNR, but they inferred a mass of 20–25M$_\odot$ for the progenitor star. PSR B0540-69 is one of the few pulsars with optical pulsations and polarized emission. Its optical spectrum is well fitted by a power-law, but joining it with the X-ray spectrum, a double break is required (Mignani et al., 2012). The braking index for PSR B0540-69 is 2.08 (Kaaret et al., 2001). A high-resolution X-ray observation was done with Chandra (Gotthelf & Wang, 2000; Kaaret et al., 2001) and there is also a compilation of the observations done with RXTE, Swift and INTEGRAL in the work by Campana et al. (2008). The flux obtained for the PWN is $\sim 8 \times 10^{-11}$ erg s^{-1} cm^{-2}. There is no detection of the PWN at VHE.

For N158A, the injection spectrum resulting from our fit is a broken power-law with break at a large energy $= 3 \times 10^{7}$ ($\sim$15.3 TeV) and a low (high) energy spectral index of 1.8 (2.6). The synchrotron component is fitted with a magnetic field of 32 G. The magnetic fraction in this case is low ($= 0.0007$). Due to the lack of information on the FIR and NIR fields, we assume a FIR field with a temperature of 80 K and compute the energy density needed for the PWN to be detected by H.E.S.S. or CTA. For H.E.S.S., a minimum energy density of 5 eV cm^{-3} is required to be detected in a 50 hours observation, according to the sensitivity curve used here. For CTA, an energy density of 0.2 eV cm^{-3} would be enough to allow detection, which foresees its identification in case our model is correct. Both models are shown in figure 5.6 (right panel) and their parameters are given in table 5.1.

The NIR photon field could also be important depending on the density of nearby stars in the N158A field and could enhance the TeV yield, at the same time reducing the required FIR densities for detection.

We conclude that N158A is a particle dominated nebulae that has been undetected because of sensitivity limitations.

5.3 High magnetization models for non-detected at TeV PWNe

According to the phase space exploration done in Torres et al. (2013), PWNe with high magnetic fractions would lead to dim X-ray PWNe and they could explain also very low fluxes at VHE for PWNe which are bright from radio to X-rays. The lack of detection of some of the cases explained in the previous sections have motivated considering alternative models in this direction (Martín et al., 2014).

For G310.6-1.6, the lack of observational constraints allows considering an alternative model in which the nebula has a magnetic fraction of $= 0.98$, well beyond equipartition. In this case (model 2, see figure 5.1), the energy break moves to higher energies ($= 6 \times 10^{6}$ or $\sim$3 TeV) and the magnetic field increases up to 306 G. Model 2 explains also well the overall X-ray flux, but fails in reproducing the break at 6 keV.

In the case of G76.9+1.0, model 3 explores whether G76.9+1.0 could be a highly magnetic PWN as speculated previously by Arzoumanian et al. (2008, 2011). We show an example with a magnetic field of 85.2 G and a magnetic fraction of $= 0.998$. The injection function in this case is a simple power-law with an spectral index of 2.65. In order to respect the upper limits in radio, we need to impose a minimum energy at injection for particles of $= 10^4$ ($\sim$5.1 GeV). The IC contribution decreases with respect the other models, as expected due to the lower contribution of spin-down energy to particles and the larger synchrotron field, which maximizes their losses.

The radio and X-ray data are also compatible with a high- model for G292.0+1.8 (see figure 5.5, model 2) with $= 0.77$ and a resulting magnetic field of 81 G (similar to the Crab Nebula). The injection in this case has an energy break of $_b = 2.5 \times 10^5$ ($\sim$130 GeV) and the high energy spectral index changes slightly (2.5). In this case, G292.0+1.8 would not be detected even with CTA also explaining the difference with G54.1+0.3. A deep TeV observation will distinguish between these two models.

We have also investigated highly magnetized models in which the detection of N158A is not possible even with CTA, unless the energy density of the FIR increases up to $\sim$500 eV cm^{-3} (assuming that there is no NIR contribution). The injection function in such models has an energy break of $_b = 6 \times 10^7$, and a low (high) spectral index is 1.45 (2.4). Taking into account that the maximum energy at injection is $_{max} = 1.2 \times 10^8$, a simple power-law model with an index of 1.45 could also be compatible with this fit. Here, we obtain a highly magnetized nebula with a magnetic fraction of 0.9 and an extreme magnetic field of 1.15 mG. But whereas the radio and the infrared data are fitted similarly well to particle dominated models, the predicted X-ray flux of these models is not quite in agreement with data. This fact and the extreme values of the parameters we have just quoted make a high model unlikely. In equipartition (i.e., $= 0.5$), the radio and X-ray flux surpasses the data flux in a factor $\sim$4. In this latter case, the magnetic field is lower (B=858 G), but the number of particles is still high to fit the flux.

5.4 Conclusions

Despite having similar spin down, the value of the magnetic field differs from one to another PWN not only because of the value of ($B \sim {}^{1/2}$) differs, but also because their size does ($B \sim R_{PWN}^{-3/2}$). Models with high values of would explain the low efficiency of some PWNe at X-rays and make them undetectable at VHE. However, we here found that models with high magnetic field and fraction can be constructed only for some of the nebulae that are non-detected at TeV, at the price of stretching other parameters. They seem to work worse than particle dominated models in general, and remain viable only for G76.9+1.0 (for which there are significantly less observational constraints) and G310.6–1.6 (pending the scrutiny of deeper TeV observations). These are the specific conclusions.

- We propose a model for 3C 58 considering a distance of 3.2 kpc, which implies a physical radius of 3.7 pc. The magnetic fraction necessary to fit the radio and X-ray data is 0.21, which is higher than the general trend seen in chapter 4, with the exception of CTA-1. The energy density of the FIR target photon field should be $\sim$5 eV cm^{-3} to be detected by MAGIC in a 50 h observation. In the case of CTA, this reduces to $\sim$0.75 eV cm^{-3}. which makes 3C 58 PWN a good candidate to be detected with the current Cherenkov telescopes. These estimations are pesimistic since they do not consider NIR contribution, which can be also important.

- We propose a low magnetization model for N157B with an age of 4.6 kyr and a magnetic field of 13 G. The size of the nebula is compatible with the one given by Lazendic et al. (2000), the age with the Sedov age of the remnant (Wang & Gotthelf, 1998) and the ejected mass with the lower limit given by Chen et al. (2006). A high magnetization model (> 0.5) does not agree with the detection of N157B at TeV energies, which would imply FIR and NIR energy densities much higher than the upper limits obtained by H.E.S.S. Collaboration et al. (2012).

- N158A non-detection seems to happen because of its smaller age (perhaps also because of a lower photon background?) rather than by having a large magnetization. If this is the case, it will certainly be detected with CTA and likely also by the current generation of instruments. Indeed, just the CMB inverse Compton contribution would produce a CTA source. Without taking into account a possible significant NIR contribution which would ease the required observation time, we find that if N158A is subject to a FIR energy density of 5 eV cm^{-3}, it can already lead to a detection by H.E.S.S. in 50 hours (lower IC target fields leads to larger integration times, but still within plausible limits). The high- model(s) explored for N158A has been disregarded as unlikely due to inability to produce a good match to the X-ray data.

- G76.9+1.0 is subject to a large uncertainty given the lack of sufficient observational constraints (only X-ray data are available). This leads to the possibility of accommodating both extremes in the magnetic fraction phase space. In none of the cases, a TeV detection is expected and it will be difficult to differentiate among models. The injection of particles is inefficient at high energies or the energy that goes to particles is so low that the energy density for the FIR and NIR target fields necessary to reach the CTA sensitivity would be more than a factor 100 in comparison with those obtained by GALPROP for model 1, and more than a factor 1000 for model 2. In such case, the inverse Compton contribution at X-ray energies would make impossible to fit the spectral slope. Other important parameters as age or the radius of the nebula are not well determined and are necessary to make a solid conclusion.

- The low- models for G310.6–1.6 and G292.0+1.8 predict their detection with H.E.S.S. given sufficient integration time. The CMB inverse Compton contribution reaches the sensitivity curve of a 50 hrs observation in the case of G310.6–1.6. The magnetic fraction for G292.0+1.8 is one order of magnitude higher than the one obtained for G54.1+0.3 in Torres et al. (2014). This fact and the slight difference in the FIR and NIR energy densities considered in both cases, could explain the lack of detection of G292.0+1.8 at TeV. In both cases, radio and X-ray data are also explained with a high- model with a magnetic field of 306 G for G310.6–1.6 and 81 G for G292.0+1.8. However, the high- model for G310.6–1.6 is not preferred due to its inability to correctly reproduce the spectral break at 6 keV. For G292.0+1.8 instead, a high- model remains viable and TeV observations would solve the degeneracy.

Chapter 6

Comparing supernova remnants around strongly magnetized and canonical pulsars

As we already commented in chapter 1, the formation mechanism of magnetars is still not clear. The alpha-dynamo model suggested by Duncan & Thompson (1992) would imply an excess of rotational energy release (with respect to normal pulsars) the effects of which could in principle be observed in the SNRs. Vink & Kuiper (2006) started the idea of studying the energetic of supernova remnants surrounding magnetar with the aim of disentangling a possible energetic difference between SNRs associated with magnetars and others surrounding normal pulsars. Their work did not find any clear evidence i.e. of an additional energy released in the remnant possibly due to an excess of rotational energy at birth.

Following this study we decided to extend their work re-analysing all available *XMM-Newton* or *Chandra* data of all confirmed and bright SNRs associated with magnetars, and to to a high-*B* pulsar that showed magnetar-like activity, and comparing in a coherent and comprehensive way all the extracted properties of these SNRs with other remnants: in particular line ionization and X-ray luminosity.

6.1 Data analysis and reduction

In this work, our approach has tried to be as conservative and model independent as possible. In particular, our target sample has been chosen such to include all confirmed associations (see the McGill catalog[1] for all proposed associations), and among those, we chose only those supernova remnants bright enough, and with sufficiently good spectra, to perform a detailed analysis and classification of their spectral lines. We analyze the X-ray spectral lines of four SNRs hosting a neutron star that showed magnetar-like activity in its center: Kes 73, CTB 109, N 49 and Kes 75. We use for all targets the best available archival data: from the *XMM-Newton* telescope in the case of Kes 73, CTB 109 and N 49, and *Chandra* for Kes 75. The observations used are summarized in table 6.1. To compare coherently all the spectral lines and fluxes we observed for these remnants we have chosen to use an empirical spectral fitting for all SNRs. We have modeled all spectra using one or two Bremsstrahlung models for the spectral continuum, plus gaussian functions for each detected spectral line. The producedure to detect a line consist in fitting firstly the continuum with the Bremsstrahlung components and then add gaussian to fit the most important lines (those visible by eye). Finally we add lines where the spectrum is worst fitted and see if this improves the fit and the centroid energy coincides with any known X-ray line. This approach is totally empirical, with respect of using more detailed ionized plasma models, but ensures a coherent comparison between different remnants.

XMM-Newton data

We use images in full-frame mode obtained from the European Photon Imaging Camera (EPIC) PN (Strüder et al., 2001) and MOS (Turner et al., 2001). The spectra of these images are fitted simultaneously in order to obtain the spectrum with the maximum possible number of counts. We used the specific software for *XMM-Newton* data, Science Analysis System (SAS) v13.5.0 with the latest calibration files. To clean images of solar flares, we used the SAS tool *tabtigen* to choose the good time intervals and extract them and the spectra with *evselect*. Source and background spectra were extracted from each single image with pattern ≤ 4 for PN images and pattern ≤ 12 for MOS. The spectra and the backgrounds corresponding to the same regions were merged using the FTOOLS routine *mathpha* and we compute the mean of the response matrices (RMF) and the ancillary files (ARF) weighted by the exposure time using the tools *addrmf* and *addarf*. Finally, we binned the spectra demanding a minimum of 25 counts per bin to allow the use of χ^2-statistics .

We analyze the spectrum of each nebula considering its entire extension. For Kes 73, the nebula is completely covered in the EPIC PN, MOS 1 and MOS 2 detectors and we consider all of them in the analysis. In the case of CTB 109, the SNR is too large to be included entirely in a single pointing. The images with the *XMM-Newton* data ID: 0057540101,

---

[1] http://www.physics.mcgill.ca/ pulsar/magnetar/main.html

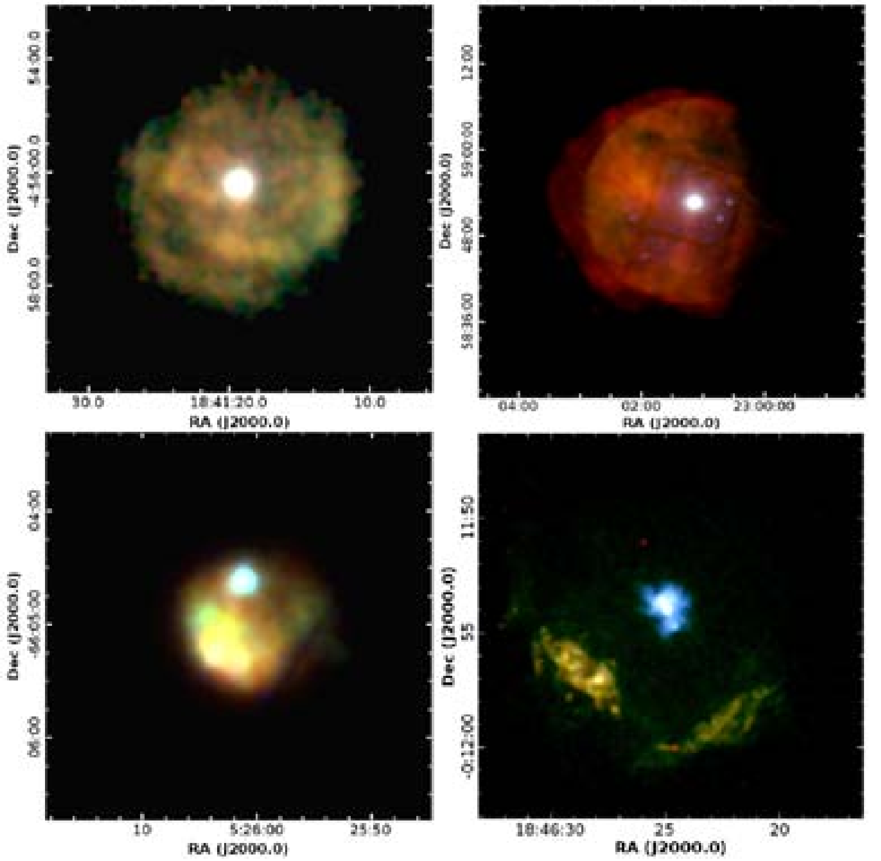
Dec (J2000.0)
54:00.0
-4:56:00.0
58:00.0
30.0
18:41:20.0
10.0
RA (J2000.0)
Dec (J2000.0)
12:00
59:00:00
48:00
58:36:00
04:00
02:00
23:00:00
RA (J2000.0)
Dec (J2000.0)
04:00
-66:05:00
06:00
10
5:26:00
25:50
RA (J2000.0)
Dec (J2000.0)
11:50
55
-0:12:00
18:46:30
25
20
RA (J2000.0)

Fig. 6.1 Combined color images of Kes 73 (top-left), CTB 109 (top-right), N49 (bottom-left) and Kes 75 (bottom-right).

Table 6.1 Observations used in this work.

SNR	Instrument	ObsID	Date	Detector	Exp. (s)
Kes73	XMM	0013340101	2002-10-05	PN	6017
				MOS1	5773
				MOS2	5771
		0013340201	2002-10-07	PN	6613
				MOS1	6372
				MOS2	6372
CTB 109	XMM	0057540101	2002-01-22	PN	12237
				MOS1	19027
				MOS2	19026
		0057540201	2002-07-09	PN	14298
				MOS1	17679
				MOS2	17679
		0057540301	2002-07-09	PN	14011
				MOS1	17379
				MOS2	17379
N49	XMM	0505310101	2007-11-10	PN	72172
Kes75	Chandra	748	2000-10-15	ACIS-S	37280
		6686	2006-06-07	ACIS-S	54070
		7337	2006-06-05	ACIS-S	17360
		7338	2006-06-09	ACIS-S	39250
		7339	2006-06-12	ACIS-S	44110

0057540201 and 0057540301 correspond to south, north and east pointings of the remnant. We computed the spectra of each pointing excluding those regions which are repeated in two or more images and we take into account them just once. In this case we also considered the EPIC PN, MOS 1 and MOS 2 cameras. For N 49, the exposure time of the MOS detectors is very low in comparison with PN. For this reason, we rejected to use the MOS data to avoid statistical noise in the data.

Chandra data

In the case of Kes 75, the best available observations were performed with *Chandra* using the Advanced CCD Imaging Spectrometer (ACIS). The ID numbers of the data used are in table 6.1. We used the standard reduction software for *Chandra*, the Chandra Interactive Analysis of Observations (CIAO) v4.5. The spectra and the backgrounds were extracted using the routine *specextract* and the RMFs and ARFs using *mkacisrmf* and *mkwarf* respectively. Finally, we combine the spectra demanding a minimum of 25 counts per energy bin

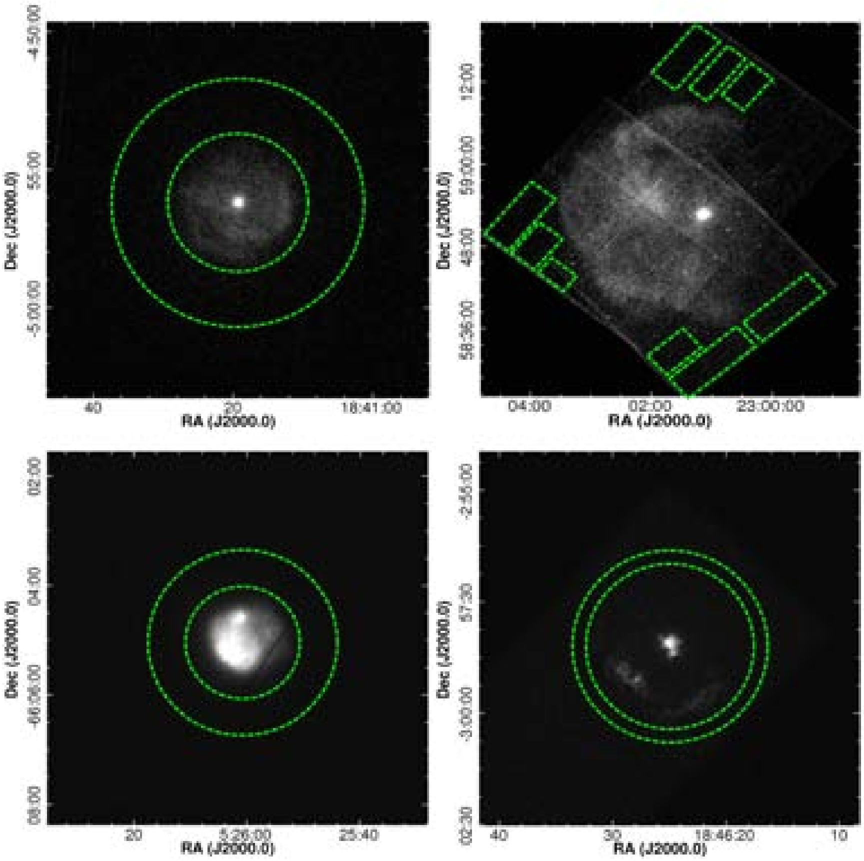
-4:50:00
55:00
-5:00:00
Dec (J2000.0)
40
20
18:41:00
RA (J2000.0)
12:00
59:00:00
48:00
58:36:00
Dec (J2000.0)
04:00
02:00
23:00:00
RA (J2000.0)
02:00
04:00
-66:06:00
08:00
Dec (J2000.0)
20
5:26:00
25:40
RA (J2000.0)
-2:55:00
57:30
-3:00:00
02:30
Dec (J2000.0)
40
30
18:46:20
10
RA (J2000.0)

Fig. 6.2 Map of the backgrounds used in the spectrum analysis. The order of the images is the same as in figure 6.1.

using *combine_spectra*.

6.2 Spectral analysis and results

We report the fitted spectra in figure 6.3, while reporting the best fitting models and relative parameters in tables 6.2 and 6.3. For the spectral analysis, we used the program *XSPEC* (Arnaud, 1996) v12.8.1 from the package *HEASOFT* v6.15. As anticipated above, we have used for all SNRs a spectral model comprising of photo-electric absorption (`phabs`), one or two Bremsstrahlung models (`bremss`), plus a series of Gaussian function to model the emission lines. Even if more physical ionized plasma models such a `vnei`, `vshock` or `vpshock` could be used to fit those SNRs: e. g., Kumar et al. (2014) for Kes 73, Sasaki et al. (2013) for CTB 109, Park et al. (2012) for N 49 and Temim et al. (2012) for Kes 75; we prefer to use a more empirical approach to compare coherently the emission lines and luminosities of those objects, which is the aim of our work. Below we summarize for each studied remnant our results in the contest of the general property of the SNR.

Kes 73

Kes 73 (also known as G27.4+0.0) is a shell-type SNR. Its dimensions are about 4.7 $\times$ 4.5 and it is located between 7.5 and 9.8 kpc (Tian & Leahy, 2008a). The central source is the magnetar AXP 1E 1841$-$045 discovered as a compact X-ray source with the Einstein Observatory (Kriss et al., 1985), and confirmed as a magnetar in Vasisht & Gotthelf (1997); Gotthelf, Vasisht & Dotani (1999). The period of the magnetar is 11.78 s and its period derivative 4.47 $\times 10^{-11}$ s s^{-1}. The resulting dipolar magnetic field is 7.3 $\times 10^{14}$ G, the spin-down luminosity 1.1 $\times 10^{33}$ erg s^{-1} and the characteristic age 4180 yr. The age of the SNR shell is estimated around 1300 yr (Vink & Kuiper, 2006), which is consistent with the age between 750 and 2100 yr estimated by Kumar et al. (2014). Kes 73 has been also observed by *ROSAT* (Helfand et al., 1994), *ASCA* (Gotthelf & Vasisht, 1997), *Chandra* (Lopez et al., 2011) and *Suzaku* (Sezer et al., 2010).

Kes 73 shows a quite spherical structure with the magnetar AXP 1E 1841-045 in the center of the remnant (see figure 6.1). In the western part of the nebula (right-hand side of the images), we distinguish a shock ring which enclose the central source from west to east of the image passing below the central source. Most of the flux is emitted between 1 and 3 keV. Finally, we analyzed the total spectrum of the nebula excluding a circle of 40” around the central source to exclude possible contamination from the central object. The background spectrum has been extracted from a surrounding annular region shown in figure 6.2, avoiding gaps between the CCDs to ensure good convergence of the response matrices. The spectrum is highly absorbed in the range between 0.3 and 1 keV. The continuum spectrum has been fitted with two plasmas with temperatures of 0.43 keV and 1.34 keV. The The absorption column density obtained is $N_{\rm H} = 2 \times 10^{22}$ cm^{-2}. We detected 6 lines. The most prominent is the Fe XXV at 6.7 keV with an equivalent width (EW) of 1.89 keV. Other lines are Mg XI at 1.35 keV (EW=95 eV), Si XIII at 1.85 keV (EW=0.37 keV), Si XIII at 2.19 keV (EW=46 eV), S XV at 2.45 keV (EW=0.38 keV) and Ar XVII at 3.13 keV (EW=0.12 keV).

CTB 109

CTB 109 (also G109.2-1.0) was discovered in X-rays with the Einstein Observatory by Gregory & Fahlman (1980), it is 30 $\times$ 45 wide and the estimated distance is about 3 kpc (Kothes, Uyaniker & Yar, 2002). The central source is the magnetar AXP 1E 2259+586 with

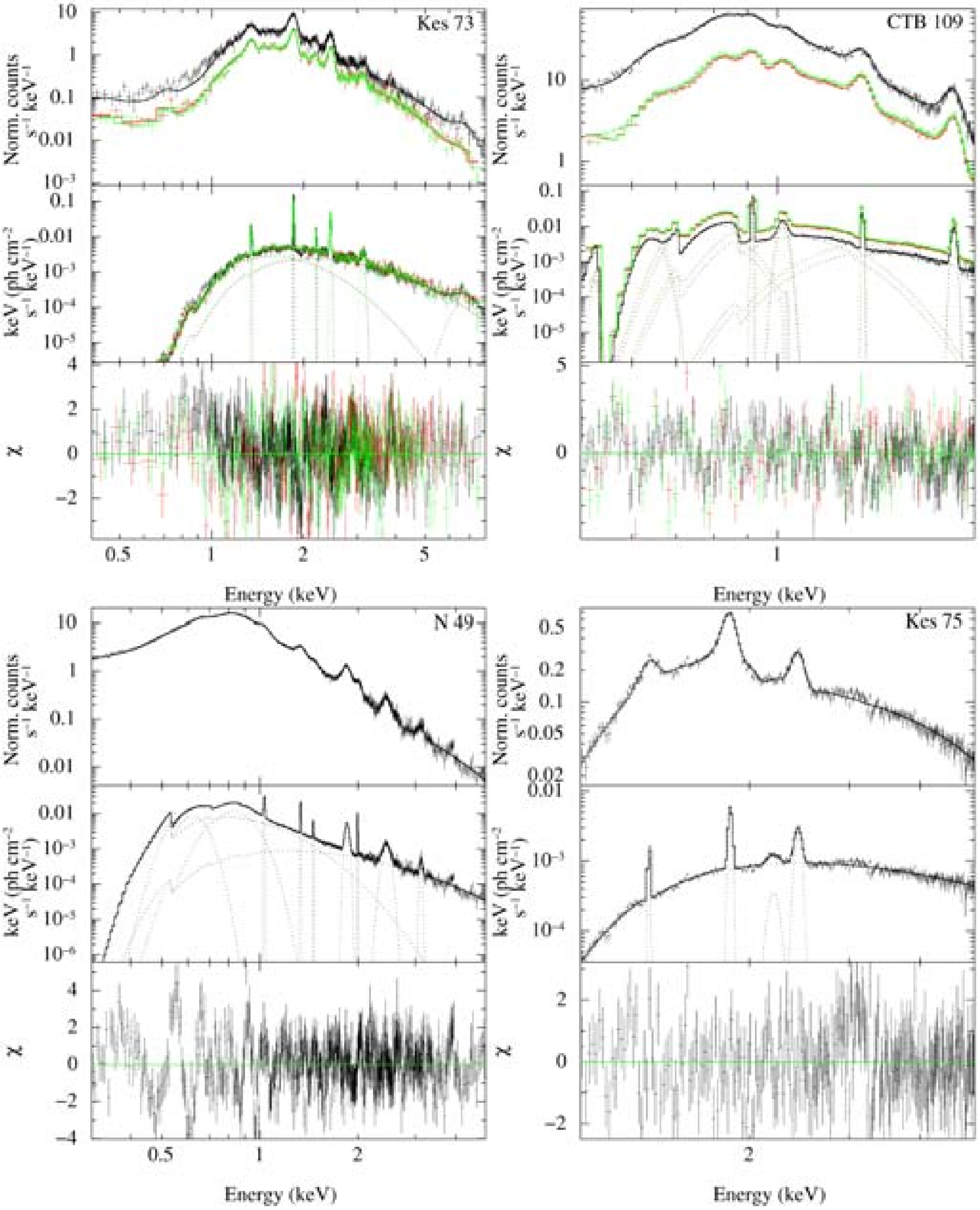

Fig. 6.3 Spectra obtained for the Kes 73, CTB 109, N 49 & Kes 75. We used the EPIC PN (in black), MOS 1 (in red) and MOS 2 (in green) data simultaneously to fit the models.

Table 6.2 Summary of the fitted models for Kes 73, CTB 109, N 49 and Kes 75.

Parameter	**Kes 73**	**CTB 109**	**N 49**[†]	**Kes 75**
N_H ($10^{22} cm^{-2}$)	$2.00^{-0.02}_{+0.01}$	$2.83^{-0.06}_{+0.10}$	$0.698^{-0.024}_{+0.006}$	$1.79^{-0.05}_{+0.06}$
kT_1 (keV)	$0.43^{-0.05}_{+0.02}$	$0.065^{-0.002}_{+0.001}$	$0.230^{-0.003}_{+0.004}$	$2.8^{-0.1}_{+0.2}$
N_1^{brems} (Norm. counts s^{-1})	$0.36^{-0.02}_{+0.15}$	$9^{-1}_{+14} \times 10^6$	$0.512^{-0.007}_{+0.067}$	$(4.5^{-0.3}_{+0.2}) \times 10^{-3}$
kT_2 (keV)	$1.34^{-0.01}_{+0.01}$	$0.20^{-0.02}_{+0.03}$	$1.14^{-0.01}_{+0.04}$	-
N_2^{brems} (Norm. counts s^{-1})	$(2.47^{-0.06}_{+0.41}) \times 10^{-2}$	18^{-4}_{+9}	$(3.5^{-0.15}_{+0.08}) \times 10^{-3}$	-
N VII (3,4 1)				
E (keV)	-	$0.515^{-0.008}_{+0.016}$	-	-
(keV)	-	$9.2^{-0.3}_{+0.1}) \times 10^{-2}$	-	-
N (Norm. counts s^{-1})	-	$(4^{-1}_{+4}) \times 10^4$	-	-
$EW^‡$ (eV)	-	737	-	-
O VII (2,5 1)				
E (keV)	-	-	$0.568^{-0.004}_{+0.004}$	-
(keV)	-	-	$(6.1^{-0.3}_{+0.1}) \times 10^{-2}$	-
N (Norm. counts s^{-1})	-	-	$(4.7^{-0.3}_{+0.7}) \times 10^{-2}$	-
$EW^‡$ (eV)	-	-	198	-
N VII (6,7 1)/O XVII (2,5,6 1)				
E (keV)	-	$0.597^{-0.002}_{+0.003}$	-	-
(keV)	-	< 0.06	-	-
N (Norm. counts s^{-1})	-	$(2.4^{-0.4}_{+1.5}) \times 10^5$	-	-
$EW^‡$ (eV)	-	472	-	-
O VIII (6,7 1)/Fe XVIII (4,5 1)				
E (keV)	-	-	$0.769^{-0.001}_{+0.001}$	-
(keV)	-	-	$0.112^{-0.003}_{+0.002}$	-
N (Norm. counts s^{-1})	-	-	$(1.78^{-0.06}_{+0.11}) \times 10^{-2}$	-
$EW^‡$ (eV)	-	-	338	-
Ne IX (2,5 1)				
E (keV)	-	$0.91^{-0.01}_{+0.01}$	-	-
(keV)	-	< 0.07	-	-
N (Norm. counts s^{-1})	-	$7.2^{-0.6}_{+0.2}$	-	-
$EW^‡$ (eV)	-	147	-	-
Ne X (3,4 1)				
E (keV)	-	$1.014^{-0.003}_{+0.002}$	$1.028^{-0.001}_{+0.004}$	-
(keV)	-	< 0.07	< 0.07	-
N (Norm. counts s^{-1})	-	$0.37^{-0.04}_{+0.03}$	$(5.9^{-0.3}_{+0.3}) \times 10^{-4}$	-
$EW^‡$ (eV)	-	68	33	-
Mg XI (2 1)				
E (keV)	$1.346^{-0.002}_{+0.001}$	$1.347^{-0.004}_{+0.003}$	$1.332^{-0.002}_{+0.006}$	$1.33^{-0.02}_{+0.02}$
(keV)	< 0.08	< 0.08	< 0.08	< 0.08
N (Norm. counts s^{-1})	$2.6^{-0.1}_{+0.1} \times 10^{-3}$	$(2.0^{-0.1}_{+0.3}) \times 10^{-3}$	$(2.03^{-0.08}_{+0.08}) \times 10^{-4}$	$(1.8^{-0.3}_{+0.3}) \times 10^{-4}$
$EW^‡$ (eV)	95	337	62	84

[†] The absorption column density of N49 is fitted using the LMC abundances: He=0.89, C=0.30, N=0.12, O=0.26, Ne=0.33, Na=0.30, Mg=0.32, Al=0.30, Si=0.30, S=0.31, Cl=0.31, Ar=0.54, Ca=0.34, Cr=0.61, Fe=0.36, Co=0.30 & Ni=0.62. We have added also the galactic absorption $N_H = 6 \times 10^{20} cm^{-2}$.

[‡] Equivalent Width.

a spin period of 6.98 s (Fahlman & Gregory, 1983) and a period derivative of 4.83 $\times 10^{-13}$ (Iwasawa, Koyama & Halpern, 1992). The dipolar magnetic field is about 5.9 $\times 10^{13}$ G, the spin down power is 5.6 $\times 10^{31}$ erg s^{-1} and the characteristic age 229 kyr. Despite of the large characteristic age of the pulsar, the estimated true age of the remnant is about 14 kyr (Sasaki et al., 2013). CTB 109 has been observed also in X-rays with *ASCA* (Rho, Petre & Ballet, 1998), *Beppo-SAX* (Parmar et al., 1998) and *ROSAT* (Hurford & Fesen, 1995; Rho & Petre, 1997).

The spectrum covers the entire shell and combines the three observations detailed in table 6.1. The background regions used are shown in figure 6.2. We observe that the main contribution to flux is in the energy range between 0.5 and 2 keV. Some known X-ray sources in the field of view have been extracted in our analysis.

In this case we used two Bremsstrahlung models to fit the continuum, with temperatures of 0.07 keV and 0.20 keV. The measured absorption density is very high ($N_{\rm H}$ =2.83 $\times 10^{22}$

cm^{-2}). We detected 6 lines: N VII at 0.52 keV (EW=0.74 keV) and at 0.60 keV (EW=0.47 keV), Ne IX at 0.91 keV (EW=0.15 keV), Ne X at 1.01 keV (EW=68 eV), Mg XI at 1.35 keV (EW=0.34 keV) and Si XIII at 1.86 keV (0.28 keV).

N 49

N49 (also SNR B0525-66.1) is a SNR located in the Large Magellanic Cloud (LMC). The associated central source is SGR 0526-66 with a period of 8.047 s (Mazets et al., 1979b) and a period derivative of 6.6 $\times 10^{-11}$ s s^{-1} (Kulkarni et al., 2003). There is some uncertainty in the association of SGR 0526-66 with N49 (see Gaensler et al. 2001). The inferred dipolar magnetic field is 7.3 $\times 10^{14}$ G. The spin-down luminosity is 4.9 $\times 10^{33}$ erg/s and the characteristic age is $\sim$2 kyr. The nebula is 1.5 × 1.5 , this means that assuming a distance of 50 kpc the diameter of N49 is $\sim$22 pc. Park et al. (2012) establish a Sedov age for the nebula of $\sim$4.8 kyr and a SN explosion energy of 1.8 $\times 10^{51}$ erg.

SGR 0526-66 is located in the north of the remnant. The brightest part of the nebula is the bulge in the south-east of the nebula due to interaction with dense interstellar clouds (Vancura et al., 1992; Banas et al., 1997; Park et al., 2012). This shock has also contribution between 3 and 10 keV, while the contribution of the rest of the nebula is clearly negligible at this range. In figure 6.1, we show a color image of N49. We analyze the total spectrum of the nebula excluding a circle of 20” around the central source to avoid contribution from the central source due to the wide point spread function (PSF) of the detectors.

The absorption of N49 has two components: one is related with the Galactic absorption and the other is the absorption produced by LMC. The Milky Way photoelectric absorption towards N49 is fixed as $N_\mathrm{H} = 6 \times 10^{20}$ cm^{-2} (Dickey & Lockman, 1990; Park et al., 2012). To compute the absorption column density due to the LMC, we needed to include abundances for LMC (Russell & Dopita, 1992; Hughes, Hayashi & Koyama, 1998; Park et al., 2012). We obtain an absorption column density of $N_\mathrm{H} = 0.7 \times 10^{22}$ cm^{-2}. The continuum is represented by two Bremsstrahlung models with temperatures of 0.23 keV and 1.14 keV. In this case, we have detected 9 lines: O VII at 0.57 keV (EW=0.20 keV), O VIII/Fe XVIII at 0.77 keV (EW=0.34 keV), Ne X at 1.03 keV (EW=33 eV), Mg XI at 1.33 keV (EW=62 eV), Mg XII at 1.46 keV (EW=20 eV), Si XIII at 1.85 keV (EW=0.30 keV), Si XIV at 2.00 keV (EW=0.13 keV), S XV at 2.44 keV (EW=0.30 keV) and Ar XVII at 3.12 keV (EW=0.11 keV).

Table 6.3 Continued.

Parameter	Kes 73	CTB 109	N 49†	Kes 75
Mg XII (3,4 1)				
E (keV)	-	-	$1.459^{-0.005}_{+0.006}$	-
(keV)	-	-	< 0.08	-
N (Norm. counts s^{-1})	-	-	$(3.9^{-0.5}_{+0.6}) \times 10^{-5}$	-
$EW^{\ddagger}$ (eV)	-	-	20	-
Si XIII (2,5,6,7 1)				
E (keV)	$1.8521^{-0.0001}_{+0.0001}$	$1.856^{-0.001}_{+0.006}$	$1.848^{-0.003}_{+0.002}$	$1.851^{-0.003}_{+0.012}$
(keV)	< 0.02	< 0.02	$(2.3^{-0.6}_{+0.6}) \times 10^{-2}$	< 0.02
N (Norm. counts s^{-1})	$2.76^{-0.06}_{+0.06} \times 10^{-3}$	$(7.0^{-0.2}_{+0.3}) \times 10^{-4}$	$(1.68^{-0.04}_{+0.06}) \times 10^{-4}$	$(2.6^{-0.1}_{+0.2}) \times 10^{-4}$
$EW^{\ddagger}$ (eV)	368	278	299	232
Si XIV (3,4 1)				
E (keV)	-	-	$1.998^{-0.002}_{+0.007}$	-
(keV)	-	-	< 0.09	-
N (Norm. counts s^{-1})	-	-	$(5.2^{-0.4}_{+0.3}) \times 10^{-5}$	-
$EW^{\ddagger}$ (eV)	-	-	132	-
Si XIII (13 1)				
E (keV)	$2.201^{-0.010}_{+0.009}$	-	-	$2.21^{-0.02}_{+0.04}$
(keV)	< 0.09	-	-	< 0.09
N (Norm. counts s^{-1})	$(1.6^{-0.2}_{+0.2}) \times 10^{-4}$	-	-	$(3.4^{-0.9}_{+1.1}) \times 10^{-5}$
$EW^{\ddagger}$ (eV)	46	-	-	45
S XV (2,5,6,7 1)				
E (keV)	$2.452^{-0.002}_{+0.002}$	-	$2.444^{-0.005}_{+0.005}$	$2.437^{-0.005}_{+0.007}$
(keV)	< 0.09	-	< 0.09	< 0.09
N (Norm. counts s^{-1})	$(8.0^{-0.3}_{+0.2}) \times 10^{-4}$	-	$(6.8^{-0.4}_{+0.4}) \times 10^{-5}$	$(1.09^{-0.12}_{+0.08}) \times 10^{-4}$
$EW^{\ddagger}$ (eV)	375	-	299	178
S XV (13 1)				
E (keV)	-	-	-	-
(keV)	-	-	-	-
N (Norm. counts s^{-1})	-	-	-	-
$EW^{\ddagger}$ (eV)	-	-	-	-
Ar XVII (2,5,6,7 1)				
E (keV)	$3.13^{-0.01}_{+0.01}$	-	$3.12^{-0.02}_{+0.02}$	-
(keV)	< 0.1	-	< 0.1	-
N (Norm. counts s^{-1})	$(9^{-1}_{+1}) \times 10^{-5}$	-	$(7^{-1}_{+1}) \times 10^{-6}$	-
$EW^{\ddagger}$ (eV)	120	-	110	-
Fe XXV (7 1)				
E (keV)	$6.7^{-0.2}_{+0.2}$	-	-	-
(keV)	$0.5^{-0.1}_{+0.2}$	-	-	-
N (Norm. counts s^{-1})	$2.9^{-0.6}_{+0.6} \times 10^{-5}$	-	-	-
$EW^{\ddagger}$ (eV)	1890	-	-	-
$^{2}_{r}$	1.57 (985)	2.05 (477)	1.84 (578)	1.12 (258)

† The absorption column density of N49 is fitted using the LMC abundances: He=0.89, C=0.30, N=0.12, O=0.26, Ne=0.33, Na=0.30, Mg=0.32, Al=0.30, Si=0.30, S=0.31, Cl=0.31, Ar=0.54, Ca=0.34, Cr=0.61, Fe=0.36, Co=0.30 & Ni=0.62. We have added also the galactic absorption $N_H = 6 \times 10^{20} cm^{-2}$.

‡ Equivalent Width.

Kes 75

Kes 75 (G29.7-0.3) is a composite SNR. The X-ray emission of the partial shell is extended in two clouds in the south-west and south-east part of the image (see figure 6.1). It was observed firstly in X-rays by *Einstein* (Becker, Helfand & Szymkowiak, 1983) showing an incomplete shell of 3' in extent. In the center of the nebula, there is a bright PWN, which was spatially resolved by the *Chandra* observation (Helfand, Collins & Gotthelf, 2003; Ng et al., 2008), and it is powered by PSR J1846-0258. This pulsar was discovered using the *RXTE* telescope and localized within an arcminute of the remnant using *ASCA* (Gotthelf et al., 2000). The period of the pulsar is $\sim$326 ms and the period derivative 7.11×10^{-12} s s^{-1} (e. g., Livingstone et al. 2011). This leads to a spin-down energy loss of 8.1×10^{36} erg s^{-1}, a magnetic field of 4.9×10^{13} G and a characteristic age of 728 yr. Livingstone et al. (2006) estimated a braking index of 2.65±0.01. Despite its early classification as a typical rotational powered pulsar, PSR J1846-0258 showed magnetar-like activity via short bursts and the outburst of its persistent emission (Gavriil et al., 2008; Kumar & Safi-Harb, 2008) enabling its classification as (at least sporadicly) magnetically powered. There is a big uncertainty in the distance of this SNR in the literature (Caswell et al., 1975; Milne, 1979; McBride et al., 2008; Becker & Helfand, 1984). Most recent estimates give a distance between ∼5.1-7.5 kpc based on H I absorption observations (Leahy & Tian, 2008), and 10.6 kpc using millimeter observations of CO lines from an adjacent molecular cloud (Su et al., 2009). In our work, we adopt this value in order to compute the X-ray luminosity and the size of the SNR.

The spectrum of Kes 75 has been fitted using only one thermal Bremsstrahlung component with a temperature of 2.8 keV and an absorption column density of 1.79×10^{22} cm^{-2}. Four clear lines are resolved using Gaussians: Mg XI line at 1.33 keV (EW=84 eV), two Si XIII lines at 1.85 (EW=0.23 keV) and 2.21 keV (EW=45 eV) and S XV at 2.44 keV (EW=0.18 keV).

6.3 Spectral line and photometric comparison with other SNRs

In this work we have re-analyzed in a coherent way the X-ray emission from SNRs around magnetars, and compared in their emission lines and luminosities. The aim of this study was to search for any possible trend or significant differences in SNRs associated to different types of neutron stars. This work complements and extends the SN explosion energy analysis in the magnetar case done by Vink & Kuiper (2006) provinding a detailed description of the spectra for Kes 73, Kes 75, N 49 and CTB 109, obtaining centroids and fluxes of the spectral lines and compared directly with other remnants with spectroscopic studies already published. We also looked for any possible trend or significant differences in the ionization state of the SNR elements, and in the remnant X-ray luminosities, of SNRs associated to different types of neutron stars.

At variance with the plasma models usually fitted to the X-ray spectra of SNRs, we proceed to fit the spectra of Kes 73, CTB 109, N 49 & Kes 75 using a thermal Bremsstrahlung model for the continuum emission and gaussian profiles for the lines. Our main aim is to have a precise estimate of line centroid energy, to identify it properly, we have then used the simplest continuum model to reduce the free parameters of the fit. One could expect that the excess of rotational energy released by the magnetar during the alpha-dynamo process could be stored in the ionization level of the lines present in the spectrum. If the energy release is higher than in a normal SNR, heavy elements as silicon (Si), sulfur (S), argon (Ar), calcium (Ca) or iron (Fe) could be systematically at a higher state of ionization. In table 6.2, we collected all SNRs with detailed spectroscopic studies in the literature and we see that the typical elements detected are O VII, O VIII, Ne IX, Ne X, Mg XI, Mg XII, Si XIII, Si XIV, S XV, S XVI, Ar XVII, Ca XIX and Fe XXV. The only lines detected in the four spectra are the Mg XI line at 1.33 keV and Si XIII at 1.85 keV. For comparison, we also fitted the spectra of the SNRs using the `vnei` and `vpshock` models (e. g., Borkowski, Lyerly & Reynolds 2001). The results are summarized in the table 6.5. For the `vnei` and `vpshock` models, we have added a thermal Bremsstrahlung component in some cases. The temperature of the Bremsstrahlung component lies between 0.3 and 0.4 keV for Kes 73 and Kes 75 and show a high temperature for the `vnei` and `vpshock` plasma. CTB 109 does not need a Bremsstrahlung component to obtain a good fit. The temperature of the `vnei` and `vpshock` plasmas is always higher than for the thermal Bremsstrahlung, with the exception of N49 in which the temperature for `vnei` is 0.17 keV (0.99 keV for Bremsstrahlung) and 0.46 keV for `vpshock` (0.90 keV for Bremsstrahlung). The abundances obtained in both models show similar tendencies. For Kes 73 and N 49, the abundances of Si and S are quite above the solar ones. CTB 109 show low abundances with respect the solar ones for O, Ne, Mg, Si and Fe. Due to the complexity of the N 49 spectrum, some lines have not been reproduced well by the plasma models and we have added them using gaussian profiles to improve the fit. In summary, our spectroscopic analysis of these sources of ionized elements shows compatible results with other non-magnetar SNRs already reported in literature.

In figure 6.4 we have collected from the literature the X-ray luminosities from 0.5 to 10 keV of all observed SNRs brighter than 10^{33} erg s^{-1}, with an age lower than 100 kyr and having a confirmed association with a central source. For these remnants, we obtain the age, distance, approximate radius, magnetic field and spin-down luminosity of the central source (whenever possible) from the literature. All this information is summarized in table 6.6. We have plotted the SNRs luminosities (excluding the contribution of the central neutron star luminosity) as a function of the SNR age and dimension (although note that the latter parameters is highly dependent on the environment of each remnant). For those remnants having a central neutron star with measured rotational properties, we plot the SNR luminosity as a function of the pulsar surface dipolar magnetic field at the equator ($B = 3.2 \times 10^{19} \quad \overline{PP}$ G), and the pulsar spin down luminosity ($L_{sd} = 3.9 \times 10^{46} P/P^3$ erg/s; always assuming the neutron star moment of inertia $I = 10^{45}\,\mathrm{g\,cm^2}$), and where P is the pulsar rotation period in seconds and P its first derivative.

Table 6.4 Summary of the line detections in X-ray for some important SNRs compared with lines detected in our analysis.

SNR	**Galaxy**	**Age (yr)**	**Element**					
			O VII (2,5,7 1) (0.574 KeV)	*O VIII (3,4 1) (0.653 KeV)*	*O VIII (6,7 1) (0.774 KeV)*	*Ne IX (2,5 1) (0.915 KeV)*	*Ne X (3,4 1) (1.022 KeV)*	*Ne X (6,7 1) (1.21 KeV)*
Kes73	MW	1100-1500						
CTB109	MW	7900-9700				X	X	
Kes75	MW	900-4300						
N49	LMC	5000	X		X	X	X	
G1.9+1.3 [2]	MW	110-170						
Kepler [3],[8],[12]	MW	408				X		
Tycho [4],[5],[6],[13]	MW	440				X		
SN1006 [10],[19]	MW	1006	X		X			X
Cas A [1],[9],[16]	MW	316-352	X	X	X	X	X	
MSH11-54 [11],[14]	MW	2930-3050	X	X	X	X	X	
Puppis A [7],[17],[18]	MW	3700-5500	X	X	X	X	X	X
B0509-67.5 [15]	LMC	400	X	X		X		

			Mg XI (2,5,6,7 1) (1.35 KeV)	*Mg XII (3,4 1) (1.47 KeV)*	*Si XIII (2,5,6,7 1) (1.86 KeV)*	*Si XIV (3,4 1) (2.00 KeV)*	*Si XIII (13 1) (2.18 KeV)*	*S XV (2,5,6,7 1) (2.46 KeV)*
Kes73	MW	1100-1500	X		X		X	X
CTB109	MW	7900-9700	X		X			
Kes75	MW	900-4300	X		X		X	X
N49	LMC	5000	X	X	X	X		X
G1.9+1.3	MW	110-170	X		X			X
Kepler	MW	408	X		X	X	X	X
Tycho	MW	440			X	X	X	X
SN1006	MW	1006	X		X			
Cas A	MW	316-352	X	X	X	X	X	X
MSH11-54	MW	2930-3050	X	X	X			X
Puppis A	MW	3700-5500	X		X		X	X
B0509-67.5	LMC	400	X		X		X	X

			S XVI (3,4 1) (2.62 keV)	*S XV (13 1) (2.88 KeV)*	*Ar XVII (2,5,6,7 1) (3.13 KeV)*	*Ca XIX (2,5,6,7 1) (3.89 KeV)*	*Fe XXV K-shell (6.65 KeV)*
Kes73	MW	1100-1500			X		X
CTB109	MW	7900-9700					
Kes75	MW	900-4300					
N49	LMC	5000			X		
G1.9+1.3	MW	110-170			X	X	X
Kepler	MW	408		X	X	X	X
Tycho	MW	440		X	X	X	X
SN1006	MW	1006					
Cas A	MW	316-352		X	X	X	X
MSH11-54	MW	2930-3050					
Puppis A	MW	3700-5500					
B0509-67.5	LMC	400			X	X	X

The references are: [1]Bleeker et al. (2001), [2]Borkowski et al. (2010), [3]Cassam-Chenaï et al. (2004), [4]Decourchelle et al. (2001), [5]Hayato et al. (2010), [6]Hwang & Gotthelf (1997), [7]Hwang, Petre & Flanagan (2008), [8]Kinugasa & Tsunemi (1999), [9]Maeda et al. (2009), [10]Miceli et al. (2009), [11]Park et al. (2007), [12]Reynolds et al. (2007), [13]Tamagawa et al. (2009), [14]Vink et al. (2004), [15]Warren & Hughes (2004), [16]Willingale et al. (2002), [17]Winkler et al. (1981b), [18]Winkler et al. (1981a), [19]Yamaguchi et al. (2008).

In order to search for any correlations in the SNRs and pulsars characteristics we have plot in Figure 6.4, we run a Spearman test. We searched for correlations between the X-ray luminosity and other features of the sources of our sample, such as dimension of the remnant, age, surface magnetic field strength and spin down power of the associated pulsar. To this end, we employed a Spearman rank correlation test, and evaluated the significance of the value of the coefficient of correlation r obtained, by computing $t = r\sqrt{(N-2)/(1-r^2)}$, which is distributed approximately as Student's distribution with $N-2$ degrees of freedom, where N is the number of couples considered. The results we obtained are listed in Table 6.7; no correlation is found at a significance level exceeding 99 per cent, or any significant difference in luminosity between SNRs surrounding magnetars and those around other classes of isolated neutron stars.

By looking at the pulsar population as a whole, we have also been looking at the number

Table 6.5 Fits for Kes 73, CTB 109, N 49 & Kes 75 using `vnei` and `vpshock` plasma models. A second thermal Bremsstrahlung component is included in some cases.

`VNEI`

Parameter	**Kes 73**	**CTB 109**	**N 49**[†]	**Kes 75**
N_H (cm^{-2})	$2.51^{-0.08}_{+0.06}$	$0.695^{-0.018}_{+0.005}$	$1.03^{-0.02}_{+0.02}$	$3.71^{-0.06}_{+0.07}$
kT$_{brems}$ (keV)	$0.41^{-0.03}_{+0.05}$	-	$0.99^{-0.01}_{+0.02}$	$0.31^{-0.04}_{+0.05}$
N$_{brems}$ (Norm. counts s^{-1})	$0.5^{-0.2}_{+0.2}$	-	$(5.4^{-0.3}_{+0.3}) \times 10^{-3}$	$0.4^{-0.2}_{+0.5}$
kT (keV)	$1.51^{-0.08}_{+0.15}$	$0.297^{-0.004}_{+0.007}$	$0.1650^{-0.0003}_{+0.0011}$	$2.0^{-0.1}_{+0.2}$
O	1 (fixed)	$0.16^{-0.02}_{+0.01}$	$0.137^{-0.003}_{+0.002}$	1 (fixed)
Ne	1 (fixed)	$0.27^{-0.01}_{+0.01}$	$0.175^{-0.004}_{+0.004}$	1 (fixed)
Mg	$1.30^{-0.11}_{+0.09}$	$0.23^{-0.02}_{+0.01}$	$0.36^{-0.01}_{+0.01}$	$0.51^{-0.08}_{+0.09}$
Si	$1.6^{-0.1}_{0.2}$	$0.49^{-0.05}_{+0.03}$	1 (fixed)	$0.56^{-0.04}_{+0.05}$
S	$2.1^{-0.2}_{+0.4}$	1 (fixed)	1 (fixed)	$0.9^{-0.1}_{+0.2}$
Ar	$3.1^{-0.6}_{+0.9}$	1 (fixed)	1 (fixed)	$1.2^{-0.6}_{+0.8}$
Ca	6^{-2}_{+4}	1 (fixed)	1 (fixed)	1 (fixed)
Fe	1 (fixed)	$0.226^{-0.024}_{+0.008}$	1 (fixed)	1 (fixed)
E_1 (keV)	-	-	$0.729^{-0.002}_{+0.005}$	-
$_1$ (keV)	-	-	< 0.07	-
N_1 (Norm. counts s^{-1})	-	-	$(5.4^{-0.3}_{+0.3}) \times 10^{-3}$	-
E_2 (keV)	-	-	$1.018^{-0.001}_{+0.001}$	-
$_2$ (keV)	-	-	< 0.07	-
N_2 (Norm. counts s^{-1})	-	-	$(1.20^{0.04}_{0.04}) \times 10^{-3}$	-
E_3 (keV)	-	-	$1.467^{-0.008}_{+0.004}$	-
$_3$ (keV)	-	-	< 0.08	-
N_3 (Norm. counts s^{-1})	-	-	$(4.9^{0.6}_{0.6}) \times 10^{-5}$	-
E_4 (keV)	-	-	$1.846^{-0.003}_{+0.003}$	-
$_4$ (keV)	-	-	< 0.09	-
N_4 (Norm. counts s^{-1})	-	-	$(1.56^{0.07}_{0.07}) \times 10^{-4}$	-
E_5 (keV)	-	-	$1.998^{-0.003}_{+0.028}$	-
$_5$ (keV)	-	-	< 0.09	-
N_5 (Norm. counts s^{-1})	-	-	$(5.3^{0.5}_{0.5}) \times 10^{-5}$	-
E_6 (keV)	-	-	$2.445^{-0.005}_{+0.005}$	-
$_6$ (keV)	-	-	< 0.1	-
N_6 (Norm. counts s^{-1})	-	-	$(6.4^{-0.4}_{+0.3}) \times 10^{-5}$	-
E_7 (keV)	-	-	$3.12^{-0.02}_{+0.02}$	-
$_7$ (keV)	-	-	< 0.1	-
N_7 (Norm. counts s^{-1})	-	-	$(7^{-1}_{+1}) \times 10^{-6}$	-
(s cm^{-3})	$(5.1^{-0.8}_{+0.6}) \times 10^{10}$	$(6.7^{-1.0}_{+0.8}) \times 10^{11}$	$(1.3^{-0.2}_{+0.1}) \times 10^{12}$	$(2.4^{-0.3}_{+0.3}) \times 10^{10}$
N (Norm. counts s^{-1})	$(3.9^{-0.9}_{+0.6}) \times 10^{-2}$	$0.35^{-0.04}_{+0.02}$	$1.69^{-0.02}_{+0.03}$	$0.021^{-0.003}_{+0.003}$
^2_r	1.56 (997)	2.60 (491)	1.87 (569)	1.19 (236)
`VPSHOCK`				
N_H (cm^{-2})	$2.51^{-0.05}_{+0.05}$	$0.562^{-0.008}_{+0.009}$	$0.26^{-0.02}_{+0.01}$	$3.57^{-0.10}_{+0.08}$
kT$_{brems}$ (keV)	$0.38^{-0.03}_{+0.03}$	-	$0.90^{-0.03}_{+0.02}$	$0.31^{-0.04}_{+0.09}$
N$_{brems}$ (Norm. counts s^{-1})	$0.6^{-0.2}_{+0.3}$	-	$(5.3^{-0.6}_{+0.3}) \times 10^{-3}$	$0.4^{-0.2}_{+0.5}$
kT (keV)	$1.44^{-0.06}_{+0.08}$	$0.572^{-0.005}_{+0.004}$	$0.459^{-0.009}_{+0.011}$	$2.0^{-0.1}_{+0.3}$
O	1 (fixed)	$0.33^{-0.04}_{+0.02}$	$0.6^{-0.1}_{+0.2}$	1 (fixed)
Ne	1 (fixed)	$0.36^{-0.02}_{+0.02}$	$1.0^{-0.3}_{+0.2}$	1 (fixed)
Mg	$1.4^{-0.1}_{+0.1}$	$0.37^{-0.02}_{+0.01}$	$0.7^{-0.2}_{+0.1}$	$0.58^{-0.09}_{+0.09}$
Si	$1.8^{-0.1}_{+0.1}$	$0.35^{-0.02}_{+0.02}$	$1.5^{-0.13}_{+0.06}$	$0.70^{-0.06}_{+0.07}$
S	$2.4^{-0.2}_{+0.3}$	1 (fixed)	$4.7^{-0.4}_{+0.3}$	$1.0^{-0.2}_{+0.2}$
Ar	$3.0^{-0.5}_{+0.6}$	1 (fixed)	1 (fixed)	$1.0^{-0.5}_{+0.6}$
Ca	4^{-1}_{+2}	1 (fixed)	1 (fixed)	1 (fixed)
Fe	1 (fixed)	$0.41^{-0.03}_{+0.01}$	$0.58^{-0.05}_{+0.05}$	1 (fixed)
E_1 (keV)	-	-	$1.990^{-0.002}_{+0.011}$	-
$_1$ (keV)	-	-	< 0.09	-
N_1 (Norm. counts s^{-1})	-	-	$(3.4^{0.3}_{0.3}) \times 10^{-5}$	-
E_2 (keV)	-	-	$3.14^{-0.02}_{+0.02}$	-
$_2$ (keV)	-	-	< 0.1	-
N_2 (Norm. counts s^{-1})	-	-	$(8^{-2}_{+2}) \times 10^{-6}$	-
$_u$ (s cm^{-3})	$(1.1^{-0.1}_{+0.1}) \times 10^{11}$	$(3.7^{-0.3}_{+0.3}) \times 10^{11}$	$(8.1^{-0.3}_{+0.5}) \times 10^{11}$	$(4.5^{-0.6}_{+0.8}) \times 10^{10}$
N (Norm. counts s^{-1})	$(4.6^{-0.6}_{+0.6}) \times 10^{-2}$	$(4.6^{-0.2}_{+0.2}) \times 10^{-2}$	$(1.4^{-0.3}_{+0.2}) \times 10^{-2}$	$0.021^{-0.004}_{+0.003}$
^2_r	1.51 (997)	3.02 (491)	3.23 (581)	1.16 (263)

[†] The absorption column density of N49 is fitted using the LMC abundances: He=0.89, C=0.30, N=0.12, O=0.26, Ne=0.33, Na=0.30, Mg=0.32, Al=0.30, Si=0.30, S=0.31, Cl=0.31, Ar=0.54, Ca=0.34, Cr=0.61, Fe=0.36, Co=0.30 & Ni=0.62. We have added also the galactic absorption $N_H = 6 \times 10^{20} cm^{-2}$.

Table 6.6 SNRs considered in our X-ray luminosity analysis. The data without references is extracted from this work or deduced from the data obtained in the literature.

Name	**Central source**	**Distance (kpc)**	**Radius (pc)**	**Age (kyr)**	E **(erg s^{-1})**	**B$_s$ (G)**	**F$_X$ (erg cm^{-2} s^{-1})**	**L$_X$ (erg s^{-1})**
SNRs with magnetars								
Kes 75	J1846-0258 [26]	10.6 [66]	$5.5^{-0.3}_{+0.3}$ [10]	0.9 [6]	8.06×10^{36} [40]	4.88×10^{13} [40]	2.69×10^{-10}	3.61×10^{36}
Kes 73	1E 1841-045 [72]	$6.7^{-1.0}_{+1.8}$ [61]	$4.5^{-0.1}_{+0.1}$ [10]	$1.3^{-0.2}_{+0.2}$ [73]	1.08×10^{33} [31]	7.34×10^{14} [31]	4.39×10^{-10}	$2.36^{-0.65}_{+1.43} \times 10^{36}$
N 49	RX J0526-6604 [36]	50 [36]	20.4 [10]	4.8 [48]	4.92×10^{33} [36]	7.32×10^{14} [36]	2.41×10^{-10}	7.21×10^{37}
CTB 109	1E 2259+586 [2]	$3^{-0.5}_{+0.5}$ [33]	$12.6^{-1.3}_{+1.3}$ [10]	14^{-2}_{+2} [62]	5.54×10^{31} [2]	5.84×10^{13} [2]	1.94×10^{-10}	$2.09^{-0.64}_{+0.75} \times 10^{35}$
SNRs with CCOs								
Cas A	CXO J2323+5848 [45]	$3.4^{-0.1}_{+0.3}$ [53]	$2.8^{-0.1}_{+0.1}$ [10]	0.326^{-27}_{+27} [17]	-	-	2.06×10^{-8} [10]	$2.85^{-0.20}_{+0.50} \times 10^{37}$ [10]
G350.1-0.3	XMMU J1720-3726 [23]	4.5 [23]	$2.5^{-0.4}_{+0.4}$ [10]	0.9 [23]	-	-	1.64×10^{-9} [10]	3.97×10^{36} [10]
G330.2+1.0	CXOU J1601-5133 [47]	$4.9^{-0.3}_{+0.3}$ [53]	$7.8^{-0.8}_{+0.8}$ [10]	1.1 [47]	-	-	1.60×10^{-11} [71]	$4.60^{-0.55}_{+0.57} \times 10^{34}$ [71]
G347.3-0.5	1 WGA J1713-3949 [38]	1 [34]	$8.7^{-0.8}_{+0.8}$ [18]	1.6 [18]	-	-	4.40×10^{-10} [51]	5.26×10^{34}
Vela Jr.	CXOU J0852-4617 [49]	$0.75^{-0.55}_{+0.25}$ [31]	13.1 [10]	$1.7^{-0}_{+2.6}$ [31]	-	-	8.30×10^{-11} [1]	$5.58^{-3.10}_{+4.34} \times 10^{33}$
RCW 103	1E 1613-5055 [25]	3.1 [55]	$4.1^{-0.1}_{+0.1}$ [10]	2 [7]	-	-	1.70×10^{-8} [10]	1.95×10^{37}
G349.7+0.2	CXOU J1718-3726 [39]	22.4 [20]	8.2 [39]	3.5 [39]	-	-	6.50×10^{-10} [39]	3.90×10^{37}
Puppis A	RX J0822-4300 [4]	$2.2^{-0.3}_{+0.3}$ [54]	$17.5^{-1.7}_{+1.7}$ [16]	$4.45^{-0.75}_{+0.75}$ [4]	-	-	2.16×10^{-8}	$1.20^{0.90}_{+1.55} \times 10^{37}$ [14]
Kes 79	J1852+0040 [63]	7.1 [8]	$9.2^{-1.0}_{+1.0}$ [10]	$6.0^{-0.2}_{+0.4}$ [67]	2.96×10^{32} [27]	3.05×10^{10} [27]	4.64×10^{-10} [67]	2.80×10^{36} [67]
G296.5+10.0	1E 1207-5209 [24]	$2.1^{-0.8}_{+1.8}$ [24]	24.8 [32]	7 [57]	9.58×10^{33} [50]	2.83×10^{12} [50]	1.67×10^{-9} [44]	$8.81^{-5.40}_{+21.60} \times 10^{34}$
SNRs with high-B PSRs								
MSH 15-52	J1513-5908 [21]	$5.2^{-1.4}_{+1.4}$ [15]	22.7 [46]	1.9 [15]	1.75×10^{37} [41]	1.54×10^{13} [41]	7.80×10^{-11} [46]	$2.52^{-1.17}_{+1.54} \times 10^{35}$
MSH 11-54	J1124-5916 [29]	$6.2^{-0.9}_{+0.9}$ [22]	$16.2^{-0.2}_{+0.2}$ [10]	$2.99^{-0.06}_{+0.06}$ [76]	1.19×10^{37} [52]	1.02×10^{13} [52]	2.09×10^{-9} [10]	$9.61^{-2.59}_{+2.99} \times 10^{36}$
G292.2-0.5	J1119-6127 [37]	$8.4^{-0.4}_{+0.4}$ [9]	$21.1^{-3.8}_{+3.8}$ [10]	$7.1^{-0.2}_{+0.5}$ [37]	2.34×10^{36} [75]	4.10×10^{13} [75]	1.98×10^{-11} [37]	$1.67^{-0.15}_{+0.16} \times 10^{35}$
SNRs with normal PSRs								
G21.5-0.9	J1833-1034 [43]	$4.7^{-0.4}_{+0.4}$ [69]	$3.2^{-0.1}_{+0.1}$ [10]	$0.87^{-1.5}_{+2.0}$ [5]	3.37×10^{37} [58]	3.58×10^{12} [58]	6.69×10^{-13}	$1.77^{-0.31}_{0.29} \times 10^{33}$ [43]
G11.2-0.3	J1811-1925 [70]	5 [30]	$2.3^{-0.1}_{+0.1}$ [10]	1.616 [68]	6.42×10^{36} [70]	1.71×10^{12} [70]	3.98×10^{-9} [10]	1.19×10^{37} [10]
G8.7-0.1	J1803-2137 [19]	4 [19]	29.1 [19]	15^{-6}_{+6} [19]	2.22×10^{36} [77]	4.92×10^{12} [77]	2.00×10^{-10} [19]	3.83×10^{35}
Vela	J0835-4510 [3]	$0.287^{-0.017}_{+0.019}$ [13]	20.1 [42]	18^{-9}_{+9} [3]	6.92×10^{36} [12]	3.38×10^{12} [12]	2.94×10^{-8}	$2.90^{-0.34}_{+0.39} \times 10^{35}$ [42]
MSH 11-61A	J1105-6107 [64]	7 [64]	$12.1^{-2.2}_{+2.2}$ [64]	20^{-5}_{+5} [64]	2.48×10^{36} [74]	1.01×10^{12} [74]	8.06×10^{-11} [10]	4.71×10^{35} [10]
W 44	J1856+0113 [11]	2.5 [11]	$10.8^{-2.0}_{+2.0}$ [11]	20^{-4}_{+4} [11]	4.30×10^{35} [28]	7.55×10^{12} [28]	1.80×10^{-9} [56]	1.35×10^{36}
CTB 80	J1952+3252 [60]	2 [65]	1.5 [60]	51 [78]	3.74×10^{36} [28]	4.86×10^{11} [28]	2.40×10^{-12}	1.15×10^{33} [59]

The references are: [1] Aharonian et al. (2007), [2] Archibald et al. (2013), [3] Aschenbach, Egger & Trümper (1995), [4] Becker et al. (2012), [5] Bietenholz & Bartel (2008), [6] Blanton & Helfand (1996), [7] Carter, Dickel & Bomans (1997), [8] Case & Bhattacharya (1998), [9] Caswell, McClure-Griffiths & Cheung (2004), [10] *Chandra* SNR catalog[a], [11] Cox et al. (1999), [12] Dodson, McCulloch & Lewis (2002), [13] Dodson et al. (2003), [14] Dubner et al. (2013), [15] Fang & Zhang (2010a), [16] Ferrand & Safi-Harb (2012), [17] Fesen et al. (2006), [18] Fesen et al. (2012), [19] Finley & Oegelman (1994), [20] Frail et al. (1996b), [21] Gaensler et al. (1999), [22] Gaensler & Wallace (2003), [23] Gaensler et al. (2008), [24] Giacani et al. (2000), [25] Gotthelf, Petre & Vasisht (1999), [26] Gotthelf et al. (2000), [27] Halpern & Gotthelf (2010), [28] Hobbs et al. (2004), [29] Hughes et al. (2003), [30] Kaspi et al. (2001), [31] Katsuda, Tsunemi & Mori (2008), [32] Kellett et al. (1987), [33] Kothes, Uyaniker & Yar (2002), [34] Koyama et al. (1997), [31] Kuiper et al. (2006), [36] Kulkarni et al. (2003), [37] Kumar, Safi-Harb & Gonzalez (2012), [38] Lazendic et al. (2003), [39] Lazendic et al. (2005), [40] Livingstone et al. (2011), [41] Livingstone & Kaspi (2011), [42] Lu & Aschenbach (2000), [43] Matheson & Safi-Harb (2010), [44] Matsui, Long & Tuohy (1988), [45] Mereghetti, Tiengo & Israel (2002), [46] Mineo et al. (2001), [47] Park et al. (2009), [48] Park et al. (2012), [49] Pavlov et al. (2001), [50] Pavlov et al. (2002), [51] Pfeffermann & Aschenbach (1996), [52] Ray et al. (2011), [53] Reed et al. (1995), [54] Reynoso et al. (1995), [55] Reynoso et al. (2004), [56] Rho et al. (1994), [57] Roger et al. (1988), [58] Roy, Gupta & Lewandowski (2012), [59] Safi-Harb, Ogelman & Finley (1994), [60] Safi-Harb, Ogelman & Finley (1995), [61] Sanbonmatsu & Helfand (1992), [62] Sasaki et al. (2013), [63] Seward et al. (2003), [64] Slane et al. (2002), [65] Strom & Stappers (2000), [66] Su et al. (2009), [67] Sun et al. (2004), [68] Tam & Roberts (2003), [69] Tian & Leahy (2008b), [70] Torii et al. (1999), [71] Torii et al. (2006), [72] Vasisht & Gotthelf (1997), [73] Vink & Kuiper (2006), [74] Wang et al. (2000), [75] Weltevrede, Johnston & Espinoza (2011), [76] Winkler et al. (2009), [77] Yuan et al. (2010), [78] Zeiger et al. (2008).

---

[a] `http://hea-www.cfa.harvard.edu/ChandraSNR/`

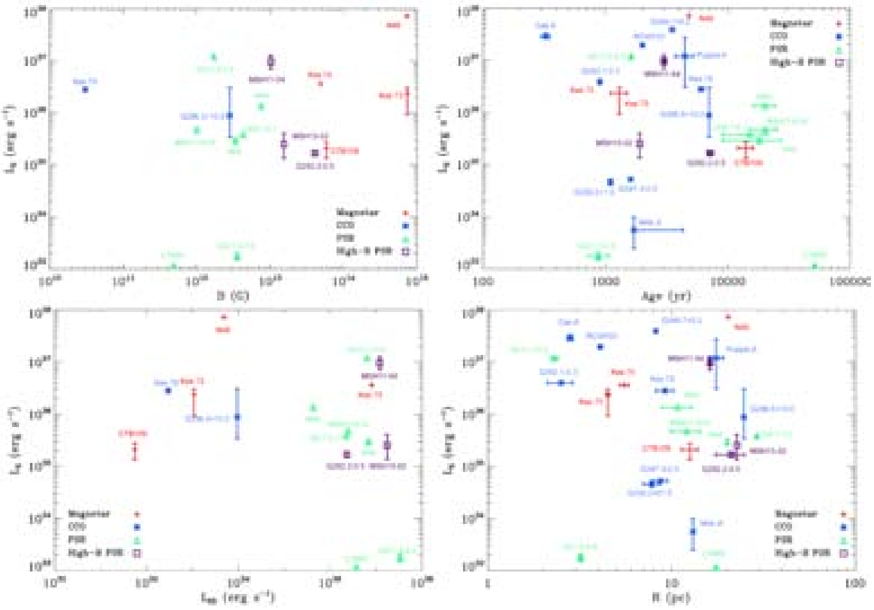

Fig. 6.4 X-ray luminosity of the all observed, and securely associated, X-ray emitting SNRs containing a magnetar, a CCO, a high-B pulsar or a normal pulsar, plotted versus magnetic-field (top-left), age (top-right), spin-down luminosity (bottom-left) and radius (bottom-right).

of pulsars having detected SNRs as a function of age, and compared it to the magnetar case. However, we caveat that there are several systematic effects in this comparison (different detection wavebands, distance, low number of magnetars in comparison with pulsars, etc.) we have been looking for a general trend. In figure 6.5 we plot the result of this comparison, where we can see how on average (taking the due caveats into consideration) for a similar age, pulsars and magnetars seems to show a similar probability to have a detected SNR.

Table 6.7 Spearman correlation coefficient (r), number of couples considered (N) and probability that the two samples are not correlated (p) evaluated by comparing the X-ray luminosity of the sources of our sample with the age, radius, surface magnetic field strength and spin-down luminosity.

Parameters	r	N	p
L_X vs. age	-0.158	24	0.46
L_X vs. radius	-0.245	24	0.25
L_X vs. B	0.271	16	0.31
L_X vs. L_{sd}	-0.309	16	0.25

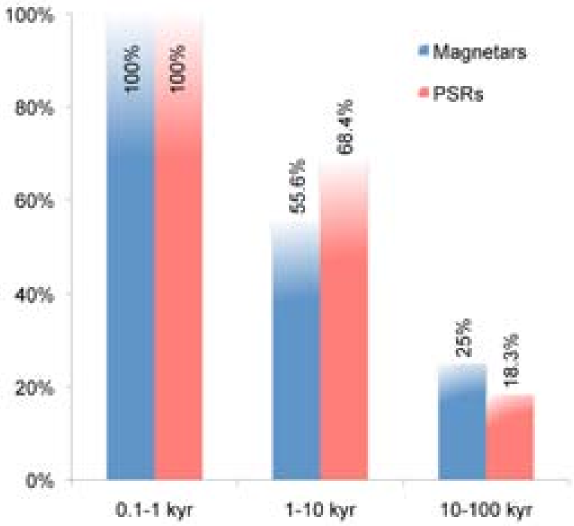

Fig. 6.5 Percentage of pulsars and magnetars having a detected SNR as a function of the age.

6.4 Conclusions

We have reported on the re-analysis of the X-ray emission of SNRs surrounding magnetars, using an empirical modeling of their spectrum with a Bremsstrahlung continuum plus several emission lines modeled by Gaussian functions. Our analysis, and the comparison of the emission of those remnants with other bright SNR surrounding normal pulsars suggest the following conclusions:

- We find no enhanced ionization states in the elements observed in magnetars' SNRs compared to similarly X-ray bright remnants observed around lower magnetic pulsars.
- No significant correlation is observed between the SNRs X-ray luminosities and the pulsar magnetic fields.
- We show that the percentage of magnetars and pulsars hosted in a detectable SNR are very similar, at a similar age.

Our findings does not support the claim of magnetars being formed via more energetic supernovae, or having a large rotational energy budget at birth that is released in the surrounding medium in the first phases of the magnetar formation. However, we caveat that although we do not find any hint in the SNRs to support such idea, we cannot exclude that: 1) most of the rotational energy has been emitted via neutrinos or gravitational waves, hence with no interaction with the remnant; or 2) we are restricted to a very small sample, and with larger statistics some correlation might be observed in the future.

Chapter 7

Concluding remarks

7.1 On this thesis

In this thesis, we have studied a few of the current open problems on pulsars, pulsar wind nebulae and supernova remnants, from a theoretical and/or observational point of view. We made special emphasis in spectral modeling of PWNe, and the comparison of the X-ray emission of SNRs surrounding magnetars with those remnants surrounding canonical pulsars.

Spectral modeling of PWNe is a useful tool to characterize the pulsar wind and obtain information about the distribution of accelerated particles as a function of the energy, degree of magnetization, energy densities of the background photon fields and the dynamical evolution of the PWN-SNR complex. The luminosity of these objects is strongly related with the characteristics of the central pulsar and the interaction of the pulsar wind with the SNR ejecta. We have developed a detailed spectral code which reproduces the electromagnetic spectrum of PWNe in free expansion, and we succeeded in fitting the spectra of many PWNe. We have studied approximations found in other models in the literature, and tested how these approximations affect the resulting PWN predicted spectra, and its time evolution. We have seen that the differences between models can be as large as 100% in flux .This introduces large uncertainties in the parameters when we apply these approximations in a PWN population study at different ages.

We have also shed light in other long standing PWN issues as: i) the synchrotron self Compton dominance in the Crab Nebula (why only in Crab? which are the configuration parameters to have a SSC dominated nebula?); ii) the particle dominance for the PWNe detected at TeV (why are they particle dominated? Is there any observational bias? can we detect magnetic dominated nebulae?); and iii) we have put some constrains the detectability at TeV of Crab-like PWNe by doing a parameter phase space exploration. In particular, we have observed that no Crab-like PWNe is SSC dominated if the spin-down luminosity is less than $\sim$70% of E_{Crab} and low ages (less than a few thousand years), and only particle dominated PWNe can be detected by the current Cherenkov telescopes (i.e. H.E.S.S.-like telescopes) above $\sim$1% of E_{Crab}. No magnetic dominated PWNe could be detected for PSRs younger than $\sim$10 kyr.

We have made a systematic study of all the young TeV-detected PWNe to evaluate the possible existence of common evolutive trends. We confirmed the unique SSC dominance in the Crab Nebula and for the rest of nebulae, the IC contribution is generally dominated by the FIR photon field. TeV-detected PWNe show similar radio, X-ray and γ-ray flux efficiencies with the exception of G292.2-0.5, for which the X-ray efficiency is very low. Generally, the electromagnetic spectrum is well described by a broken power law spectrum, which falls in a mean Lorentz factor of 10^5. Multiplicities are large $> 10^5$ and they are generally particle dominated. We do not find significant correlations between the efficiencies of emission at different frequencies and the magnetization. The same happens with the pulsar's characteristic age and the radio and X-ray luminosities. On the other hand, we find correlations of the radio and X-ray with the spin-down luminosity. Some anti-correlations have been found between the ratios of IC to synchrotron luminosities and the spin-down luminosity, and also between the γ-ray luminosity and the characteristic age.

The existence of PWNe with relatively high spin-down luminosity PSRs non-detected at TeV made us wondering if this could be explained in the classical context of low magnetized nebulae, or otherwise these cases could be candidates of PWNe with high magnetization. We have modeled the non-detected at TeV PWNe with PSRs with an spin-down luminosity $> 10^{37}$ erg s^{-1} and we have noticed that the non-detection of these nebulae can be explained with low magnetization models and predict the detection of G292.0+1.8 and G310.6-1.6 in a reasonable exposure time with H.E.S.S. The synchrotron spectrum of these nebulae have been fitted assuming high magnetization with some caveats, which predict no detection of these sources neither H.E.S.S.-like or CTA-like telescopes. Future observations will discern between both models.

Regarding the X-ray analysis of supernova remnants, X-ray spectroscopy gives us a powerful tool to know about the energetics, kinetics, chemical composition, abundances, level of ionization and interaction with the ambient medium of these objects. Here, we applied this technique to investigate further on the formation mechanism of magnetars. The alpha-dynamo mechanism proposed in the 1990's is believed to release a large rotational energy that might be observed in the SNRs characteristics. Vink & Kuiper (2006) studied the energetics of the explosion observing SNRs in X-rays with an associated magnetar, but they did not find any clear evidence for this additional energy. We have extended this work and looked for the element ionization and the X-ray luminosity in comparison with other SNRs with an associated neutron star. Our main conclusions have been that we have not found enhanced ionization states in the elements observed in SNRs with magnetars compared to other X-ray bright SNRs observed around lower magnetic pulsars, and no significant correlation is observed between the X-ray luminosities of the SNRs and the PSR magnetic fields.

7.2 Ongoing work

As we said in the introduction, the current number of PWNe detected at TeV is $\sim$30, but this number will increase severely with the forthcoming generation of Cherenkov radiation telescopes, as CTA. The new level of sensitivity, spatial resolution and number of new sources will be challenging for these models, which will have to include high precision at radiative and magnetohydrodynamic level. It is important to be prepared for that moment and continue the improvement of the current radiative codes for PWNe to have enough capacity at physical and programming level to analyse the data. We are currently working on the implementation of new subroutines in TIDE-PWN to reproduce the interaction of the reverse shock of the SNR with the PWN. When the reverse shock collides with the PWN shell, the PWN contracts itself, increasing the magnetic field and burning off the high energy electrons. The introduction of the dynamics after the reverberation phase increase the number of PWNe suitable for modeling.

References

Abdo A. A. et al., 2009a, ApJ, 706, 1331

Abdo A. A. et al., 2010a, ApJ, 708, 1254

Abdo A. A. et al., 2010b, ApJS, 187, 460

Abdo A. A. et al., 2009b, ApJL, 699, L102

Abdo A. A. et al., 2008, Science, 322, 1218

Abdo A. A. et al., 2013, ApJS, 208, 17

Abdo A. A. et al., 2012, ApJ, 744, 146

Acciari V. A. et al., 2010, ApJL, 719, L69

Acero F. et al., 2013, ApJ, 773, 77

Ackermann M. et al., 2011, ApJ, 726, 35

Actis M. et al., 2011, Experimental Astronomy, 32, 193

Aharonian F. et al., 2002, A&A, 393, L37

Aharonian F. et al., 2004, ApJ, 614, 897

Aharonian F. et al., 2005a, A&A, 432, L25

Aharonian F. et al., 2005b, A&A, 435, L17

Aharonian F. et al., 2008, A&A, 477, 353

Aharonian F. et al., 2006a, A&A, 457, 899

Aharonian F. et al., 2006b, ApJ, 636, 777

Aharonian F. et al., 2007, ApJ, 661, 236

Aharonian F. A., Atoyan A. M., 1999, A&A, 351, 330

Aharonian F. A., Atoyan A. M., Kifune T., 1997, MNRAS, 291, 162

Ahmad I., Greene J. P., Moore E. F., Ghelberg S., Ofan A., Paul M., Kutschera W., 2006, Phys. Rev. C., 74, 065803

Albert J. et al., 2006a, ApJL, 637, L41

Albert J. et al., 2006b, ApJL, 643, L53

Albert J. et al., 2008a, ApJ, 674, 1037

Albert J. et al., 2008b, ApJL, 675, L25

Aleksić J. et al., 2012, Astroparticle Physics, 35, 435

Aleksić J. et al., 2014, ArXiv e-prints

Aliu E. et al., 2013, ApJ, 764, 38

Altenhoff W. J., Downes D., Pauls T., Schraml J., 1979, A&AS, 35, 23

Anderhub H. et al., 2010, ApJ, 710, 828

Anderson P. W., Itoh N., 1975, Nature, 256, 25

Antoniadis J. et al., 2013, Science, 340, 448

Archibald R. F. et al., 2013, Nature, 497, 591

Arendt R. G., 1991, AJ, 101, 2160

Arnaud K. A., 1996, in Astronomical Society of the Pacific Conference Series, Vol. 101, Astronomical Data Analysis Software and Systems V, Jacoby G. H., Barnes J., eds., p. 17

Arons J., 2002, in Astronomical Society of the Pacific Conference Series, Vol. 271, Neutron Stars in Supernova Remnants, Slane P. O., Gaensler B. M., eds., p. 71

Arumugasamy P., Pavlov G., Kargaltsev O., 2013, in The Fast and the Furious: Energetic Phenomena in Isolated Neutron Stars, Pulsar Wind Nebulae and Supernova Remnants, Ness J.-U., ed.

Arzoumanian Z., Gotthelf E. V., Ransom S. M., Safi-Harb S., Kothes R., Landecker T. L., 2011, ApJ, 739, 39

Arzoumanian Z., Safi-Harb S., Landecker T. L., Kothes R., Camilo F., 2008, ApJ, 687, 505

Aschenbach B., Egger R., Trümper J., 1995, Nature, 373, 587

Asvarov A. I., Guseinov O. H., Kasumov F. K., Dogel' V. A., 1990, A&A, 229, 196

Atoyan A. M., Aharonian F. A., 1996, MNRAS, 278, 525

Baade W., Zwicky F., 1934, Physical Review, 46, 76

Backer D., Kulkarni S., Heiles C., Davis M., Goss M., 1982, IAU Circ., 3743, 2

Baldwin J. E., 1971, in IAU Symposium, Vol. 46, The Crab Nebula, Davies R. D., Graham-Smith F., eds., p. 22

Banas K. R., Hughes J. P., Bronfman L., Nyman L.-A., 1997, ApJ, 480, 607

Becker R. H., Helfand D. J., 1984, ApJ, 283, 154

Becker R. H., Helfand D. J., Szymkowiak A. E., 1983, ApJL, 268, L93

Becker R. H., Kundu M. R., 1976, ApJ, 204, 427

Becker W., Prinz T., Winkler P. F., Petre R., 2012, ApJ, 755, 141

Becker W., Truemper J., 1997, A&A, 326, 682

Bednarek W., Bartosik M., 2003, A&A, 405, 689

Bednarek W., Bartosik M., 2005, Journal of Physics G Nuclear Physics, 31, 1465

Beiersdorfer P., Phillips T., Jacobs V. L., Hill K. W., Bitter M., von Goeler S., Kahn S. M., 1993, ApJ, 409, 846

Bietenholz M. F., 2006, ApJ, 645, 1180

Bietenholz M. F., Bartel N., 2008, MNRAS, 386, 1411

Bietenholz M. F., Hester J. J., Frail D. A., Bartel N., 2004, ApJ, 615, 794

Blanton E. L., Helfand D. J., 1996, ApJ, 470, 961

Bleeker J. A. M., Willingale R., van der Heyden K., Dennerl K., Kaastra J. S., Aschenbach B., Vink J., 2001, A&A, 365, L225

Blondin J. M., Chevalier R. A., Frierson D. M., 2001, ApJ, 563, 806

Blumenthal G. R., 1971, PhRvD, 3, 2308

Blumenthal G. R., Gould R. J., 1970, Reviews of Modern Physics, 42, 237

Bocchino F., van der Swaluw E., Chevalier R., Bandiera R., 2005, A&A, 442, 539

Bocchino F., Warwick R. S., Marty P., Lumb D., Becker W., Pigot C., 2001, A&A, 369, 1078

Bock D. C.-J., Gaensler B. M., 2005, ApJ, 626, 343

Bogovalov S. V., Chechetkin V. M., Koldoba A. V., Ustyugova G. V., 2005, MNRAS, 358, 705

Bogovalov S. V., Khangoulyan D. V., 2002, Astronomy Letters, 28, 373

Borkowski K. J., Lyerly W. J., Reynolds S. P., 2001, ApJ, 548, 820

Borkowski K. J., Reynolds S. P., Green D. A., Hwang U., Petre R., Krishnamurthy K., Willett R., 2010, ApJL, 724, L161

Brazier K. T. S., Reimer O., Kanbach G., Carraminana A., 1998, MNRAS, 295, 819

Brogan C. L., Gaensler B. M., Gelfand J. D., Lazendic J. S., Lazio T. J. W., Kassim N. E., McClure-Griffiths N. M., 2005, ApJL, 629, L105

Bucciantini N., Amato E., Bandiera R., Blondin J. M., Del Zanna L., 2004, A&A, 423, 253

Bucciantini N., Arons J., Amato E., 2011, MNRAS, 410, 381

Bucciantini N., Blondin J. M., Del Zanna L., Amato E., 2003, A&A, 405, 617

Buras R., Janka H.-T., Rampp M., Kifonidis K., 2006a, A&A, 457, 281

Buras R., Rampp M., Janka H.-T., Kifonidis K., 2006b, A&A, 447, 1049

Burgay M. et al., 2003, Nature, 426, 531

Büsching I., de Jager O. C., Potgieter M. S., Venter C., 2008, ApJL, 678, L39

Camilo F., Kaspi V. M., Lyne A. G., Manchester R. N., Bell J. F., D'Amico N., McKay N. P. F., Crawford F., 2000, ApJ, 541, 367

Camilo F., Lorimer D. R., Bhat N. D. R., Gotthelf E. V., Halpern J. P., Wang Q. D., Lu F. J., Mirabal N., 2002, ApJL, 574, L71

Camilo F. et al., 2004, ApJL, 611, L25

Camilo F., Ransom S. M., Gaensler B. M., Lorimer D. R., 2009, ApJL, 700, L34

Camilo F., Ransom S. M., Gaensler B. M., Slane P. O., Lorimer D. R., Reynolds J., Manchester R. N., Murray S. S., 2006, ApJ, 637, 456

Campana R., Mineo T., de Rosa A., Massaro E., Dean A. J., Bassani L., 2008, MNRAS, 389, 691

Caraveo P. A., Bignami G. F., Mereghetti S., Mombelli M., 1992, ApJL, 395, L103

Caraveo P. A., De Luca A., Marelli M., Bignami G. F., Ray P. S., Saz Parkinson P. M., Kanbach G., 2010, ApJL, 725, L6

Carrigan S. et al., 2013, ArXiv e-prints

Carter L. M., Dickel J. R., Bomans D. J., 1997, PASP, 109, 990

Case G. L., Bhattacharya D., 1998, ApJ, 504, 761

Cassam-Chenaï G., Decourchelle A., Ballet J., Hwang U., Hughes J. P., Petre R., et al., 2004, A&A, 414, 545

Castelletti G., Giacani E., Dubner G., Joshi B. C., Rao A. P., Terrier R., 2011, A&A, 536, A98

Castro D., Slane P., Carlton A., Figueroa-Feliciano E., 2013, ApJ, 774, 36

Caswell J. L., Haynes R. F., 1987, A&A, 171, 261

Caswell J. L., McClure-Griffiths N. M., Cheung M. C. M., 2004, MNRAS, 352, 1405

Caswell J. L., Milne D. K., Wellington K. J., 1981, MNRAS, 195, 89

Caswell J. L., Murray J. D., Roger R. S., Cole D. J., Cooke D. J., 1975, A&A, 45, 239

Chadwick J., 1932, Nature, 129, 312

Chandrasekhar S., 1935, MNRAS, 95, 226

Chang C., Pavlov G. G., Kargaltsev O., Shibanov Y. A., 2012, ApJ, 744, 81

Chaves R. C. G., de Oña Wilhemi E., Hoppe S., 2008, in American Institute of Physics Conference Series, Vol. 1085, American Institute of Physics Conference Series, Aharonian F. A., Hofmann W., Rieger F., eds., pp. 219–222

Chen Y., Wang Q. D., Gotthelf E. V., Jiang B., Chu Y.-H., Gruendl R., 2006, ApJ, 651, 237

Chevalier R. A., 1982, ApJ, 258, 790

Chevalier R. A., 1998, MmSAI, 69, 977

Chevalier R. A., 2004, Advances in Space Research, 33, 456

Chevalier R. A., 2005, ApJ, 619, 839

Clark D. H., Stephenson F. R., 1982, in NATO ASIC Proc. 90: Supernovae: A Survey of Current Research, Rees M. J., Stoneham R. J., eds., pp. 355–370

Condon J. J., Broderick J. J., Seielstad G. A., 1989, AJ, 97, 1064

Condon J. J., Griffith M. R., Wright A. E., 1993, AJ, 106, 1095

Cordes J. M., Lazio T. J. W., 2003, ArXiv Astrophysics e-prints

Cox D. P., 1972, ApJ, 178, 159

Cox D. P., Shelton R. L., Maciejewski W., Smith R. K., Plewa T., Pawl A., Rózyczka M., 1999, ApJ, 524, 179

Crawford F., Gaensler B. M., Kaspi V. M., Manchester R. N., Camilo F., Lyne A. G., Pivovaroff M. J., 2001, ApJ, 554, 152

Danilenko A., Kirichenko A., Mennickent R. E., Pavlov G., Shibanov Y., Zharikov S., Zyuzin D., 2012, A&A, 540, A28

Davies B., Figer D. F., Kudritzki R.-P., Trombley C., Kouveliotou C., Wachter S., 2009, ApJ, 707, 844

de Jager O. C., Djannati-Ataï A., 2009, in Astrophysics and Space Science Library, Vol. 357, Astrophysics and Space Science Library, Becker W., ed., p. 451

de Oña-Wilhelmi E. et al., 2013, Astroparticle Physics, 43, 287 de Rosa A., Ubertini P., Campana R., Bazzano A., Dean A. J., Bassani L., 2009, MNRAS, 393, 527

Decourchelle A. et al., 2001, A&A, 365, L218

Del Zanna L., Amato E., Bucciantini N., 2004, A&A, 421, 1063

Del Zanna L., Volpi D., Amato E., Bucciantini N., 2006, A&A, 453, 621

DeLaney T., Rudnick L., 2003, ApJ, 589, 818

Demorest P. B., Pennucci T., Ransom S. M., Roberts M. S. E., Hessels J. W. T., 2010, Nature, 467, 1081

Dickey J. M., Lockman F. J., 1990, ARA&A, 28, 215

Djannati-Ataï A., 2009, in MA

Dodson R., Legge D., Reynolds J. E., McCulloch P. M., 2003, ApJ, 596, 1137

Dodson R. G., McCulloch P. M., Lewis D. R., 2002, ApJL, 564, L85

Donati J.-F., Babel J., Harries T. J., Howarth I. D., Petit P., Semel M., 2002, MNRAS, 333, 55

Donati J.-F., Howarth I. D., Bouret J.-C., Petit P., Catala C., Landstreet J., 2006, MNRAS, 365, L6

Du Plessis I., de Jager O. C., Buchner S., Nel H. I., North A. R., Raubenheimer B. C., van der Walt D. J., 1995, ApJ, 453, 746

Dubner G., Giacani E., Decourchelle A., 2008, A&A, 487, 1033

Dubner G., Loiseau N., Rodríguez-Pascual P., Smith M. J. S., Giacani E., Castelletti G., 2013, A&A, 555, A9

Dubner G. M., Gaensler B. M., Giacani E. B., Goss W. M., Green A. J., 2002, AJ, 123, 337

Duncan A. R., Haynes R. F., Stewart R. T., Jones K. L., 1995, MNRAS, 277, 319

Duncan R. C., Thompson C., 1992, ApJL, 392, L9

Duncan R. C., Thompson C., 1996, in American Institute of Physics Conference Series, Vol. 366, High Velocity Neutron Stars, Rothschild R. E., Lingenfelter R. E., eds., pp. 111–117

Espinoza C. M., Lyne A. G., Stappers B. W., Kramer M., 2011, MNRAS, 414, 1679

Esposito P. et al., 2007, A&A, 476, 321

Fahlman G. G., Gregory P. C., 1981, Nature, 293, 202

Fahlman G. G., Gregory P. C., 1983, in IAU Symposium, Vol. 101, Supernova Remnants and their X-ray Emission, Danziger J., Gorenstein P., eds., pp. 445–453

Fang J., Zhang L., 2010a, A&A, 515, A20

Fang J., Zhang L., 2010b, ApJ, 718, 467

Ferrand G., Safi-Harb S., 2012, Advances in Space Research, 49, 1313

Ferrario L., Wickramasinghe D., 2006, MNRAS, 367, 1323

Fesen R., Rudie G., Hurford A., Soto A., 2008, ApJS, 174, 379

Fesen R. A. et al., 2006, ApJ, 645, 283

Fesen R. A., Kremer R., Patnaude D., Milisavljevic D., 2012, AJ, 143, 27

Figer D. F., Najarro F., Geballe T. R., Blum R. D., Kudritzki R. P., 2005, ApJL, 622, L49

Finley J. P., Oegelman H., 1994, ApJL, 434, L25

Forot M., Hermsen W., Renaud M., Laurent P., Grenier I., Goret P., Khelifi B., Kuiper L., 2006, ApJL, 651, L45

Frail D. A., Giacani E. B., Goss W. M., Dubner G., 1996a, ApJL, 464, L165

Frail D. A., Goss W. M., Reynoso E. M., Giacani E. B., Green A. J., Otrupcek R., 1996b, AJ, 111, 1651

Fryer C. L., Warren M. S., 2004, ApJ, 601, 391

Fuchs Y., Mirabel F., Chaty S., Claret A., Cesarsky C. J., Cesarsky D. A., 1999, A&A, 350, 891

Funk S. et al., 2007a, A&A, 470, 249

Funk S., Hinton J. A., Pühlhofer G., Aharonian F. A., Hofmann W., Reimer O., Wagner S., 2007b, ApJ, 662, 517

Gabici S., Aharonian F. A., Casanova S., 2009, MNRAS, 396, 1629

Gaensler B. M., Arons J., Kaspi V. M., Pivovaroff M. J., Kawai N., Tamura K., 2002, ApJ, 569, 878

Gaensler B. M., Brazier K. T. S., Manchester R. N., Johnston S., Green A. J., 1999, MNRAS, 305, 724

Gaensler B. M., McClure-Griffiths N. M., Oey M. S., Haverkorn M., Dickey J. M., Green A. J., 2005, ApJL, 620, L95

Gaensler B. M., Pivovaroff M. J., Garmire G. P., 2001, ApJL, 556, L107

Gaensler B. M., Slane P. O., 2006, ARA&A, 44, 17

Gaensler B. M., Slane P. O., Gotthelf E. V., Vasisht G., 2001, ApJ, 559, 963

Gaensler B. M. et al., 2008, ApJL, 680, L37

Gaensler B. M., Wallace B. J., 2003, ApJ, 594, 326

Gallant Y. A. et al., 2008, in American Institute of Physics Conference Series, Vol. 983, 40 Years of Pulsars: Millisecond Pulsars, Magnetars and More, Bassa C., Wang Z., Cumming A., Kaspi V. M., eds., pp. 195–199

Gallant Y. A., Tuffs R. J., 1998, MmSAI, 69, 963

Gallant Y. A., Tuffs R. J., 1999, in ESA Special Publication, Vol. 427, The Universe as Seen by ISO, Cox P., Kessler M., eds., p. 313

Gast H. et al., 2011, International Cosmic Ray Conference, 7, 157

Gavriil F. P., Gonzalez M. E., Gotthelf E. V., Kaspi V. M., Livingstone M. A., Woods P. M., 2008, Science, 319, 1802

Gelfand J. D., Slane P. O., Zhang W., 2009, ApJ, 703, 2051

Giacani E., Rovero A., Cillis A. N., Pichel A., Dubner G., 2013

Giacani E. B., Dubner G. M., Green A. J., Goss W. M., Gaensler B. M., 2000, AJ, 119, 281

Giacani E. B., Dubner G. M., Kassim N. E., Frail D. A., Goss W. M., Winkler P. F., Williams B. F., 1997, AJ, 113, 1379

Giacconi R., Gursky H., Kellogg E., Schreier E., Tananbaum H., 1971, ApJL, 167, L67

Ginzburg V. L., 1979, Theoretical physics and astrophysics. Pergamon Press

Ginzburg V. L., Syrovatskii S. I., 1964, The Origin of Cosmic Rays. Springer

Ginzburg V. L., Syrovatskii S. I., 1965, ARA&A, 3, 297

Goldreich P., Julian W. H., 1969, ApJ, 157, 869

Gonzalez M., Safi-Harb S., 2003, ApJL, 591, L143

Gonzalez M. E., Kaspi V. M., Camilo F., Gaensler B. M., Pivovaroff M. J., 2005, ApJ, 630, 489

Gotthelf E. V., Halpern J. P., 2009, ApJL, 700, L158

Gotthelf E. V., Helfand D. J., Newburgh L., 2007, ApJ, 654, 267

Gotthelf E. V., Petre R., Vasisht G., 1999, ApJL, 514, L107

Gotthelf E. V., Vasisht G., 1997, ApJL, 486, L133

Gotthelf E. V., Vasisht G., Boylan-Kolchin M., Torii K., 2000, ApJL, 542, L37

Gotthelf E. V., Vasisht G., Dotani T., 1999, ApJL, 522, L49

Gotthelf E. V., Wang Q. D., 2000, ApJL, 532, L117

Grasdalen G. L., 1979, PASP, 91, 436

Green D. A., 1986, MNRAS, 218, 533

Green D. A., 1994, ApJS, 90, 817

Green D. A., 2009, Bulletin of the Astronomical Society of India, 37, 45

Green D. A., Scheuer P. A. G., 1992, MNRAS, 258, 833

Green D. A., Tuffs R. J., Popescu C. C., 2004, MNRAS, 355, 1315

Gregory P. C., Fahlman G. G., 1980, Nature, 287, 805

Griffith M., Langston G., Heflin M., Conner S., Lehar J., Burke B., 1990, ApJS, 74, 129

Griffith M. R., Wright A. E., 1993, AJ, 105, 1666

H. E. S. S. Collaboration, :, Djannati-Atai A., De Jager O. C., Terrier R., Gallant Y. A., Hoppe S., 2007, ArXiv e-prints

Hall T. A., Wakely S. P., VERITAS Collaboration, 2001, International Cosmic Ray Conference, 6, 2485

Halpern J. P., Camilo F., Gotthelf E. V., Helfand D. J., Kramer M., Lyne A. G., Leighly K. M., Eracleous M., 2001, ApJL, 552, L125

Halpern J. P., Gotthelf E. V., 2010, ApJ, 709, 436

Halpern J. P., Gotthelf E. V., Camilo F., 2012, ApJL, 753, L14

Halpern J. P., Gotthelf E. V., Camilo F., Collins B., Helfand D. J., 2002, in Astronomical Society of the Pacific Conference Series, Vol. 271, Neutron Stars in Supernova Remnants, Slane P. O., Gaensler B. M., eds., p. 199

Halpern J. P., Gotthelf E. V., Camilo F., Helfand D. J., Ransom S. M., 2004, ApJ, 612, 398

Harding A. K., 2013, Frontiers of Physics, 8, 679

Harris D. E., Roberts J. A., 1960, PASP, 72, 237

Haug E., 1998, Solar Physics, 178, 341

Haug E., 2004, A&A, 423, 793

Hayato A. et al., 2010, ApJ, 725, 894

Heger A., Fryer C. L., Woosley S. E., Langer N., Hartmann D. H., 2003, ApJ, 591, 288

Helfand D. J., Becker R. H., 1987, ApJ, 314, 203

Helfand D. J., Becker R. H., Hawkins G., White R. L., 1994, ApJ, 434, 627

Helfand D. J., Collins B. F., Gotthelf E. V., 2003, ApJ, 582, 783

Helfand D. J., Gotthelf E. V., Halpern J. P., Camilo F., Semler D. R., Becker R. H., White R. L., 2007, ApJ, 665, 1297

Hennessy G. S. et al., 1992, ApJL, 395, L13

H.E.S.S. Collaboration et al., 2012, A&A, 545, L2

H.E.S.S. Collaboration et al., 2011a, A&A, 533, A103

H.E.S.S. Collaboration et al., 2011b, A&A, 525, A46

Hester J. J. et al., 1996, ApJ, 456, 225

Hewish A., Bell S. J., Pilkington J. D. H., Scott P. F., Collins R. A., 1968, Nature, 217, 709

Hillas A. M. et al., 1998, ApJ, 503, 744

Hinton J. A., Hofmann W., 2009, ARA&A, 47, 523

Hobbs G., Lyne A. G., Kramer M., Martin C. E., Jordan C., 2004, MNRAS, 353, 1311

Holler M., Schöck F. M., Eger P., Kießling D., Valerius K., Stegmann C., 2012, A&A, 539, A24

Hughes J. P., Hayashi I., Koyama K., 1998, ApJ, 505, 732

Hughes J. P., Helfand D. J., 1985, ApJ, 291, 544

Hughes J. P., Slane P. O., Burrows D. N., Garmire G., Nousek J. A., Olbert C. M., Keohane J. W., 2001, ApJL, 559, L153

Hughes J. P., Slane P. O., Park S., Roming P. W. A., Burrows D. N., 2003, ApJL, 591, L139

Hurford A. P., Fesen R. A., 1995, MNRAS, 277, 549

Hurley-Walker N. et al., 2009, MNRAS, 396, 365

Hwang U., Gotthelf E. V., 1997, ApJ, 475, 665

Hwang U., Petre R., Flanagan K. A., 2008, ApJ, 676, 378

Indebetouw R. et al., 2009, ApJ, 694, 84

Itoh H., 1977, PASJ, 29, 813

Iwasawa K., Koyama K., Halpern J. P., 1992, PASJ, 44, 9

Jackson J. D., 1962, Classical Electrodynamics. Wiley

Jones F. C., 1968, Physical Review, 167, 1159

Kaaret P. et al., 2001, ApJ, 546, 1159

Kaastra J. S., Jansen F. A., 1993, A&AS, 97, 873

Kaastra J. S., Paerels F. B. S., Durret F., Schindler S., Richter P., 2008, SSRv, 134, 155

Kargaltsev O., Pavlov G. G., 2008, in American Institute of Physics Conference Series, Vol. 983, 40 Years of Pulsars: Millisecond Pulsars, Magnetars and More, Bassa C., Wang Z., Cumming A., Kaspi V. M., eds., pp. 171–185

Kargaltsev O., Pavlov G. G., 2010, X-ray Astronomy 2009; Present Status, Multi-Wavelength Approach and Future Perspectives, 1248, 25

Kargaltsev O., Pavlov G. G., Wong J. A., 2009, ApJ, 690, 891

Kaspi V. M., Boydstun K., 2010, ApJL, 710, L115

Kaspi V. M., Crawford F., Manchester R. N., Lyne A. G., Camilo F., D'Amico N., Gaensler B. M., 1998, ApJL, 503, L161

Kaspi V. M., Manchester R. N., Siegman B., Johnston S., Lyne A. G., 1994, ApJL, 422, L83

Kaspi V. M., Roberts M. E., Vasisht G., Gotthelf E. V., Pivovaroff M., Kawai N., 2001, ApJ, 560, 371

Katsuda S., Tsunemi H., Mori K., 2008, ApJL, 678, L35

Keek S., Kuiper L., Hermsen W., 2006, The Astronomer's Telegram, 810, 1

Kellett B. J., Branduardi-Raymont G., Culhane J. L., Mason I. M., Mason K. O., Whitehouse D. R., 1987, MNRAS, 225, 199

Kennel C. F., Coroniti F. V., 1984a, ApJ, 283, 694

Kennel C. F., Coroniti F. V., 1984b, ApJ, 283, 710

Khelifi B., 2002, PhD thesis, University of Caen

Khélifi B., Masterson C., Pita S., et al., 2008, International Cosmic Ray Conference, 2, 803

Kinugasa K., Tsunemi H., 1999, PASJ, 51, 239

Kirshner R. P., Morse J. A., Winkler P. F., Blair W. P., 1989, ApJ, 342, 260

Klein O., Nishina Y., 1929, Z. Phys., 52, 853

Komissarov S. S., Lyubarsky Y. E., 2004, MNRAS, 349, 779

Konopelko A., 2008, International Cosmic Ray Conference, 2, 767

Koo B.-C. et al., 2008, ApJL, 673, L147

Koo B.-C. et al., 2011, ApJ, 732, 6

Kothes R., 2010, in Astronomical Society of the Pacific Conference Series, Vol. 438, Astronomical Society of the Pacific Conference Series, Kothes R., Landecker T. L., Willis A. G., eds., p. 347

Kothes R., Reich W., Uyan ker B., 2006, ApJ, 638, 225

Kothes R., Uyaniker B., Pineault S., 2001, ApJ, 560, 236

Kothes R., Uyaniker B., Yar A., 2002, ApJ, 576, 169

Koyama K., Kinugasa K., Matsuzaki K., Nishiuchi M., Sugizaki M., Torii K., Yamauchi S., Aschenbach B., 1997, PASJ, 49, L7

Kriss G. A., Becker R. H., Helfand D. J., Canizares C. R., 1985, ApJ, 288, 703

Kuiper L., Hermsen W., 2009, ArXiv e-prints

Kuiper L., Hermsen W., Cusumano G., Diehl R., Schönfelder V., Strong A., Bennett K., McConnell M. L., 2001, A&A, 378, 918

Kuiper L., Hermsen W., den Hartog P. R., Collmar W., 2006, ApJ, 645, 556

Kuiper L., Hermsen W., Krijger J. M., Bennett K., Carramiñana A., Schönfelder V., Bailes M., Manchester R. N., 1999, A&A, 351, 119

Kulkarni S. R., Kaplan D. L., Marshall H. L., Frail D. A., Murakami T., Yonetoku D., 2003, ApJ, 585, 948

Kumar H. S., Safi-Harb S., 2008, ApJL, 678, L43

Kumar H. S., Safi-Harb S., Gonzalez M. E., 2012, ApJ, 754, 96

Kumar H. S., Safi-Harb S., Slane P. O., Gotthelf E. V., 2014, ApJ, 781, 41

Laming J. M., 2001, ApJ, 546, 1149

Landau L., 1932, Phy. Z. Sowejtunion, 1, 285

Landecker T. L., Higgs L. A., Wendker H. J., 1993, A&A, 276, 522

Landi R., de Rosa A., Dean A. J., Bassani L., Ubertini P., Bird A. J., 2007, MNRAS, 380, 926

Lang C. C., Wang Q. D., Lu F., Clubb K. I., 2010, ApJ, 709, 1125

Lazendic J. S., Dickel J. R., Haynes R. F., Jones P. A., White G. L., 2000, ApJ, 540, 808

Lazendic J. S., Slane P. O., Gaensler B. M., Plucinsky P. P., Hughes J. P., Galloway D. K., Crawford F., 2003, ApJL, 593, L27

Lazendic J. S., Slane P. O., Hughes J. P., Chen Y., Dame T. M., 2005, ApJ, 618, 733

Leahy D. A., Tian W., Wang Q. D., 2008, AJ, 136, 1477

Leahy D. A., Tian W. W., 2008, A&A, 480, L25

Lemiere A., Slane P., Gaensler B. M., Murray S., 2009, ApJ, 706, 1269

Lemoine-Goumard M. et al., 2011, A&A, 533, A102

Li H., Chen Y., Zhang L., 2010, MNRAS, 408, L80

Lin L. C. C., Huang R. H. H., Takata J., Hwang C. Y., Kong A. K. H., Hui C. Y., 2010, ApJL, 725, L1

Livingstone M. A., Kaspi V. M., 2011, ApJ, 742, 31

Livingstone M. A., Kaspi V. M., Gavriil F. P., 2005, ApJ, 633, 1095

Livingstone M. A., Kaspi V. M., Gavriil F. P., Manchester R. N., 2005, ApJ, 619, 1046

Livingstone M. A., Kaspi V. M., Gotthelf E. V., Kuiper L., 2006, ApJ, 647, 1286

Livingstone M. A., Ng C.-Y., Kaspi V. M., Gavriil F. P., Gotthelf E. V., 2011, ApJ, 730, 66

Longair M. S., 1994, High energy astrophysics. Volume 2. Stars, the Galaxy and the interstellar medium. Cambridge University Press

Lopez L. A., Ramirez-Ruiz E., Badenes C., Huppenkothen D., Jeltema T. E., Pooley D. A., 2009, ApJL, 706, L106

Lopez L. A., Ramirez-Ruiz E., Huppenkothen D., Badenes C., Pooley D. A., 2011, ApJ, 732, 114

Lu F. J., Aschenbach B., 2000, A&A, 362, 1083

Lu F. J., Aschenbach B., Song L. M., 2001, A&A, 370, 570

Lu F. J., Wang Q. D., Aschenbach B., Durouchoux P., Song L. M., 2002, ApJL, 568, L49

Lyne A. G., Pritchard R. S., Smith F. G., 1988, MNRAS, 233, 667

Macías-Pérez J. F., Mayet F., Aumont J., Désert F.-X., 2010, ApJ, 711, 417

Maeda Y. et al., 2009, PASJ, 61, 1217

Malizia A. et al., 2007, ApJ, 668, 81

Manchester R. N., Hobbs G. B., Teoh A., Hobbs M., 2005, AJ, 129, 1993

Manchester R. N., Staveley-Smith L., Kesteven M. J., 1993, ApJ, 411, 756

Manchester R. N., Tuohy I. R., Damico N., 1982, ApJL, 262, L31

Marsden P. L., Gillett F. C., Jennings R. E., Emerson J. P., de Jong T., Olnon F. M., 1984, ApJL, 278, L29

Martín J., Torres D. F., Cillis A., de Oña Wilhelmi E., 2014, ArXiv e-prints

Martín J., Torres D. F., Rea N., 2012, MNRAS, 427, 415

Matheson H., Safi-Harb S., 2005, Advances in Space Research, 35, 1099

Matheson H., Safi-Harb S., 2010, ApJ, 724, 572

Matsui Y., Long K. S., Tuohy I. R., 1988, ApJ, 329, 838

Mattana F. et al., 2009, ApJ, 694, 12

Mattox J. R., Koh D. T., Lamb R. C., Macomb D. J., Prince T. A., Ray P. S., 1996, A&AS, 120, C95

Mayer M., 2010, PhD thesis, Erlangen Center for Astroparticle physics

Mazets E. P., Golenetskij S. V., Guryan Y. A., 1979, Soviet Astronomy Letters, 5, 343

Mazets E. P., Golentskii S. V., Ilinskii V. N., Aptekar R. L., Guryan I. A., 1979a, Nature, 282, 587

Mazets E. P., Golentskii S. V., Ilinskii V. N., Aptekar R. L., Guryan I. A., 1979b, Nature, 282, 587

McBride V. A. et al., 2008, A&A, 477, 249

Méhault J., 2011, International Cosmic Ray Conference, 7, 181

Melatos A., 1998, MmSAI, 69, 1009

Mendoza C., Kallman T. R., Bautista M. A., Palmeri P., 2004, A&A, 414, 377

Mereghetti S., 2008, A&ARv, 15, 225

Mereghetti S., Sidoli L., Israel G. L., 1998, A&A, 331, L77

Mereghetti S., Tiengo A., Israel G. L., 2002, ApJ, 569, 275

Mewe R., 1999, in Lecture Notes in Physics, Berlin Springer Verlag, Vol. 520, X-Ray Spectroscopy in Astrophysics, van Paradijs J., Bleeker J. A. M., eds., p. 109

Miceli M. et al., 2009, A&A, 501, 239

Micelotta E. R., Brandl B. R., Israel F. P., 2009, A&A, 500, 807

Mignani R. P., 2012, in Astronomical Society of the Pacific Conference Series, Vol. 466, Electromagnetic Radiation from Pulsars and Magnetars, Lewandowski W., Maron O., Kijak J., eds., p. 3

Mignani R. P., De Luca A., Hummel W., Zajczyk A., Rudak B., Kanbach G., S owikowska A., 2012, A&A, 544, A100

Mignani R. P., de Luca A., Rea N., Shearer A., Collins S., Torres D. F., Hadasch D., Caliandro A., 2013, MNRAS, 430, 1354

Milne D. K., 1979, Australian Journal of Physics, 32, 83

Mineo T., Cusumano G., Maccarone M. C., Massaglia S., Massaro E., Trussoni E., 2001, A&A, 380, 695

Misanovic Z., Kargaltsev O., Pavlov G. G., 2011, ApJ, 735, 33

Mori K. et al., 2013, ApJL, 770, L23

Morsi H. W., Reich W., 1987, A&As, 69, 533

Morton D. C., 1964, Nature, 201, 1308

Morton T. D., Slane P., Borkowski K. J., Reynolds S. P., Helfand D. J., Gaensler B. M., Hughes J. P., 2007, ApJ, 667, 219

Muno M. P. et al., 2006, ApJL, 636, L41

Murphy T., Mauch T., Green A., Hunstead R. W., Piestrzynska B., Kels A. P., Sztajer P., 2007, MNRAS, 382, 382

Murray S. S., Slane P. O., Seward F. D., Ransom S. M., Gaensler B. M., 2002, ApJ, 568, 226

Nagataki S., Hashimoto M.-A., Sato K., Yamada S., Mochizuki Y. S., 1998, ApJL, 492, L45

Nakamori T. et al., 2008, ApJ, 677, 297

Ney E. P., Stein W. A., 1968, ApJL, 152, L21

Ng C.-Y., Slane P. O., Gaensler B. M., Hughes J. P., 2008, ApJ, 686, 508

Olausen S. A., Kaspi V. M., 2014, ApJS, 212, 6

Oppenheimer J. R., Volkoff G. M., 1939, Physical Review, 55, 374

Oskinova L. M., Todt H., Ignace R., Brown J. C., Cassinelli J. P., Hamann W.-R., 2011, MNRAS, 416, 1456

Pacini F., Salvati M., 1973, ApJ, 186, 249

Palmeri P., Mendoza C., Kallman T. R., Bautista M. A., Meléndez M., 2003, A&A, 410, 359

Parent D. et al., 2011, ApJ, 743, 170

Park S., Hughes J. P., Slane P. O., Burrows D. N., Gaensler B. M., Ghavamian P., 2007, ApJL, 670, L121

Park S., Hughes J. P., Slane P. O., Burrows D. N., Lee J.-J., Mori K., 2012, ApJ, 748, 117

Park S., Kargaltsev O., Pavlov G. G., Mori K., Slane P. O., Hughes J. P., Burrows D. N., Garmire G. P., 2009, ApJ, 695, 431

Parmar A. N., Oosterbroek T., Favata F., Pightling S., Coe M. J., Mereghetti S., Israel G. L., 1998, A&A, 330, 175

Patnaude D. J., Fesen R. A., 2009, ApJ, 697, 535

Pavlov G. G., Sanwal D., K z ltan B., Garmire G. P., 2001, ApJL, 559, L131

Pavlov G. G., Zavlin V. E., Sanwal D., Trümper J., 2002, ApJL, 569, L95

Pedaletti G., de Oña Wilhelmi E., Torres D. F., 2014, ArXiv e-prints

Pfeffermann E., Aschenbach B., 1996, in Roentgenstrahlung from the Universe, Zimmermann H. U., Trümper J., Yorke H., eds., pp. 267–268

Pineault S., Joncas G., 2000, AJ, 120, 3218

Pineault S., Landecker T. L., Madore B., Gaumont-Guay S., 1993, AJ, 105, 1060

Pineault S., Landecker T. L., Swerdlyk C. M., Reich W., 1997, A&A, 324, 1152

Pletsch H. J. et al., 2012, ApJL, 755, L20

Porquet D., Decourchelle A., Warwick R. S., 2003, A&A, 401, 197

Porter T. A., Moskalenko I. V., Strong A. W., 2006, ApJL, 648, L29

Prantzos N., 2011, ArXiv e-prints

Qiao W.-F., Zhang L., Fang J., 2009, Research in Astronomy and Astrophysics, 9, 449

Ray P. S. et al., 2011, ApJS, 194, 17

Rea N., Esposito P., 2011, in High-Energy Emission from Pulsars and their Systems, Torres D. F., Rea N., eds., p. 247

Rea N. et al., 2013, ApJL, 775, L34

Rea N. et al., 2010, Science, 330, 944

Rea N. et al., 2012, ApJ, 754, 27

Rea N., Viganò D., Israel G. L., Pons J. A., Torres D. F., 2014, ApJL, 781, L17

Reed J. E., Hester J. J., Fabian A. C., Winkler P. F., 1995, ApJ, 440, 706

Rees M. J., Gunn J. E., 1974, MNRAS, 167, 1

Reich W., Fuerst E., Altenhoff W. J., Reich P., Junkes N., 1985, A&A, 151, L10

Reich W., Fuerst E., Haslam C. G. T., Steffen P., Reif K., 1984, A&AS, 58, 197

Reimer O., Hinton J., Hofmann W., et al., 2008, International Cosmic Ray Conference, 2, 567

Renaud M., 2009, ArXiv e-prints

Renaud M. et al., 2010, ApJ, 716, 663

Reynolds S. P., 1985, ApJ, 291, 152

Reynolds S. P., 1988, ApJ, 327, 853

Reynolds S. P., 1998, ApJ, 493, 375

Reynolds S. P., 2003, ArXiv Astrophysics e-prints

Reynolds S. P., Aller H. D., 1988, ApJ, 327, 845

Reynolds S. P., Borkowski K. J., Hwang U., Hughes J. P., Badenes C., Laming J. M., Blondin J. M., 2007, ApJL, 668, L135

Reynolds S. P., Chevalier R. A., 1984, ApJ, 278, 630

Reynoso E. M., Dubner G. M., Goss W. M., Arnal E. M., 1995, AJ, 110, 318

Reynoso E. M., Green A. J., Johnston S., Goss W. M., Dubner G. M., Giacani E. B., 2004, PASA, 21, 82

Rho J., Petre R., 1997, ApJ, 484, 828

Rho J., Petre R., Schlegel E. M., Hester J. J., 1994, ApJ, 430, 757

Rho J.-H., Petre R., Ballet J., 1998, Advances in Space Research, 22, 1039

Rieger F. M., de Oña-Wilhelmi E., Aharonian F. A., 2013, Frontiers of Physics, 8, 714

Ritchie B. W., Clark J. S., Negueruela I., Langer N., 2010, A&A, 520, A48

Roberts D. A., Goss W. M., Kalberla P. M. W., Herbstmeier U., Schwarz U. J., 1993, A&A, 274, 427

Roger R. S., Milne D. K., Kesteven M. J., Wellington K. J., Haynes R. F., 1988, ApJ, 332, 940

Roy J., Gupta Y., Lewandowski W., 2012, MNRAS, 424, 2213

Rudie G. C., Fesen R. A., 2007, in Revista Mexicana de Astronomia y Astrofisica Conference Series, Vol. 30, Revista Mexicana de Astronomia y Astrofisica Conference Series, pp. 90–95

Russell S. C., Dopita M. A., 1992, ApJ, 384, 508

Rybicki G. B., Lightman A. P., 1979, Radiative processes in astrophysics. Wiley

Safi-Harb S., Harrus I. M., Petre R., Pavlov G. G., Koptsevich A. B., Sanwal D., 2001, ApJ, 561, 308

Safi-Harb S., Kumar H. S., 2008, ApJ, 684, 532

Safi-Harb S., Kumar H. S., 2013, in IAU Symposium, Vol. 291, IAU Symposium, van Leeuwen J., ed., pp. 480–482

Safi-Harb S., Ogelman H., Finley J. P., 1994, in Bulletin of the American Astronomical Society, Vol. 26, American Astronomical Society Meeting Abstracts #184, p. 950

Safi-Harb S., Ogelman H., Finley J. P., 1995, ApJ, 439, 722

Salter C. J., Reynolds S. P., Hogg D. E., Payne J. M., Rhodes P. J., 1989, ApJ, 338, 171

Sanbonmatsu K. Y., Helfand D. J., 1992, AJ, 104, 2189

Sasaki M., Plucinsky P. P., Gaetz T. J., Bocchino F., 2013, A&A, 552, A45

Schlickeiser R., 2002, Cosmic Ray Astrophysics. Springer

Schure K. M., Kosenko D., Kaastra J. S., Keppens R., Vink J., 2009, A&A, 508, 751

Sedov L. I., 1959, Similarity and Dimensional Methods in Mechanics. CRC Press

Seward F. D., Harnden, Jr. F. R., 1982, ApJL, 256, L45

Seward F. D., Harnden, Jr. F. R., Helfand D. J., 1984, ApJL, 287, L19

Seward F. D., Harnden, Jr. F. R., Szymkowiak A., Swank J., 1984, ApJ, 281, 650

Seward F. D., Schmidt B., Slane P., 1995, ApJ, 453, 284

Seward F. D., Slane P. O., Smith R. K., Sun M., 2003, ApJ, 584, 414

Seward F. D., Wang Z.-R., 1988, ApJ, 332, 199

Sezer A., Gük F., Hudaverdi M., Aktekin E., Ercan E. N., 2010, in Astronomical Society of the Pacific Conference Series, Vol. 424, 9th International Conference of the Hellenic Astronomical Society, Tsinganos K., Hatzidimitriou D., Matsakos T., eds., p. 171

Sguera V., Romero G. E., Bazzano A., Masetti N., Bird A. J., Bassani L., 2009, ApJ, 697, 1194

Shapiro S. L., Teukolsky S. A., 2004, Black Holes, White Dwarfs and Neutron Stars, Verlag W.-V., ed. Cornell University

Sidoli L., Mereghetti S., Israel G. L., Bocchino F., 2000, A&A, 361, 719

Slane P., Castro D., Funk S., Uchiyama Y., Lemiere A., Gelfand J. D., Lemoine-Goumard M., 2010, ApJ, 720, 266

Slane P., Chen Y., Schulz N. S., Seward F. D., Hughes J. P., Gaensler B. M., 2000, ApJL, 533, L29

Slane P., Helfand D. J., Reynolds S. P., Gaensler B. M., Lemiere A., Wang Z., 2008, ApJL, 676, L33

Slane P., Helfand D. J., van der Swaluw E., Murray S. S., 2004a, ApJ, 616, 403

Slane P., Seward F. D., Bandiera R., Torii K., Tsunemi H., 1997, ApJ, 485, 221

Slane P., Smith R. K., Hughes J. P., Petre R., 2002, ApJ, 564, 284

Slane P., Zimmerman E. R., Hughes J. P., Seward F. D., Gaensler B. M., Clarke M. J., 2004b, ApJ, 601, 1045

Slane P. O., Helfand D. J., Murray S. S., 2002, ApJL, 571, L45

Slowikowska A., Kanbach G., Borkowski J., Becker W., 2007, in WE-Heraeus Seminar on Neutron Stars and Pulsars 40 years after the Discovery, Becker W., Huang H. H., eds., p. 44

Smith N., 2003, MNRAS, 346, 885

Smith R. K., Hughes J. P., 2010, ApJ, 718, 583

Spitkovsky A., 2008, ApJL, 682, L5

Stephenson F. R., 1971, Q. J. R. Astron. Soc., 12, 10

Stephenson F. R., Green D. A., 2002, Historical supernovae and their remnants, by F. Richard Stephenson and David A. Green. International series in astronomy and astrophysics, vol. 5. Oxford: Clarendon Press, 2002, ISBN 0198507666, 5

Strom R. G., Stappers B. W., 2000, in Astronomical Society of the Pacific Conference Series, Vol. 202, IAU Colloq. 177: Pulsar Astronomy - 2000 and Beyond, Kramer M., Wex N., Wielebinski R., eds., p. 509

Strüder L. et al., 2001, A&A, 365, L18

Su Y., Chen Y., Yang J., Koo B.-C., Zhou X., Jeong I.-G., Zhang C.-G., 2009, ApJ, 694, 376

Sun M., Seward F. D., Smith R. K., Slane P. O., 2004, ApJ, 605, 742

Syrovatskii S. I., 1959, Soviet Astronomy, 3, 22

Tam C., Roberts M. S. E., 2003, ApJL, 598, L27

Tamagawa T. et al., 2009, PASJ, 61, 167

Tanaka S. J., Takahara F., 2010, ApJ, 715, 1248

Tanaka S. J., Takahara F., 2011, ApJ, 741, 40

Tanaka S. J., Takahara F., 2013, MNRAS, 429, 2945

Taylor G. I., 1946, Royal Society of London Proceedings Series A, 186, 273

Taylor J. H., Cordes J. M., 1993, ApJ, 411, 674

Taylor J. H. et al., 1974, IAU Circ., 2704, 1

Taylor J. H., Manchester R. N., Lyne A. G., 1993, ApJS, 88, 529

Temim T. et al., 2006, AJ, 132, 1610

Temim T., Slane P., Arendt R. G., Dwek E., 2012, ApJ, 745, 46

Temim T., Slane P., Gaensler B. M., Hughes J. P., Van Der Swaluw E., 2009, ApJ, 691, 895

Temim T., Slane P., Reynolds S. P., Raymond J. C., Borkowski K. J., 2010, ApJ, 710, 309

Thompson C., Duncan R. C., 1993, ApJ, 408, 194

Thompson C., Duncan R. C., 1996, ApJ, 473, 322

Tian W. W., Leahy D. A., 2008a, ApJ, 677, 292

Tian W. W., Leahy D. A., 2008b, MNRAS, 391, L54

Tian W. W., Li Z., Leahy D. A., Wang Q. D., 2007, ApJL, 657, L25

Toledo-Roy J. C., Velázquez P. F., de Colle F., González R. F., Reynoso E. M., Kurtz S. E., Reyes-Iturbide J., 2009, MNRAS, 395, 351

Tomsick J. A., Chaty S., Rodriguez J., Walter R., Kaaret P., 2009, ApJ, 701, 811

Torii K., Slane P. O., Kinugasa K., Hashimotodani K., Tsunemi H., 2000, PASJ, 52, 875

Torii K., Tsunemi H., Dotani T., Mitsuda K., Kawai N., Kinugasa K., Saito Y., Shibata S., 1999, ApJL, 523, L69

Torii K., Uchida H., Hasuike K., Tsunemi H., Yamaguchi Y., Shibata S., 2006, PASJ, 58, L11

Torres D. F., Cillis A., Martín J., de Oña Wilhelmi E., 2014, Journal of High Energy and Astrophysics, 1, 31

Torres D. F., Cillis A. N., Martín Rodriguez J., 2013, ApJL, 763, L4

Torres D. F., Marrero A. Y. R., de Cea Del Pozo E., 2010, MNRAS, 408, 1257

Torres D. F., Martín J., de Oña Wilhelmi E., Cillis A., 2013, MNRAS, 436, 3112

Trussoni E., Massaglia S., Caucino S., Brinkmann W., Aschenbach B., 1996, A&A, 306, 581

Tsujimoto M. et al., 2011, A&A, 525, A25

Turner M. J. L. et al., 2001, A&A, 365, L27

Tziamtzis A., Lundqvist P., Djupvik A. A., 2009, A&A, 508, 221

Ubertini P. et al., 2005, ApJL, 629, L109

van den Bergh S., 1978, ApJL, 220, L9

van der Swaluw E., 2003, A&A, 404, 939

van der Swaluw E., 2004, Advances in Space Research, 33, 475

Van Der Swaluw E., Achterberg A., Gallant Y. A., 1998, MmSAI, 69, 1017 van der Swaluw E., Achterberg A., Gallant Y. A., Tóth G., 2001, A&A, 380, 309

van der Swaluw E., Downes T. P., Keegan R., 2004, A&A, 420, 937

Van Etten A., Romani R. W., 2011, ApJ, 742, 62

van Veelen B., Langer N., Vink J., García-Segura G., van Marle A. J., 2009, A&A, 503, 495

Vancura O., Blair W. P., Long K. S., Raymond J. C., 1992, ApJ, 394, 158

Vasisht G., Gotthelf E. V., 1997, ApJL, 486, L129

Velusamy T., Becker R. H., 1988, AJ, 95, 1162

Venter C., de Jager O. C., 2007, in WE-Heraeus Seminar on Neutron Stars and Pulsars 40 years after the Discovery, Becker W., Huang H. H., eds., p. 40

Veron-Cetty M. P., Woltjer L., 1993, A&A, 270, 370

Vink J., 2012, A&ARv, 20, 49

Vink J., Bleeker J., Kaastra J. S., Rasmussen A., 2004, Nuclear Physics B Proceedings Supplements, 132, 62

Vink J., Bloemen H., Kaastra J. S., Bleeker J. A. M., 1998, A&A, 339, 201

Vink J., Kaastra J. S., Bleeker J. A. M., 1996, A&A, 307, L41

Vink J., Kaastra J. S., Bleeker J. A. M., 1997, A&A, 328, 628

Vink J., Kuiper L., 2006, MNRAS, 370, L14

Vinyaikin E. N., 2007, Astronomy Reports, 51, 570

Volpi D., Del Zanna L., Amato E., Bucciantini N., 2008, A&A, 485, 337

Vorster M. J., Moraal H., 2013, ApJ, 765, 30

Vorster M. J., Tibolla O., Ferreira S. E. S., Kaufmann S., 2013, ApJ, 773, 139

Vrba F. J., Henden A. A., Luginbuhl C. B., Guetter H. H., Hartmann D. H., Klose S., 2000, ApJL, 533, L17

Wang N., Manchester R. N., Pace R. T., Bailes M., Kaspi V. M., Stappers B. W., Lyne A. G., 2000, MNRAS, 317, 843

Wang Q. D., Gotthelf E. V., 1998, ApJ, 494, 623

Wang Q. D., Gotthelf E. V., Chu Y.-H., Dickel J. R., 2001, ApJ, 559, 275

Wang Z. R., Liu J. Y., Gorenstein P., Zombeck M. V., 1986, Highlights of Astronomy, 7, 583

Warren J. S., Hughes J. P., 2004, ApJ, 608, 261

Warwick R. S. et al., 2001, A&A, 365, L248

Weekes T. C. et al., 1989, ApJ, 342, 379

Weiler K. W., Panagia N., 1978, A&A, 70, 419

Weisberg J. M., Stanimirović S., Xilouris K., Hedden A., de la Fuente A., Anderson S. B., Jenet F. A., 2008, ApJ, 674, 286

Weisskopf M. C. et al., 2000, ApJL, 536, L81

Weltevrede P., Johnston S., Espinoza C. M., 2011, MNRAS, 411, 1917

Whiteoak J. B. Z., Green A. J., 1996, A&AS, 118, 329

Wickramasinghe D. T., Ferrario L., 2005, MNRAS, 356, 1576

Williams B. J. et al., 2008, ApJ, 687, 1054

Willingale R., Aschenbach B., Griffiths R. G., Sembay S., Warwick R. S., Becker W., Abbey A. F., Bonnet-Bidaud J.-M., 2001, A&A, 365, L212

Willingale R., Bleeker J. A. M., van der Heyden K. J., Kaastra J. S., Vink J., 2002, A&A, 381, 1039

Wilson A. S., Weiler K. W., 1976, A&A, 53, 89

Winkler P. F., Clark G. W., Markert T. H., Kalata K., Schnopper H. W., Canizares C. R., 1981a, ApJL, 246, L27

Winkler P. F., Clark G. W., Markert T. H., Petre R., Canizares C. R., 1981b, ApJ, 245, 574

Winkler P. F., Twelker K., Reith C. N., Long K. S., 2009, ApJ, 692, 1489

Woltjer L., 1964, ApJ, 140, 1309

Woods P. M., Thompson C., 2006, Soft gamma repeaters and anomalous X-ray pulsars: magnetar candidates, Lewin W. H. G., van der Klis M., eds., Cambridge University Press, pp. 547–586

Yamaguchi H. et al., 2008, PASJ, 60, 141

Yuan J. P., Wang N., Manchester R. N., Liu Z. Y., 2010, MNRAS, 404, 289

Zajczyk A. et al., 2012, A&A, 542, A12

Zeiger B. R., Brisken W. F., Chatterjee S., Goss W. M., 2008, ApJ, 674, 271

Zhang L., Chen S. B., Fang J., 2008, ApJ, 676, 1210

Zhang L., Jiang Z. J., Lin G. F., 2009, ApJ, 699, 507

Zharikov S. V., Shibanov Y. A., Zyuzin D. A., Mennickent R. E., Komarova V. N., 2008, A&A, 492, 805

Zharikov S. V., Zyuzin D. A., Shibanov Y. A., Mennickent R. E., 2013, A&A, 554, A120

Ziegler M., Baughman B. M., Johnson R. P., Atwood W. B., 2008, ApJ, 680, 620

Zirakashvili V. N., Aharonian F., 2007, A&A, 465, 695

Appendix A

Energy losses equations

Synchrotron energy losses

To derive equation (2.24), we will consider the second Newton's law in its relativistic version

$$f \; = \frac{dp}{d} \tag{A.1}$$

where f is the four-vector force, p is the four-momentum and is the proper time. The electromagnetic force is given by

$$f \; = \frac{q}{c} F \; u \tag{A.2}$$

where q is the charge of the particle, c is the speed of light and u is the four-velocity defined as $u \; = (\; c, \; \vec{v})$. F is the so-called Faraday tensor. In the absence of electric field, equation (A.2) yields

$$m \frac{d}{dt} (\; \vec{v}) = \frac{q}{c} \vec{v} \times \vec{B}, \tag{A.3}$$

$$m \frac{d}{dt} (\; c) = 0. \tag{A.4}$$

The second equation implies that is constant and it can be written out of the derivative. Now, we take the first equation and we separate the velocity in components along the magnetic field ($\vec{v}$) an the perpendicular one ($\vec{v}$)

$$\frac{d\vec{v}}{dt} = 0, \tag{A.5}$$

$$\frac{d\vec{v}}{dt} = \frac{q}{mc}\vec{v}\ \ \times \vec{B}. \tag{A.6}$$

The solution of equation (A.6) is a circular motion projected on the normal plane to the magnetic field. The frequency of rotation is called *gyration* and is given by

$${}_{B} = \frac{qB}{mc}. \tag{A.7}$$

The relativistic form of Larmor's formula, decomposed by the parallel and perpendicular components of the acceleration, is given by

$$\left(\frac{dE}{dt}\right)_L = \frac{2q^2}{3c^3}\ {}^4\left(a^2\ +\ {}^2a^2\right). \tag{A.8}$$

Taking into account that the acceleration is perpendicular to the velocity with magnitude $a\ \ =\ \ {}_{B}v\ \ $, substituing this in equation 1.4, we find

$$\frac{dE}{dt} = \frac{2}{3}r_0^2c\ \ {}^2\ \ {}^2B^2, \tag{A.9}$$

where $r_0 = q^4/(mc^2)^2$ is the classical radius of the electron and $\ \ = v\ \ /c$. If we consider an isotropic distribution of velocities, we must do the average over all possible pitch angles

$$<\ \ {}^2 >= \frac{2}{4}\int \sin^2\ \ d\Omega = \frac{2}{3}\ \ {}^2. \tag{A.10}$$

Subtituting this result in equation (A.9), expliciting the sign of the derivative and writing in terms of the Lorentz factor, we recover equation (2.24)

$${}_{sync}(\ \ ,t) = -\frac{4}{3}\frac{{}_{T}}{m_ec}U_B(t)\ \ {}^2. \tag{A.11}$$

Note that we assume 1.

IC energy losses

The IC energy losses are calculated with the formalism used in Blumenthal & Gould (1970). Consider a target photon gas with a differential number density d$n = n(\ \ {}_i,\hat{\imath})d\ \ {}_id\Omega$, such that d$n$ is the number of photons per cm^{-3} with a frequency within $\ \ {}_i$ and $\ \ {}_i +$ d$\ \ {}_i$ moving in the direction defined by the unitary vector $\hat{\imath}$. In the most general case, the interacting electrons passing through the gas would be described by d$n_e = n_e(\ ,\hat{i}_e)$. The distribution of the scattered photons with frequency $\ _f$ per unit volume and unit time is this case is very complicated to treat, but for our purpose we can do some approximations as considering all the electrons with $\ \gg 1$. Depending on the energy of the target photons in the electron rest frame, we will consider two different regimes: the Thomson limit ($h\ _i \ll m_ec^2$) or the extreme Klein-Nishina limit ($h\ _i \gg m_ec^2$).

The IC energy losses of the electrons would be the same the the energy cointained in the emitted radiation, thus

$${}_{IC} = -\frac{1}{m_ec^2}\frac{dE_{rad}}{dt}. \tag{A.12}$$

In the Thomson limit, the energy of the photons $\ $ in the electron rest frame before and after scattering is $\ _f = \ _i$. The quantity dE_{rad}/dt is invariant since it is the ratio of the same components of two parallel four-vectors. Then,

$${}_{IC} = -\frac{1}{m_ec^2}\frac{dE_{rad}}{dt} = -\frac{1}{m_ec^2}\int \ _Tc \ \ \mathrm{d}n \ = -\frac{{}_TU}{m_ec}, \tag{A.13}$$

being $\ _T$ the Thomson cross section and U the target photon energy density. In the laboratory frame,

$$U \ = \ {}^2\int(1-\cos\ )^2\ \ \mathrm{d}n. \tag{A.14}$$

Considering an isotropic distribution of photons, we average over angles, $<(1-\cos\ )^2>= 4/3$, and we get

$$U \ = \frac{4}{3}\ {}^2\int \ \ \mathrm{d}n = \frac{4}{3}\ {}^2U\ , \tag{A.15}$$

and finally,

$${}_{IC} = -\frac{4}{3}\frac{{}_T}{m_ec}U\ \ {}^2, \tag{A.16}$$

recovering equation (2.25). As we said before, equation (2.25) give the IC energy losses for electrons when the scattering is produced in the Thomson regime. The general case is solved using the Klein-Nishina cross section (Blumenthal & Gould, 1970)

$$\frac{d\ _{KN}}{d\Omega_f d\ _f} = \frac{3}{16}h\ _T\left(\frac{{}_f}{{}_i}\right)^2\left(\frac{{}_i}{{}_f}+\frac{{}_f}{{}_i}-\sin^2\ _f\right)\ \left(\ _f-\frac{{}_i}{1+(\ _i/m_ec^2)(1-\cos\ _f)}\right) \tag{A.17}$$

Jones (1968) computed the scattered photon spectrum per electron is this case giving

$$\frac{dN}{dtd\ _f} = \frac{3}{4}\frac{c\ _T}{{}^2}\frac{n(\ _i)\mathrm{d}\ }{{}_i}f(q,\Gamma\ ), \tag{A.18}$$

where $f(q,\Gamma\ )$, $\Gamma\ $ and q are defined by equations (2.27), (2.28) and (2.29), respectively. The total energy loss rate is given by

$$_{IC} = -\frac{h}{m_e c^2}\int(\ _f - \ _i)\frac{dN}{dtd\ _f}\mathrm{d}\ _f. \qquad \text{(A.19)}$$

The final frequency $\ _f$ will be in general much greater than the initial one $\ _i$. Then, we neglect $\ _i$ and substituing equation (A.18) inside the integral, we get

$$_{IC}(\ ) = -\frac{3}{4}\frac{\ _T h}{m_e c}\frac{1}{\ ^2}\int_0^\infty \ _f\mathrm{d}\ _f\int_0^\infty\frac{n(\ _i)}{\ _i}f(q,\Gamma\ )H(1-q)H\left(q-\frac{1}{4\ ^2}\right)\mathrm{d}\ _i. \qquad \text{(A.20)}$$

The Heaviside functions make explicit the extrem values of the kinematic coefficient q ($1/4\ ^2 \leq q \leq 1$, see Jones 1968).

Bremsstrahlung energy losses

The average energy loss per unit time by Bremsstrahlung emission of an electron is (Haug, 2004)

$$_{Brems} = -Nv\int_0^{\ -1} k\frac{\mathrm{d}\ }{\mathrm{d}k}\mathrm{d}k, \qquad \text{(A.21)}$$

where N is the number density of particles in the medium, v is the velocity of the electrons, $k = h\ /mc^2$ is the photon energy in units of the electron rest energy and $\mathrm{d}\ /\mathrm{d}k$ is the Bremsstrahlung differential cross section. The velocity v can be expressed in terms of the Lorentz factor as $v = c\sqrt{\ ^2-1}/\ $. The exact Breemsstrahlung cross section is a very complicated expression (see e.g., Haug 1998), but we can obtain some useful formulae in the Born approximation. We distinguish two kinds of Bremsstrahlung interaction: the electron-nuclei and the electron-electron Breemsstrahlung.

For the electron-nuclei Breemsstrahlung, the cross section in Born approximation is proportional to the sum S given in equation (2.31). The integral of the cross section can be derived avoiding the calculation of the dilogarithm ocurring in the exact formula.

$$\int_0^{\ -1} k\frac{\mathrm{d}\ }{\mathrm{d}k}\mathrm{d}k \quad \frac{3}{\ } \quad \ _T Z^2\frac{\ ^3}{\ ^2+p^2}\left[\frac{\ }{p}\ln(\ +p) - \frac{1}{3} + \frac{p^2}{\ ^6}\left(\frac{2}{9}\ ^2 - \frac{19}{675}\ p^2 - 0.06\frac{p^4}{\ }\right)\right], \qquad \text{(A.22)}$$

where $p = \sqrt{\ ^2-1}$ is the linear momentum of the electron. This expression has a relative error less than 0.54% throughout (Haug, 2004). For the electron-electron Bremsstrahlung, the integral has a defined upper limit $k_{max} = (\ -1)/(\ -p+1)$. The integral of the cross section in this case is fitted using the function Φ^{e-e}_{rad} defined as

$$\Phi^{e-e}_{rad} = \frac{1}{\;-1}\int_0^{k_{max}} k\frac{\mathrm{d}}{\mathrm{d}k}\mathrm{d}k. \tag{A.23}$$

The fits of this function are given in equation (2.33). Summing both contributions and substituing in equation A.21, we obtain

$$\begin{aligned}{}_{Brems} = \frac{3}{\;}cS\frac{{}^{2}}{{}^{2}+p^2}\left[\;\ln(\;+p)-\frac{p}{3}+\frac{p^3}{{}^{6}}\left(\frac{2}{9}\;{}^{2}-\frac{19}{675}\;p^2-0.06\frac{p^4}{\;}\right)\right]+ \\ c\left(\sum_Z ZN_Z\right)\frac{p}{\;}(\;-1)\Phi^{ee}_{rad}(\;).\end{aligned} \tag{A.24}$$

Adiabatic energy losses

To derive the expression of this energy loss, let us assume that electrons form a non-relativistic Maxwellian gas (afterwards, we will show the relativistic expression). The loss of internal energy dU due to the work done by the expanding gas in a volume dV is

$$\mathrm{d}U = -P\mathrm{d}V, \tag{A.25}$$

where P is the pressure of the gas. Assuming a perfect gas, we can write its equation of state

$$U = \frac{3}{2}nkTV, \tag{A.26}$$

$$P = nkT, \tag{A.27}$$

where n is the number density of particles. Thus, combining these two equations and taking into account that the average energy of each particle is $E = \frac{3}{2}kT$, we can deduce

$$\mathrm{d}U = nV\mathrm{d}E. \tag{A.28}$$

Therefore, diving by the unit time interval dt, from equations (A.25) and (A.28), we get

$$\frac{dE}{dt} = -\frac{2}{3}\frac{E}{V}\frac{dV}{dt}. \tag{A.29}$$

The term dV/dt is the expansion rate of the volume V and this depends on the expansion velocity of the gas $\vec{v}(\vec{r})$. Considering a volume as a cube of sides dx, dy and dz moving with the flow, we can write the expansion of the volume as

$$\frac{\mathrm{d}V}{\mathrm{d}t} = \left(v_{x+\mathrm{d}x} - v_x\right)\mathrm{d}y\,\mathrm{d}z + \left(v_{y+\mathrm{d}y} - v_y\right)\mathrm{d}x\,\mathrm{d}z + \left(v_{z+\mathrm{d}z} - v_z\right)\mathrm{d}x\,\mathrm{d}y. \tag{A.30}$$

Expanding this expression using Taylor series, we find

$$\frac{\mathrm{d}V}{\mathrm{d}t} = \left(\frac{\ v_x}{\ x} + \frac{\ v_y}{\ y} + \frac{\ v_z}{\ z}\right)\mathrm{d}x\,\mathrm{d}y\,\mathrm{d}z = \left(\vec{\nabla}\cdot\vec{v}\right)V. \tag{A.31}$$

Substituting this result into equation (A.29), we get in terms of the Lorentz factor

$${}_{ad} = -\frac{2}{3}\left(\vec{\nabla}\cdot\vec{v}\right)\quad , \tag{A.32}$$

which is the general expression for the adiabatic energy losses. If we want to obtain the expression for the relativistic case, we do the same procedure but we have to consider the internal energy of the gas and its pressure as $U = 3nkTV$ and $P = \frac{1}{3}U$, respectively. Finally, the relativistic form of the adiabatic losses is

$${}_{ad} = -\frac{1}{3}\left(\vec{\nabla}\cdot\vec{v}\right)\quad , \tag{A.33}$$

which differs only in a factor 2 with the non-relativistic expression. In our model, we consider the PWN as an uniform expanding sphere, so the expansion velocity of the gas can be written as

$$v(r) = v_{PWN}(t)\left[\frac{r}{R_{PWN}(t)}\right]. \tag{A.34}$$

The divergence operator for a vector $\vec{f}(r,\ ,\ )$ in spherical coordinates has the form

$$\vec{\nabla}\cdot\vec{f}(r,\ ,\ ) = \frac{1}{r^2}\frac{}{\ r}\left[r^2 f_r(r,\ ,\ )\right] + \frac{1}{r\sin}\frac{}{}\left[\sin\ f\ (r,\ ,\ )\right] + \frac{1}{r\sin}\frac{\ f\ (r,\ ,\ )}{}, \tag{A.35}$$

thus, applying this operator to equation (A.34), we obtain

$$\vec{\nabla}\cdot\vec{v} = \frac{1}{r^2}\frac{\ \ v(r)}{\ r} = 3\frac{v_{PWN}(t)}{R_{PWN}(t)}. \tag{A.36}$$

Finally, subtituting in equation (A.33), we get the expression that we use in our model for the adiabatic energy losses

$${}_{ad}(\ ,t) = -\frac{v_{PWN}(t)}{R_{PWN}(t)}\quad . \tag{A.37}$$

Appendix B

Luminosity equations

Synchrotron luminosity

The formula for the synchrotron luminosity is explained in detail in many publications (e.g., Ginzburg & Syrovatskii 1964, 1965; Blumenthal & Gould 1970; Rybicki & Lightman 1979). In this appendix, we will summarized the calculations following the prescription given by Blumenthal & Gould (1970). For an electron with energy $\ \gg 1$ spiraling around a magnetic field line (see figure B.1), its velocity vector is described as

$$\vec{\ } = \ (\hat{\imath}\cos\Omega t + \hat{\jmath}\sin\Omega t) \tag{B.1}$$

In the laboratory frame, the energy emitted by an electron per unit observer's time ($\tilde{t}$) per unit solid angle in the direction $\hat{n}$ is given by Jackson (1962):

$$\frac{dP(t)}{d\Omega_{\hat{n}}} = \frac{e^2}{4\ \ c}\frac{\ \hat{n}\times[(\hat{n}-\vec{\ })\times\vec{\ }]\ ^2}{(1-\hat{n}\cdot\vec{\ })^6} \tag{B.2}$$

It can be demonstrated (see appendix of Blumenthal & Gould 1970) that the spectrum of the radiation is written as

$$\frac{dI}{d\Omega_{\hat{n}}} = \frac{e^2}{4\ \ c}\ f\ \ \ ^2 \tag{B.3}$$

with

$$f\ \ = \int_{-\infty}^{\infty}\frac{\hat{n}\times[(\hat{n}-\vec{\ })\times\vec{\ }]}{(1-\hat{n}\cdot\vec{\ })^3}\exp(i\ \ \tilde{t})\mathrm{d}\tilde{t}. \tag{B.4}$$

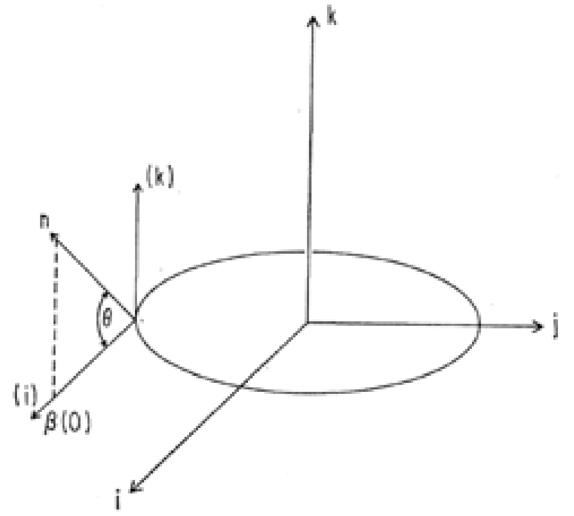

Fig. B.1 Trajectory of an electron spiraling a magnetic field line in the synchrotron luminosity calculation. The energy is emitted in the direction $\vec{n}$. Image taken from Blumenthal & Gould (1970).

The time t at electron's rest frame is related with $\tilde{t}$ by

$$\frac{d\tilde{t}}{dt} = 1 - \hat{n} \cdot \vec{}. \tag{B.5}$$

Integrating this expression, for very distant observers, we have

$$\tilde{t} = t - \frac{\hat{n} \cdot \vec{r(t)}}{c}, \tag{B.6}$$

where a constant term has been ignored as it only contributes an over-all phase factor to f . Changing the variable $\tilde{t}$ by t in equation (B.4) and integrating, we obtain

$$f \;\; = \;\; \int_{-\infty}^{\infty} \hat{n} \times (\hat{n} \times \vec{}) \exp\left[i \quad \left(t - \frac{\hat{n} \cdot \vec{r}}{c} \right) \right] \mathrm{d}t. \tag{B.7}$$

In the laboratory frame, the synchrotron radiation is emitted in an angle $\sim {}^{-1}$. Thus, the electron radiates in a given direction for a time $\Delta t \sim (\Omega \;)^{-1}$. For times greater than this, the exponential in f oscillates rapidly and the integral ends to zero. Jackson (1962) gives an expression for $t - \hat{n} \cdot \vec{r}/c$ as a function of , and Ω

$$t - \frac{\hat{n} \cdot \vec{r}}{c} \quad \frac{1}{2} \left[\left({}^{2} + \frac{1}{{}_{2}} \right) t + \frac{\Omega^2 t^3}{3} \right]. \tag{B.8}$$

In order to solve the double cross product inside the integral in equation (B.7), we change the coordinate system defining the unitary vector $\hat{e} = \hat{n} \times \hat{j}$. In this system, the velocity has the form

$$\vec{\ } = \ (\hat{j}\sin\Omega t + \hat{e}\sin\ \ \cos\Omega t + \hat{n}\cos\ \ \cos\Omega t), \tag{B.9}$$

and then, reducing to the lowest order in and Ωt, we have

$$\hat{n} \times (\hat{n} \times \vec{\ }) = (\hat{e}\ \ + \hat{j}\Omega t). \tag{B.10}$$

Defining $\ = \Omega t$ and substituting in equation (B.7), we get

$$f\ \ = \frac{}{\Omega}\int_{-\infty}^{\infty}(\hat{e}\ \ + \hat{j}\ \ )\exp\left\{\frac{i}{2\Omega}\left[\left(\ ^{2} + \frac{1}{\ ^{2}}\right)\ \ + \frac{\ ^{3}}{3}\right]\right\}\mathrm{d}\ \ . \tag{B.11}$$

To compute the square of $f\ $, we define first the parameters $\ = \ /2\Omega$ and $\ ^{2} = \ ^{2} + 1/\ ^{2}$. We also make a change of variables, defining $x = u + v$ and $y = u - v$ (note that the Jacobian is 2.). Thus,

$$f\ \ ^{2} = \frac{2\ \ ^{2}}{\Omega^{2}}\int_{-\infty}^{\infty}\exp\left[2i\ \ \left(\ ^{2}v + \frac{1}{3}v^{3}\right)\right]\mathrm{d}v\int_{-\infty}^{\infty}(u^{2} - v^{2} + \ ^{2})e^{2i\ \ vu^{2}}\mathrm{d}u. \tag{B.12}$$

We perform the integration in u obtaining

$$f\ \ ^{2} = \frac{2\ \ \bar{\ }\ \ ^{2}}{\Omega^{2}}\int_{-\infty}^{\infty}\left[\sqrt{2\ \ v}e^{i\ \ (\ ^{2} - v^{2})} - \frac{1}{2}(2\ \ v)^{-3/2}e^{-i\frac{}{4}}\right]\exp\left[2i\ \ \left(\ ^{2}v + \frac{1}{3}v^{3}\right)\right]\mathrm{d}v. \tag{B.13}$$

Now, we can substitute $f\ \ ^{2}$ in $dI\ \ /d\Omega_{\hat{n}}$. To integrate the latter term over the solid angle, we can approximate the differential section of solid angle as $d\Omega_{\hat{n}} = 2\ \ \sin(\ /2 - \ )d\ \ \ \ 2\ \ d\ $. Applying this approximation, one integrates $dI\ \ /d\Omega_{\hat{n}}$ and gets

$$I\ \ = -\frac{e^{2}\ \ i}{\Omega c}\int_{-\infty}^{\infty}\left[v - \frac{1}{2\ \ iv^{2}}\right]\exp\left[2i\ \ \left(\frac{v}{\ ^{2}} + \frac{1}{3}v^{3}\right)\right]\mathrm{d}v. \tag{B.14}$$

The second term may be integrated by parts to yield,

$$I\ \ = -\frac{e^{2}\ \ i}{\Omega c}\int_{-\infty}^{\infty}\left(2v - \frac{1}{\ ^{2}v}\right)\exp\left[2i\ \ \left(\frac{v}{\ ^{2}} + \frac{1}{3}v^{3}\right)\right]\mathrm{d}v. \tag{B.15}$$

We can rewrite equation (B.15) such that

$$I \quad = -\frac{e^2\ \ i}{\Omega c}(I^{(1)}+I^{(2)}). \tag{B.16}$$

Setting $v = x/\ $ and $\ = 4\ \ /3\ \ ^3$, the function $I^{(1)}$ yields

$$I^{(1)} = \frac{2}{\ ^2}\int_{-\infty}^{\infty} x\exp\left[i\frac{3}{2}\ \ \left(x+\frac{1}{3}x^3\right)\right]\mathrm{d}x. \tag{B.17}$$

It is useful to write the integrand of the latter equation as an integral,

$$I^{(1)} = -\frac{i}{\ ^2}\int_{\frac{2}{3\Omega\ ^3}}^{\infty}\mathrm{d}\ \ \int_{-\infty}^{\infty}(3x^2+x^4)\left[i\frac{3}{2}\ \ \left(x+\frac{1}{3}x^3\right)\right]\mathrm{d}x. \tag{B.18}$$

Regarding the term $I^{(2)}$, we have

$$I^{(2)} = \frac{1}{\ ^2}\int_{-\infty}^{\infty}\frac{1}{v}\exp\left[2i\ \ \left(\frac{v}{\ ^2}+\frac{1}{3}v^3\right)\right]\mathrm{d}v. \tag{B.19}$$

Differentiating with respect to $\ ^{-2}$ and then integrating from $\ ^{-2}$ to infinity, we get

$$I^{(2)} = -\frac{2i}{\ ^2}\int_{\frac{1}{\ ^2}}^{\infty}\mathrm{d}y\int_{-\infty}^{\infty}\exp\left[2i\ \ \left(vy+\frac{1}{3}v^3\right)\right]\mathrm{d}v. \tag{B.20}$$

Finally, substituting $\ =\ \ /2\Omega$ and changing the variables $x = vy^{-1/2}$ and $\ = (4/3)\ \ y^{3/2}$ yields

$$I^{(2)} = -\frac{i}{\ ^2}\int_{\frac{2}{3\Omega\ ^3}}^{\infty}\mathrm{d}\ \ \int_{-\infty}^{\infty}\exp\left[i\frac{3}{2}\ \ \left(x+\frac{1}{3}x^3\right)\right]\mathrm{d}x. \tag{B.21}$$

Using the expressions obtained for $I^{(1)}$ and $I^{(2)}$, the formula for $I\ \ $ leads

$$I \quad = -\frac{e^2}{\ ^2\Omega c}\int_{\frac{2}{3\Omega\ ^3}}^{\infty}\mathrm{d}\ \ \int_{-\infty}^{\infty}(1+3x^2+x^4)\exp\left[i\frac{3}{2}\ \ \left(x+\frac{1}{3}x^3\right)\right]\mathrm{d}x. \tag{B.22}$$

Integrating over x gives

$$I \quad = \frac{2e^2}{\overline{3}\ \ ^2\Omega c}\int_{\frac{2}{3\Omega\ ^3}}^{\infty}K_{5/3}(\ \ )\mathrm{d}\ \ , \tag{B.23}$$

where $K_{5/3}(\ \ )$ is the modified Bessel function of 5/3 order. The latter equation gives the spectrum of the electron per revolution. To obtain the total power, we must multiply by

$\Omega/2$ and considering that $\ =\ /2$, we recover equation (2.36)

$$P_{syn}(\ ,\ ,B(t)) = \frac{\overline{3}e^3B}{m_ec^2}\frac{}{\ _c}\int_{\frac{}{\ _c}}^{\infty} K_{5/3}(\ )\mathrm{d}\ \qquad \text{(B.24)}$$

with $\ _c$ defined as in equation (1.26). Finally, the total synchrotron luminosity for a distribution of electrons is given by equation (2.39).

IC luminosity

As for the synchrotron luminosity, we also use the prescription given by Blumenthal & Gould (1970). The IC luminosity is deduced easily using equation (A.18), which is the scattered photon spectrum per electron used in the computation of the IC energy losses. Multiplying equation (A.18) by the energy of each photon, we recover equation (2.40)

$$P_{IC}(\ ,\ ,t) = \frac{3}{4}\frac{\ _T ch}{\ ^2}\int_0^{\infty}\frac{n(\ _i)}{\ _i}f(q,\Gamma\ )H(1-q)H\left(q-\frac{1}{4\ ^2}\right)\mathrm{d}\ _i. \qquad \text{(B.25)}$$

The total IC luminosity is finally obtained by doing

$$L_{IC}(\ ,t) = \int_0^{\infty} N(\ ,t)P_{IC}(\ ,\ ,t)\mathrm{d}\ , \qquad \text{(B.26)}$$

recovering equation (2.41).

Bremsstrahlung luminosity

According to Blumenthal & Gould (1970), the Bremsstrahlung spectrum per electron is given by

$$\frac{dN}{dtd\ } = c\sum_s ns\frac{d\ _s}{d\ }, \qquad \text{(B.27)}$$

where $\ $ is the radiated photon frequency. The quantity $d\ _s/d\ $ is the differential Bremsstrahlung cross section, which is given by

$$\frac{d\ _s}{d\ } = \frac{3}{8}\frac{\ d\ }{\ }\frac{1}{\ _i^2}\left[(\ _i^2+\ _f^2)\ _1 - \frac{2}{3}\ _i\ _f\ _2\right], \qquad \text{(B.28)}$$

where $\ _i$, $\ _f$ are the initial and final energies of the electron. The functions $\ _1$ and $\ _2$ depend on $\ _i$, $\ _f$ and $\ $. Assuming a complete ionized plasma, $\ _1 = \ _2 = Z^2\ _u$ with Z is the ion charge number. The function $\ {}_u$ is given by

$$ {}_u = 4\left[\ln\left(\frac{2\ {}_i\ {}_f m_e c^2}{h\ }\right)-\frac{1}{2}\right]. \tag{B.29}$$

Substituting equation (B.28) in equation (B.27), we obtain

$$P_{Brems}(\ {}_i,\ ) = h\ \frac{dN}{dtd\ } = \frac{3}{2}\frac{\ {}_T hcS}{\ {}_i^2}\left(\ {}_i^2 + \ {}_f^2 - \frac{2}{3}\ {}_i\ {}_f\right)\left(\ln\frac{2\ {}_i\ {}_f mc^2}{h\ } - \frac{1}{2}\right), \tag{B.30}$$

where S is given by equation (2.31). From the kinetic condition $h\ /m_e c^2 = \ {}_i - \ {}_f$ and the factor $\ln[2\ {}_i\ {}_f m_e c^2/(h\ )] - 1/2$, we get the minimum initial energy of the electron for a given frequency and final energy of the electron $\ {}_f$

$$ {}_i^{min}(\ ) = \frac{1}{2}\left[\frac{h\ }{m_e c^2} + \sqrt{\left(\frac{h\ }{m_e c^2}\right)^2 + \frac{2h\ }{m_e c^2}\ \exp\left(\frac{1}{2}\right)}\right]. \tag{B.31}$$

Thus, the total Bremsstrahlung luminosity from a distribution of electrons is

$$L_{Brems}(\ ,t) = h\ \int N(\ ,t)\frac{dN}{dtd\ }\mathrm{d}\ = \frac{3}{2}\ \ {}_T hcS\int_{\ {}_i^{min}(\ )}^{\ max}\frac{N(\ {}_i)}{\ {}_i^2}\left(\ {}_i^2 + \ {}_f^2 - \frac{2}{3}\ {}_i\ {}_f\right) \times\left(\ln\frac{2\ {}_i\ {}_f mc^2}{h\ } - \frac{1}{2}\right)\mathrm{d}\ {}_i. \tag{B.32}$$

as is written in equation (2.48).